

„Scale-up and design of gas-assisted atomizers“

Zur Erlangung des akademischen Grades eines
DOKTORS DER INGENIEURWISSENSCHAFTEN (DR.-ING.)

von der KIT-Fakultät für Chemieingenieurwesen und Verfahrenstechnik des
Karlsruher Instituts für Technologie (KIT)
genehmigte

DISSERTATION

von

Simon Wachter, M.Sc.

aus Viernheim

Tag der mündlichen Prüfung: 28.04.2023

Erstgutachter: Prof. Dr.-Ing. Thomas Kolb

Zweitgutachter: Prof. Dr.-Ing. Nikolaos Zarzalis

Acknowledgements

The present dissertation was written during my time as research associate at the Engler-Bunte Institute and the Institute for Technical Chemistry in Karlsruhe. In the following, I would like to thank all those, who have accompanied me during this turbulent and intensive time.

I would particularly like to thank my thesis advisor Prof. Dr.-Ing. Thomas Kolb, who always supported me with his experience and technical knowledge. I thank Prof. Dr.-Ing. Nikolaos Zarzalis for taking over the co-lecture and for the valuable discussions in the field of fluid dynamics.

My work would not have been possible without the support of many colleagues at the institute. Thanks go to Mr. Reis and Mr. Kuntz from the workshop, who repeatedly outed themselves as precision mechanics. I thank Mrs. Bengert for her administrative support and sympathetic ear. I would especially like to thank Mr. Walther for his energetic support during plant maintenance and certification preparation.

In addition, I would like to thank all my student assistants for their active support to this thesis, namely Franz Grossl, Lukas Schröder, Martin Ritter, Jannis Götz, Marius Müller, Felix Dittmar, Benedikt von Lewinski, Patrick Mika, Merlin Wolske, Pia Münzer, Maximilian Wörner, Moritz Dahlinger and Michael Böhm. You have been a gigantic squad.

For the support and many professional discussions, I would like to express my special thanks to my office colleagues Christian Hotz and Manuel Haas as well as the other member of the fluid mechanics group, Friedemann Mörs.

A big thank you goes to Tobias Jakobs. During my time, he provided me with professional support, motivated me and always got me back on track.

My greatest support is my family, Irina and Emilia, as well as Wendelin and Maria-Theresia Wachter.

Simon Wachter

28th October 2022, Stutensee-Friedrichstal

Abstract

The economical and industrial transition towards a circular economy is a main challenge over the next decades. One of the key technologies enabling the closure of the anthropogenic carbon cycle is the entrained flow gasification for chemical recycling of carbon-based materials (e.g. waste and biomass-based residues). In order to achieve complete carbon conversion in a high pressure entrained flow gasifier, the typically suspension based fuels are atomized into fine droplets, leading to high surface area for liquid evaporation and subsequent gasification. The required spray characteristics produced by the commonly applied gas-assisted coaxial atomizers, ranges from a defined spray angle over droplet size and velocity distributions up to integral Sauter mean diameter values. To fit these demands, atomizer geometry, flow configurations and conditions need to be adjusted to fit operating conditions and fuel specifications of the latter industrial process. The focus of this work is therefore set on the scale-up of such atomizers towards increased system pressure and liquid mass flow as well as the comparison of different liquid flow configurations.

First, the effect of system pressure on the resulting spray characteristics was investigated over a wide range of system pressures, gas slit widths, gas velocities and corresponding gas mass flows. As a result, gas momentum flow was identified as a major influencing parameter of resulting droplet size and an empirical correlation for design of gas-assisted coaxial atomizers with central liquid jet towards increased system pressures was derived.

In a second investigation, the effect of liquid mass flow on resulting droplet size was determined for central liquid jet atomizers. The experiments were conducted at constant Weber number, Gas-to-Liquid mass flow ratio and liquid velocity for increasing liquid mass flow. An increase in droplet size with higher liquid mass flow was detected, which was explained by a decrease in gas velocity to achieve the constant Weber number as well as a decrease in the ratio between shearing surface and volume of the liquid phase.

Furthermore, the effect of a variation in the gas channel angle of central liquid jet atomizers was evaluated. It was shown, that a decrease in droplet size with increasing gas channel angle was only achieved for application of low gas velocities. Via measurement of the gas phase velocity, an acceleration of the gas phase and therefore increase in aerodynamic forces was detected for angled gas channels, caused by a reduction in the cross-sectional area of the gas flow after exiting the atomizer orifice.

For ideal comparison of different liquid flow configurations at constant gas momentum flow, velocity and mass flow, an atomizer with three identical (central and annular) orifices was designed. As a major result, the liquid sheet configuration with an outer annular gas stream produced a spray with small integral droplet size over a wide range of liquid viscosities as well as a wide spray angle, compared to the configurations with central liquid jet and annular gas stream or central gas stream and annular liquid sheet. Here, an ideal liquid flow configuration can be expected for the liquid mass flow scale-up of gas-assisted coaxial atomizers towards industrial scale.

Kurzfassung

Der wirtschaftliche und industrielle Übergang zu einer Kreislaufwirtschaft ist eine der größten Herausforderungen der nächsten Jahrzehnte. Eine der Schlüsseltechnologien, die die Schließung des anthropogenen Kohlenstoffkreislaufs ermöglichen, ist die Flugstromvergasung zum chemischen Recycling von kohlenstoffhaltigen Materialien (zum Beispiel Abfälle und Rückstände aus Biomasse). Um eine vollständige Kohlenstoffumwandlung in einem Hochdruck-Flugstromvergaser zu erreichen, werden die typischerweise suspensionsbasierten Brennstoffe in feine Tropfen zerstäubt, um eine große Oberfläche für die Verdampfung der Flüssigkeit und anschließende Vergasung zu generieren. Die erforderlichen Sprayeigenschaften, welche üblicherweise eingesetzte, gasgestützte Zerstäuberdüsen erzeugen, reichen von definiertem Spraywinkel über Tropfengrößen- und Geschwindigkeitsverteilungen bis hin zu integralen Sauterdurchmessern. Um diese Anforderungen zu erfüllen, werden Zerstäubergeometrie, Strömungskonfiguration und –bedingungen an die Betriebsparameter und Brennstoffspezifikationen des jeweiligen industriellen Prozesses angepasst. Der Schwerpunkt dieser Arbeit liegt daher auf der Skalierung solcher Zerstäuberdüsen für erhöhte Systemdrücke und Flüssigkeitsmassenströme, sowie auf dem Vergleich unterschiedlicher Strömungskonfigurationen der Flüssigkeit.

Zu Beginn wurde der Einfluss des Systemdrucks auf die resultierenden Sprayeigenschaften über eine weite Spanne an Systemdrücken, Gasspaltweiten, Gasgeschwindigkeiten und entsprechenden Gasmassenströmen untersucht. Als Ergebnis konnte der Gasimpulsstrom als ein wesentlicher Einflussparameter auf die resultierende Tropfengröße identifiziert und eine empirische Korrelation zur Auslegung gasgestützter Zerstäuberdüsen mit zentraler Strahlvorlage bei erhöhtem Systemdruck abgeleitet werden.

In einer zweiten Untersuchung wurde der Einfluss des Flüssigkeitsmassenstroms auf die resultierende Tropfengröße beim Einsatz von Zerstäuberdüsen zentraler Strahlvorlage ermittelt. Die Experimente wurden bei konstanter Weber-Zahl, konstantem Massenstromverhältnis von Gas- zu Flüssigphase und konstanter Flüssigkeitgeschwindigkeit bei steigendem Flüssigkeitsmassenstrom durchgeführt. Eine Zunahme der Tropfengröße mit steigendem Flüssigkeitsmassenstrom wurde detektiert, was durch eine Verringerung der Gasgeschwindigkeit zum Erreichen konstanter Weber-Zahlen, sowie durch eine Verringerung des Verhältnisses aus Scherfläche und Volumen der Flüssigphase erklärt werden konnte.

Weiterhin wurde die Auswirkung einer Variation des Gasanstellwinkels von Zerstäuberdüsen zentraler Strahlvorlage untersucht. Es konnte gezeigt werden, dass eine Abnahme der Tropfengröße mit steigendem Gasanstellwinkel nur bei Einsatz geringer Gasgeschwindigkeiten erreicht wird. Durch Messung der Gasgeschwindigkeit wurde eine Beschleunigung der Gasphase und damit eine Steigerung der aerodynamischen Kräfte bei angestelltem Gaskanal festgestellt, welche durch eine Verringerung der Querschnittsfläche des Gasstroms nach dem Austritt aus dem Zerstäuber verursacht wird.

Zum idealen Vergleich unterschiedlicher Strömungskonfigurationen der Flüssigkeit bei konstantem Gasimpulsstrom, konstanter Gasgeschwindigkeit und konstantem Gasmassenstrom wurde eine Zerstäuberdüse mit drei identischen (zentralen und ringförmigen) Austrittsöffnungen entworfen. Ein wesentliches Ergebnis war, dass die Strömungskonfiguration mit Zugabe der flüssigen Phase über inneren Ringspalt und Gasstrom über äußeren Ringspalt ein Spray mit geringer integraler Tropfengröße und großem Spraywinkel erzeugte. Vor allem verglichen mit den Strömungskonfigurationen bei denen die Flüssigkeit als zentraler Strahl mit ringförmigem Gasstrom oder Flüssigkeit aus dem inneren Ringspalt und der Gasstrom zentral austritt. Dies lässt eine ideale Strömungskonfiguration der Flüssigkeit für die Skalierung des Flüssigkeitsmassenstroms gasgestützter Zerstäuberdüsen in den industriellen Maßstab erwarten.

Table of contents

Table of contents	VIII
List of figures	X
List of symbols and abbreviations	XII
Latin symbols	XII
Greek symbols	XIII
Dimensionless numbers.....	XIV
Abbreviations	XIV
1 Introduction and scope	1
2 Literature review and approach	3
2.1 System pressure.....	3
2.2 Mass flow scale up	4
2.3 Gas channel angle.....	4
2.4 Comparison of atomizer configuration	5
3 Materials and methods	8
3.1 Atomizer concepts	8
3.2 Atmospheric spray test rig (ATMO)	9
3.3 Pressurized atomization test rig (PAT)	10
3.4 Burner test rig (BTR)	11
3.5 Measurement techniques	12
4 Results and discussion	15
4.1 System pressure.....	15
4.1.1 Influence of system pressure for constant v_{gas} , GLR and J_{gas}	15
4.1.2 Influence of J_{gas}	18
4.2 Mass flow scale up	20
4.3 Gas channel angle.....	22
4.4 Liquid flow configuration	25
5 Summary	30
Appendix	33
A Additional measurements for paper I.....	33
B Additional measurements for paper II	38

C	Additional measurements for paper IV	44
D	Additional measurements for proceeding II.....	46
E	Additional measurements for proceeding I and paper III	49
F	Free jet theory	51
G	Detection of measurement position for mass flow scaled atomizers	52
Literature.....		54
Publications relevant for this thesis.....		62
Complete publication list.....		69

List of figures

Figure 1: Feedstocks and process steps for carbon conversion from wastes and biomass-based residue streams to fuels and chemicals via entrained flow gasification ([3] image modified).....	1
Figure 2: Schematics of the applied atomizer flow configurations as side and front view.	8
Figure 3: Schematics of applied atomizers with straight (left) and angled (right) gas channel.....	9
Figure 4: Schematic of the atmospheric spray test rig with three-fluidic lance and the horizontal cross-sectional view (A - A) in the measurement plane.....	9
Figure 5: Scheme of the pressurized atomization test rig with horizontal cross-sectional view (A - A) of the pressure chamber.....	10
Figure 6: Scheme of the burner test rig with a mounted twin-fluid lance and high-speed camera.....	11
Figure 7: $v_{dr,z,mean}$ (left) and D_{32} (right) as function of radial position at varying p_{sys} . Configuration (i), $d_{liq} = 2$ mm, $\dot{M}_{liq} = 20$ kg·h ⁻¹ , $v_{gas} = 60$ m·s ⁻¹ ($GLR = 0.6$), $\eta_{liq} = 100$ mPa·s.	15
Figure 8: $ID_{32,m}$ as function of p_{sys} for varying v_{gas} (GLR) (left), HSC images of the primary breakup for $v_{gas} = 60$ m·s ⁻¹ at a) $p_{sys} = 1$ bar and b) $p_{sys} = 11$ bar (right). Configuration (i), $d_{liq} = 2$ mm, $\dot{M}_{liq} = 20$ kg·h ⁻¹ , $\eta_{liq} = 100$ mPa·s.	16
Figure 9: $j_{gas,local}$ as function of radial position at varying p_{sys} . Configuration (i), $d_{liq} = 2$ mm, $\dot{M}_{liq} = 20$ kg·h ⁻¹ , $\eta_{liq} = 100$ mPa·s, $v_{gas} = 100$ m·s ⁻¹ ($GLR = 1.0$).	17
Figure 10: D_{32} as function of radial position for varying p_{sys} (left) and s_{gas} (right). Configuration (i), $d_{liq} = 2$ mm, $\dot{M}_{liq} = 20$ kg·h ⁻¹ , $\eta_{liq} = 1$ mPa·s.	18
Figure 11: $ID_{32,m}$ as function of J_{gas} at varying p_{sys} (left). Parity plot of the calculated and measured $ID_{32,m}$ for varying p_{sys} (right). Configuration (i), $d_{liq} = 2$ mm, $\dot{M}_{liq} = 20$ kg·h ⁻¹ , $\eta_{liq} = 1$ mPa·s.	19
Figure 12: $ID_{32,m}$ as function of \dot{M}_{liq} (d_{liq}) at varying We_{aero} (GLR). Configuration (i), $\eta_{liq} = 1$ mPa·s, $p_{sys} = 1$ bar.	20

Figure 13: ID_{32} as function of J_{gas} for varying \dot{M}_{liq} (d_{liq}) (left), Parity plot for comparison between measured and calculated ID_{32} values (right). Configuration (i), $\eta_{liq} = 1$ mPa·s, $p_{sys} = 1$ bar.....	21
Figure 14: D_{32} and $v_{dr,z,mean}$ as function of radial position at varying α (left), v_{abs} for varying α (right). Configuration (i), $d_{liq} = 2$ mm, $p_{sys} = 1$ bar, $v_{gas} = 60$ m·s ⁻¹	23
Figure 15: HSC images of the primary jet breakup applying atomizers with $\alpha = 0 / 15 / 30^\circ$ at $v_{gas} = 60$ m·s ⁻¹ ($GLR = 0.6$), $\eta_{liq} = 200$ mPa·s and $p_{sys} = 1$ bar (left). Scheme of the emerging gas and liquid phase as well as the corresponding impact area for $\alpha = 15 / 30^\circ$ (right).....	23
Figure 16: $ID_{32,m}$ as function of α for varying η_{liq} , v_{gas} (GLR), p_{sys} (left), HSC images of the primary jet breakup at $v_{gas} = 60$ m·s ⁻¹ ($GLR = 0.6$) and $\eta_{liq} = 1$ mPa·s for a) $\alpha = 0^\circ$, $p_{sys} = 11$ bar, b) $\alpha = 30^\circ$, $p_{sys} = 11$ bar, c) $\alpha = 0^\circ$, $p_{sys} = 1$ bar and d) $\alpha = 30^\circ$, $p_{sys} = 1$ bar (right). Configuration (i), $d_{liq} = 2$ mm, $\dot{M}_{liq} = 20$ kg·h ⁻¹	24
Figure 17: $ID_{32,m}$ as function of v_{gas} (GLR) at varying atomizer configuration (left), HSC images of the primary jet and sheet breakup for: a) configuration (i), $v_{gas} = 60$ m·s ⁻¹ ($GLR = 0.2$), b) configuration (i), $v_{gas} = 150$ m·s ⁻¹ ($GLR = 0.5$), c) configuration (ii), $v_{gas} = 60$ m·s ⁻¹ ($GLR = 0.2$) and d) configuration (ii), $v_{gas} = 150$ m·s ⁻¹ ($GLR = 0.5$) (right). $\dot{M}_{liq} = 30$ kg·h ⁻¹ , $\eta_{liq} = 1$ mPa·s, $p_{sys} = 1$ bar.....	25
Figure 18: $ID_{32,m}$ as function of GLO for varying GLR (left) and J_{gas} for varying GLR (right). Configuration (iii), $\dot{M}_{liq} = 30$ kg·h ⁻¹ , $\eta_{liq} = 1$ mPa·s, $p_{sys} = 1$ bar.	27
Figure 19: $ID_{32,m}$ as function of η_{liq} at varying configurations and GLO (left). HSC images of the primary breakup for a) configuration (i) at $GLR = 0.5$ and $\eta_{liq} = 1$ mPa·s, b) configuration (iii) at $GLO = 0.5$ and $\eta_{liq} = 1$ mPa·s, c) configuration (i) at $GLR = 0.5$ and $\eta_{liq} = 400$ mPa·s as well as d) configuration (iii) at $GLO = 0.5$ and $\eta_{liq} = 400$ mPa·s. $\dot{M}_{liq} = 30$ kg·h ⁻¹ , $p_{sys} = 1$ bar, $GLR = 0.5$	28
Figure 20: Context of the discussed research topics and the significance in the field of burner development.....	32

List of symbols and abbreviations

Latin symbols

symbol	unit	name
A	-	correlation parameter
A_{gas}	m ²	gas orifice area
A_i	m ²	annulus area at position i
b	mm	tube thickness
B	-	correlation parameter
C	-	correlation parameter
d_{eq}	mm	equivalent diameter
d_{gas}	mm	gas orifice diameter
d_{liq}	mm	liquid jet diameter
$d_{liq,sheet}$	mm	liquid sheet diameter
D	μm	droplet diameter
$D_{20,i}$	μm	surface mean diameter at position i
$D_{30,i}$	μm	volume mean diameter at position i
D_{32}	μm	Sauter mean diameter
f_{HSC}	mm	focal length of HSC
i	mm	measurement position / rel. phase
ID_{32}	μm	integral Sauter mean diameter
$ID_{32,m}$	μm	integral, mass-weighted Sauter mean diameter
$ID_{32,m,calculated}$	μm	integral, mass-weighted Sauter mean diameter (calculated)
$ID_{32,m,measured}$	μm	integral, mass-weighted Sauter mean diameter (measured)
\dot{j}_{gas}	N·m ⁻²	gas momentum flux
$\dot{j}_{gas,local}$	N·m ⁻²	local gas momentum flux
J_{gas}	N	gas momentum flow
$J_{gas,i}$	N	gas momentum flow of inner jet
$J_{gas,o}$	N	gas momentum flow of outer jet
J_{liq}	N	liquid momentum flow
l_{slit}	μm	slit width (PDA)

symbol	unit	name
\dot{m}_i	$\text{kg}\cdot\text{m}^{-2}\cdot\text{h}^{-1}$	mass flux at position i
\dot{M}_{gas}	$\text{kg}\cdot\text{h}^{-1}$	gas mass flow
\dot{M}_{liq}	$\text{kg}\cdot\text{h}^{-1}$	liquid mass flow
$\dot{M}_{liq,P1}$	$\text{kg}\cdot\text{h}^{-1}$	liquid mass flow range of P1
$\dot{M}_{liq,P2}$	$\text{kg}\cdot\text{h}^{-1}$	liquid mass flow range of P2
p_{sys}	bar	system pressure
p_{vessel}	bar	vessel pressure
S_{gas}	mm	gas slit width
S_{liq}	mm	liquid sheet thickness
V_{abs}	$\text{m}\cdot\text{s}^{-1}$	absolute velocity
$V_{dr,z,mean}$	$\text{m}\cdot\text{s}^{-1}$	mean droplet velocity (z direction)
V_{gas}	$\text{m}\cdot\text{s}^{-1}$	gas velocity
$V_{gas,i}$	$\text{m}\cdot\text{s}^{-1}$	gas velocity of inner jet
$V_{gas,o}$	$\text{m}\cdot\text{s}^{-1}$	gas velocity of outer jet
V_{liq}	$\text{m}\cdot\text{s}^{-1}$	liquid velocity
V_{rel}	$\text{m}\cdot\text{s}^{-1}$	relative velocity
\dot{V}_{gas}	$\text{m}^3\cdot\text{h}^{-1}$	gas volume flow
x	mm	x-direction
y	mm	y-direction
z	mm	z-direction

Greek symbols

symbol	unit	name
α	$^\circ$	gas channel angle
δ	-	empirical constant
Δ	-	difference
η_{liq}	$\text{mPa}\cdot\text{s}$	dynamic viscosity
λ_{laser}	nm	wave length of laser light
ρ_{gas}	$\text{kg}\cdot\text{m}^{-3}$	gas density
σ	$\text{N}\cdot\text{m}^{-1}$	surface tension
Φ / Φ_R	$^\circ$	off-axis angle

Dimensionless numbers

symbol	name	definition
GLI	inner Gas-to-Liquid mass flow ratio	$GLI = \frac{\dot{M}_{gas,i}}{\dot{M}_{liq}}$
GLO	outer Gas-to-Liquid mass flow ratio	$GLO = \frac{\dot{M}_{gas,o}}{\dot{M}_{liq}}$
GLR	Gas-to-Liquid mass flow ratio	$GLR = \frac{\dot{M}_{gas}}{\dot{M}_{liq}}$
j	momentum flux ratio	$j = \frac{v_{gas}^2 \cdot \rho_{gas}}{v_{liq}^2 \cdot \rho_{liq}}$
J	momentum flow ratio	$J = \frac{v_{gas}^2 \cdot \rho_{gas} \cdot A_{gas}}{v_{liq}^2 \cdot \rho_{liq} \cdot A_{liq}}$
Re_{liq}	Reynolds number of liquid phase	$Re_{liq} = \frac{\rho_{liq} \cdot v_{liq} \cdot d_{liq}}{\eta_{liq}}$
We_{aero}	aerodynamic Weber number	$We_{aero} = \frac{v_{rel}^2 \cdot \rho_{gas} \cdot d_{liq}}{\sigma}$
$We_{aero,sheet}$	aerodynamic Weber number for sheet nozzles	$We_{aero,sheet} = \frac{v_{rel}^2 \cdot \rho_{gas} \cdot S_{liq}}{\sigma}$

Abbreviations

symbol	name
ATMO	Atmospheric spray test rig
BTR	Burner test rig
CCD	Charge-coupled device
DEHS	Di-ethyl-hexyl-sebacat
EFG	Entrained flow gasification
HSC	High-speed camera
KHI	Kelvin-Helmholtz instability
KIT	Karlsruhe Institute of Technology
LDA	Laser Doppler anemometry
LED	Light-emitting diode
PAT	Pressurized atomization test rig
PDA	Phase Doppler anemometry
PIV	Particle image velocimetry
SZ	Shadowsizer

1 Introduction and scope

In order to achieve sustainable growth, the European Commission introduced the European Green Deal in 2020, in which one of the main tasks, besides the reduction of greenhouse gases, is the transition towards a carbon circular economy [1]. Therefore key technologies that enable the chemical recycling of carbon-based materials, e.g. into synthesis gas (CO/H_2), must be identified. One of these technologies is the entrained flow gasification (EFG), which fits both biomass-based as well as anthropogenic waste and residue streams (see Figure 1) [2].

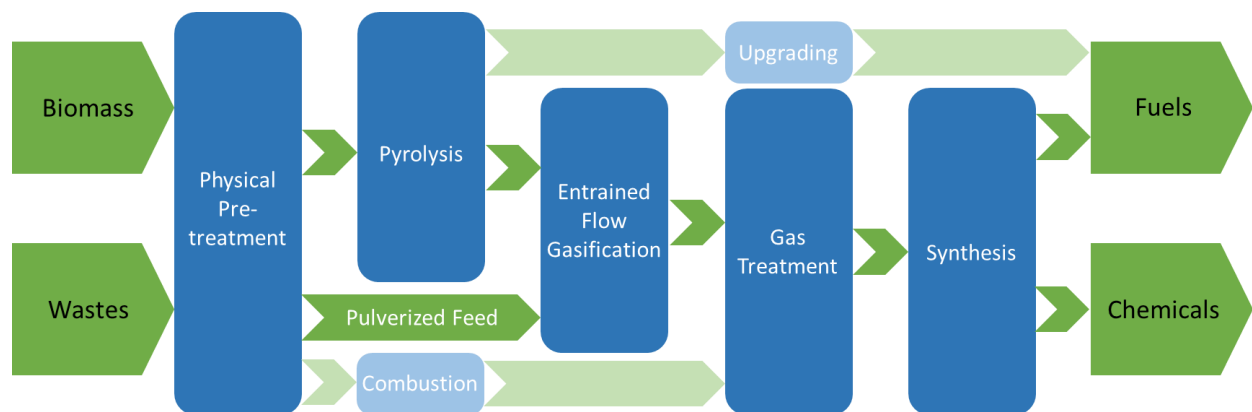


Figure 1: Feedstocks and process steps for carbon conversion from wastes and biomass-based residue streams to fuels and chemicals via entrained flow gasification ([3] image modified).

For proof of concept and technology investigation from the lab to the demo scale, at the Karlsruhe Institute of Technology (KIT) an EFG unit with system pressure of 40 bar is operated [4]. Here, the feedstocks are typically suspension fuels that feature viscosities of up to 1000 mPa·s and additional complex rheological flow behavior. In the gasifier, the fuel jet is atomized into droplets. The liquid phase of the droplets evaporates, whereas remaining solid particles are converted via heterogeneous gasification reactions. As latter process steps in the gasifier require a high surface area for fast evaporation and complete carbon conversion, the atomization of the introduced jet into a fine and homogeneous spray is one of the main challenges in EFG operation. For atomization of these liquids, external-mixing, gas-assisted burner nozzles with various flow configurations are commonly applied. Here, the slowly moving liquid is disintegrated by a high-velocity gas stream after exiting the atomizer orifice. As the atomization agent also serves as reactant, the operating conditions of the atomizers are typically limited in terms of gas-to-liquid mass flow ratio (GLR) to $GLR < 1$ [5,6]. External-mixing, gas-assisted atomizers are often utilized at significantly higher GLR , indicating that the disintegration of high-viscosity fuels

under increased system pressure conditions is a challenging task. The present dissertation aims for the design of an atomizer for EFG operation with technical fuels. As EFG is typically performed at elevated system pressures, research question 1 “**How are spray characteristics affected by an increase in system pressure?**” (paper I & II) is focused first. Additionally, these systems are utilized in the industrial scale at high liquid throughputs. Therefore, research question 2 “**How are spray characteristics affected by an increase in liquid mass flow?**” (paper IV) must be replied. In industrial application, typical external-mixing atomizers are constructed with an angle between liquid jet and surrounding gas channel. This arises research question 3 “**How is the disintegration process of a liquid jet influenced by an angle between gas and liquid phase at the atomizer orifice?**” (proceeding II). Beside the typical central liquid jet configuration of coaxial atomizers, also other liquid flow configurations via liquid sheet appear utilizable. Hence, research question 4 “**Which atomizer flow configuration (liquid jet or liquid sheet) results in smaller droplet sizes?**” (proceeding I & paper III) needs to be answered.

In order to answer these research questions the following cumulative dissertation, which is based on four scientific journal articles and two conference proceedings was written. Chapter 2 gives a short literature review on the topics of the respective research question and an approach to achieve the corresponding answers. An overview on the atomizer design, applied test rigs and measurement techniques is shown in chapter 3. Major results from the journal articles and the proceedings are discussed in chapter 4, whereas the complete publications are attached to the thesis in the appendix. Chapter 5 gives a summary on the answers to the research questions and an outlook.

2 Literature review and approach

2.1 System pressure

The disintegration of a liquid jet into droplets via external-mixing gas-assisted atomizers is typically performed with an annular gas stream at high momentum flow. Here, the typically fast moving gas phase shears the exiting liquid near the atomizer orifice, which induces liquid instabilities, followed by primary and secondary breakup. For description of the atomization process and the resulting droplet size, commonly dimensionless numbers as aerodynamic Weber number We_{aero} or momentum flow ratio J are utilized.

Regarding a solely increase in system pressure, which equals an increase in the aforementioned We_{aero} and J , a decrease in droplet size and an enhancement of the atomization process is expected. This effect was confirmed by many authors for various system pressure ranges, atomizer configurations and liquid viscosities [7–12]. As an additional boundary condition, an increase in GLR with increasing system pressure was required in order to keep exiting gas velocity constant. As against this, Risberg et al. [13] and Gullberg et al. [14] investigated the atomization process at various system pressures, but constant gas velocity and GLR (adjusting \dot{M}_{liq}). This resulted in an increasing primary breakup length and droplet size for higher system pressures. Further experiments by Jakobs et al. [15] and Fong et al. [16] led to similar results for increasing system pressure while keeping We_{aero} constant, as therefore v_{gas} needs to be reduced with every system pressure step.

As can be seen from this literature summary, the effect of an increase in system pressure on the resulting spray characteristics is always dependent on the applied boundary conditions of gas velocity, gas mass flow, GLR and J . In order to keep these identified boundary conditions constant while increasing p_{sys} and to answer research question 1, two investigations were performed. In the first set of experiments, an increase in system pressure was realized, while keeping v_{gas} , GLR and \dot{M}_{gas} constant, as these parameters affect atomization and are of interest for the later process application (e.g. EFG). To achieve these constant parameters, for every system pressure step, one atomizer with corresponding gas orifice area (i.e. s_{gas}) was utilized. In a second investigation, the effect of all parameters forming J_{gas} was investigated by varying v_{gas} , p_{sys} , s_{gas} and GLR with the objective of an empirical system pressure scaling approach.

2.2 Mass flow scale up

While performing a literature review on gas-assisted coaxial atomizers, found studies are mostly investigated at low liquid or gas mass flows in order to see the influencing effect on primary jet breakup more clearly or to apply laser-based measuring systems for detection of droplet size at their optimum. A conversion of these results towards increased liquid mass flows is often necessary for industrial application, but challenging, as an increase in v_{liq} or \dot{M}_{liq} utilizing one atomizer leads to a significant higher droplet size [17]. Therefore, Leroux et al. [18,19] performed experiments in the atomizer near and far field (e.g. primary breakup and resulting droplet size) with three d_{liq} and three d_{gas} , which can be compared individually. As a scaling approach the authors kept Re_{liq} and j constant, while changing d_{liq} in a range of $d_{liq} = 0.4 - 2.0$ mm. With increasing d_{liq} , a change in primary breakup from prompt atomization to the formation of large droplets and ligaments occurred.

Regarding this study, keeping Re_{liq} and j constant, led to a significant decrease in J for higher d_{liq} . As J represents the aerodynamic forces relevant for the atomization process, an increase in droplet size was detected. A scaling rule for keeping the resulting droplet size constant, while increasing liquid mass flow, was not specified.

To answer research question 2 and start to fill the knowledge gap regarding the topic of liquid mass flow scale up of gas-assisted coaxial atomizers, an approach for derivation of scaling rules from the lab to the industrial scale was needed. In the present study, therefore atomizers according to the following design were investigated: (i) v_{liq} was kept constant while increasing \dot{M}_{liq} , which required an increase in d_{liq} and one atomizer for every \dot{M}_{liq} step. (ii) GLR was kept constant, which requires increasing \dot{M}_{gas} for higher \dot{M}_{liq} . (iii) We_{aero} was kept constant, which results in lower v_{gas} , as d_{liq} increases with higher \dot{M}_{liq} .

2.3 Gas channel angle

Typically, research studies on gas-assisted coaxial atomization are performed with atomizers, consisting of a central, straight tube for liquid supply, surrounded by a straight, annular exit for the high velocity gas phase. As against this, for industrial application, often coaxial atomizers with a converging (straight inner wall, angled outer wall) or angled gas channel (angled inner and outer wall) are applied [6,20–23]. Hardalupas et al. [24] performed experiments, which compare the resulting droplet size of an atomizer with straight and converging ($\alpha = 28^\circ$) gas channel. As a result, a decrease in droplet size was detected for the converging atomizer. Above a gas-to-liquid velocity ratio of $v_{gas}/v_{liq} = 50$, no further changes in droplet size were measurable, without further explanation. Varga et

al. [25] also compared a straight and converged atomizer, determining a similar effect on droplet size over all measuring conditions. In this study, the decrease in droplet size was attributed to a decrease in the boundary layer thickness. Bieber et al. [26] compared two gas-assisted coaxial atomizers with straight gas channel and gas channel of $\alpha = 45^\circ$. For $\alpha = 45^\circ$, a smaller droplet size and corresponding higher $v_{dr,z,mean}$ was found. The results were explained by an increased shear rate at the atomizer orifice while applying an angled gas channel.

As shown, previous investigations mainly focused on the comparison between straight and angled gas channel atomizers. Research on the increment effect of this angle leading to changes in primary breakup and resulting droplet size have not been performed yet. Additionally, the decrease in resulting droplet size for angled gas channel atomizers was explained by three different effects (i.e. ratio of gas-to-liquid velocity, change in boundary layer thickness, variation in the shear rate).

In order to answer research question 3 and clarify the effect of gas channel angle on primary breakup as well as resulting droplet size, atomizers with different gas channel angles were used and investigated at a wide range of operating conditions (i.e. v_{gas} (GLR), p_{sys} and η_{liq}). For explanation of the gas channel angle effects, the gas phase was seeded and gas velocity measured via particle image velocimetry.

2.4 Comparison of atomizer configuration

Regarding the liquid and gas flow concerning gas-assisted coaxial atomizers, a wide field of flow configurations is possible. Beside the aforementioned research on central liquid jet atomization, in the literature also configurations with an annular liquid sheet and central gas jet or additional gas sheet can be found. These sheet configurations allow among others for small liquid sheet thickness, also for significant increment in liquid mass flow. Investigations on liquid sheet atomization with one central gas jet were performed by Leboucher et al. [27] and Zhao et al. [28], presenting morphological classifications of the liquid sheet breakup via high-speed camera. Main difference between both regime diagrams is the application over J_{gas} and J_{liq} as against $We_{aero,sheet}$ and $S_{liq}/d_{liq,sheet}$. First radial droplet size measurements were only recorded at $v_{gas} > 180 \text{ m}\cdot\text{s}^{-1}$ by Li et al. [29], showing a V-shaped profile and a slight dependence of droplet size on changes in v_{gas} . Taking an additional angled outer gas sheet into account, Carvalho et al. [30] recorded high-speed camera images of the resulting spray at varying v_{liq} , $v_{gas,i}$, $v_{gas,o}$, S_{liq} as well as an outer gas swirl ratio. As $v_{gas,i}$ was changed up to $v_{gas,i} = 200 \text{ m}\cdot\text{s}^{-1}$ and $v_{gas,o}$ was only increased to $v_{gas,o} = 40 \text{ m}\cdot\text{s}^{-1}$, $v_{gas,i}$ was identified in this study to be more relevant for liquid sheet disintegration. Wahono et al. [31] used a high-speed camera in order to detect

primary breakup mechanisms of a liquid sheet in further detail, utilizing an atomizer with straight inner and outer gas exit channels. As a result, it was shown, that primary breakup of the sheet was mainly affected by $J_{gas,o}$, $J_{gas,i}$ and J_{gas} . A dependency between a sheet rupturing Kelvin-Helmholtz surface wave and $J_{gas,o}$ was found. An additional instability for liquid sheet breakup was found by Duke et al. [32,33], whereas the previously detected Kelvin-Helmholtz instability was only formed for sufficiently high relative velocity ($\Delta v > 30 \text{ m}\cdot\text{s}^{-1}$) between liquid sheet and outer gas stream. Further details on stability investigations can be found in Cao et al. [34], Ibrahim et al. [35] and Lee et al. [36]. Summarizing the results of these stability studies, a higher atomization efficiency was ascribed to the inner gas jet in contrast to the outer gas stream. Further scale up experiments for these atomizers were performed by Duke et al. [37], showing that s_{liq} has a dominant effect on the resulting spray characteristics. Continuing the studies mentioned before, Leboucher et al. [38] conducted radial droplet size measurements of annular liquid sheet atomizers at varying gas swirl ratio. In this study, mainly the inner gas jet led to a reduction in droplet size, compared to the outer gas stream. While the $v_{gas,i}$ was set up to $v_{gas,i} = 180 \text{ m}\cdot\text{s}^{-1}$, $v_{gas,o}$ was only investigated up to $v_{gas,o} = 90 \text{ m}\cdot\text{s}^{-1}$. Zhao et al. [39] performed laser diffraction measurements, where a maximum in droplet size was found at $v_{gas,o} = 30 - 40 \text{ m}\cdot\text{s}^{-1}$, with no effect by $v_{gas,i}$. By the authors, the assumption was made, that the liquid sheet is accelerated by the outer gas stream, leading to a decrease in relative velocity between liquid sheet and the dominant, inner gas jet.

As described in the literature review, many studies were performed on the influence of the inner and outer gas stream, regarding the resulting spray characteristics. Most of the studies revealed, that the inner gas jet has a dominant effect on the resulting droplet size, compared to the outer gas stream. However, the outer gas stream velocity was kept at least a factor of two smaller in comparison with the inner gas jet velocity for all investigations [30,34–36,38]. The main reason for this gas velocity arrangement is the geometrical setup of annular liquid sheet atomizers, which are designed with a small central gas jet diameter, implying small gas mass flows lead to high $v_{gas,i}$. Additionally, large outer gas orifice areas arise as a result of positioning, where comparable gas mass flows lead to small $v_{gas,o}$. Taking a closer look from a geometrical point of view, the outer gas stream should have an increased influence on droplet size, as the impact area for shear forces on the liquid sheet is increased, as against the inner sheet surface area.

In order to answer research question 4 and describe the effect of gas velocity arrangement on primary breakup and resulting droplet size more clearly, an atomizer design with annular liquid sheet, central gas jet and outer gas stream was designed with three identical exiting orifice areas. This allows in a first set of experiments for ideal comparison of gas velocity influence between inner and outer gas stream. Furthermore,

by changes in flow configuration, an optimal comparison between all three flow configurations is made possible, as atomization relevant parameters (i.e. v_{gas} , v_{liq} , GLR and J) remain constant. Additionally, liquid viscosity was increased for designated operating conditions in order to identify the dependency of droplet size on viscosity for liquid sheet atomizers.

3 Materials and methods

Experimental investigations and measurements for this thesis were performed with three different atomizer configurations in three different test rigs, which are described in the chapters 3.1 - 3.4. In chapter 3.5, the measurement techniques, applied settings and extracted data are discussed.

3.1 Atomizer concepts

3 different external-mixing gas-assisted atomizer concepts were utilized for the experiments performed in this work. The following enumeration was chosen to differentiate between the applied atomizer concepts. Configuration (i) defines the central liquid jet (d_{liq}) atomizer with annular gas stream (s_{gas}). Configuration (ii) represents the annular liquid sheet (s_{liq}) atomizer only using gas from the central gas tube (d_{gas}). Configuration (iii) specifies the annular liquid sheet (s_{liq}) atomizer while applying gas mass flows via both gas orifices (d_{gas} and s_{gas}). Figure 2 depicts the sectional drawings, as well as a front view of the atomizer flow configurations.

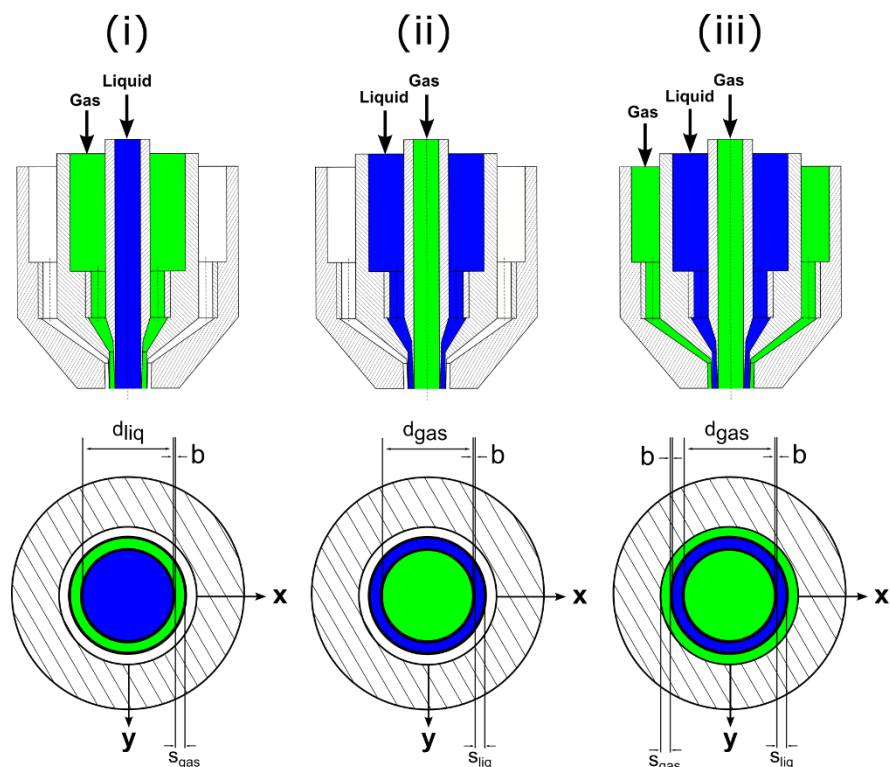


Figure 2: Schematics of the applied atomizer flow configurations as side and front view.

In order to reduce the influence of gas boundary layer and enable undisturbed gas flow avoiding vortex formation directly at the atomizer orifice, the tube thicknesses between

gas and liquid phase are reduced to $b = 0.1$ mm. In accordance to Tian et al. [40] this size guarantees for undisturbed flow. The depicted atomizers feature parallel channels for gas and liquid phase to enable optimal comparison with results presented already in literature [17,41,42]. An angle between gas and liquid phase, which is typically applied for industrial application, is defined with α (see Figure 3).

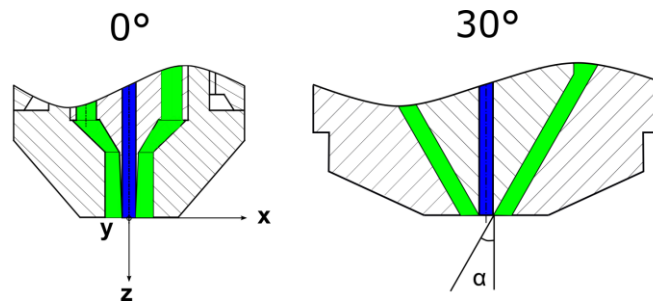


Figure 3: Schematics of applied atomizers with straight (left) and angled (right) gas channel.

3.2 Atmospheric spray test rig (ATMO)

The measurements for papers III, IV and proceeding I, II were performed at the atmospheric spray test rig (ATMO), which is depicted in Figure 4 as schematic for operation of liquid sheet nozzles.

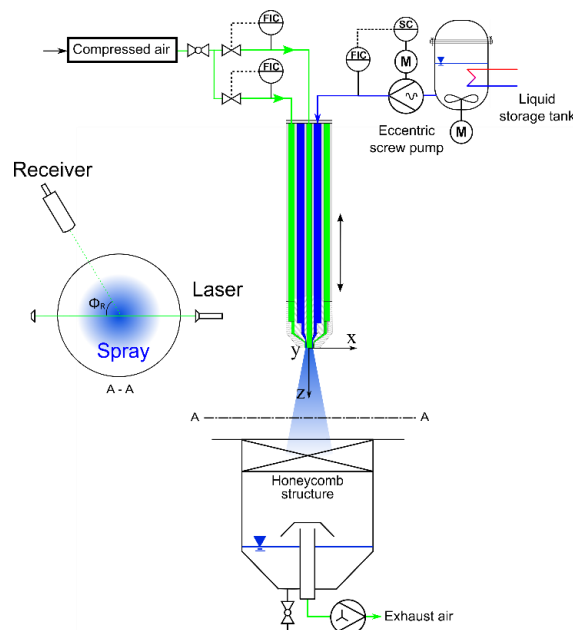


Figure 4: Schematic of the atmospheric spray test rig with three-fluidic lance and the horizontal cross-sectional view (A - A) in the measurement plane.

The ATMO consists of a two- or three-fluidic lance, where the nozzle is mounted, a collection container with exhaust air system and separate liquid as well as gas supply system. The liquid or suspension is fed out of a stirred and tempered tank with an

eccentric screw pump, controlled by Coriolis density and mass flow meter (range: $\dot{M}_{liq} = 5 - 100 \text{ kg}\cdot\text{h}^{-1}$). The atomizing air flow is delivered by the compressed air system, whereas two parallel hot wire anemometers with integrated valve measures and regulates the gas mass flow in a range of $\dot{M}_{gas} = 0.5 - 90 \text{ kg}\cdot\text{h}^{-1}$, respectively. The measurement techniques are mounted on a 2D traverse system with motion in x/y -plane, shown as horizontal cross-sectional view (A – A). In order to reduce recirculation effects of droplets, a honeycomb structure was mounted in the container and utilized as a flow straightener and coalescence promoter. The exhaust air is removed by a suction system.

3.3 Pressurized atomization test rig (PAT)

The pressurized atomization test rig (PAT) enables for spray characterization at increased system pressures of $p_{sys} = 1 - 21 \text{ bar}$. The test rig was used for data acquisition in papers I, II and proceeding II. A scheme of the test rig is shown in Figure 5.

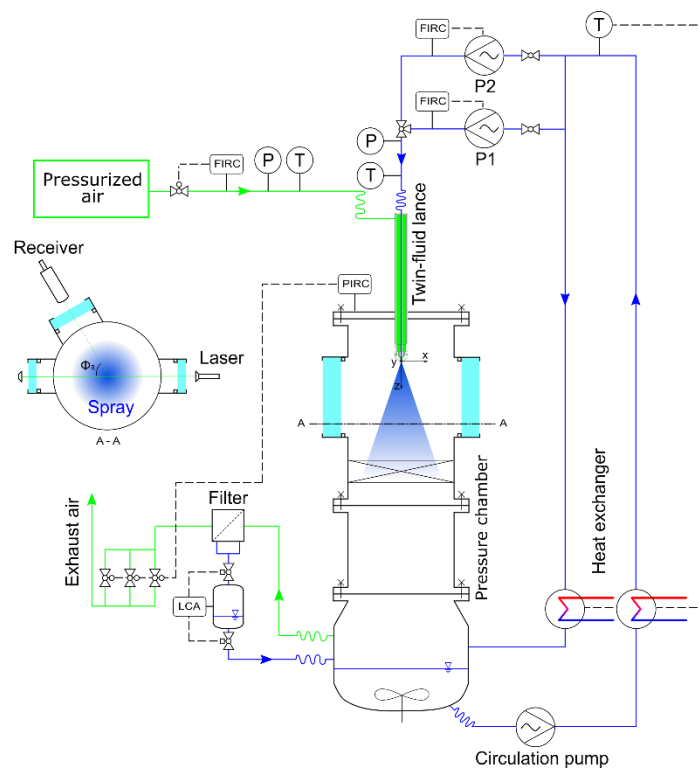


Figure 5: Scheme of the pressurized atomization test rig with horizontal cross-sectional view (A - A) of the pressure chamber.

The test rig consists of a pressure chamber with a twin-fluid lance entering the chamber at the top, a tempered liquid circulation system, a pressurized air supply system as well as a filter system for exhaust air. In the pressure chamber with an internal diameter of 300 mm and total height of 3000 mm, a honeycomb structure is mounted for reduction of droplet recirculation. In the circulation system, the liquid is pumped, while the eccentric

screw pumps P1 and P2 feature liquid towards the twin-fluid lance. Liquid mass flow is controlled by Coriolis flow meters in a range of $\dot{M}_{liq,P1} = 10 - 60 \text{ kg}\cdot\text{h}^{-1}$ and $\dot{M}_{liq,P2} = 60 - 200 \text{ kg}\cdot\text{h}^{-1}$, respectively. In the pressurized air supply system, a turbine meter is used for volume flow detection in a range of $V_{gas} = 0.85 - 25 \text{ m}^3\cdot\text{h}^{-1}$. Gas mass flow is calculated via the ideal gas law with the aid of temperature and pressure measurements directly behind the turbine. System pressure control is performed by three parallel valves after the exhaust air filtering system. The pressure chamber is equipped with three glass windows for spray characterization via optical or laser-based measurement techniques. Optical ports are located at the angles of $\Phi = 0, 70$ and 180° , as shown in the horizontal cross-sectional view (A – A) of Figure 5.

3.4 Burner test rig (BTR)

The burner test rig (BTR) was applied for spray measurements at increased liquid and gas mass flows as investigated in paper IV. A scheme of the test rig is shown in Figure 6.

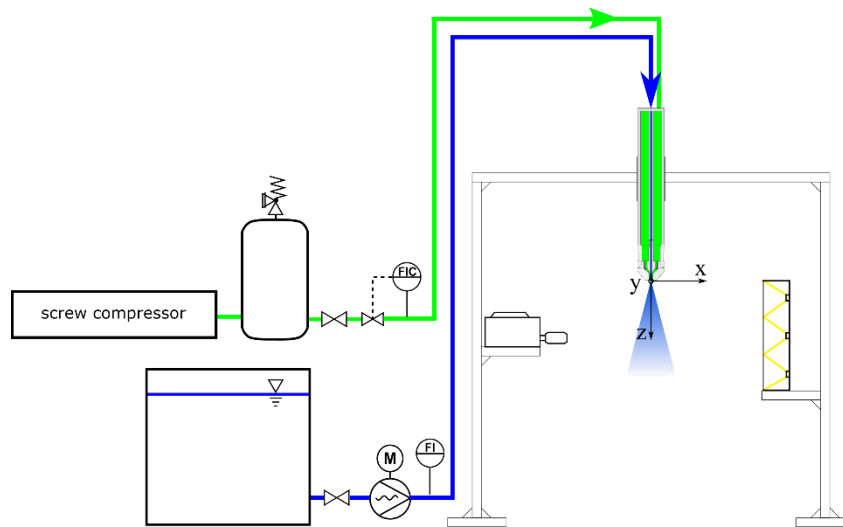


Figure 6: Scheme of the burner test rig with a mounted twin-fluid lance and high-speed camera.

As the test rig is typically operated open-air, due to the increased liquid mass flows, a simple setup was chosen, which consists of a liquid and gas supply system, as well as a rack for the twin-fluid lance and measurement technique. Out of a 1 m^3 liquid storage tank, the liquid is pumped towards the mounted lance via an eccentric screw pump within a mass flow range of $\dot{M}_{liq} = 400 - 1300 \text{ kg}\cdot\text{h}^{-1}$, which is measured by a Coriolis mass flow and density meter. The supply of pressurized gas is ensured by a screw compressor with a pressure vessel at $p_{vessel} = 11 \text{ bar}$. A hot wire anemometer with integrated valve allows for regulation of the gas mass flow in a range of $\dot{M}_{gas} = 50 - 400 \text{ kg}\cdot\text{h}^{-1}$.

3.5 Measurement techniques

For the detailed investigation of primary breakup as well as to detect local droplet size and velocity distributions optical and laser-based measurement techniques were applied.

The qualitative investigation of primary breakup and the detection of large droplets was performed by a Photron SA4 high-speed camera (HSC). This camera enables a frame rate of 3600 Hz at a resolution of 1024 x 1024 pixels as well as frame rates up to 500 kHz at reduced resolution. For image recording, a lens with focal length of $f_{HSC} = 105$ mm was applied. The images were captured applying back-light illumination with a 9 x 4500 lm high-power LED array. To detect fast motion sequences at less motion blur, very short exposure times were required. Images used for illustration were processed with a background image in order to remove greyscale fluctuations caused by the back-light illumination. Each set of images included at least 1000 images, as all spray phenomena in different time scales should be recorded. The set frame rates ranged from 3.6 kHz up to 25 kHz, dependent on the time scale of the captured spray phenomena (e.g. primary breakup of liquid jets or instability formation and spread). Chosen frame rates were always in accordance with the Nyquist stability criterion [43,44]. For the analysis of following spray characteristics the high speed camera images were used: primary breakup morphology, primary ligament length, Kelvin-Helmholtz wave frequency, spray angle, sphericity check of droplets and droplet size detection in coarse sprays.

For deeper insight into the spray, a far-field microscope with an adjustable focal-length in the range of 350 – 600 mm and a CCD-camera by Dantec Dynamics was used in combination with a pulse-laser ($\lambda_{laser} = 532$ nm) flash light as back-light illumination (also called shadowsizer (SZ)). This laser-optical measurement technique allows for droplet size and sphericity measurement, due to a field of view of 2.8 x 2.8 mm² and a high resolution of 2048 x 2048 pixels. With a calibration target, the maximum measurement error was estimated to be < 10 μ m. For the detection of the maximum droplet diameter, a set of 1000 images was taken with the SZ at each operating condition, to guarantee for a reliable number of droplets. The maximum droplet diameter was determined as a validation criterion for the quantitative results of the laser-based measurement techniques.

Another laser-optical measurement technique, leading to a deeper insight in gas phase dynamics, is the particle image velocimetry (PIV). Here, a double-pulse laser is equipped with a sheet optic, while a CCD-camera is located in perpendicular direction and focused on the emitted laser sheet. As typically the air flow velocity is investigated, very small droplets or particles must be seeded into the gas phase. Particle seeding was generated via a seeding generator from LaVision, featuring di-ethyl-hexyl-sebacat (DEHS) droplets

of 1 – 5 μm size range in order to follow the gas phase perfectly [45]. When the laser sheet hits the seeded gas phase, the small droplets emit the laser light also in direction of the camera. The application of the double pulse laser with sufficient small time between pulses enables the calculation of gas phase velocity and detection of vortex structures.

Laser Doppler anemometry (LDA) is a commonly applied laser-based technique for local droplet velocity distribution measurement. Here, a laser beam is first splitted up in two beams, whereas one is subsequently frequency shifted via a Bragg cell. Afterwards both beams pass a lens and are intersected in the measurement volume, where they form a spheroidal measurement volume, exhibiting interference fringes [46]. When a droplet passes the measurement volume, the laser light is refracted by the droplet. The refracted signal is detected via photo multipliers and shows the Doppler frequency. This enables for the calculation of the related droplet velocity.

Beside the information on local droplet velocity, the radial droplet diameter distribution can be characterized via phase Doppler anemometry (PDA). For this purpose, the previously mentioned LDA-setup of laser beams is extended by a receiver optic with three detectors (photomultipliers), arranged in a specific off-axis angle Φ_R alignment. Additionally, the receiver optic is equipped with different masks for detection error minimization as well as droplet size range adjustment and various slits for measurement volume reduction in horizontal direction. When a droplet passes the measurement volume, the respective scattering signal (intensity and signal dependent on the off-axis angle) is detected by each photomultiplier with a phase difference in-between the photomultipliers, which is a function of the geometric alignment, refractive index of the liquid phase and droplet diameter. As geometric properties and refractive index are user defined or measureable, the related droplet size can be calculated. As only one phase difference between two detectors is necessary to obtain the size information, the second phase difference information is used as validation criterion and to enlarge the measuring range in terms of droplet size. The alignment and the adjustment of PDA systems is of major importance for the accuracy of the latter achieved results. As a high amount of system parameters show increased sensitivity and can change the measurement results, typically a sensitivity study is performed before data acquisition of a new set of measurements. Details of a sensitivity study procedure are discussed in Kapulla et al. [47]. The following limitations of a PDA system can be enumerated: (i) trajectory effect or Gaussian beam effect (which leads to detection of large phantom droplets by increased scattered light) [48], (ii) shadowing due to high droplet number density (that results in an increase of calculated droplet size as detection of small droplets is inhibited) [49], (iii) slit effect (leading to unwanted measuring errors) [50] and (iv) aspherical droplets (resulting in a random shift of droplet size) [51–53]. Phase Doppler anemometry is often applied in

1st order refraction to achieve high signal intensity and low noise (typical $\Phi_R = 70^\circ$ off-axis angle). Therefore the measurements are limited to transparent liquids. In this thesis, two different phase Doppler analyzer were applied. For data curation in paper I, a fiber PDA system by Dantec Dynamics was utilized with $\lambda_{laser} = 514.5$ nm. Measurements for papers II – IV and proceeding I, II were performed with a fiber PDA and SprayExplorer system by Dantec Dynamics at $\lambda_{laser} = 561$ nm. For all measurements the asymmetrical mask B, as well as a slit of $l_{slit} = 200$ μm were applied in order to (i) achieve a well-defined measurement volume, (ii) ensure for high data rates in dense sprays and (iii) enable for liquid mass flux calculation. Lenses with a focal length of 1000 mm were used for transmitter and receiver optics to enable droplet size measurements up to a maximum diameter range of $D = 1330 - 1380$ μm , dependent on refractive index of the utilized liquids. As position for droplet size and velocity measurement in papers I - III and proceeding I, II $z = 200$ mm was chosen. For paper IV, the measurement position was evaluated according to a method described in appendix section G. For all PDA measurements radial profiles in the whole spray cone with a radial increment of $\Delta x = 2 - 4$ mm as well as a data basis of 50.000 droplets or duration of 60 s were set. At every radial measurement position, typically Sauter mean diameter D_{32} and axial mean droplet velocity $v_{dr,z,mean}$ was calculated [54].

$$ID_{32,m} = \frac{\sum_{i=1}^N D_{30,i}^3 \cdot \dot{m}_i \cdot A_i}{\sum_{i=1}^N D_{20,i}^2 \cdot \dot{m}_i \cdot A_i} \quad (1)$$

The global spray characterization was performed by calculation of a mass-weighted integral Sauter mean diameter ($ID_{32,m}$) according to equation (1). Here, $D_{30,i}$ and $D_{20,i}$ represent the local volume and surface mean diameter, respectively. A_i is the annulus area and \dot{m}_i is the local mass flux at the corresponding measurement position i . The computation was performed by the toolbox SprayCAT. Further information on computation can be obtained by DIN SPEC 91325 [55] and Albrecht [50]. Each measurement was repeated at least three times, whereas one full profile was recorded for symmetry check and two half-profiles were taken and mirrored after symmetry was proven. Therefore all figures with radial profiles show mirrored data as open symbols.

4 Results and discussion

4.1 System pressure

4.1.1 Influence of system pressure for constant v_{gas} , GLR and J_{gas}

The results from this subsection are part of the master thesis Grossl [56] and paper I: “Experimental investigation on the influence of system pressure on resulting spray quality and jet breakup applying pressure adapted twin-fluid nozzles” by Wachter et al. [57]. Here, the effect of system pressure on primary jet breakup, resulting droplet velocity and size was analyzed during the application of atomizers with pressure adapted gas orifice areas. Reduction of gas orifice area with increasing system pressure allows for constant v_{gas} , GLR and J_{gas} at every system pressure step without changing the gas mass flow. The operating conditions comprise five system pressure steps ($p_{sys} = 1 / 2 / 6 / 11 / 16$ bar) with five adapted central liquid jet atomizers (flow configuration (i)), which were operated at three different gas velocities $v_{gas} = 60 / 80 / 100 \text{ m}\cdot\text{s}^{-1}$ ($GLR = 0.6 / 0.8 / 1.0$) and constant $\dot{M}_{liq} = 20 \text{ kg}\cdot\text{h}^{-1}$. Experiments were conducted in the test rig PAT with $\eta_{liq} = 1 \text{ mPa}\cdot\text{s}$ and $100 \text{ mPa}\cdot\text{s}$, applying water and a glycerol/water – mixture.

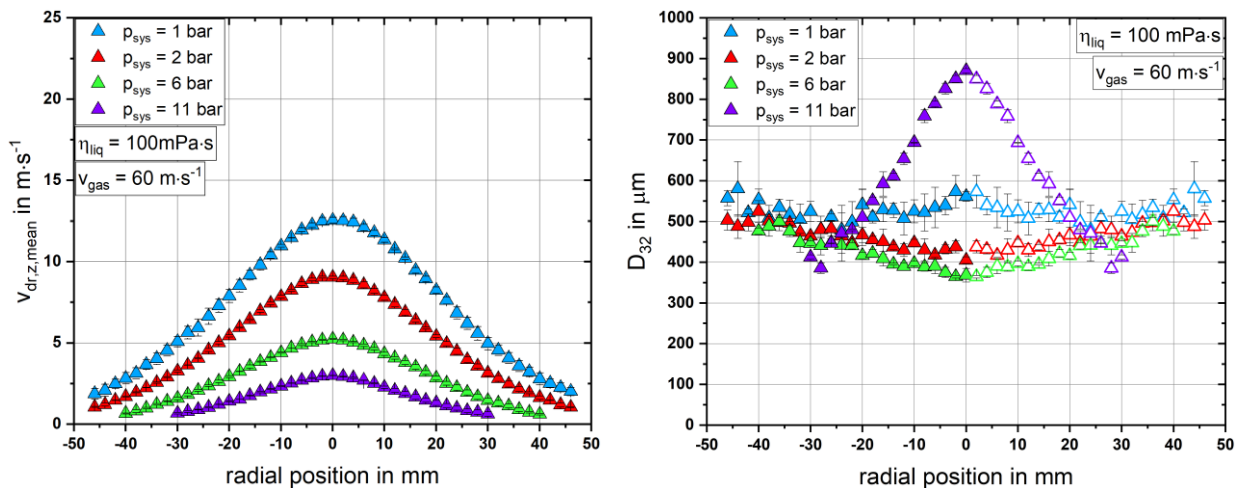


Figure 7: $V_{dr,z,mean}$ (left) and D_{32} (right) as function of radial position at varying p_{sys} . Configuration (i), $d_{liq} = 2 \text{ mm}$, $\dot{M}_{liq} = 20 \text{ kg}\cdot\text{h}^{-1}$, $v_{gas} = 60 \text{ m}\cdot\text{s}^{-1}$ ($GLR = 0.6$), $\eta_{liq} = 100 \text{ mPa}\cdot\text{s}$.

To discuss the influence of system pressure on resulting droplet velocity and size, the PDA measurements for $v_{gas} = 60 \text{ m}\cdot\text{s}^{-1}$ ($GLR = 0.6$) and $\eta_{liq} = 100 \text{ mPa}\cdot\text{s}$ are shown in Figure 7. Corresponding measurements for other operating conditions are illustrated in the appendix section A. As Figure 7 (left) shows, for all droplet velocity measurements with the PDA system, the typical Gaussian shaped radial profile for gas-assisted central

liquid jet atomizers was detected, which is also in accordance with the free jet theory described in the appendix chapter F. Additionally, with increasing system pressure, a decrease in resulting droplet velocity was observed, although gas velocity at the atomizer exit remained constant. Against this, the droplet diameter showed a different behavior at increasing system pressure, as depicted in Figure 7 (right). Here, for $p_{sys} = 1 - 6$ bar a slight decrease in droplet size was measured, followed by a significant rise and change in radial profile shape from v-shape with a minimum on the spray axis to a pronounced peak in the spray center. This inverse effect on resulting Sauter mean diameter was detected for all investigated v_{gas} (GLR), which is shown by the calculated $ID_{32,m}$ values in Figure 8 (left). In addition, Figure 8 (right) presents the corresponding HSC images at $p_{sys} = 1$ and 11 bar for $v_{gas} = 60 \text{ m}\cdot\text{s}^{-1}$ ($GLR = 0.6$) and $\eta_{liq} = 100 \text{ mPa}\cdot\text{s}$.

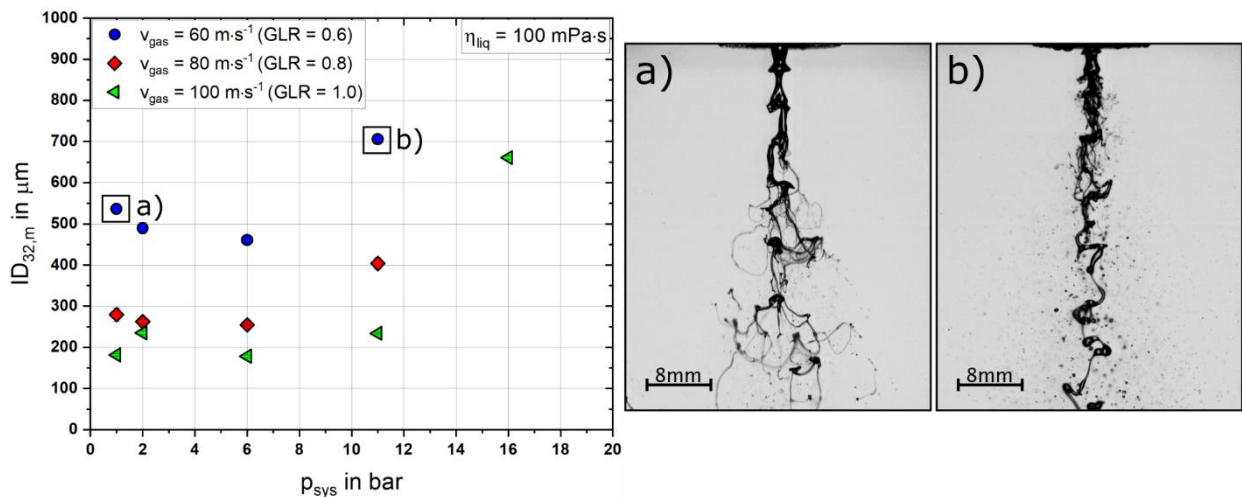


Figure 8: $ID_{32,m}$ as function of p_{sys} for varying v_{gas} (GLR) (left), HSC images of the primary breakup for $v_{gas} = 60 \text{ m}\cdot\text{s}^{-1}$ at a) $p_{sys} = 1$ bar and b) $p_{sys} = 11$ bar (right). Configuration (i), $d_{liq} = 2 \text{ mm}$, $\dot{M}_{liq} = 20 \text{ kg}\cdot\text{h}^{-1}$, $\eta_{liq} = 100 \text{ mPa}\cdot\text{s}$.

When comparing the primary jet breakup morphology for $p_{sys} = 1$ and 11 bar, it can be stated, that for higher system pressure, the primary ligament remained intact for a significantly longer distance after leaving the nozzle orifice. Furthermore, the radial displacement of ligaments and membrane formation is reduced at $p_{sys} = 11$ bar.

In order to explain this effect of increased system pressure on droplet size, the local dynamic pressure of the gas jet j_{gas} needs to be taken into account, which is influenced in an opposite way by two parameters:

- An increase in system pressure, results in higher gas density and therefore in higher dynamic pressure of the gas jet j_{gas} at constant v_{gas} . The higher shear stress between gas and liquid phase leads to smaller droplet sizes as visible for an increase in p_{sys} between 1 – 6 bar.

- When the gas phase exits the atomizer, the gas velocity decreases with increasing atomizer distance due to gas phase entrainment, in accordance with the free jet theory (appendix chapter F). This effect is enhanced, due to d_{eq} reduction for every system pressure step and results in a decrease of local dynamic pressure of the gas jet $j_{gas,local}$ at fixed atomizer distance $z = 200$ mm, which leads to higher droplet sizes.

To clarify those opposing effects at different system pressures, $j_{gas,local}$ was calculated locally in the measuring plane ($z = 200$ mm) by using the droplet velocity of all droplets in the size range 1 - 5 μm , as these represent the gas phase velocity [45]. Figure 9 depicts the influence of system pressure on $j_{gas,local}$, while applying pressure adapted atomizers at $p_{sys} = 1 / 6 / 16$ bar for $v_{gas} = 100 \text{ m}\cdot\text{s}^{-1}$ ($GLR = 1.0$) and $\eta_{liq} = 100 \text{ mPa}\cdot\text{s}$.

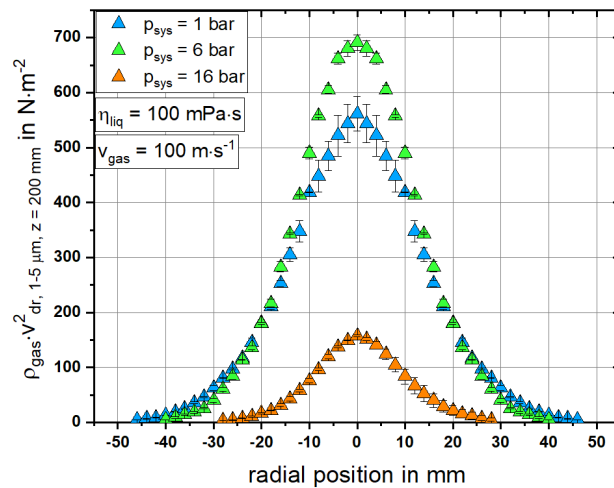


Figure 9: $j_{gas,local}$ as function of radial position at varying p_{sys} . Configuration (i), $d_{liq} = 2$ mm, $\dot{M}_{liq} = 20 \text{ kg}\cdot\text{h}^{-1}$, $\eta_{liq} = 100 \text{ mPa}\cdot\text{s}$, $v_{gas} = 100 \text{ m}\cdot\text{s}^{-1}$ ($GLR = 1.0$).

The maximum in $j_{gas,local}$ is clearly visible for $p_{sys} = 6$ bar, which results in a maximum in gas / liquid interaction and therefore a minimum in Sauter mean diameter. For a further increase towards $p_{sys} = 16$ bar, a significant decrease in local j_{gas} was found, which is responsible for the high droplet size detected according to Figure 8 (left). A comparison of measurements for different liquid viscosities, revealed that an increase in viscosity led to higher droplet sizes but similar results concerning the effect of system pressure, as can be seen in the appendix section A.

After gathering a deeper insight concerning the influence of J_{gas} at corresponding p_{sys} on resulting droplet size and primary breakup, an investigation of the three parameters (s_{gas} , p_{sys} and v_{gas}) affecting the aerodynamic forces (J_{gas}) and therefore the liquid disintegration was performed.

4.1.2 Influence of J_{gas}

The results of this subsection are part of paper II: “Towards system pressure scaling of gas assisted coaxial burner nozzles – An empirical model” by Wachter et al. [58]. Following the conclusions of the previous subsection, in this chapter, the effect of gas momentum flow was studied in order to derive a scaling approach for gas-assisted atomizers with central liquid jet (configuration (i)). Three atomizers with different gas gap widths $s_{gas} = 0.6 / 1.2 / 2.0$ mm were operated at $v_{gas} = 60 / 80 / 100$ m·s⁻¹ and $p_{sys} = 1 / 3 / 6 / 11 / 16 / 21$ bar, leading to J_{gas} variation between 0.06 - 2.5 N. Water ($\eta_{liq} = 1$ mPa·s) was atomized in the PAT at constant $\dot{M}_{liq} = 20$ kg·h⁻¹.

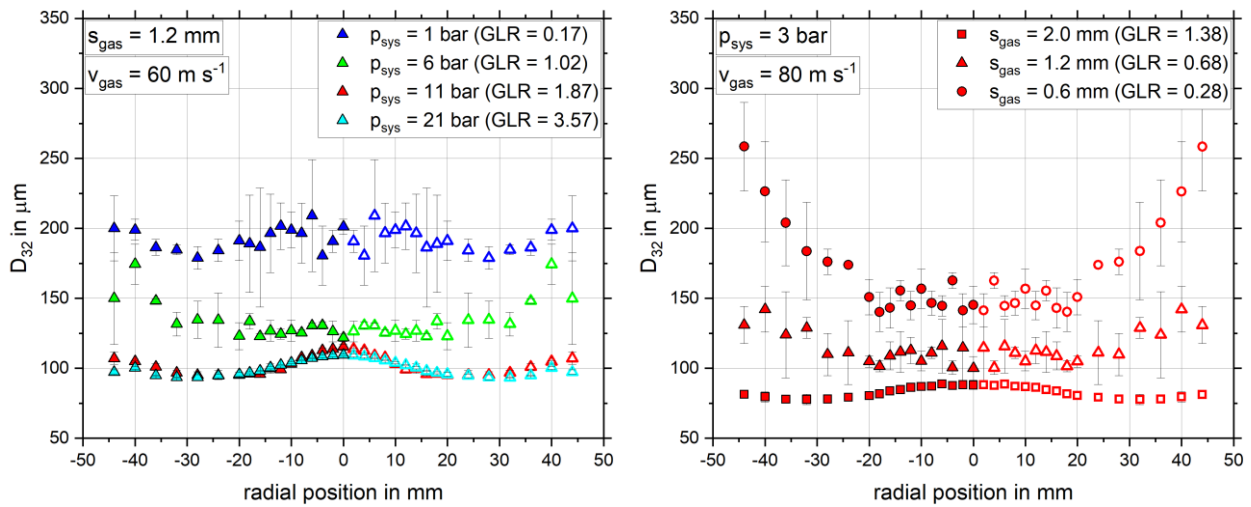


Figure 10: D_{32} as function of radial position for varying p_{sys} (left) and s_{gas} (right). Configuration (i), $d_{liq} = 2$ mm, $\dot{M}_{liq} = 20$ kg·h⁻¹, $\eta_{liq} = 1$ mPa·s.

For discussion of the results concerning the variation of p_{sys} and s_{gas} , radial droplet size profiles are depicted in Figure 10. Corresponding measurements for other operating conditions are illustrated in the appendix section B. An increase in p_{sys} between 1 – 11 bar, while also increasing GLR but constant v_{gas} , led to a significant decrease in droplet size over the whole spray cone (see Figure 10 (left)). For $p_{sys} > 6$ bar, homogeneity of the radial droplet size distribution without larger droplet size deviations was obtained, which is attributable to the increased aerodynamic forces (i.e. J_{gas}). Especially an increment in p_{sys} over 11 bar showed, that the dependency on Sauter mean diameter levels off completely and nearly constant droplet size distributions are achieved. Similar effects on the measured droplet size distribution resulted from an increase in s_{gas} for constant v_{gas} and p_{sys} , illustrated in Figure 10 (right). All measured dependencies were also verified by HSC images of primary jet breakup, where a significant intensification of the disintegration process was identified between $v_{gas} = 60$ to 100 m·s⁻¹, $p_{sys} = 1$ to 21 bar and $s_{gas} = 0.6$ to 2.0 mm (see appendix section B). Nevertheless, all recorded breakup morphologies

represented the fiber type breakup, which is the common breakup mode for low-viscosity atomizer operation at sufficient gas momentum flow [12,59,60].

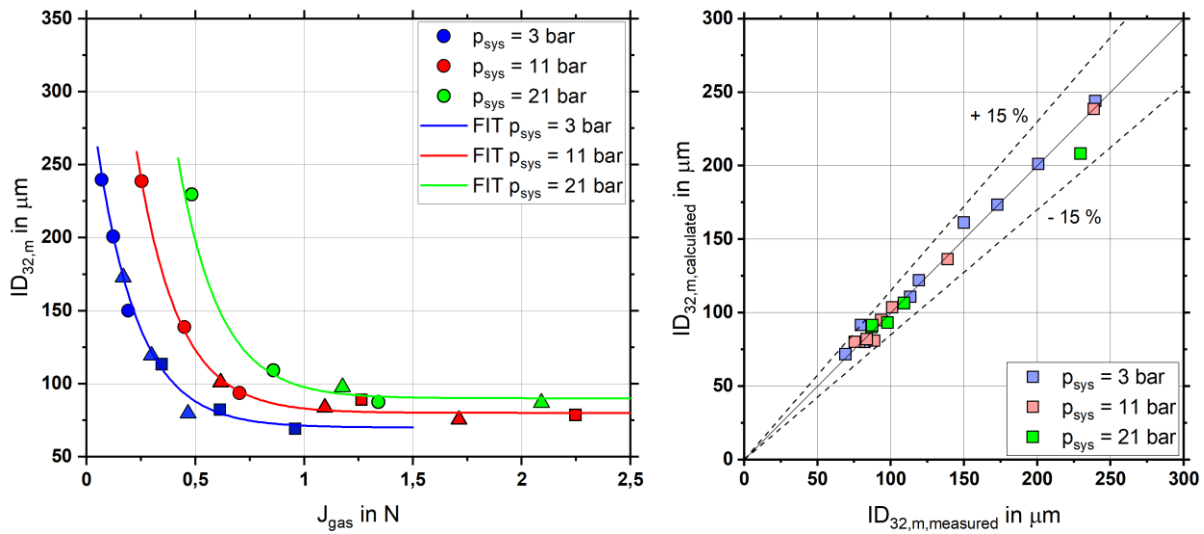


Figure 11: $ID_{32,m}$ as function of J_{gas} at varying p_{sys} (left). Parity plot of the calculated and measured $ID_{32,m}$ for varying p_{sys} (right). Configuration (i), $d_{liq} = 2$ mm, $\dot{M}_{liq} = 20$ kg·h⁻¹, $\eta_{liq} = 1$ mPa·s.

As the impact on and dependency of resulting droplet size regarding all parameters forming J_{gas} were similar, an empirical model for system pressure scaling of central liquid jet atomizers was derived out of the recorded data for $p_{sys} = 3 / 11 / 21$ bar. The residual system pressure steps were used for model validation. For model fitting of the experimental data, a potential fit was chosen, as shown in Figure 11 (left) and equation (2) with two pressure dependent parameters A and C from equations (3) and (4). B was set constant to 0.19 N.

$$ID_{32,m} = A(p_{sys}) \cdot e^{-\frac{J_{gas}}{B}} + C(p_{sys}) \quad (2)$$

$$A(p_{sys}) = 3.0 \cdot p_{sys}^2 + 220 \quad (3)$$

$$C(p_{sys}) = 1.1 \cdot p_{sys} + 67 \quad (4)$$

The model accuracy is illustrated by a parity plot in Figure 11 (right), which compares measured versus calculated $ID_{32,m}$ values. As maximum percentage deviation 12.7 % at $p_{sys} = 3$ bar, $v_{gas} = 100$ m·s⁻¹ and $s_{gas} = 1.2$ mm was found. The validation measurements showed lower variance than 12 % except for $p_{sys} = 6$ bar and $J_{gas} = 0.69$ N with $\Delta ID_{32,m} = 18$ μm , which equals 22 %. Model applicability was proven in a range of $p_{sys} = 1 - 21$ bar, $J_{gas} = 0.07 - 2.5$ N and $\dot{M}_{liq} = 20$ kg·h⁻¹.

By applying J_{gas} as characteristic parameter for atomization performance, the understanding of the influence of system pressure on spray formation was deepened and an empirical model for system pressure scaling of central liquid jet atomizers was derived and validated.

4.2 Mass flow scale up

The results in this chapter are part of the bachelor thesis Müller [61] and paper IV: "Mass Flow Scaling of Gas-Assisted Coaxial Atomizers" by Wachter et al. [62]. Here, the effect of liquid mass flow on primary jet breakup and the resulting droplet size was analyzed at constant We_{aero} in order to derive a model for scale-up of central liquid jet atomizers (flow configuration (i)) at atmospheric pressure conditions. Four liquid mass flow steps ($\dot{M}_{liq} = 20 / 50 / 100 / 500 \text{ kg}\cdot\text{h}^{-1}$) were investigated with similar atomizer setups in central tube diameter $d_{liq} = 2.0 / 3.2 / 4.5 / 10 \text{ mm}$, that allow for constant $v_{liq} = 1.77 \text{ m}\cdot\text{s}^{-1}$. As operating conditions, $We_{aero} = 250 / 500 / 750 / 1000$ ($GLR = 0.36 / 0.50 / 0.61 / 0.70$) were applied, which requires for constant We_{aero} and increasing \dot{M}_{liq} , a decrease in v_{gas} due to an increase in d_{liq} . For the investigations, water ($\eta_{liq} = 1 \text{ mPa}\cdot\text{s}$) was atomized in the test rigs ATMO and BTR. At $\dot{M}_{liq} = 500 \text{ kg}\cdot\text{h}^{-1}$ droplet size was measured qualitatively via HSC images and an algorithm applying a global threshold according to Otsu et al. [63] and subsequent circle fitting.

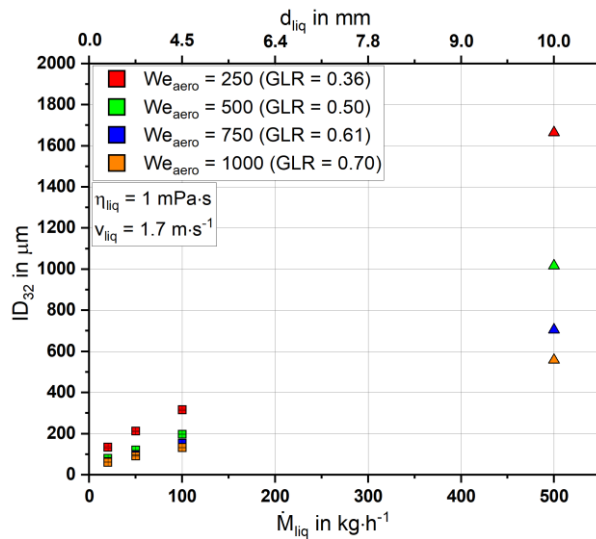


Figure 12: $ID_{32,m}$ as function of \dot{M}_{liq} (d_{liq}) at varying We_{aero} (GLR). Configuration (i), $\eta_{liq} = 1 \text{ mPa}\cdot\text{s}$, $p_{sys} = 1$ bar.

The resulting droplet size measurements for PDA and HSC are illustrated in Figure 12 for all utilized operating conditions. Corresponding radial measurements for all operating conditions are illustrated in the appendix section C. For an increase in We_{aero} (i.e. GLR) a decrease in droplet size was detected, which is related to an increase in v_{gas} and aerodynamic forces, shearing the liquid jet. With higher aerodynamic forces, the influence of a further increase in v_{gas} is decreasing, as already discussed in chapter 4.1 for an increase in J_{gas} . In contrast to this, for an increase in \dot{M}_{liq} , significant higher droplet sizes were measured keeping We_{aero} constant. Beside this, also the primary ligament length was extended up to $z = 130 \text{ mm}$ for $\dot{M}_{liq} = 500 \text{ kg}\cdot\text{h}^{-1}$ (as depicted in the appendix Figure

G 1). The effects on droplet size and primary ligament length were generated by two changes in parameters, while increasing \dot{M}_{liq} . At first, for increasing \dot{M}_{liq} at constant We_{aero} , a decrease in v_{gas} and therefore in j_{gas} and J_{gas} is calculated. As v_{gas} decreases, lower aerodynamic forces remain for disintegration of the liquid jet. Furthermore, increasing \dot{M}_{liq} is related to an increase in d_{liq} . For this condition, the ratio between shearing surface of the liquid jet and the volume of the jet decreases, which leads to a remaining intact liquid jet core over longer distance from the atomizer orifice.

With the measured data plotted over J_{gas} , an empirical model for scaling of central liquid jet atomizers concerning the applied \dot{M}_{liq} was derived. The influence of J_{gas} on the resulting droplet size as well as the derived model are shown in Figure 13 (left). Here, the effect of J_{gas} on resulting droplet size is also in accordance with the results from chapter 4.1.2. Therefore, again a potential fit was used with 3 different parameters A, B and C, which were correlated via the least-square method. The model and the fitted parameters are presented in equations (5)-(8).

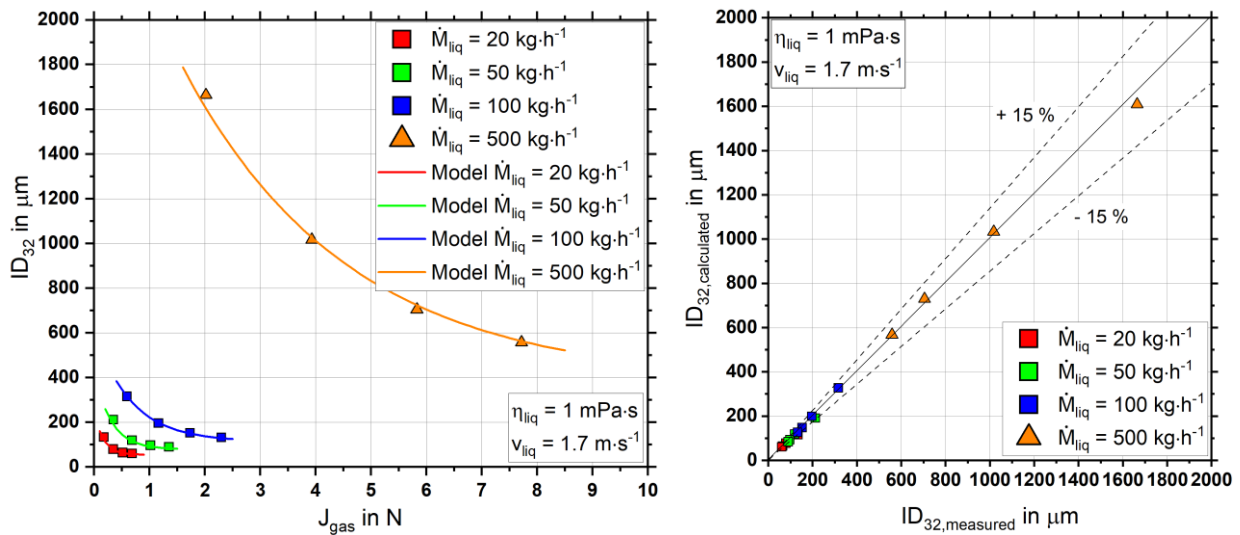


Figure 13: ID_{32} as function of J_{gas} for varying \dot{M}_{liq} (d_{liq}) (left), Parity plot for comparison between measured and calculated ID_{32} values (right). Configuration (i), $\eta_{liq} = 1 \text{ mPa}\cdot\text{s}$, $p_{sys} = 1 \text{ bar}$.

$$ID_{32} = A(\dot{M}_{liq}) \cdot e^{-\frac{J_{gas}}{B(\dot{M}_{liq})}} + C(\dot{M}_{liq}) \quad (5)$$

$$A(\dot{M}_{liq}) = 4.6 \cdot \dot{M}_{liq} + 91 \quad (6)$$

$$B(\dot{M}_{liq}) = 0.006 \cdot \dot{M}_{liq} + 0.03 \quad (7)$$

$$C(\dot{M}_{liq}) = 0.67 \cdot \dot{M}_{liq} + 45 \quad (8)$$

In addition, the parity plot shown in Figure 13 (right) illustrates the model accuracy, comparing measured and calculated droplet sizes. The maximum deviation between measured data and the model approach was reached at $\dot{M}_{liq} = 100 \text{ kg}\cdot\text{h}^{-1}$ and $We_{aero} =$

250 with 13.2 % ($\Delta/D_{32} = 17.6 \mu\text{m}$). For $\dot{M}_{liq} = 500 \text{ kg}\cdot\text{h}^{-1}$ and $We_{aero} = 250$ the highest absolute deviation in droplet size between model and measured data occurred with $\Delta/D_{32} = 55.5 \mu\text{m}$, which equals a percentage variance of only 3.3 %. The model was considered to be adequate in a range of $\dot{M}_{liq} = 20 - 500 \text{ kg}\cdot\text{h}^{-1}$ at $v_{liq} = 1.7 \text{ m}\cdot\text{s}^{-1}$.

One of the main influencing parameters for an increase in droplet size, when applying increasing \dot{M}_{liq} was the simultaneously rising d_{liq} , which led to an unfavorable shift in the ratio between shear surface for the gas jet and liquid volume. In order to overcome this - in terms of mass flow scale up limiting effect - a variation in liquid flow configurations was tested. Here, especially the liquid sheet configurations provide the advantage of \dot{M}_{liq} scaling at constant sheet thickness as against central liquid jet atomizers. The investigation was performed at constant conditions concerning atomization relevant parameters, which is described in detail in the following chapter 4.4.

4.3 Gas channel angle

The results in this subsection are part of the bachelor thesis Ritter [64] and proceeding II: "Effect of gas jet angle on primary breakup and droplet size applying coaxial gas-assisted atomizers" by Wachter et al. [65]. In the following subsection, the effect of the gas jet angle on primary jet breakup and the resulting droplet size and velocity is discussed. For this investigation, 3 atomizers with different gas channel angles $\alpha = 0 / 15 / 30^\circ$ were applied at system pressure of $p_{sys} = 1$ and 11 bar. The gas orifices of the central liquid jet atomizers were designed according to the pressure adapted nozzles approach (refer to chapter 4.1.1). As liquids, water ($\eta_{liq} = 1 \text{ mPa}\cdot\text{s}$) and a glycerol/water-mixture ($\eta_{liq} = 200 \text{ mPa}\cdot\text{s}$) were atomized in the test rig PAT at constant $\dot{M}_{liq} = 20 \text{ kg}\cdot\text{h}^{-1}$ and at $v_{gas} = 60 / 100 \text{ m}\cdot\text{s}^{-1}$ ($GLR = 0.6 / 1.0$). In order to analyze the gas flow velocity and behavior, the PIV system with gas phase seeding was applied at the test rig ATMO. A black colored pin was mounted in the central atomizer tubing, which represented the emerging liquid jet.

In order to quantify the effect of gas channel angle on resulting droplet size and axial velocity, Figure 14 (left) illustrates the measured radial distributions for different angles α , at $v_{gas} = 60 \text{ m}\cdot\text{s}^{-1}$ ($GLR = 0.6$), $\eta_{liq} = 200 \text{ mPa}\cdot\text{s}$ and $p_{sys} = 1$ bar. Corresponding measurements for other operating conditions are illustrated in the appendix section D. In accordance to the literature [24,25], for the utilization of atomizers with gas channel angle, a decrease in droplet size was detected compared to the parallel exiting gas channels. The impact on droplet size decrement is typically related to an increase in J_{gas} i.e. aerodynamic forces (as shown in chapter 4.1). Corresponding to this result, also an increase in droplet mean velocity $v_{dr,z,mean}$ was measured for higher α , especially in the

spray center (see Figure 14 (left)). As v_{gas} at the nozzle orifice remained constant for varying α , double pulse PIV measurements of the seeded gas phase were performed in order to detect possible changes in the flow field, shown in Figure 14 (right) for $\alpha = 0$ and 30° with absolute gas phase velocity v_{abs} (calculated via axial and radial velocity component). Applying an atomizer with $\alpha = 0^\circ$, the gas phase emerges from the atomizer orifice and shears the pin while gas velocity decreases. Against this, for $\alpha = 30^\circ$, the exiting gas phase hits the pin, leading to smaller cross-sectional area and therefore to an increase of $\Delta v_{gas} \approx 20 \text{ m}\cdot\text{s}^{-1}$. As v_{gas} remains increased after the impact, this effect causes higher aerodynamic forces and the changes in droplet size and velocity detected in the spray center.

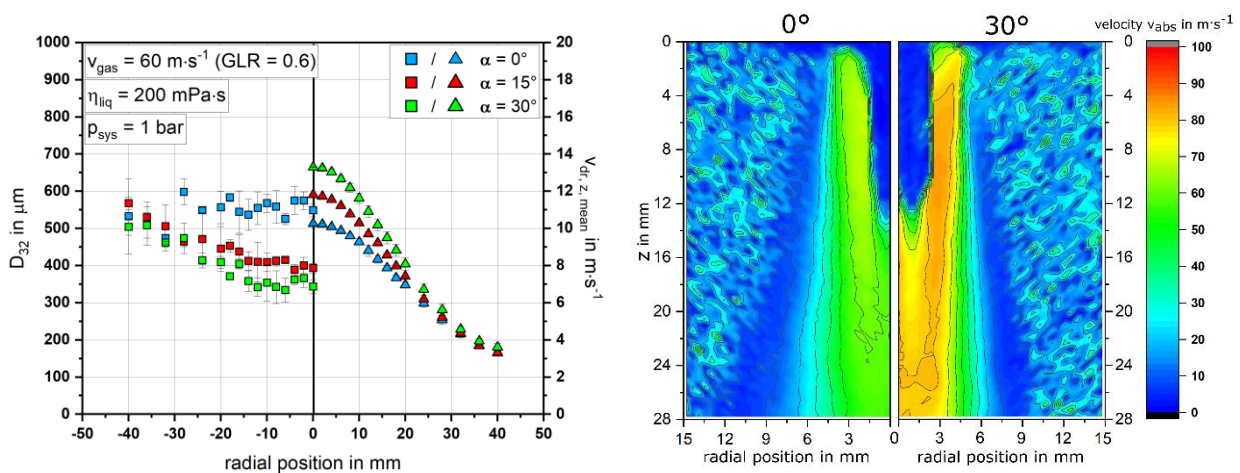


Figure 14: D_{32} and $v_{dr,z,mean}$ as function of radial position at varying α (left), v_{abs} for varying α (right). Configuration (i), $d_{liq} = 2 \text{ mm}$, $p_{sys} = 1 \text{ bar}$, $v_{gas} = 60 \text{ m}\cdot\text{s}^{-1}$.

Investigating the effect of gas channel angle on the primary jet breakup via HSC, no changes in the breakup morphology were detected, as illustrated for $v_{gas} = 60 \text{ m}\cdot\text{s}^{-1}$ (GLR = 0.6), $\eta_{liq} = 200 \text{ mPa}\cdot\text{s}$ and $p_{sys} = 1 \text{ bar}$ in Figure 15 (left).

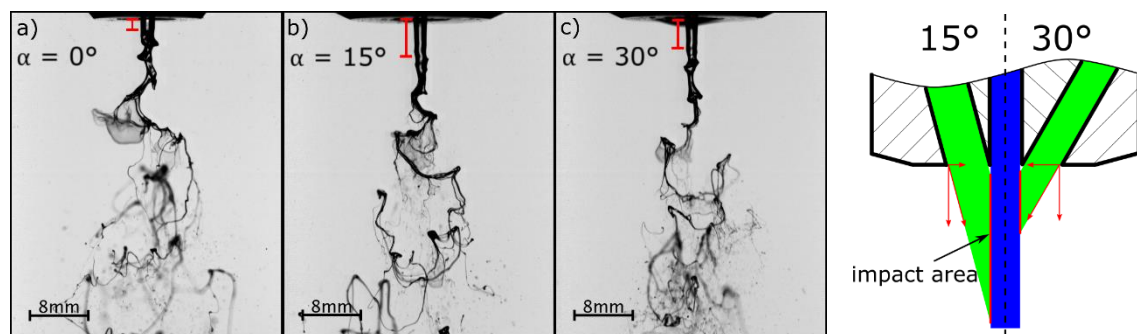


Figure 15: HSC images of the primary jet breakup applying atomizers with $\alpha = 0 / 15 / 30^\circ$ at $v_{gas} = 60 \text{ m}\cdot\text{s}^{-1}$ (GLR = 0.6), $\eta_{liq} = 200 \text{ mPa}\cdot\text{s}$ and $p_{sys} = 1 \text{ bar}$ (left). Scheme of the emerging gas and liquid phase as well as the corresponding impact area for $\alpha = 15 / 30^\circ$ (right).

The main difference in the HSC images is highlighted with a red mark and represents an area on the emerging liquid jet, where no typical disturbances or instabilities (as KHI) were formed. For an increase in α , from 0° to 15° a significant increase of the mentioned zone in axial direction was found. A further increment from 15° to 30° led to a decrease in impact area. This dependency leads to the conclusion, that the undisturbed area is related to the gas channel angle and the impacting radial forces of the gas phase, which lead to a stabilization of the liquid jet. The scheme in Figure 15 (right) depicts the decrement of the zone size with increasing gas channel angle. Furthermore, the increase in stabilizing radial force between $\alpha = 15^\circ$ and 30° also led to an increase in necessary v_{gas} (i.e. GLR) for KHI formation on the liquid jet surface.

A general overview on the influence of gas channel angle on $ID_{32,m}$ at varying operating conditions as v_{gas} (GLR), η_{liq} and p_{sys} is given by Figure 16 (left). In addition, related images of the primary jet breakup at different v_{gas} (GLR) and p_{sys} are shown in Figure 16 (right). For all investigated liquids and system pressures it can be stated, that an increase in α applying $v_{gas} = 60 \text{ m}\cdot\text{s}^{-1}$ ($GLR = 0.6$) resulted in a slight shift towards lower $ID_{32,m}$ values. The intensified primary jet breakup for an increased α was also recorded in the HSC images, especially for increased p_{sys} . Here, an increase in α led to a complete disintegration of the liquid jet, which remained intact for the atomizer with straight exit even after leaving the field of view in z-direction (see Figure 16 (right, a) and b)). As can be seen in Figure 16 (left) for increased v_{gas} of $100 \text{ m}\cdot\text{s}^{-1}$ ($GLR = 1.0$) no further influence of α was detected, which is comparable to the literature [24]. Here, the effect of α was negligibly small for both atomized liquids, as an already high J_{gas} , leads to lower influence of an additional, angle-dependent increase of aerodynamic forces [17,21,66].

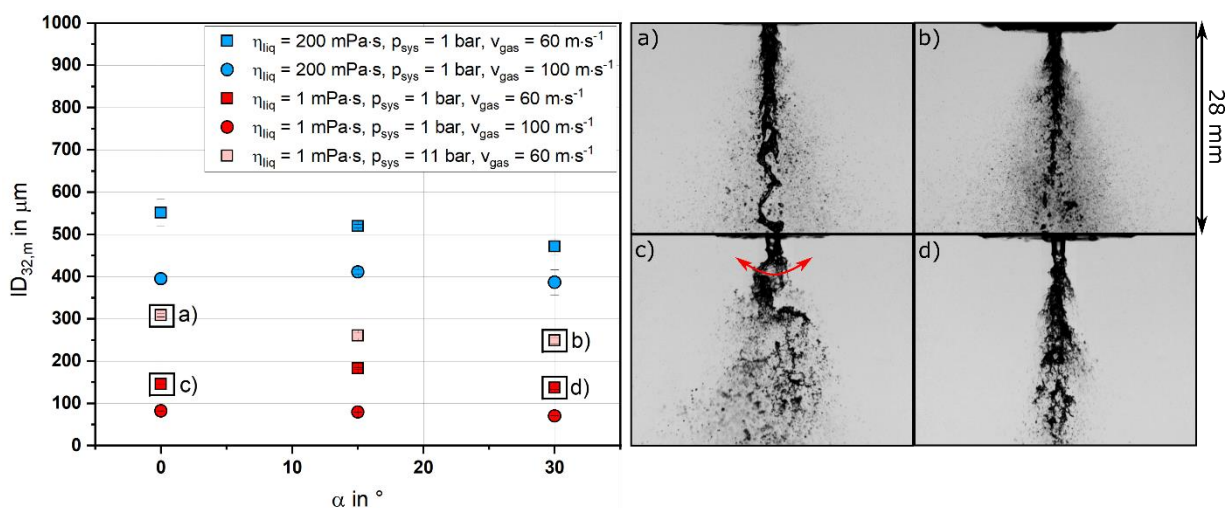


Figure 16: $ID_{32,m}$ as function of α for varying η_{liq} , v_{gas} (GLR), p_{sys} (left), HSC images of the primary jet breakup at $v_{gas} = 60 \text{ m}\cdot\text{s}^{-1}$ ($GLR = 0.6$) and $\eta_{liq} = 1 \text{ mPa}\cdot\text{s}$ for a) $\alpha = 0^\circ$, $p_{sys} = 11 \text{ bar}$, b) $\alpha = 30^\circ$, $p_{sys} = 11 \text{ bar}$, c) $\alpha = 0^\circ$, $p_{sys} = 1 \text{ bar}$ and d) $\alpha = 30^\circ$, $p_{sys} = 1 \text{ bar}$ (right). Configuration (i), $d_{liq} = 2 \text{ mm}$, $\dot{M}_{liq} = 20 \text{ kg}\cdot\text{h}^{-1}$.

After the detailed investigation of all relevant gas phase and gas orifice parameters (v_{gas} , ρ_{sys} , A_{gas} (s_{gas}), α), which affect the primary breakup and resulting droplet size, a deeper insight into parameters of the liquid phase (d_{liq} , \dot{M}_{liq}) was carried out in order to perform liquid mass flow scaling, as described in the following chapter.

4.4 Liquid flow configuration

The results in this chapter are part of the bachelor thesis Götz [67] and proceeding I: "Comparison of spray quality for two different flow configurations: Central liquid jet versus annular liquid sheet" by Wachter et al. [68] as well as paper III: "Comparison of Central Jet and Annular Sheet Atomizer at Identical Gas Momentum Flows" by Wachter et al. [69]. Different liquid flow configurations were investigated at comparable operating conditions as \dot{M}_{liq} , \dot{M}_{gas} , v_{liq} , v_{gas} , GLR , J_{gas} and J_{liq} . To achieve this comparison, an annular liquid sheet atomizer design was applied with equal exiting orifice areas for gas and liquid phase ($d_{gas} = 5.4$ mm, $s_{liq} = 1.09$ mm, $s_{gas} = 0.83$ mm), respectively. Here, 3 flow configurations can be evaluated, according to Figure 2. For all experiments $\dot{M}_{liq} = 30$ kg·h⁻¹ was kept constant, while atomizing water ($\eta_{liq} = 1$ mPa·s) and 3 glycerol/water – mixtures ($\eta_{liq} = 100 / 200 / 400$ mPa·s) in the test rig ATMO.

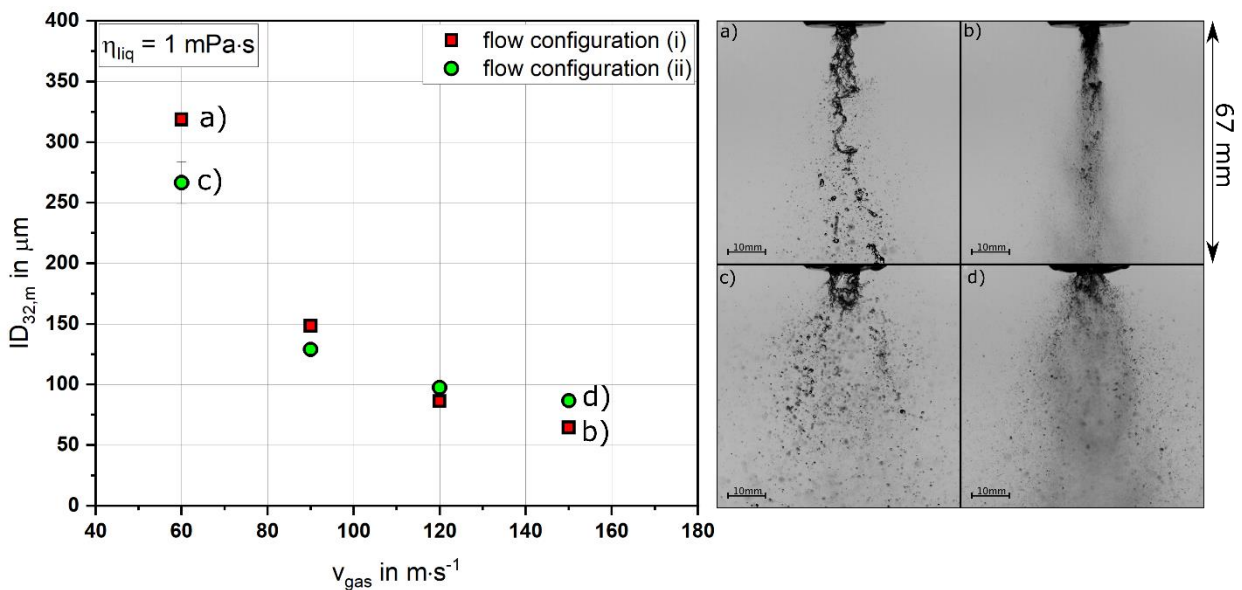


Figure 17: $ID_{32,m}$ as function of v_{gas} (GLR) at varying atomizer configuration (left), HSC images of the primary jet and sheet breakup for: a) configuration (i), $v_{gas} = 60$ m·s⁻¹ ($GLR = 0.2$), b) configuration (i), $v_{gas} = 150$ m·s⁻¹ ($GLR = 0.5$), c) configuration (ii), $v_{gas} = 60$ m·s⁻¹ ($GLR = 0.2$) and d) configuration (ii), $v_{gas} = 150$ m·s⁻¹ ($GLR = 0.5$) (right). $\dot{M}_{liq} = 30$ kg·h⁻¹, $\eta_{liq} = 1$ mPa·s, $\rho_{sys} = 1$ bar.

As first set of experiments, a comparison of the flow configurations (i) and (ii) was performed at $v_{gas} = 60 / 90 / 120 / 150$ m·s⁻¹ ($GLR = 0.2 / 0.3 / 0.4 / 0.5$). Additionally,

measurements at different outer and inner Gas-to-Liquid mass flow ratios (GLO and GLI), but constant $GLR = 0.3 / 0.5 / 0.7$ were conducted.

For comparison between flow configuration (i) and (ii), Figure 17 (left) shows the influence of resulting $ID_{32,m}$ for varying v_{gas} (i.e. GLR). Corresponding radial measurements for all operating conditions are illustrated in the appendix section E. In addition, Figure 17 (right) depicts HSC images of the primary jet and sheet breakup at $v_{gas} = 60 \text{ m}\cdot\text{s}^{-1}$ ($GLR = 0.2$) and $v_{gas} = 150 \text{ m}\cdot\text{s}^{-1}$ ($GLR = 0.5$). With increasing v_{gas} (i.e. GLR), for both investigated flow configurations a decrease in droplet size was detected. As can be seen for both configurations, the effect of v_{gas} on resulting droplet size decreases with increasing v_{gas} . For configuration (ii), the measured $ID_{32,m}$ was higher at low $v_{gas} < 120 \text{ m}\cdot\text{s}^{-1}$ ($GLR < 0.4$), compared to configuration (i). At higher $v_{gas} > 120 \text{ m}\cdot\text{s}^{-1}$ ($GLR > 0.4$), the decreasing effect on droplet size resulting from the liquid jet atomizer (i) leveled off. This effect can be explained via a comparison of the primary breakup of liquid jet and sheet. At low v_{gas} , the liquid jet disintegrated into large droplets and liquid fragments. Here, droplet size is mainly dependent on the liquid jet diameter d_{liq} . Resulting droplet size of the liquid sheet atomizer (ii) is influenced by the sheet thickness s_{liq} , which is smaller than d_{liq} and therefore liquid breakup at low GLR led to an intensified disintegration into smaller droplets. For increased v_{gas} (i.e. GLR) the primary breakup of the liquid jet led to a lower $ID_{32,m}$, as the liquid jet core is encased by fast shearing gas. As against this, utilizing configuration (ii) led to high aerodynamic force in the spray center, while large droplets at the spray boundary remained in size, due to a lack in aerodynamic forces. This breakup morphology was still observed for higher v_{gas} (i.e. GLR), leading to low sensitivity of $ID_{32,m}$ towards a further increase in aerodynamic forces.

In a second set of experiments, nozzle configuration (iii) was utilized at varying GLO / GLI and constant GLR values in order to detect the influence of the outer and inner gas stream on resulting droplet size and primary breakup. The detected droplet sizes are plotted over GLO and J_{gas} in Figure 18 (left) and (right), respectively. As shown in Figure 18 (left), the influence of GLO on droplet size is dependent on the absolute GLR value, whereas for increased $GLR > 0.5$, the sensitivity of GLO on resulting droplet size is reduced significantly. First, with increasing GLO , which results in a decrease in GLI , a higher droplet size was detected. The maximum in droplet size was typically found at $GLO \approx GLI$. An increase of GLO beyond this point led to a decrease in droplet size. The observed maximum can be explained by two effects. At first, for $GLO \approx GLI$ the total value of J_{gas} applied for atomization is minimized. Furthermore, due to the equal orifice areas of the atomizer gas exits, the operating condition $GLO \approx GLI$ also implicates $v_{gas,o} \approx v_{gas,i}$, which may lead to parallel formation of KHI waves on the liquid sheets' inner and outer surface and therefore to a morphological change in primary sheet breakup.

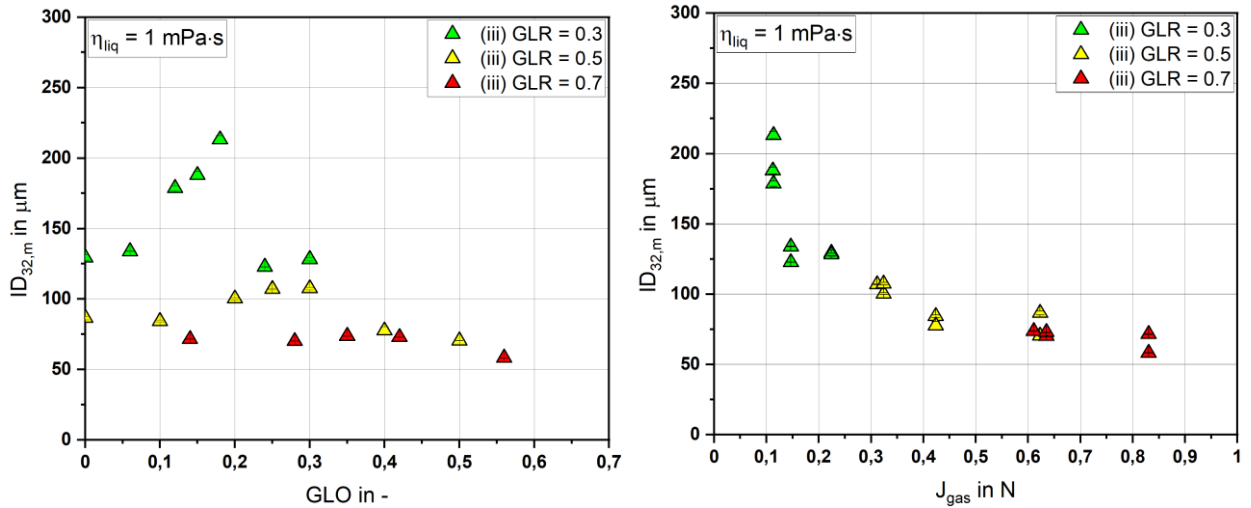


Figure 18: $ID_{32,m}$ as function of GLO for varying GLR (left) and J_{gas} for varying GLR (right). Configuration (iii), $\dot{M}_{liq} = 30 \text{ kg}\cdot\text{h}^{-1}$, $\eta_{liq} = 1 \text{ mPa}\cdot\text{s}$, $p_{sys} = 1 \text{ bar}$.

Here, the typical sheet breakup is changed into a pulsation mode with low frequency ($f_{KHI} \approx 100 \text{ Hz}$, calculated from HSC imaging), resulting in large liquid fragments without further disintegration. With increasing GLR , also $v_{gas,o}$ and $v_{gas,i}$ increased, which led to smaller droplet sizes for all GLO settings and especially for $GLO \approx GLI$ due to a higher pulsation frequency and increased aerodynamic forces. At $GLR = 0.7$, no maximum in droplet size for $GLO \approx GLI$ was detectable.

For comparison of the applied liquid flow configurations at $GLR = 0.5$, Figure 19 (left) represents the resulting $ID_{32,m}$ as a function of η_{liq} . Figure 19 (right) illustrates the primary jet or sheet breakup of configuration (i) at $GLR = 0.5$ and (iii) at $GLO = 0.5$ for $\eta_{liq} = 1$ and $400 \text{ mPa}\cdot\text{s}$. In accordance with previous measurements and the literature [12,59,70], for an increase in η_{liq} , a rising droplet size was detected for all liquid flow configurations. For every configuration a distinct dependence between an increase in η_{liq} and the corresponding increment in $ID_{32,m}$ was found. The highest droplet size for all atomized liquids was observed for flow configuration (iii) at $GLO = GLI = 0.25$, which was related to the comparably low total J_{gas} and the pulsation in primary breakup. For the atomization of water ($\eta_{liq} = 1 \text{ mPa}\cdot\text{s}$), the difference in resulting droplet size between $GLO = 0$ and $GLO = GLI$ was comparably small with $\Delta ID_{32,m} = 21 \mu\text{m}$.

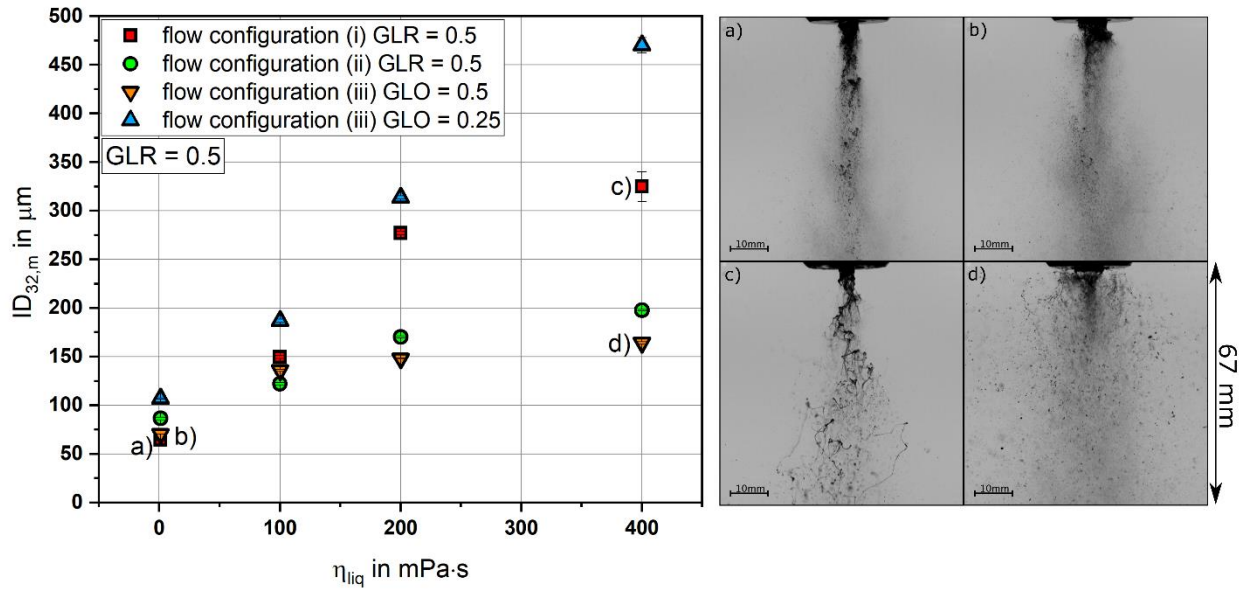


Figure 19: $ID_{32,m}$ as function of η_{liq} at varying configurations and GLO (left). HSC images of the primary breakup for a) configuration (i) at $GLR = 0.5$ and $\eta_{liq} = 1$ mPa·s, b) configuration (iii) at $GLO = 0.5$ and $\eta_{liq} = 1$ mPa·s, c) configuration (i) at $GLR = 0.5$ and $\eta_{liq} = 400$ mPa·s as well as d) configuration (iii) at $GLO = 0.5$ and $\eta_{liq} = 400$ mPa·s. $\dot{M}_{liq} = 30$ kg·h⁻¹, $p_{sys} = 1$ bar, $GLR = 0.5$.

As against this, for atomization of liquids with increased viscosity ($\eta_{liq} = 400$ mPa·s), the effect on droplet size was distinct with $\Delta ID_{32,m} = 272$ μm. The smallest droplet size was achieved with configuration (i) at $GLR = 0.5$ and $\eta_{liq} = 1$ mPa·s. For increased viscosity, the resulting $ID_{32,m}$ was rising significantly towards the second highest value in the investigation, due to the formation of large ligaments and fibers after primary breakup (see also Figure 19 (right)). Smallest droplet sizes at high viscosity were found for the liquid sheet configurations (ii) and (iii) at $GLR = 0.5$ and $GLO = 0.5$, respectively. Comparing these configurations, the observed $ID_{32,m}$ was even smaller for configuration (iii) at $GLO = 0.5$. This effect was explained by two reasons, namely the primary breakup morphology and the available shear surface of the gas phase. The primary breakup for configuration (ii) at $GLR = 0.5$ typically produces small droplets in the spray center, while remaining sheet fragments at the spray boundary receive low aerodynamic forces, due to their distance to the gas jet core. As against this, for configuration (iii) at $GLO = 0.5$ the liquid sheet is surrounded by a fast annular gas stream, which leads to low local gas pressures and a radial force guiding the liquid fragments radially through the gas jet core (see Figure 19 (right)). The transition of the liquid ligaments through the high-velocity gas stream enables for complete disintegration into small droplets. Additionally, comparing the shear area between gas and liquid phase reveals, that for configuration (iii) at $GLO = 0.5$, this shear surface is around 40% larger, compared to the shear surface for configuration (ii) at $GLR = 0.5$, which also leads to a more intense primary breakup and results therefore in smaller droplet sizes.

To sum up, the change in atomizer flow configuration from (i) over (ii) towards (iii) led to an atomizer concept with nearly equal resulting droplet size between liquid jet and liquid sheet. Here, the configuration (i) led to smaller droplet size at high v_{gas} (GLR), whereas for configuration (ii) smaller droplet sizes were measured at low v_{gas} (GLR). Furthermore, the sensitivity on droplet size is significantly reduced especially for configuration (iii) at $GLO = 0.5$ compared to configuration (i) at $GLR = 0.5$.

5 Summary

In order to conclude the main results of this work, the research questions according to chapter 1 are answered.

Question 1: *How are spray characteristics affected by an increase in system pressure?*
(paper I & II)

Atomization experiments with central liquid jet atomizers (configuration (i)) were performed in the test rig PAT at varying gas velocity, system pressure and gas gap width in order to change all variables forming the gas momentum flow. Experimental data reveal, that for operation of one atomizer at varying system pressure, an increase in system pressure led to a decrease in droplet size, if also gas mass flow is increased to keep other influencing parameters as gas velocity constant. Additional experiments were conducted following the approach to keep atomizer operating conditions constant and independent of system pressure. This was achieved by an adaption of the gas orifice area. Here, first a decrease of droplet size due to the aerodynamic forces, followed by an increase in droplet size was observed for increasing system pressure. The significant increase was attributed to the decrement in gas orifice area, leading to a faster deceleration of the gas phase after exiting the atomizer. Knowing about the relevance of gas orifice area, investigations were performed varying all parameters that form gas momentum flow.

Based on those data, an empirical model was derived, allowing for system pressure scaling of central liquid jet atomizers. With the aforementioned empirical model, a tool is given to calculate atomizer dimensions that are necessary to keep droplet size constant with increasing system pressure. In order to apply system pressure scaling, droplet size, system pressure, and GLR need to be specified, while gas velocity and gas gap width are calculated via gas momentum flow and gas mass flow.

Question 2: *How are spray characteristics affected by an increase in liquid mass flow?*
(paper IV)

Measurements on the influence of liquid mass flow concerning primary jet breakup and droplet size were conducted in the test rigs ATMO and BTR with configuration (i) applying water. Here, liquid velocity, aerodynamic Weber number and GLR were kept constant, which led - for four liquid mass flow steps - to four atomizers, respectively. With increasing liquid mass flow a significant increase in droplet size and primary ligament length was detected, even though We_{aero} was kept constant. Both spray characteristics were influenced by two effects. Due to the atomization at constant aerodynamic Weber number and liquid velocity, an increase in liquid mass flow led to larger liquid jet diameters and

therefore to a decrease in gas velocity. This results in a reduction of the aerodynamic forces relevant for atomization. As a second effect, the higher liquid mass flow leads to an increase in liquid jet diameter to keep liquid velocity constant. With increasing liquid jet diameter the impact area of the gas phase for liquid jet disintegration to liquid volume ratio was shifted towards lower values, which increases the primary ligament length significantly.

Question 3: *How is the disintegration process of a liquid jet influenced by an angle between gas and liquid phase at the atomizer orifice?* (proceeding II)

Investigations on the influence of gas channel angle on liquid jet disintegration were performed in the test rigs PAT and ATMO applying configuration (i) with water and glycerol/water-mixtures. The disintegration process of a liquid jet was found to be influenced by destabilizing and stabilizing effects, applying a gas channel angle at the atomizer orifice. For a higher gas channel angle an impact of the gas stream on the liquid jet occurs, which results in a local increment of gas velocity. This increase correlates with a reduction of the cross-sectional area of the gas flow and leads to higher aerodynamic forces. In consequence the liquid jet is destabilized more intense, causing higher droplet velocity and smaller droplet size. Besides this, at the impact zone of the gas phase on the liquid jet, a stabilized region was observed. The region is formed and maintained by the equal radial force components of the surrounding gas stream and shifts the formation of Kelvin-Helmholtz instability towards increased gas velocities. Overall, it can be stated, that the influence of gas channel angle was especially observed at sufficiently small aerodynamic forces and in this case low gas velocity. For higher aerodynamic forces, the effect of gas channel angle was negligibly small.

Question 4: *Which atomizer flow configuration (liquid jet or liquid sheet) results in smaller droplet sizes?* (proceeding I & paper III)

The comparison of 3 different liquid flow configurations was performed in the test rig ATMO for (i) a central liquid jet with annular gas stream, (ii) an annular liquid sheet with central gas jet and (iii) an annular liquid sheet with central and outer gas streams applying water and glycerol/water-mixtures. The atomizer was designed with equal orifice areas to guarantee for constant flow conditions at constant mass flows for each operating configuration. The experimental data reveal, that for low viscosity and high gas velocity the central liquid jet atomizer achieved the smallest droplet size compared to the liquid sheet configurations. This result was explained by the shearing gas stream around the liquid jet, leading to a complete disintegration of the liquid into small droplets when performed in the lab scale. For atomization of liquids with high viscosity, the spray of configuration (i) showed large ligaments after primary breakup resulting in large droplets.

Here, liquid sheet atomizers and especially flow configuration (iii) applying only the outer gas stream, generated a spray without ligaments and comparably small droplet size. The formation of small droplets was induced mainly by the primary breakup morphology, where the liquid sheet is radially accelerated by the high velocity gas stream and the resulting lower local gas pressure. After passing the gas stream, the sheet is completely disintegrated into small droplets generating a wide spray angle.

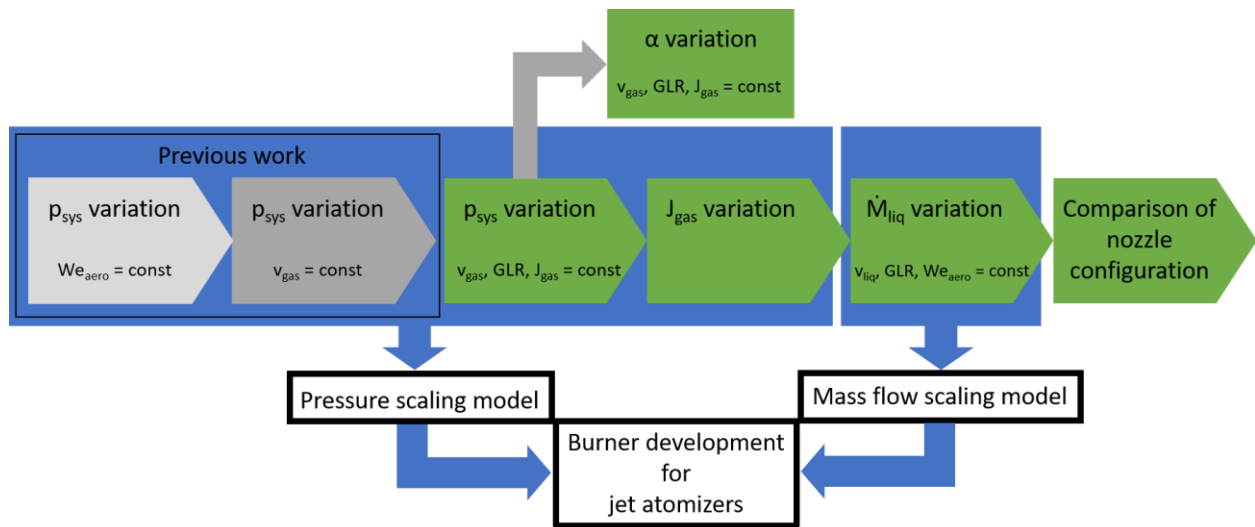


Figure 20: Context of the discussed research topics and the significance in the field of burner development.

Following the previous research, regarding investigations on increased system pressure ($We_{aero} = \text{const}$ and $v_{gas} = \text{const}$), the discussed work from this thesis (see Figure 20) enables the possibility for system pressure scaling of a liquid jet atomizer, while resulting droplet size and liquid mass flow remain constant. In addition with the introduced model for mass flow scaling of liquid jet atomizers, an opportunity for burner development in terms of EFG is given. In order to further optimize the resulting spray characteristics and expand liquid mass flows, a first step into the research topic of liquid sheet atomizers was performed by a configuration comparison.

Besides the contribution of this work towards the understanding of atomization phenomena, spray processes and atomizer design, also a basis for future research topics is provided. These topics are mainly focused on resulting spray characteristics of potentially scalable liquid sheet atomizers with inner and outer gas stream. Here, especially the influence of system pressure, gas orifice and velocity arrangement as well as liquid sheet thickness and corresponding liquid mass flow should be of major interest for advanced burner development in terms of entrained flow gasification.

Appendix

A Additional measurements for paper I

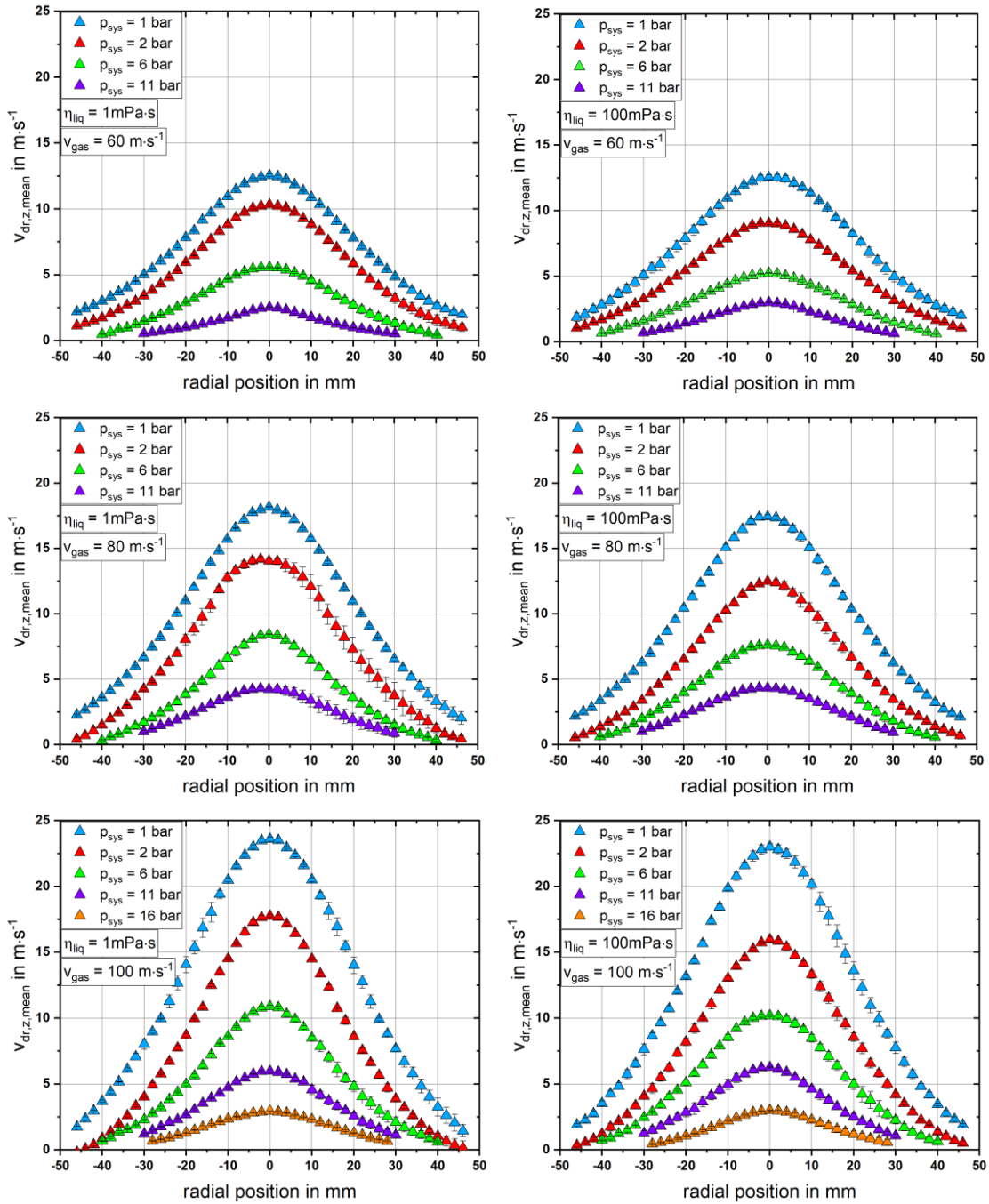


Figure A 1: $v_{dr,z,mean}$ as function of radial position at varying p_{sys} , v_{gas} (GLR) and η_{liq} . Configuration (i), $d_{liq} = 2 \text{ mm}$, $\dot{M}_{liq} = 20 \text{ kg}\cdot\text{h}^{-1}$.

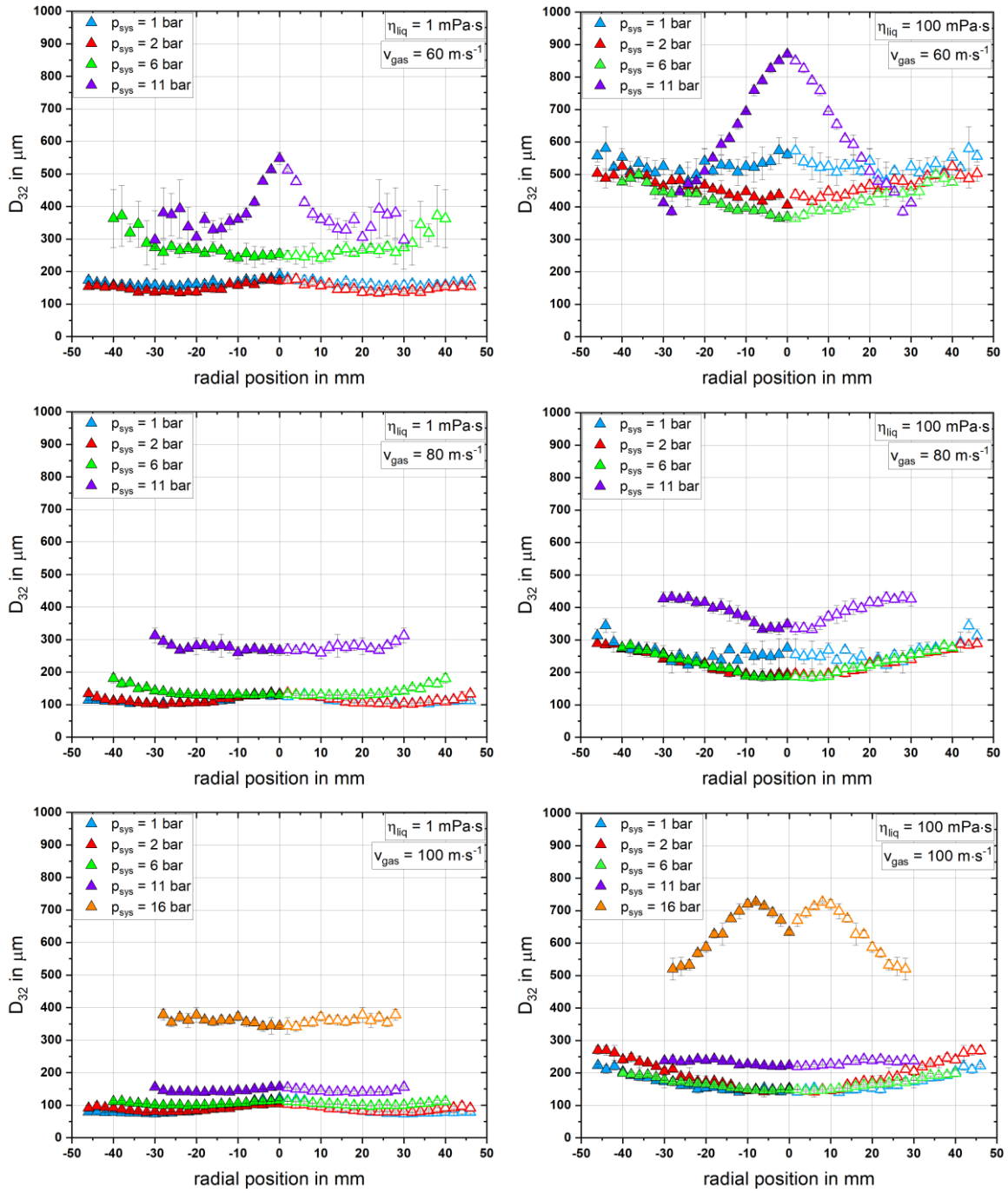


Figure A 2: D_{32} as a function of radial position at varying p_{sys} , v_{gas} (GLR) and η_{liq} . Configuration (i), $d_{liq} = 2 \text{ mm}$, $\dot{M}_{liq} = 20 \text{ kg}\cdot\text{h}^{-1}$.

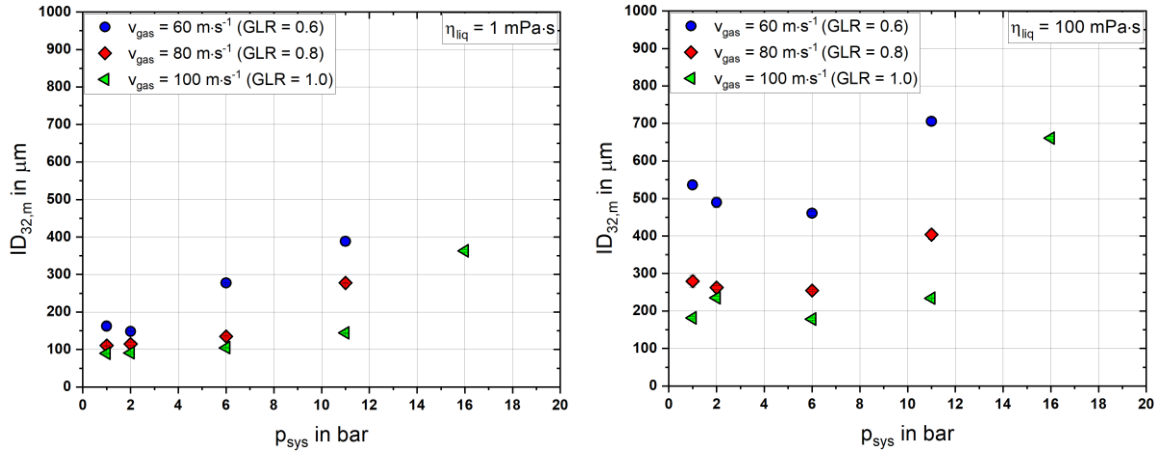


Figure A 3: $ID_{32,m}$ as function of p_{sys} at varying v_{gas} (GLR) and η_{liq} . Configuration (i), $d_{\text{liq}} = 2 \text{ mm}$, $\dot{M}_{\text{liq}} = 20 \text{ kg}\cdot\text{h}^{-1}$.

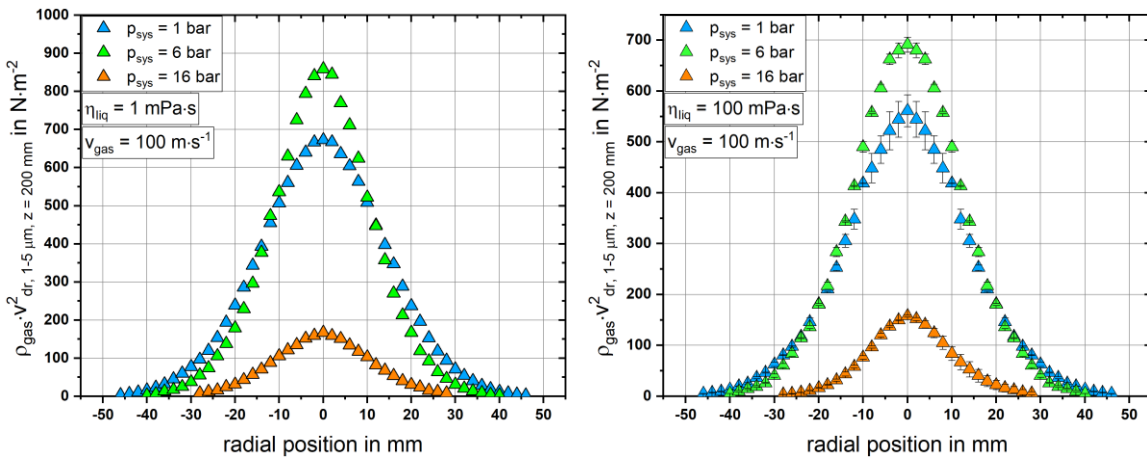


Figure A 4: $j_{\text{gas},\text{local}}$ as function of radial position at varying p_{sys} and η_{liq} . Configuration (i), $d_{\text{liq}} = 2 \text{ mm}$, $\dot{M}_{\text{liq}} = 20 \text{ kg}\cdot\text{h}^{-1}$, $v_{\text{gas}} = 100 \text{ m}\cdot\text{s}^{-1}$ (GLR = 1.0).

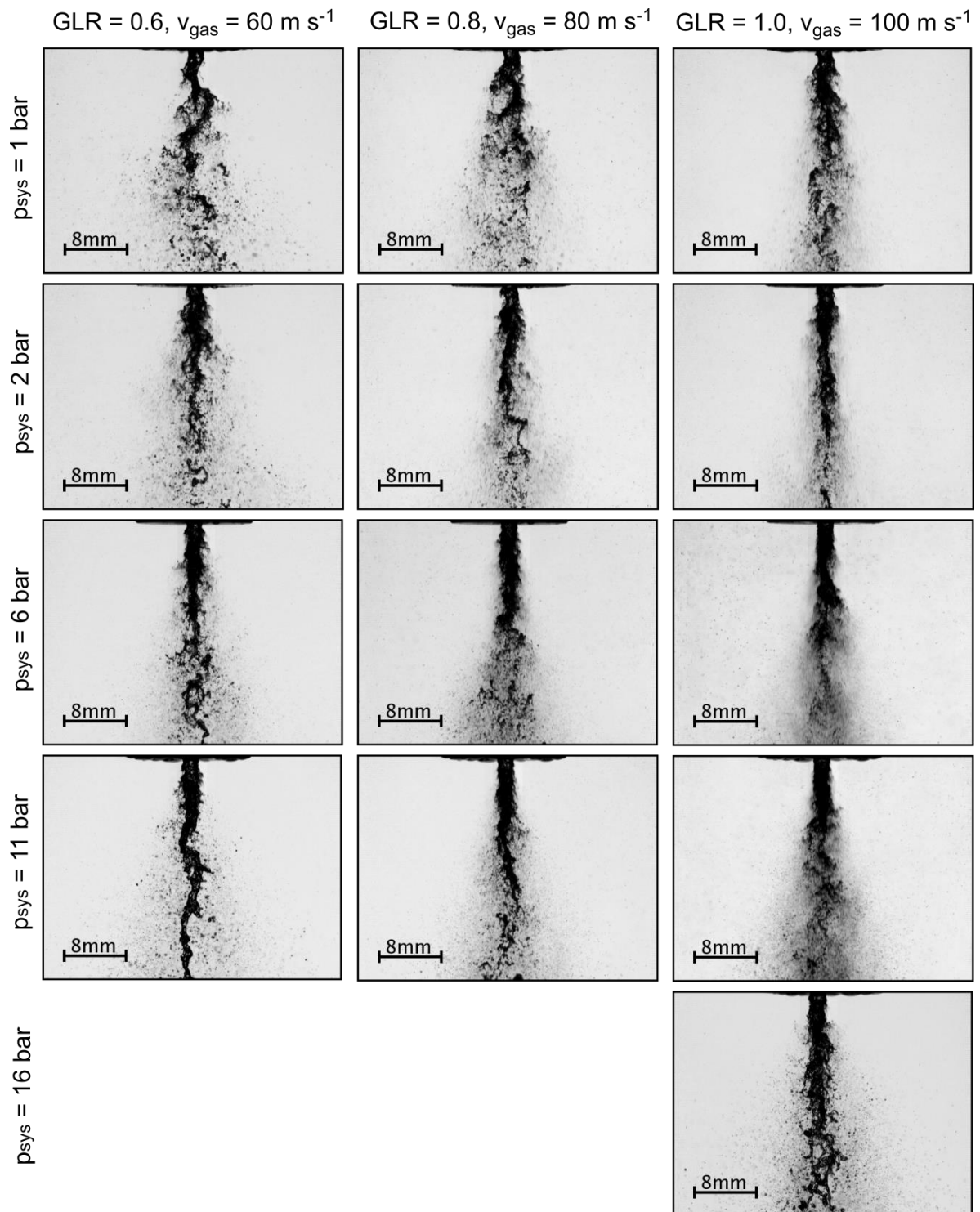


Figure A 5: HSC images of the primary jet breakup as function of p_{sys} and v_{gas} (GLR). Configuration (i), $d_{\text{liq}} = 2 \text{ mm}$, $\dot{M}_{\text{liq}} = 20 \text{ kg}\cdot\text{h}^{-1}$, $\eta_{\text{liq}} = 1 \text{ mPa}\cdot\text{s}$.

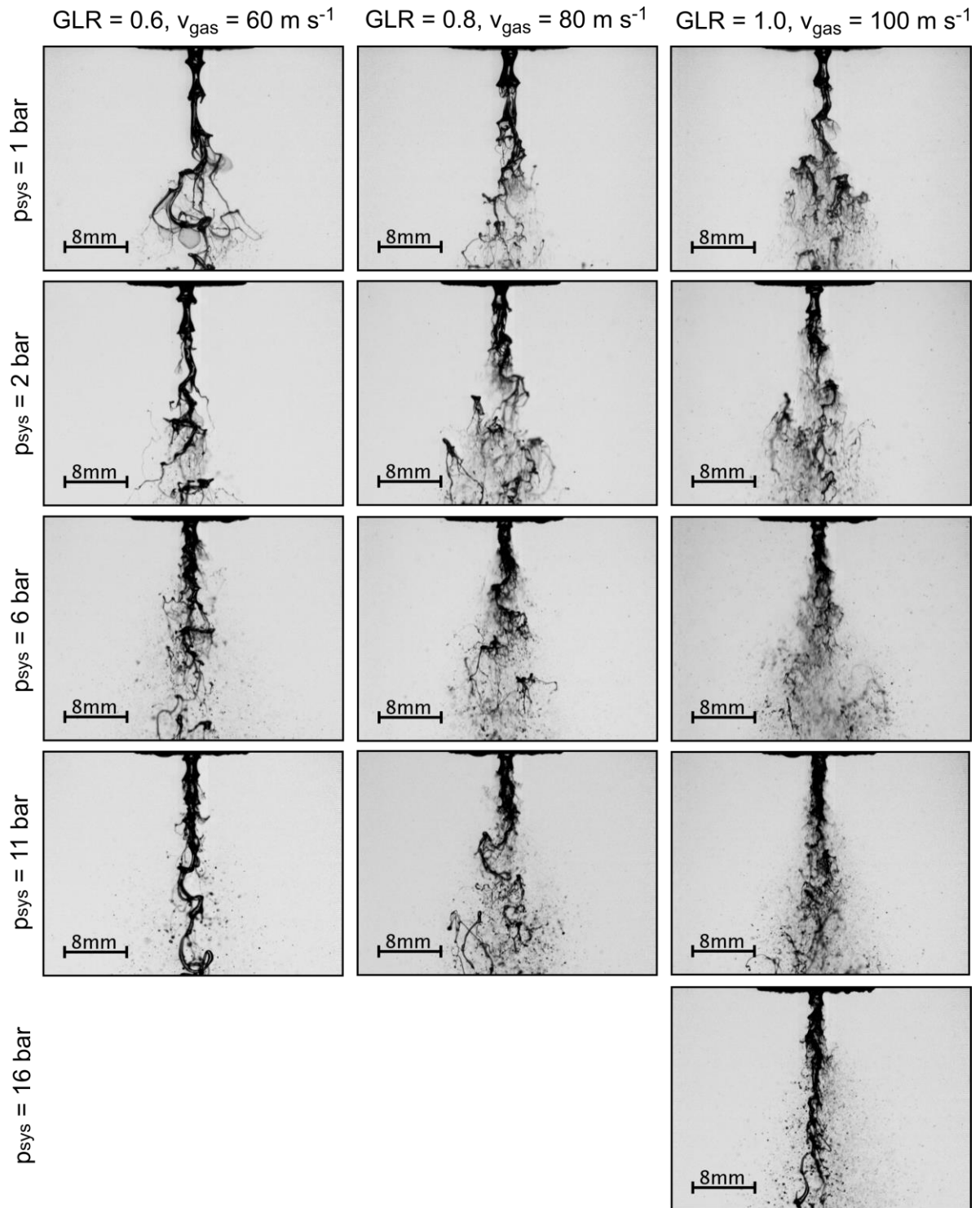


Figure A 6: HSC images of the primary jet breakup as function of p_{sys} and v_{gas} (GLR). Configuration (i), $d_{liq} = 2 \text{ mm}$, $\dot{M}_{liq} = 20 \text{ kg}\cdot\text{h}^{-1}$, $\eta_{liq} = 100 \text{ mPa}\cdot\text{s}$.

B Additional measurements for paper II

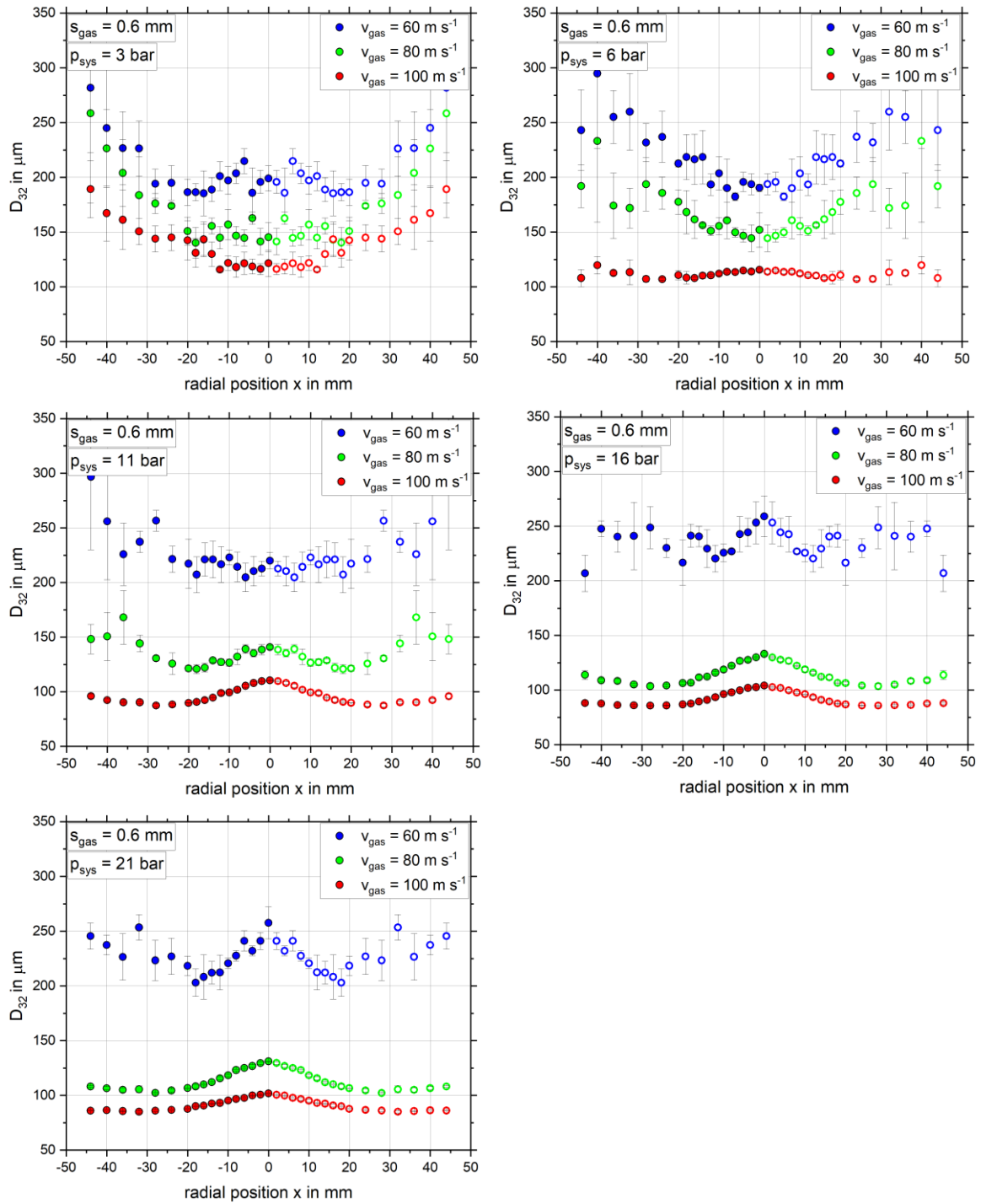


Figure B 1: D_{32} as function of radial position at varying v_{gas} (GLR) and p_{sys} . Configuration (i), $d_{liq} = 2$ mm, $\dot{M}_{liq} = 20$ kg·h⁻¹, $\eta_{liq} = 1$ mPa·s, $s_{gas} = 0.6$ mm.

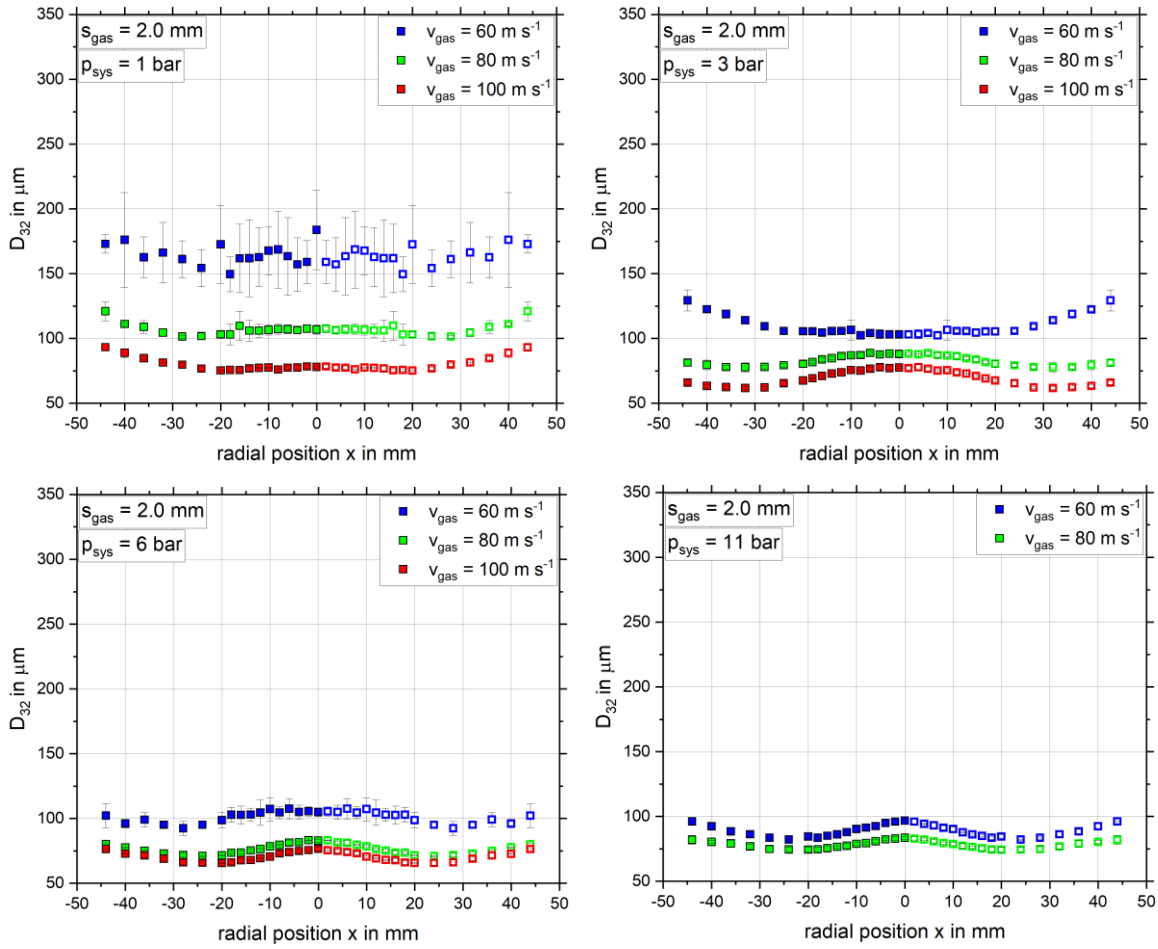


Figure B 3: D_{32} as function of radial position at varying v_{gas} (GLR) and p_{sys} . Configuration (i), $d_{\text{liq}} = 2 \text{ mm}$, $\dot{M}_{\text{liq}} = 20 \text{ kg}\cdot\text{h}^{-1}$, $\eta_{\text{liq}} = 1 \text{ mPa}\cdot\text{s}$, $s_{\text{gas}} = 2.0 \text{ mm}$.

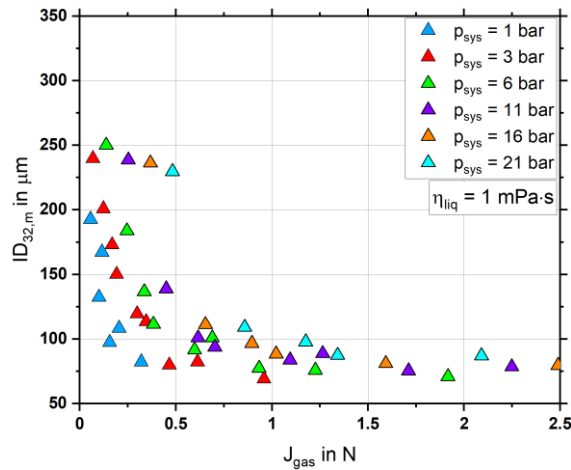


Figure B 4: $ID_{32,m}$ as function of J_{gas} at varying p_{sys} . Configuration (i), $d_{\text{liq}} = 2 \text{ mm}$, $\dot{M}_{\text{liq}} = 20 \text{ kg}\cdot\text{h}^{-1}$, $\eta_{\text{liq}} = 1 \text{ mPa}\cdot\text{s}$.

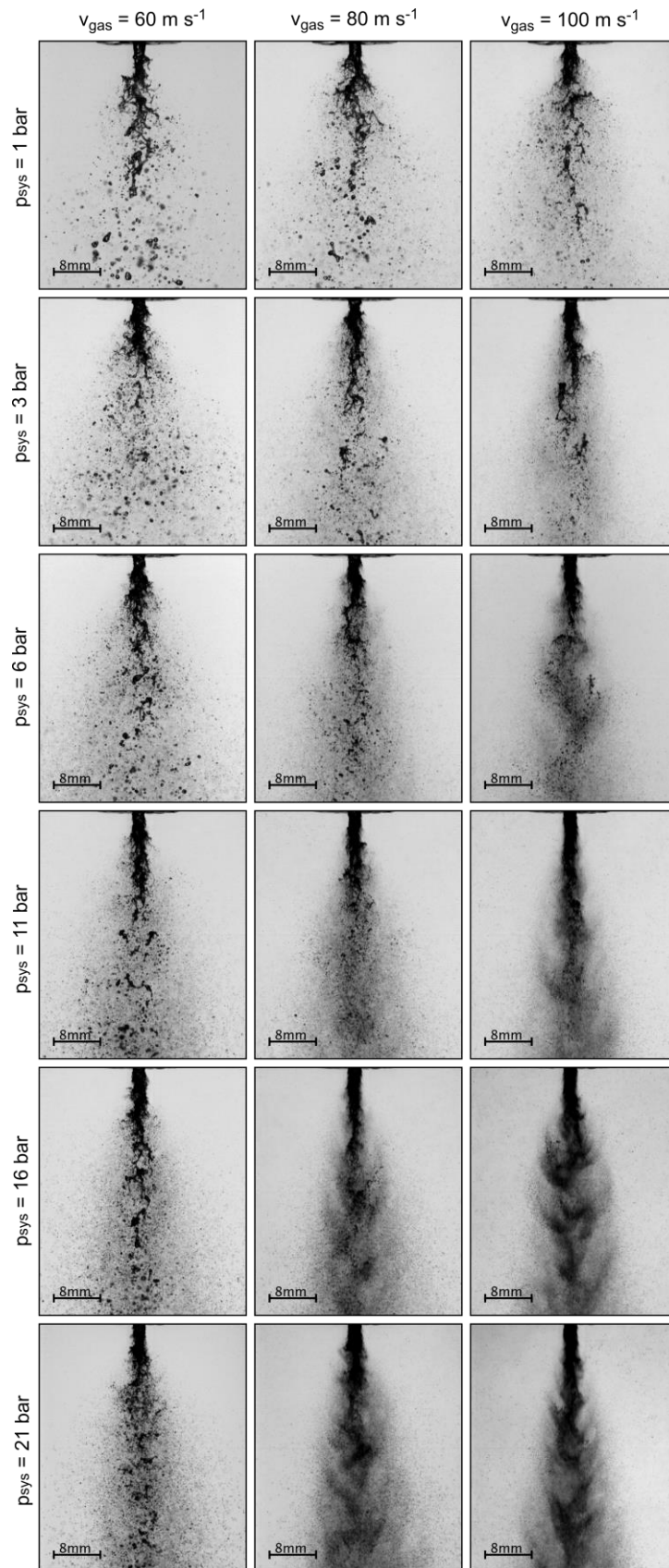


Figure B 5: HSC images of the primary jet breakup as function of p_{sys} and v_{gas} (GLR). Configuration (i), $d_{liq} = 2 \text{ mm}$, $\dot{M}_{liq} = 20 \text{ kg} \cdot \text{h}^{-1}$, $\eta_{liq} = 1 \text{ mPa} \cdot \text{s}$, $s_{gas} = 0.6 \text{ mm}$.

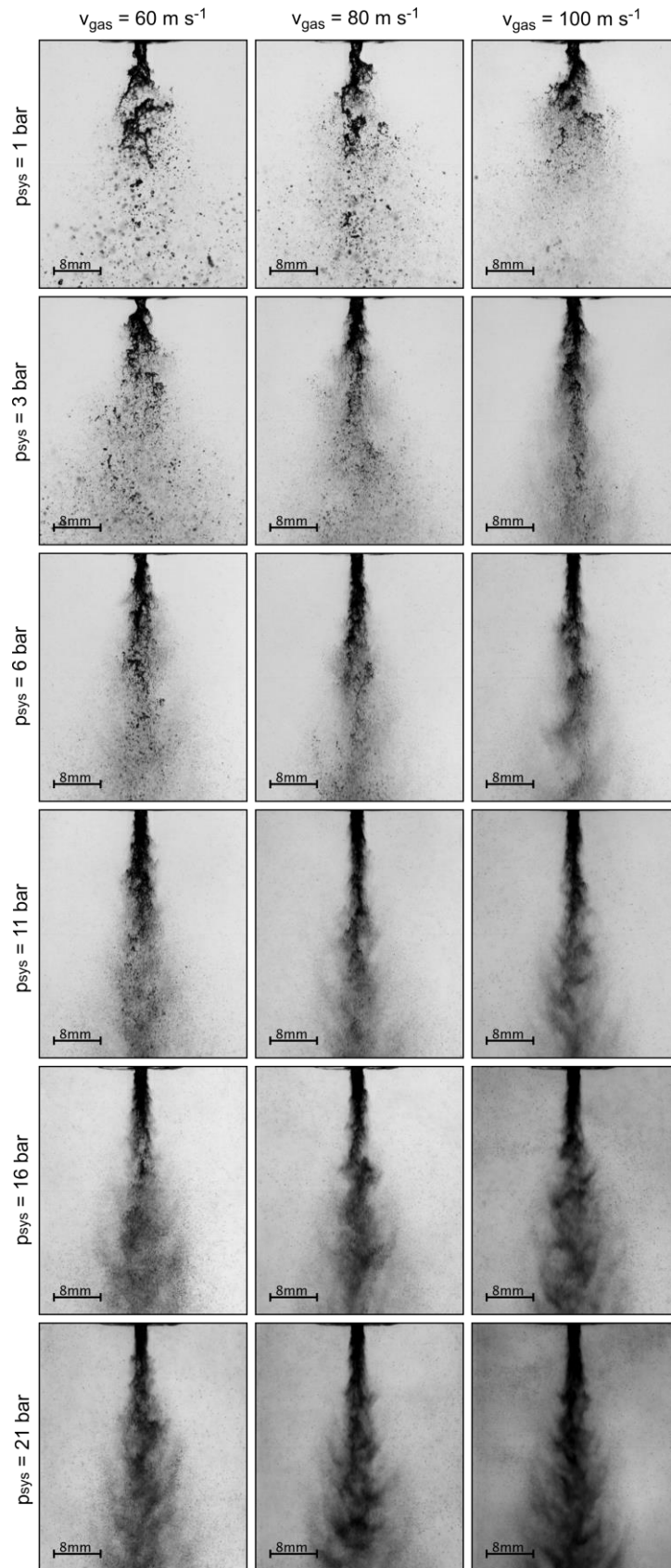


Figure B 6: HSC images of the primary jet breakup as function of p_{sys} and v_{gas} (GLR). Configuration (i), $d_{\text{liq}} = 2 \text{ mm}$, $\dot{M}_{\text{liq}} = 20 \text{ kg} \cdot \text{h}^{-1}$, $\eta_{\text{liq}} = 1 \text{ mPa} \cdot \text{s}$, $s_{\text{gas}} = 1.2 \text{ mm}$.

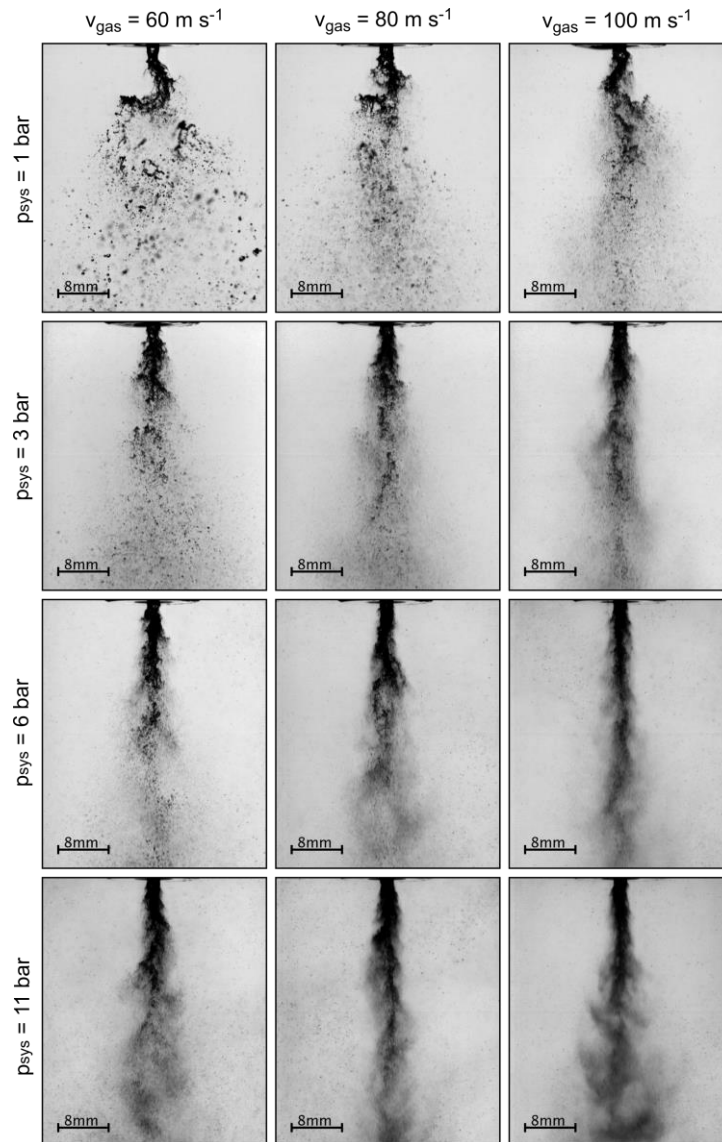


Figure B 7: HSC images of the primary jet breakup as function of p_{sys} and v_{gas} (GLR). Configuration (i), $d_{liq} = 2 \text{ mm}$, $\dot{M}_{liq} = 20 \text{ kg} \cdot \text{h}^{-1}$, $\eta_{liq} = 1 \text{ mPa} \cdot \text{s}$, $s_{gas} = 2.0 \text{ mm}$.

C Additional measurements for paper IV

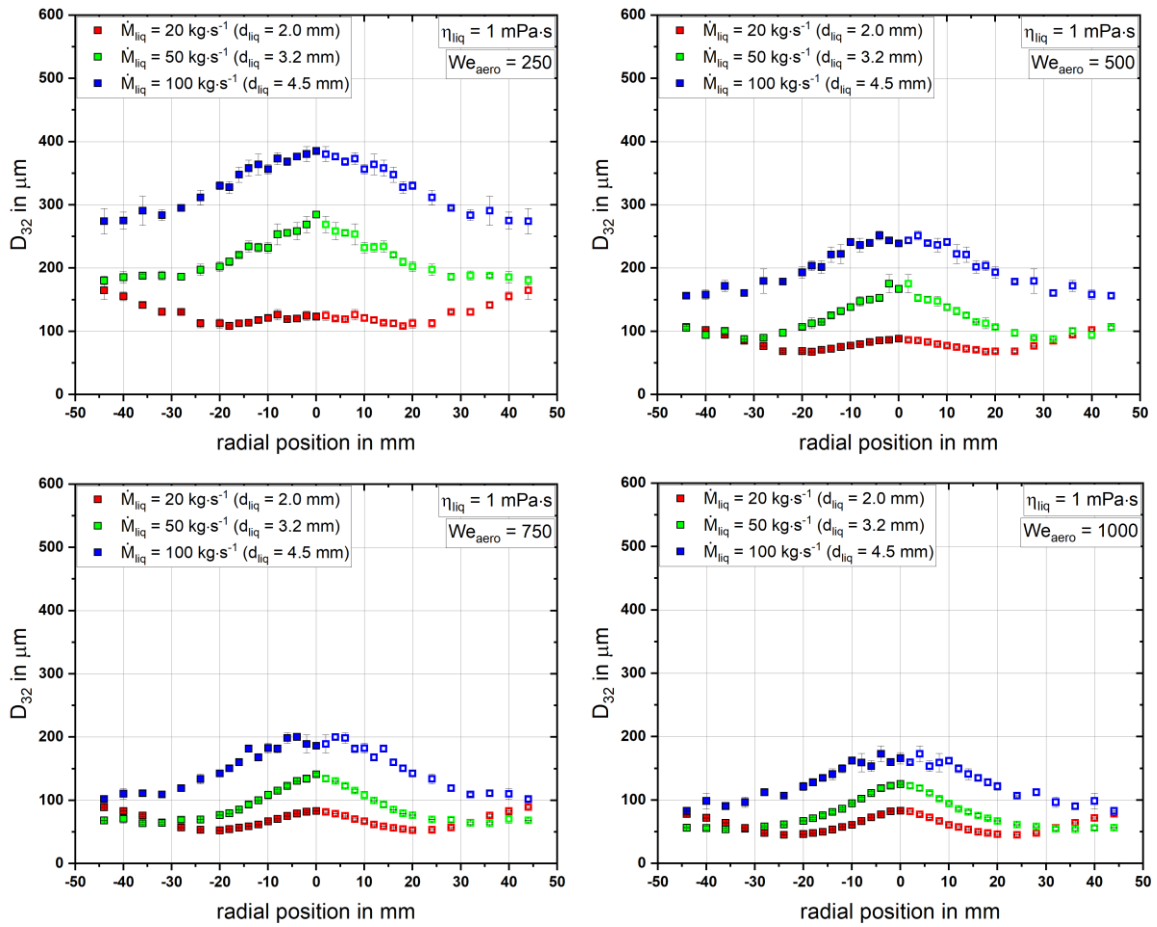


Figure C 1: D_{32} as function of radial position at varying \dot{M}_{liq} (d_{liq}) and We_{aero} . Configuration (i), $\eta_{liq} = 1 \text{ mPa}\cdot\text{s}$, $p_{sys} = 1 \text{ bar}$.

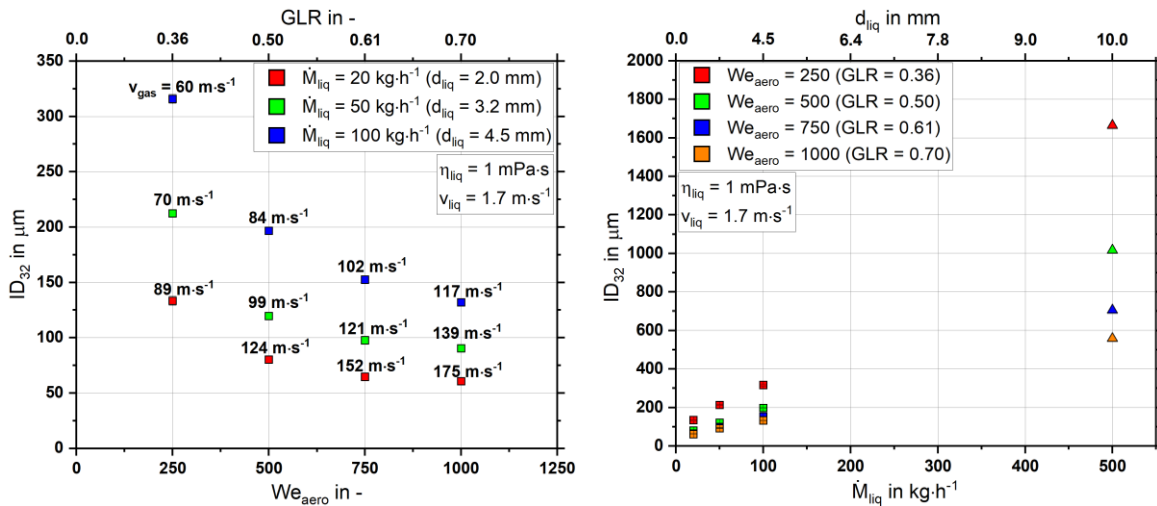


Figure C 2: $ID_{32,m}$ as function of We_{aero} (GLR) at varying \dot{M}_{liq} (d_{liq}) (left) and \dot{M}_{liq} (d_{liq}) at varying We_{aero} (GLR) (right). Configuration (i), $\eta_{liq} = 1 \text{ mPa}\cdot\text{s}$, $p_{sys} = 1 \text{ bar}$.

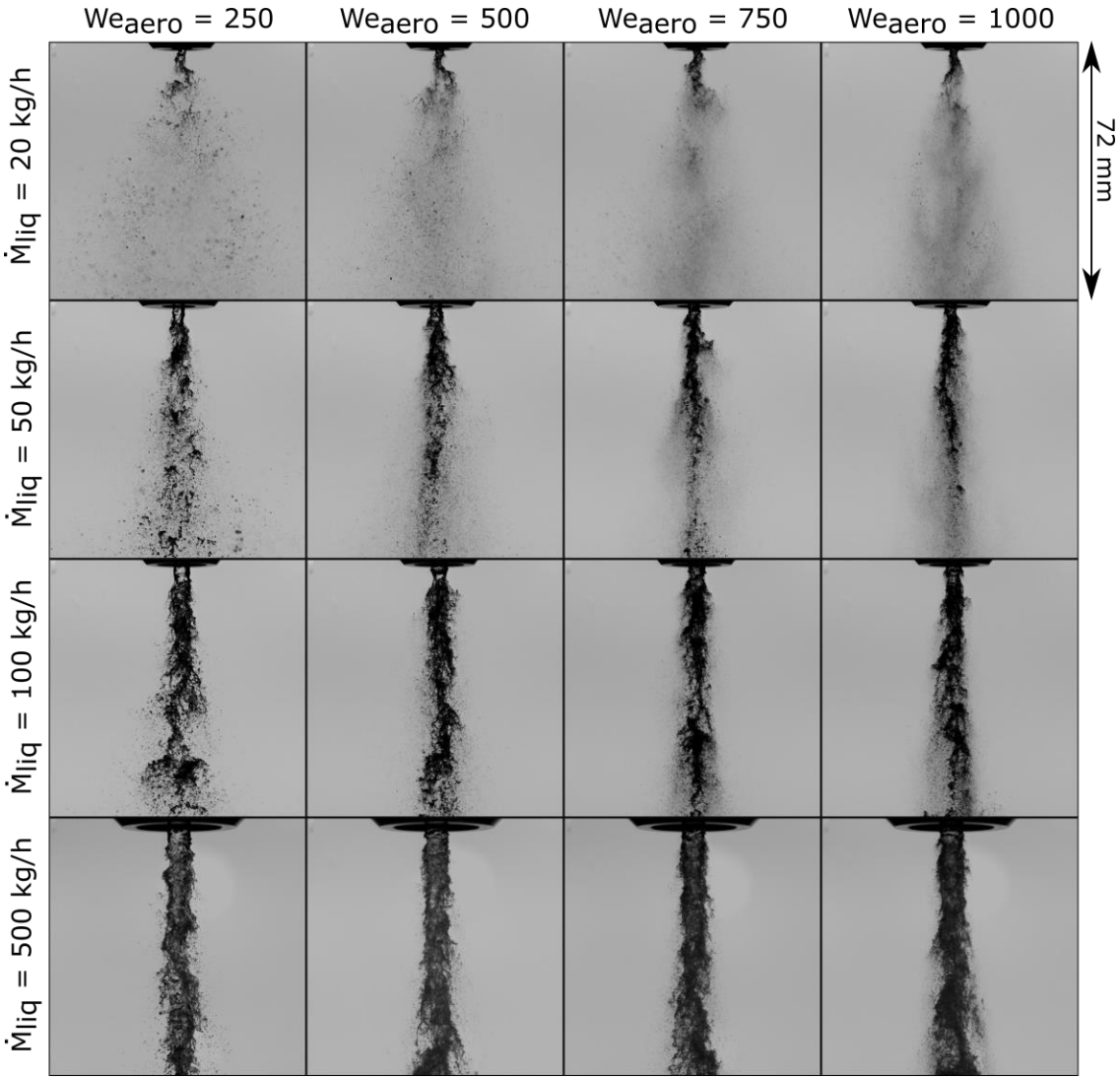


Figure C 3: HSC images of the primary jet breakup as function of \dot{M}_{liq} (d_{liq}) and We_{aero} (GLR). Configuration (i), $\eta_{liq} = 1 \text{ mPa}\cdot\text{s}$, $p_{sys} = 1 \text{ bar}$.

D Additional measurements for proceeding II

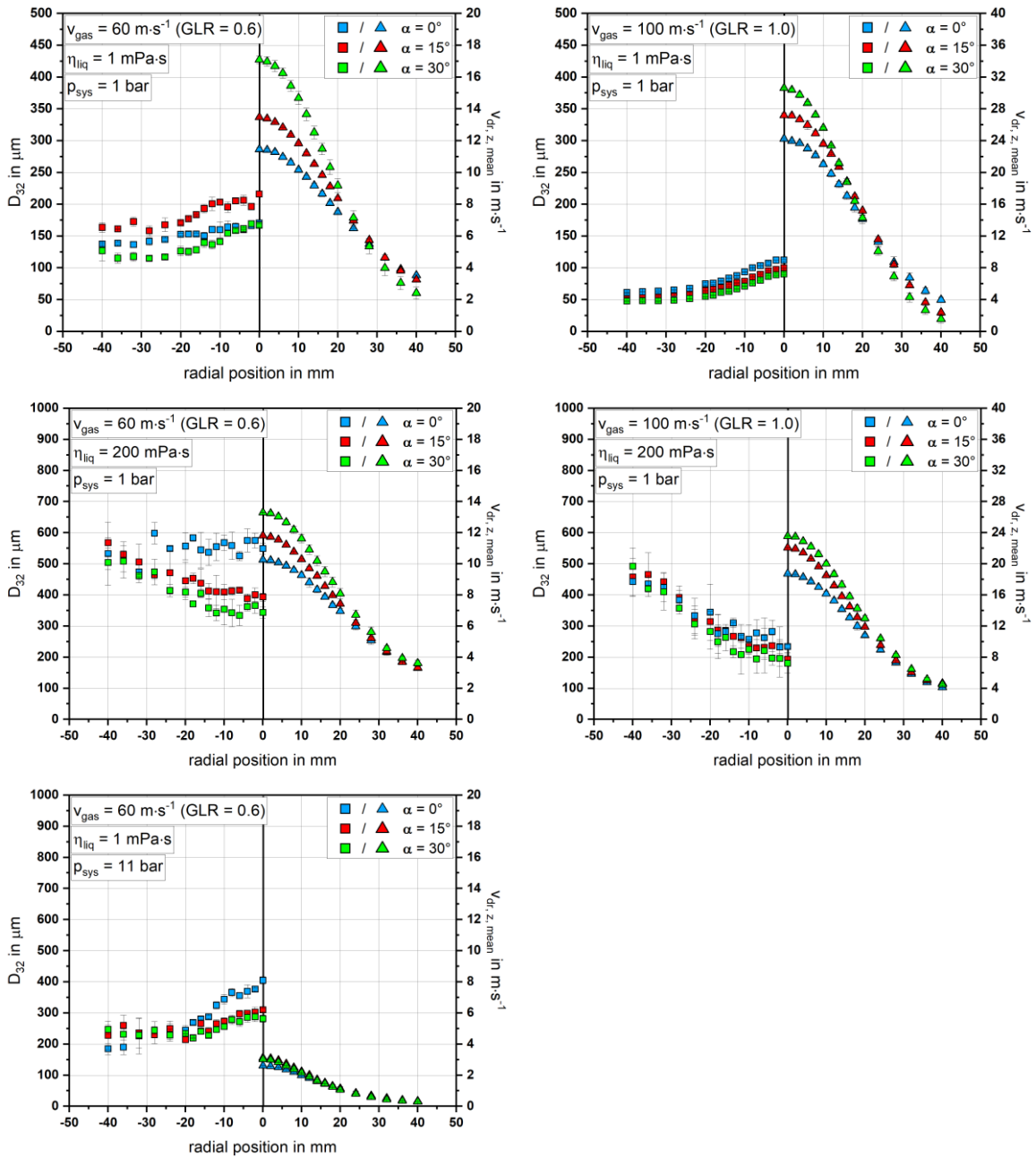


Figure D 1: D_{32} and $v_{dr,z,mean}$ as function of radial position at varying α , v_{gas} (GLR), p_{sys} and η_{liq} . Configuration (i), $d_{liq} = 2 \text{ mm}$, $\dot{M}_{liq} = 20 \text{ kg}\cdot\text{h}^{-1}$.

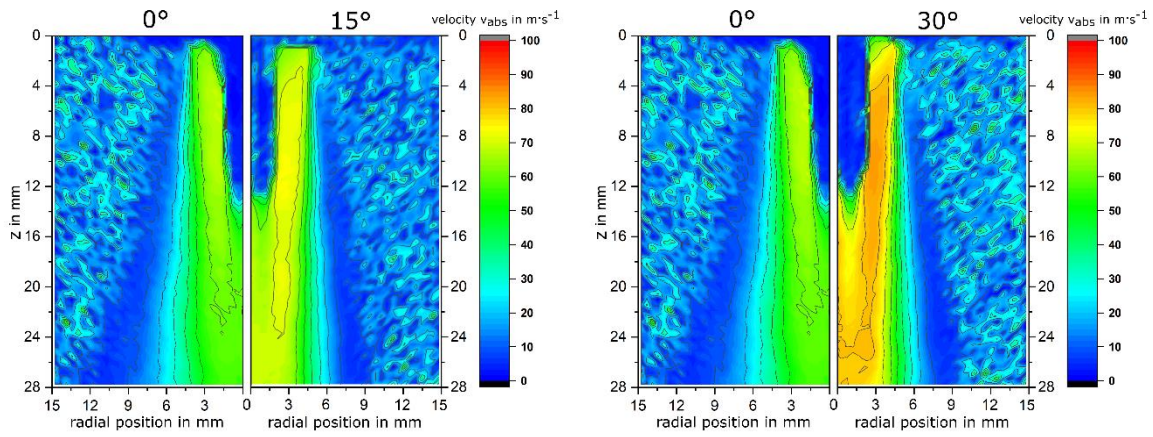


Figure D 2: PIV measurements of gas velocity v_{abs} for varying α in the atomizer nearfield. Configuration (i), $d_{liq} = 2 \text{ mm}$, $\dot{M}_{liq} = 20 \text{ kg}\cdot\text{h}^{-1}$, $s_{gas} = 2.0 \text{ mm}$, $v_{gas} = 60 \text{ m}\cdot\text{s}^{-1}$, $p_{sys} = 1 \text{ bar}$.

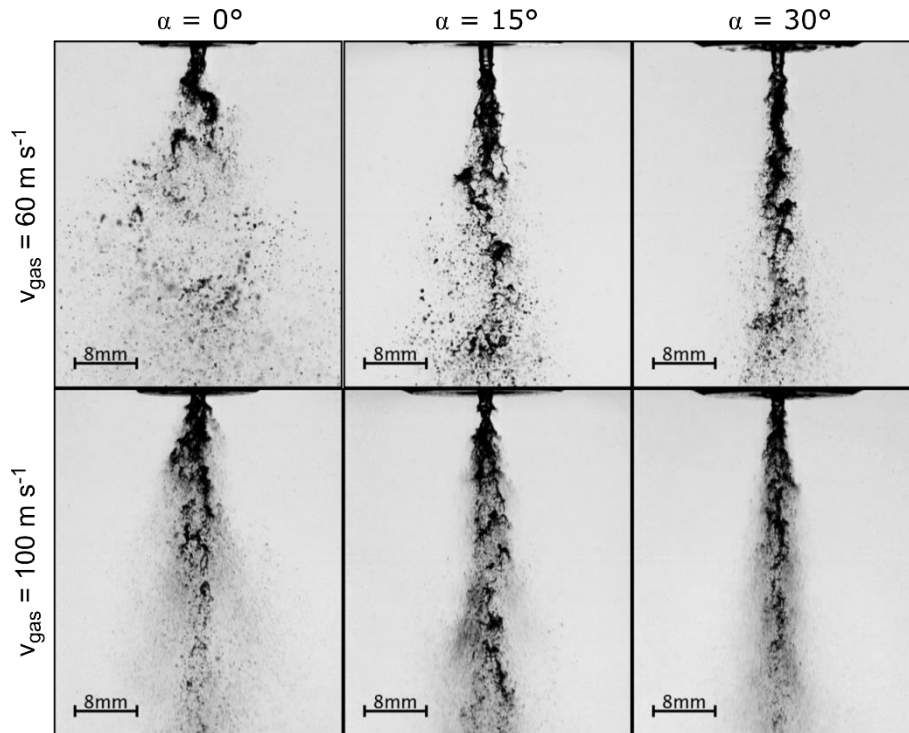


Figure D 3: HSC images of the primary jet breakup as function of α and v_{gas} (GLR). Configuration (i), $d_{liq} = 2 \text{ mm}$, $\dot{M}_{liq} = 20 \text{ kg}\cdot\text{h}^{-1}$, $\eta_{liq} = 1 \text{ mPa}\cdot\text{s}$, $s_{gas} = 2.0 \text{ mm}$, $p_{sys} = 1 \text{ bar}$.

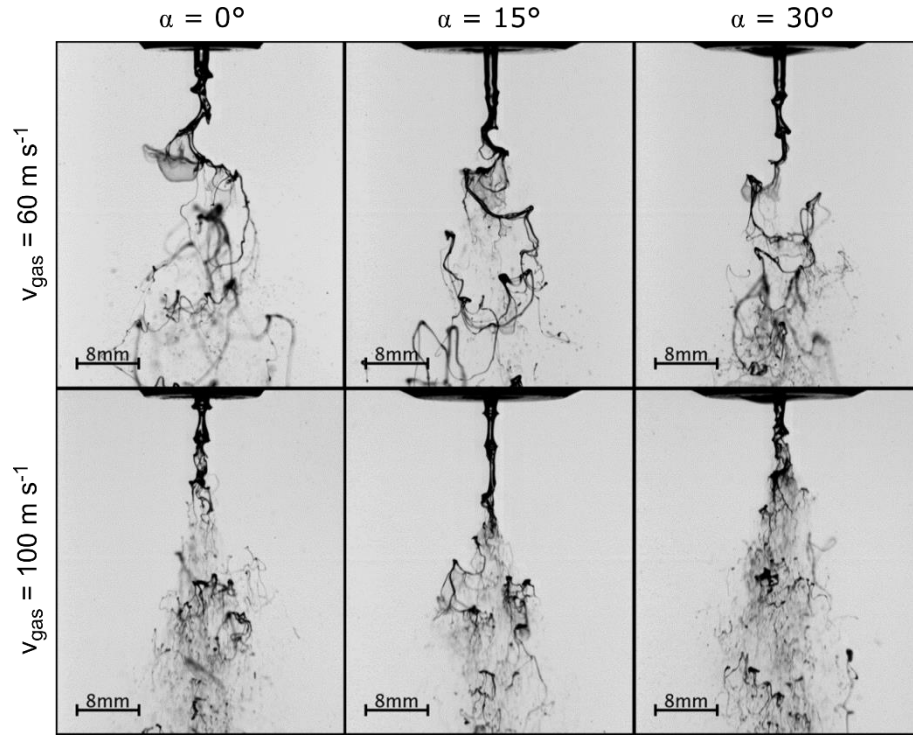


Figure D 4: HSC images of the primary jet breakup as function of α and v_{gas} (GLR). Configuration (i), $d_{liq} = 2$ mm, $\dot{M}_{liq} = 20$ kg·h⁻¹, $\eta_{liq} = 100$ mPa·s, $s_{gas} = 2.0$ mm, $p_{sys} = 1$ bar.

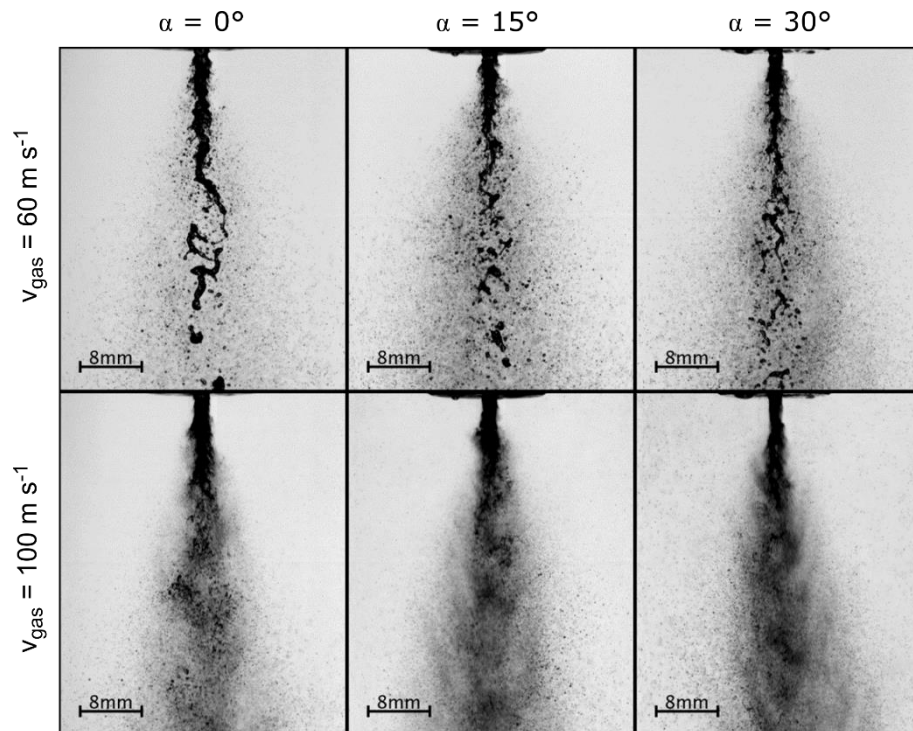


Figure D 5: HSC images of the primary jet breakup as function of α and v_{gas} (GLR). Configuration (i), $d_{liq} = 2$ mm, $\dot{M}_{liq} = 20$ kg·h⁻¹, $\eta_{liq} = 1$ mPa·s, $s_{gas} = 0.5$ mm, $p_{sys} = 11$ bar.

E Additional measurements for proceeding I and paper III

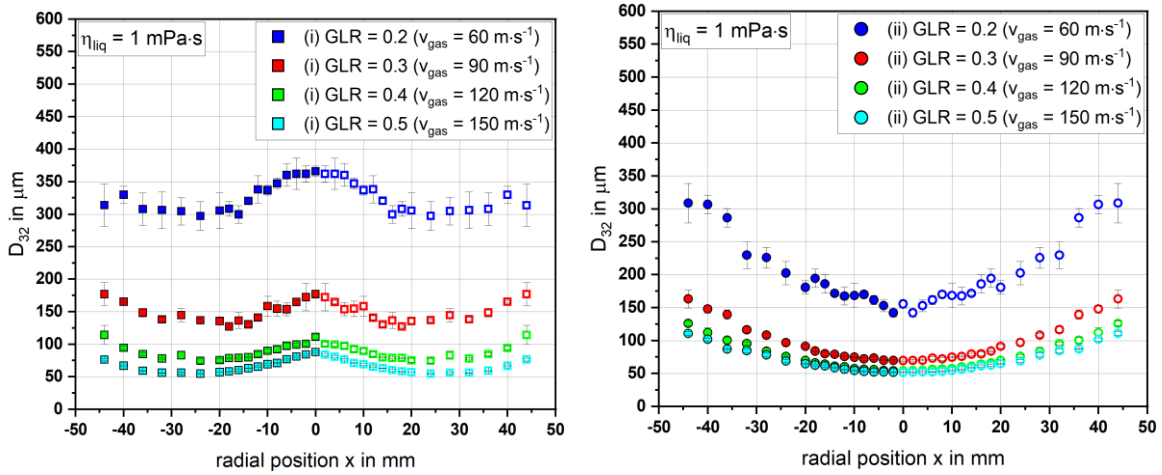


Figure E 1: D_{32} as function of radial position at varying v_{gas} (GLR) for configuration (i) (left) and configuration (ii) (right). $\dot{M}_{liq} = 30 \text{ kg}\cdot\text{h}^{-1}$, $\eta_{liq} = 1 \text{ mPa}\cdot\text{s}$, $p_{sys} = 1 \text{ bar}$.

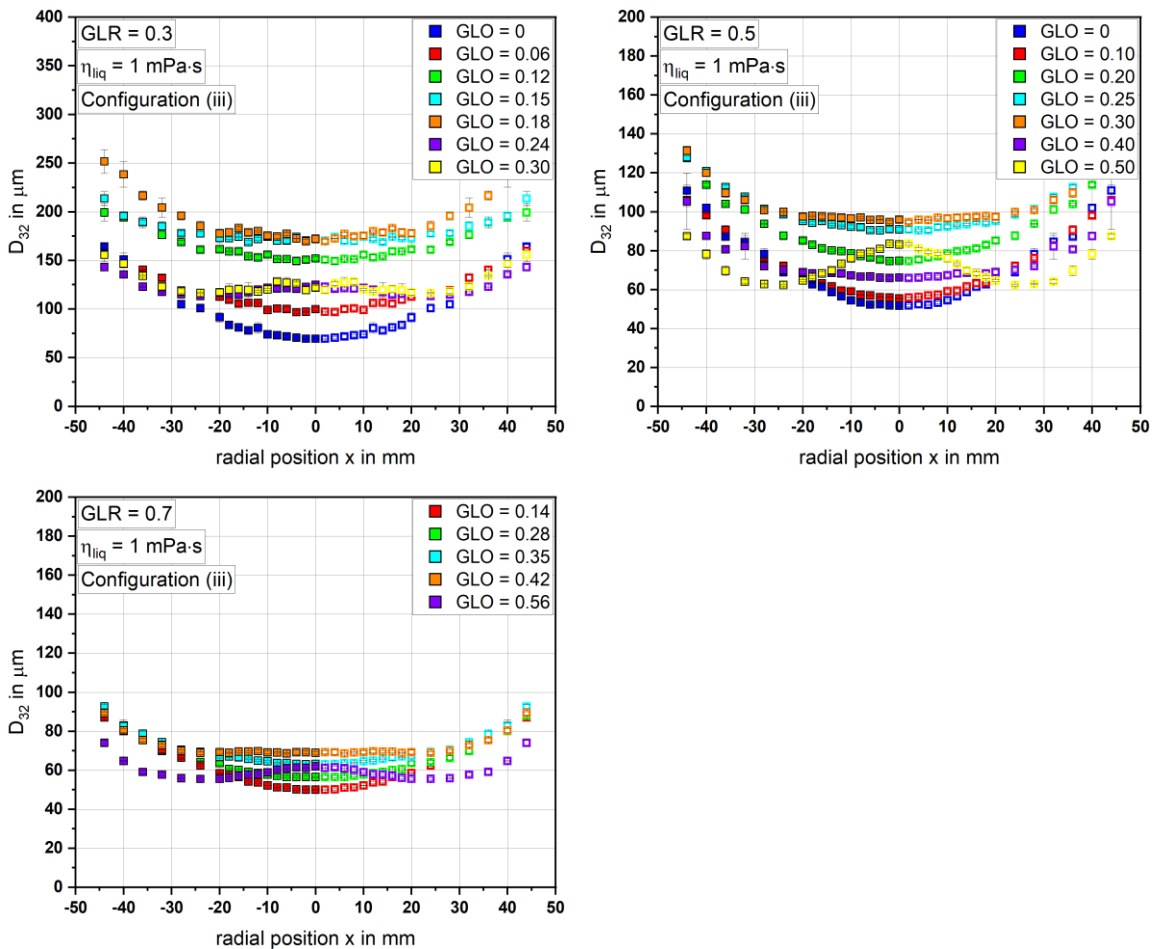


Figure E 2: D_{32} as function of radial position at varying GLO and GLR. Configuration (iii), $\dot{M}_{liq} = 30 \text{ kg}\cdot\text{h}^{-1}$, $\eta_{liq} = 1 \text{ mPa}\cdot\text{s}$, $p_{sys} = 1 \text{ bar}$.

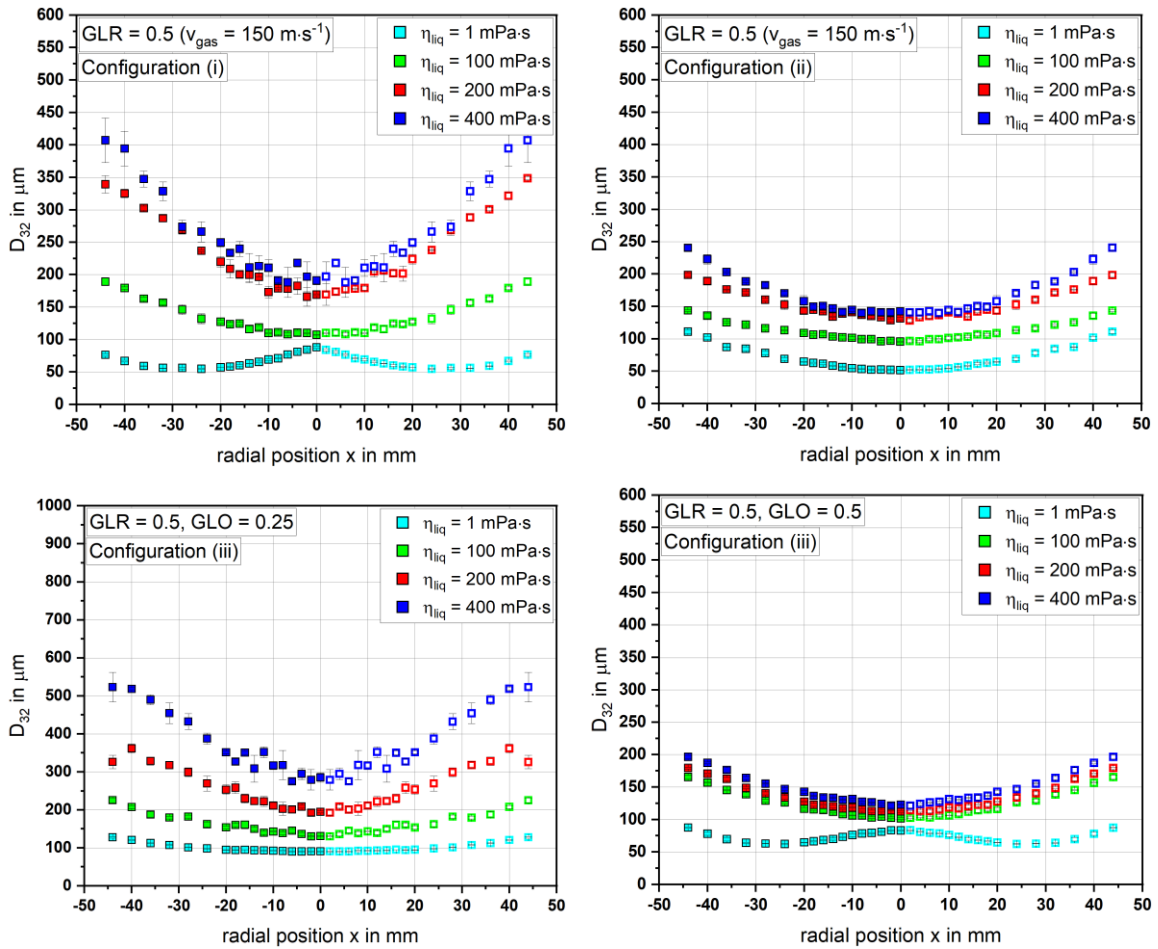


Figure E 3: D_{32} as function of radial position at varying η_{liq} , configuration and GLO . $\dot{M}_{liq} = 30 \text{ kg}\cdot\text{h}^{-1}$, $\eta_{liq} = 1 \text{ mPa}\cdot\text{s}$, $p_{sys} = 1 \text{ bar}$, $GLR = 0.5$.

F Free jet theory

In this chapter the behavior of the gas free jet is described once the gas phase is leaving the atomizer orifice with diameter d_0 . Three regions, namely core region, transition region and self-similar region can be distinguished for characterization according to Figure F 1.

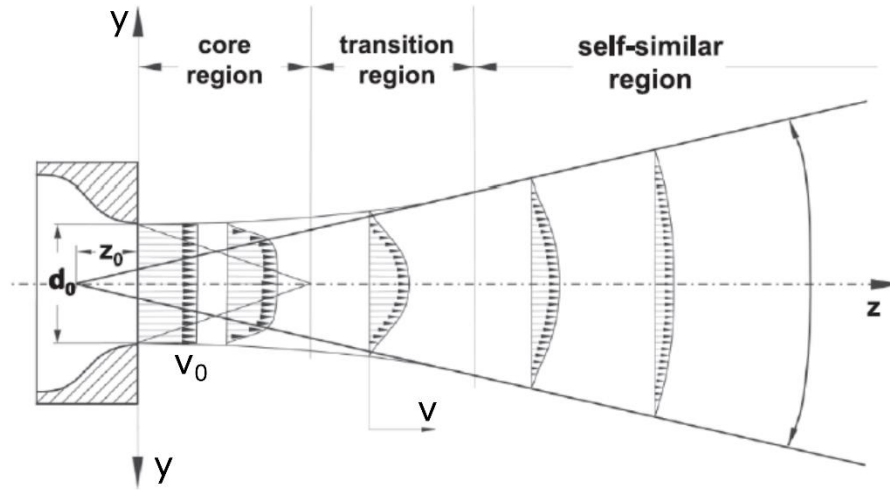


Figure F 1: Scheme of an emerging gas free jet with self-similar velocity profiles and classification of the 3 characteristic regions [71,72].

The core region is characterized by a gas velocity of $v(z) = v_{gas}$ in the jet center (radial component $y = 0$ mm), which remains constant until an axial distance of $z \approx 4 \cdot d_0$ is reached. Beginning with the self-similar region at $z \approx 6 \cdot d_0 - 8 \cdot d_0$, turbulent momentum exchange between the quiescent surrounding gas phase and the gas jet occurs [73–75]. Therefore, surrounding gas phase entrains into the gas jet, which leads to an increase in moving mass (according to equation (9)) and decrease in gas velocity under the terms of momentum conservation [76,77]. As shown in Figure F 1, self-similar, Gaussian shaped gas velocity profiles are formed with further distance from the origin $z = z_0$ [74]. Here, z_0 represents the virtual jet point source, which is not discussed in further detail here. The self-similar region is typically characterized by the spread of the emerging gas phase in 18° angle.

$$\frac{\dot{M}_{gas}(z)}{\dot{M}_{gas}} = 0.32 \cdot \frac{z - z_0}{d_0} \quad (9)$$

Equation (10) defines the center gas velocity as a function of axial orifice distance z and the orifice diameter d_0 , disregarding differences between emerging and surrounding gas density. δ represents an empirical constant, which is typically set to $\delta = 0.017$ in accordance with [78].

$$\frac{v(z)}{v_{gas}} = \frac{\sqrt{3}}{16 \cdot \delta} \cdot \frac{d_0}{z - z_0} \quad (10)$$

As in this work, the gas phase is mostly emerging through annular gaps, the orifice diameter d_o is replaced by the equivalent diameter d_{eq} , calculated according to equation (11) [79]. This equivalent diameter represents a circular area, which equals the size of the prementioned annular gap.

$$d_{eq} = \sqrt{\frac{4 \cdot A_{gas}}{\pi}} \quad (11)$$

G Detection of measurement position for mass flow scaled atomizers

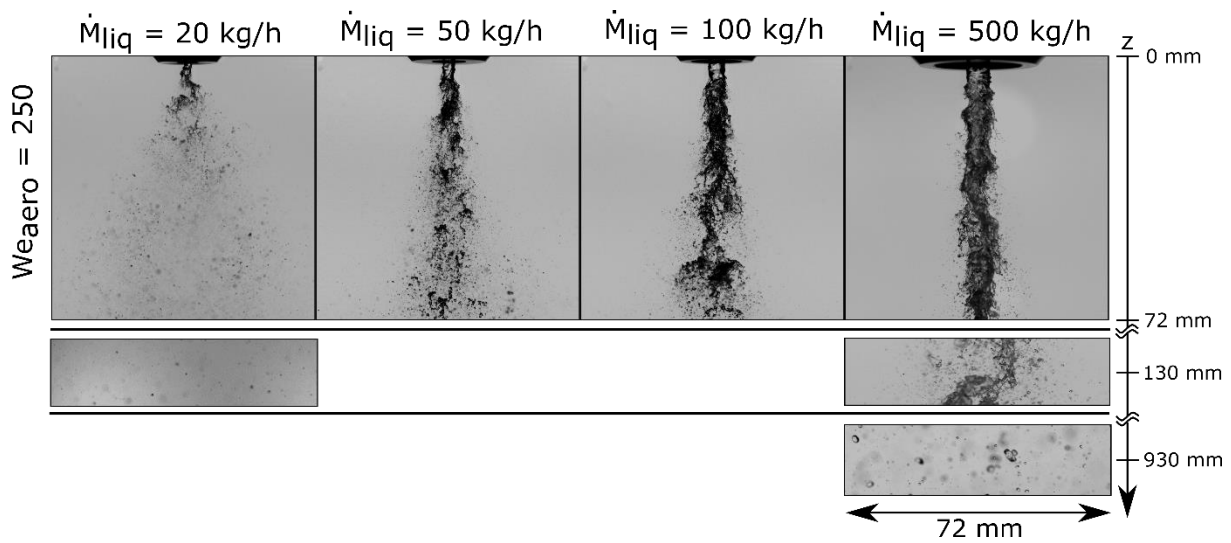


Figure G 1: HSC images of the primary jet breakup for all investigated \dot{M}_{liq} and in a distance of $z = 130 / 930$ mm downstream the atomizer orifice.

In order to find a comparable measurement position several criteria relevant for PDA droplet detection must be fulfilled: (i) adequate number density to avoid shading and Gaussian beam effect errors, (ii) high droplet sphericity and (iii) completed secondary breakup. In order to find this measurement position, the lowest We_{aero} was chosen for all atomizers at the corresponding \dot{M}_{liq} as liquid fragments will remain over the longest distance from the atomizer orifice, until round droplets are formed. Figure G 1 shows HSC images of the primary jet breakup for varying \dot{M}_{liq} at $z = 0$ mm, as well as images at the axial positions $z = 130 / 930$ mm.

In order to achieve a comparable and valid data base in droplet size, the measurement plane was derived in a fixed distance of $z d_{eq}^{-1}$ according to the free jet theory [72,78] and equation (11). For $\dot{M}_{liq} = 20 \text{ kg}\cdot\text{h}^{-1}$, a distance of $z d_{eq}^{-1} = 26$ ($z = 130$ mm) was found to be sufficient for droplet detection via PDA, as all necessary criteria were fulfilled. As shown in Figure G 1, the transfer of this result to $\dot{M}_{liq} = 500 \text{ kg}\cdot\text{h}^{-1}$, led also to a reliable

measurement plane at $z \cdot d_{eq}^{-1} = 26$ ($z = 930$ mm), which was thus chosen for all operating conditions of this investigation.

Literature

- [1] European Commission. The European Green Deal - Communication from the Commission to the European Parliament, the European Council, the Council, the European Economic and Social Committee of the Regions; 2019.
- [2] Higman C, van der Burgt M. Gasification. 2nd ed. Amsterdam, Boston: Gulf Professional Pub./Elsevier Science; 2008; ISBN 978-0750685283.
- [3] Karlsruhe Institute of Technology. Feedstocks, material flows, processes and digitization of the Anthropogenic Carbon Cycle: <https://www.mtet.kit.edu/89.php> (obtained 23.06.2022).
- [4] Eberhard M, Santo U, Michelfelder B, Günther A, Weigand P, Matthes J et al. The bioliq® Entrained-Flow Gasifier – A Model for the German Energiewende. *ChemBioEng Reviews* 2020;7(4):106–18. <https://doi.org/10.1002/cben.202000006>.
- [5] Giuffrida A, Romano MC, Lozza G. Thermodynamic analysis of air-blown gasification for IGCC applications. *Applied Energy* 2011;88(11):3949–58. <https://doi.org/10.1016/j.apenergy.2011.04.009>.
- [6] Fleck S, Santo U, Hotz C, Jakobs T, Eckel G, Mancini M et al. Entrained flow gasification Part 1: Gasification of glycol in an atmospheric-pressure experimental rig. *Fuel* 2018;217:306–19. <https://doi.org/10.1016/j.fuel.2017.12.077>.
- [7] Rizkalla AA, Lefebvre AH. The Influence of Air and Liquid Properties on Airblast Atomization. *Journal of Fluids Engineering* 1975;97(3):316–20. <https://doi.org/10.1115/1.3447309>.
- [8] Jasuja AK. Plain-Jet Airblast Atomization of Alternative Liquid Petroleum Fuels Under High Ambient Air Pressure Conditions. *The american society of mechanical engineers* 1982(3). <https://doi.org/10.1115/82-GT-32>.
- [9] Elkotb MM, El-Sayed Mahdy MA, Montaser ME. Investigation of external mixing air blast atomizers. *International Conference on Liquid Atomization and Spray Systems (ICLASS)* 1982.
- [10] Rizk NK, Lefebvre AH. Spray characteristics of plain-jet airblast atomizers. *The american society of mechanical engineers* 1984;634(106):634–8. <https://doi.org/10.1115/1.3239617>.

- [11] Mayer WOH. Coaxial atomization of a round liquid jet in a high speed gas stream: A phenomenological study. *Experiments in Fluids* 1994;16(6):401–10. <https://doi.org/10.1007/BF00202065>.
- [12] Sanger A, Jakobs T, Djordjevic N, Kolb T. Experimental investigation on the influence of ambient pressure on twin-fluid atomization of liquids with various viscosities. 13th Triennial International Conference on Liquid Atomization and Spray Systems, Tainan, Taiwan, August 23-27, 2015 (ICLASS).
- [13] Risberg M, Marklund M. Visualization of Gas Assisted Atomization of Black Liquor and Syrup Water Mixtures at elevated ambient Pressures. *Atomization and Sprays* 2009;19(10):957–67. <https://doi.org/10.1615/AtomizSpr.v19.i10.40>.
- [14] Gullberg M, Marklund M. Spray Characterization of Twin Fluid External Mixing Atomization of Pyrolysis Oil. *Atomization and Sprays* 2012;22(11):897–919. <https://doi.org/10.1615/AtomizSpr.2013006240>.
- [15] Jakobs T, Djordjevic N, Sanger A, Zarzalis N, Kolb T. Influence of reactor pressure on twin-fluid atomization: Basic investigations on burner design for high-pressure entrained flow gasifier. *Atomization and Sprays* 2015;25(12):1081–105. <https://doi.org/10.1615/AtomizSpr.2015011558>.
- [16] Fong KO, Xue X, Osuna-Orozco R, Aliseda A. Two-fluid coaxial atomization in a high-pressure environment. *Journal of Fluid Mechanics* 2022;946:82. <https://doi.org/10.1017/jfm.2022.586>.
- [17] Lefebvre AH. Twin-Fluid atomization Factors influencing mean drop size. *Atomization and Sprays* 1992;2:101–19. <https://doi.org/10.1615/AtomizSpr.v2.i2.30>.
- [18] Leroux B, Delabroy O, Lacas F. Experimental study of coaxial atomizers scaling. Part 1: Dense core zone. *Atomization and Sprays* 2007;17:381–407. <https://doi.org/10.1615/AtomizSpr.v17.i5.10>.
- [19] Leroux B, Delabroy O, Lacas F. Experimental study of coaxial atomizers scaling. Part 2: Diluted zone. *Atomization and Sprays* 2007;17:409–30. <https://doi.org/10.1615/AtomizSpr.v17.i5.20>.
- [20] Nasr GG, Yule AJ, Bendig L. *Industrial sprays and atomization: Design, analysis and applications*. London, New York: Springer; 2002; ISBN 978-1-84996-875-1.
- [21] Kim KY, Marshall, Jr., W. R. Drop-Size Distributions from pneumatic atomizers. *AIChE Journal* 1971;17(3). <https://doi.org/10.1002/aic.690170318>.

- [22] Yuan K, Chen L, Wu C. Study on characteristics of different types of nozzles for coal-water slurry atomization. *Journal of Thermal Science* 2001;10(4). <https://doi.org/10.1007/s11630-001-0040-7>.
- [23] Carlsson P, Gebart R, Grönberg C, Marklund M, Risberg M, Wiinikka H et al. Spatially resolved measurements of gas composition in a pressurised black liquor gasifier. *Environmental Progress & Sustainable Energy* 2009;28(3):316–23. <https://doi.org/10.1002/ep.10380>.
- [24] Hardalupas Y, Whitelaw JH. Characteristics of sprays produced by coaxial airblast atomizers. *Journal of Propulsion and Power* 1994;10(4):453–60. <https://doi.org/10.2514/3.23795>.
- [25] Varga CM, Lasheras JC, Hopfinger EJ. Atomization of a small-diameter liquid by a high-speed gas stream; 2001.
- [26] Bieber M, Al-Khatib M, Fröde F, Pitsch H, Reddemann MA, Schmid H-J et al. Influence of angled dispersion gas on coaxial atomization, spray and flame formation in the context of spray-flame synthesis of nanoparticles. *Experiments in Fluids* 2021;62(5):1–13. <https://doi.org/10.1007/s00348-021-03196-6>.
- [27] Leboucher N, Roger F, Carreau J-L. Characteristics of the spray produced by the atomization of an annular liquid sheet assisted by an inner gas jet. *Atomization and Spray* 2012;22(6):515–42. <https://doi.org/10.1615/AtomizSpr.2012004530>.
- [28] Zhao H, Xu J-L, Wu J-H, Li W-F, Liu H-F. Breakup morphology of annular liquid sheet with an inner round air stream. *Chemical Engineering Science* 2015;137:412–22. <https://doi.org/10.1016/j.ces.2015.06.062>.
- [29] Li X, Shen J. Experimental Study of Sprays from Annular Liquid Jet Breakup. *Journal of Propulsion and Power* 1999;15(1):103–10. <https://doi.org/10.2514/2.5397>.
- [30] Carvalho IS, Heitor MV. Liquid film break-up in a model of a prefilming airblast nozzle. *Experiments in Fluids* 1998;24(5-6):408–15. <https://doi.org/10.1007/s003480050190>.
- [31] Wahono S, Honnery D, Soria J, Ghajel J. High-speed visualisation of primary break-up of an annular liquid sheet. *Experiments in Fluids* 2008;44(3):451–9. <https://doi.org/10.1007/s00348-007-0361-8>.
- [32] Duke D, Honnery D, Soria J. Experimental investigation of nonlinear instabilities in annular liquid sheets. *Journal of Fluid Mechanics* 2012;691:594–604. <https://doi.org/10.1017/jfm.2011.516>.

- [33] Duke D, Honnery D, Soria J. The growth of instabilities in annular liquid sheets. *Experimental Thermal and Fluid Science* 2015;68:89–99. <https://doi.org/10.1016/j.expthermflusci.2015.04.013>.
- [34] Cao J. Theoretical and experimental study of atomization from an annular liquid sheet. *Proceedings of the Institution of Mechanical Engineers, Part D: Journal of Automobile Engineering* 2005;217(8):735–43. <https://doi.org/10.1243/09544070360692122>.
- [35] Ibrahim AA, Jog MA. Nonlinear instability of an annular liquid sheet exposed to gas flow. *International Journal of Multiphase Flow* 2008;34(7):647–64. <https://doi.org/10.1016/j.ijmultiphaseflow.2007.12.003>.
- [36] LEE J-G, CHEN L-D. Linear stability analysis of gas-liquid interface. *AIAA Journal* 1991;29(10):1589–95. <https://doi.org/10.2514/3.10779>.
- [37] Duke D, Honnery D, Soria J. Empirical Scaling Analysis of Atomising Annular Liquid Sheets. 12th Triennial International Conference on Liquid Atomization and Spray Systems, Heidelberg, Germany, September 2-6, 2012 (ICLASS).
- [38] Leboucher N, Roger F, Carreau JL. Atomization characteristics of an annular liquid sheet with inner and outer gas flows. *Atomization and Sprays* 2014;24(12):1065–88. <https://doi.org/10.1615/AtomizSpr.2014010670>.
- [39] Zhao H, Wu Z-W, Li W-F, Xu J-L, Liu H-F. Nonmonotonic Effects of Aerodynamic Force on Droplet Size of Prefilming Air-Blast Atomization. *Industrial & Engineering Chemistry Research* 2018;57(5):1726–32. <https://doi.org/10.1021/acs.iecr.7b05026>.
- [40] Tian X-S, Zhao H, Liu H-F, Li W-F, Xu J-L. Effect of central tube thickness on wave frequency of coaxial liquid jet. *Fuel Processing Technology* 2014;119:190–7. <https://doi.org/10.1016/j.fuproc.2013.11.011>.
- [41] Chigier N, Faragó Z. Morphological Classification of Disintegration of Round Liquid Jets in a Coaxial Air Stream. *Atomization and Sprays* 1992;2(2):137–53. <https://doi.org/10.1615/AtomizSpr.v2.i2.50>.
- [42] Lasheras JC, Villermaux E, Hopfinger EJ. Break-up and atomization of a round water jet by high-speed annular air jet. *Journal of Fluid Mechanics* 1998;357:351–79. <https://doi.org/10.1017/S0022112097008070>.
- [43] Baghani A, Brant A, Salcudean S, Rohling R. A high-frame-rate ultrasound system for the study of tissue motions. *Transactions on Ultrasonics, Ferroelectrics and Frequency Control* 2010;57(7):1535–47. <https://doi.org/10.1109/TUFFC.2010.1584>.

- [44] Versluis M. High-speed imaging in fluids. *Experiments in Fluids* 2013;54(2):1–35. <https://doi.org/10.1007/s00348-013-1458-x>.
- [45] Tropea C, Yarin AL, Foss JF. *Handbook Of Experimental Fluid Mechanics*. 1st ed. Springer Berlin Heidelberg; 2007; ISBN 978-3-662-49162-1.
- [46] Vom Stein HD, Pfeifer HJ, Koch B. Geschwindigkeitsmessungen an kurzzeitigen strömungsvorgängen mittels laser-strahlung. *Optics Communications* 1969;1(5):207–10. [https://doi.org/10.1016/0030-4018\(69\)90036-4](https://doi.org/10.1016/0030-4018(69)90036-4).
- [47] Kapulla R, Najera SB. Operation conditions of a phase Doppler anemometer: droplet size measurements with laser beam power, photomultiplier voltage, signal gain and signal-to-noise ratio as parameters. *Measurement Science and Technology* 2006;17(1):221–7. <https://doi.org/10.1088/0957-0233/17/1/034>.
- [48] Araneo L, Damaschke N, Tropea C. Measurement and Prediction of the Gaussian Beam Effect in the PDA. *Laser Techniques for Fluid Mechanics* 2002:189–207. https://doi.org/10.1007/978-3-662-08263-8_12.
- [49] Widmann JF, Presser C, Leigh SD. Improving phase Doppler volume flux measurements in low data rate applications. *Measurement Science and Technology* 2001;12(8):1180–90. <https://doi.org/10.1088/0957-0233/12/8/327>.
- [50] Albrecht H-E. *Laser doppler and phase doppler measurement techniques*. Berlin, New York: Springer; 2003; ISBN 978-3-540-67838-0.
- [51] Damaschke N, Gouesbet G, Grehan G, Mignon H, Tropea C. Response of Phase Doppler Anemometer systems to nonspherical droplets. *Applied Optics* 1998;37(10). <https://doi.org/10.1364/AO.37.001752>.
- [52] Alexander DR, Wiles KJ, Schaub SA, Seeman MP. Effects Of Non-Spherical Drops On A Phase Doppler Spray Analyzer. *Particle Sizing and Spray Analysis* 1985;573:67. <https://doi.org/10.1117/12.978037>.
- [53] Bachalo WD. The Phase Doppler Method: Analysis, performance evaluations, and applications. *Particle & Particle Systems Characterization* 1994;11(1):73–83. <https://doi.org/10.1002/ppsc.19940110110>.
- [54] Mugele RA, Evans HD. Droplet Size Distribution in Sprays. *Industrial & Engineering Chemistry* 1951;43(6):1317–24. <https://doi.org/10.1021/ie50498a023>.
- [55] DIN SPEC 91325:2015-06, Charakterisierung von Sprays und Sprühprozessen durch die Messung der Größe und der Geschwindigkeit nicht-transparenter Tropfen. Berlin: Beuth Verlag GmbH; 2015. <https://doi.org/10.31030/2313048>.

- [56] Grossl F. Untersuchung zum Einfluss des Reaktordrucks auf die Zerstäubung Newtonscher Fluide mit außenmischenden Zweistoffdüsen. Karlsruhe: master thesis; 2018.
- [57] Wachter S, Jakobs T, Kolb T. Experimental investigation on the influence of system pressure on resulting spray quality and jet breakup applying pressure adapted twin-fluid nozzles. *International Journal of Multiphase Flow* 2020;125:103189. <https://doi.org/10.1016/j.ijmultiphaseflow.2019.103189>.
- [58] Wachter S, Jakobs T, Kolb T. Towards system pressure scaling of gas assisted coaxial burner nozzles – An empirical model. *Applications in Energy and Combustion Science* 2021;5:100019. <https://doi.org/10.1016/j.jaecs.2020.100019>.
- [59] Zhao H, Liu H-F, Xu J-L, Li W-F, Cheng W. Breakup and atomization of a round coal water slurry jet by an annular air jet. *Chemical Engineering Science* 2012;78:63–74. <https://doi.org/10.1016/j.ces.2012.05.007>.
- [60] Aliseda A, Hopfinger EJ, Lasheras JC, Kremer DM, Berchielli A, Connolly EK. Atomization of viscous and non-newtonian liquids by a coaxial, high-speed gas jet. Experiments and droplet size modeling. *International Journal of Multiphase Flow* 2008;34(2):161–75. <https://doi.org/10.1016/j.ijmultiphaseflow.2007.09.003>.
- [61] Müller M. Untersuchung zur Massenstromskalierung gasgestützter Düsen. Karlsruhe: bachelor thesis; 2020.
- [62] Wachter S, Jakobs T, Kolb T. Mass Flow Scaling of Gas-Assisted Coaxial Atomizers. *Applied Sciences* 2022;12(4):2123. <https://doi.org/10.3390/app12042123>.
- [63] Otsu N. A Threshold Selection Method from Gray-Level Histograms. *Transactions on Systems, Man, and Cybernetics* 1979;9(1):62–6. <https://doi.org/10.1109/TSMC.1979.4310076>.
- [64] Ritter M. Untersuchung zum Einfluss des Gasanstellwinkels auf die Zerstäubung Newtonscher Fluide mit außenmischenden Zweistoffdüsen bei variierendem Systemdruck. Karlsruhe: bachelor thesis; 2019.
- [65] Wachter S, Jakobs T, Kolb T. Effect of gas jet angle on primary breakup and droplet size applying coaxial gas-assisted atomizers. 15th Triennial International Conference on Liquid Atomization and Spray Systems, Edinburgh, United Kingdom, August 29 - September 2, 2021 (ICLASS).
- [66] Liu H-F, Li W-F, Gong X, Cao X-K, Xu J-L, Chen X-L et al. Effect of liquid jet diameter on performance of coaxial two-fluid airblast atomizers. *Chemical*

- Engineering and Processing 2006;45:240–5.
<https://doi.org/10.1016/j.cep.2005.08.003>.
- [67] Götz J. Experimentelle Untersuchung einer 3-flutigen Zerstäuberdüse. Karlsruhe: bachelor thesis; 2020.
- [68] Wachter S, Jakobs T, Kolb T. Comparison of spray quality for two different flow configurations: Central liquid jet versus annular liquid sheet. 29th European Conference on Liquid Atomization and Spray Systems, Paris, France, September 2-4, 2019 (ILASS).
- [69] Wachter S, Jakobs T, Kolb T. Comparison of Central Jet and Annular Sheet Atomizers at Identical Gas Momentum Flows. *Industrial & Engineering Chemistry Research* 2021;60(30):11502–12. <https://doi.org/10.1021/acs.iecr.1c01526>.
- [70] Li LKB, Dressler DM, Green SI, Davy MH. Experiments on air-blast atomization of viscoelastic liquids, Part 1: quiescent conditions. *Atomization and Sprays* 2009;19(2):157–90. <https://doi.org/10.1615/AtomizSpr.v19.i2.30>.
- [71] Fast G. Laseroptische Strömungsdiagnostik zu Selbstzündungsprozessen bei Freistrahlen [Dissertation]. Eggenstein-Leopoldshafen: Forschungszentrum Karlsruhe; 2007.
- [72] Hotz C, Haas M, Wachter S, Fleck S, Kolb T. Two-phase free jet model of an atmospheric entrained flow gasifier. *Fuel* 2021;304:121392. <https://doi.org/10.1016/j.fuel.2021.121392>.
- [73] Dowling DR, Dimotakis PE. Similarity of the concentration field of gas-phase turbulent jets. *Journal of Fluid Mechanics* 1990;218(-1):109. <https://doi.org/10.1017/S0022112090000945>.
- [74] Hinze JO. *Turbulence*. 2nd ed. New York, NY: McGraw-Hill; 1975; ISBN 978-0070290372.
- [75] Richards CD, Pitts WM. Global density effects on the self-preservation behaviour of turbulente jets. *Journal of Fluid Mechanics* 1993(254):417–35. <https://doi.org/10.1017/S0022112093002204>.
- [76] Ricou FP, Spalding DB. Measurements of entrainment by axisymmetrical turbulent jets. *Journal of Fluid Mechanics* 1961;11(1):21–32. <https://doi.org/10.1017/S0022112061000834>.
- [77] Hussein HJ, Capp SP, George WK. Velocity measurements in a high-Reynolds-number, momentum-conserving, axisymmetric, turbulent jet. *Journal of Fluid Mechanics* 1994;258(-1):31. <https://doi.org/10.1017/S002211209400323X>.

- [78] Schlichting H, Gersten K, Krause E. Grenzschicht-Theorie. 10th ed. Berlin, Heidelberg: Springer; 2006; ISBN 978-3-540-23004-5.
- [79] Thring MW, Newby MP. Combustion length of enclosed turbulent jet flames. Symposium (International) on Combustion 1953;4(1):789–96.
[https://doi.org/10.1016/S0082-0784\(53\)80103-7](https://doi.org/10.1016/S0082-0784(53)80103-7).

Publications relevant for this thesis

Journal articles

Wachter, Simon; Jakobs, Tobias; Kolb, Thomas (2020): Experimental investigation on the influence of system pressure on resulting spray quality and jet breakup applying pressure adapted twin-fluid nozzles. In: International Journal of Multiphase Flow 125, Art. No. 103189. DOI: 10.1016/j.ijmultiphaseflow.2019.103189

Wachter, Simon; Jakobs, Tobias; Kolb, Thomas (2021): Towards system pressure scaling of gas assisted coaxial burner nozzles – An empirical model. Applications in Energy and Combustion Science 5, Art. No. 100019. DOI: 10.1016/j.jaecs.2020.100019

Wachter, Simon; Jakobs, Tobias; Kolb, Thomas (2021): Comparison of Central Jet and Annular Sheet Atomizer at Identical Gas Momentum Flows. Industrial & Engineering Chemistry Research 60 (30), 11502 – 11512. DOI: 10.1021/acs.iecr.1c01526

Wachter, Simon; Jakobs, Tobias; Kolb, Thomas (2022): Mass Flow Scaling of Gas-Assisted Coaxial Atomizers. Applied Sciences 12, Art. No. 2123. DOI: 10.3390/app12042123

Conference contribution

Presentations and proceedings

Wachter, Simon; Jakobs, Tobias; Kolb, Thomas: „Comparison of spray quality for two different flow configurations: Central liquid jet versus annular liquid sheet“, 29th European Conference on Liquid Atomization and Spray Systems (ILASS), Paris, France, 02-04. September 2019

Wachter, Simon; Jakobs, Tobias; Kolb, Thomas: „Effect of gas jet angle on primary breakup and droplet size applying coaxial gas-assisted atomizers“, 15th Triennial International Conference on Liquid Atomization and Spray Systems (ICLASS), Edinburgh, United Kingdom, 29. August - 02. September 2021

Verification of the contribution from the co-authors

Title: Experimental investigation on the influence of system pressure on resulting spray quality and jet breakup applying pressure adapted twin-fluid nozzles

Journal: International Journal of Multiphase Flow

Authors: Simon Wachter, Tobias Jakobs, Thomas Kolb

DOI: 10.1016/j.ijmultiphaseflow.2019.103189

Position in the dissertation:

The content of this paper was included in chapter 4.1.1.

Contribution of Simon Wachter: Conceptualization (80%), Validation, Formal analysis, Investigation, Visualization, Writing – original draft

Contribution of Tobias Jakobs: Conceptualization (20%), Supervision, Review (50%)

Contribution of Thomas Kolb: Research supervision, Review (50%)

Signature of the authors:

<i>Author</i>	<i>Date</i>	<i>Signature</i>
Simon Wachter		
Tobias Jakobs		
Thomas Kolb		

Title: Towards system pressure scaling of gas assisted coaxial burner nozzles – An empirical model

Journal: Applications in Energy and Combustion Science

Authors: Simon Wachter, Tobias Jakobs, Thomas Kolb

DOI: 10.1016/j.jaecs.2020.100019

Position in the dissertation:

The content of this paper was included in chapter 4.1.2.

Contribution of Simon Wachter: Conceptualization (80%), Validation, Formal analysis, Investigation, Visualization, Writing – original draft

Contribution of Tobias Jakobs: Conceptualization (20%), Supervision, Review (50%)

Contribution of Thomas Kolb: Research supervision, Review (50%)

Signature of the authors:

<i>Author</i>	<i>Date</i>	<i>Signature</i>
Simon Wachter		
Tobias Jakobs		
Thomas Kolb		

Title: **Comparison of Central Jet and Annular Sheet Atomizer at Identical Gas Momentum Flows**

Journal: Industrial & Engineering Chemistry Research

Authors: Simon Wachter, Tobias Jakobs, Thomas Kolb

DOI: 10.1021/acs.iecr.1c01526

Position in the dissertation:

The content of this paper was included in chapter 4.4.

Contribution of Simon Wachter: Conceptualization (80%), Validation, Formal analysis, Investigation, Visualization, Writing – original draft

Contribution of Tobias Jakobs: Conceptualization (20%), Supervision, Review (50%)

Contribution of Thomas Kolb: Research supervision, Review (50%)

Signature of the authors:

<i>Author</i>	<i>Date</i>	<i>Signature</i>
Simon Wachter		
Tobias Jakobs		
Thomas Kolb		

Title: **Mass Flow Scaling of Gas-Assisted Coaxial Atomizers**

Journal: Applied Sciences

Authors: Simon Wachter, Tobias Jakobs, Thomas Kolb

DOI: 10.3390/app12042123

Position in the dissertation:

The content of this paper was included in chapter 4.2.

Contribution of Simon Wachter: Conceptualization (80%), Investigation, Data curation, Visualization, Writing – original draft

Contribution of Tobias Jakobs: Conceptualization (20%), Review (50%)

Contribution of Thomas Kolb: Research supervision, Review (50%)

Signature of the authors:

<i>Author</i>	<i>Date</i>	<i>Signature</i>
Simon Wachter		
Tobias Jakobs		
Thomas Kolb		

Title: **Comparison of spray quality for two different flow configurations: Central liquid jet versus annular liquid sheet**

Conference: 29th European Conference on Liquid Atomization and Spray Systems (ILASS), Paris, France, 02-04. September 2019

Authors: Simon Wachter, Tobias Jakobs, Thomas Kolb

DOI: 10.5445/IR/1000098689

Position in the dissertation:

The content of this proceeding was included in chapter 4.4.

Contribution of Simon Wachter: Conceptualization (80%), Validation, Formal analysis, Investigation, Visualization, Writing – original draft

Contribution of Tobias Jakobs: Conceptualization (20%), Supervision, Review (50%)

Contribution of Thomas Kolb: Research supervision, Review (50%)

Signature of the authors:

<i>Author</i>	<i>Date</i>	<i>Signature</i>
Simon Wachter		
Tobias Jakobs		
Thomas Kolb		

Title: Effect of gas jet angle on primary breakup and droplet size applying coaxial gas-assisted atomizers

Conference: 15th Triennial International Conference on Liquid Atomization and Spray Systems, Edinburgh, United Kingdom, 29. August - 2. September 2021

Authors: Simon Wachter, Tobias Jakobs, Thomas Kolb

DOI: 10.2218/iclass.2021.5808

Position in the dissertation:

The content of this proceeding was included in chapter 4.3.

Contribution of Simon Wachter: Conceptualization (80%), Validation, Formal analysis, Investigation, Visualization, Writing – original draft

Contribution of Tobias Jakobs: Conceptualization (20%), Supervision, Review (50%)

Contribution of Thomas Kolb: Research supervision, Review (50%)

Signature of the authors:

<i>Author</i>	<i>Date</i>	<i>Signature</i>
Simon Wachter		
Tobias Jakobs		
Thomas Kolb		

Complete publication list

2023

Zhang, F.; **Wachter, S.**; Zirwes, T.; Jakobs, T.; Zarzalis, N.; Trimis, D.; Kolb, T.; Stapf, D.; Effect of nozzle upscaling on coaxial, gas-assisted atomization, *Physics of Fluids*, 2023, doi: 10.1063/5.0141156

Hotz, C.; Haas, M.; **Wachter, S.**; Fleck, S.; Kolb, T.; Experimental investigation on entrainment in two-phase free jets, *Fuel*, 2022, doi:10.1016/j.fuel.2022.126912

Zhang, F.; Zirwes, T.; **Wachter, S.**; Jakobs, T.; Habisreuther, P.; Zarzalis, N.; Trimis, D.; Kolb, T.; Bockhorn, H.; Stapf, D.; Numerical simulations of air-assisted primary atomization at different air-to-liquid injection angles, *International journal of multiphase flow*, 2022, doi:10.1016/j.ijmultiphaseflow.2022.104304

2022

Jakobs, T.; **Wachter, S.**; Haas, M.; Fleck, S.; Kolb, T.; Burner Development for High Pressure Entrained Flow Gasification, *Chemie-Ingenieur-Technik*, 2022, doi:10.1002/cite.202255022

Wachter, S.; Jakobs, T.; Kolb, T.; Mass Flow Scaling of Gas-Assisted Coaxial Atomizers, *Applied Sciences*, 2022, doi:10.3390/app12042123

2021

Zhang, F.; Zirwes, T.; **Wachter, S.**; Jakobs, T.; Habisreuther, P.; Zarzalis, N.; Trimis, D.; Kolb, T.; Bockhorn, H.; Simulations of Air-assisted Primary Atomization at Different Air-to-Liquid Injection Angles for Entrained Flow Gasification, 2021, 30. Deutscher Flammentag, Presentation & Proceeding

Wachter, S.; Jakobs, T.; Kolb, T.; Effect of gas jet angle on primary breakup and droplet size applying coaxial gas-assisted atomizers, 2021, ICLASS Edinburgh, Presentation & Proceeding

Hotz, C.; Haas, M.; **Wachter, S.**; Fleck, S.; Kolb, T.; Two-phase free jet model of an atmospheric entrained flow gasifier, *Fuel*, 2021, doi:10.1016/j.fuel.2021.121392

Wachter, S.; Jakobs, T.; Kolb, T.; Comparison of Central Jet and Annular Sheet Atomizers at Identical Gas Momentum Flows, *Industrial & engineering chemistry research*, 2021, doi:10.1021/acs.iecr.1c01526

Wachter, S.; Jakobs, T.; Kolb, T.; Towards system pressure scaling of gas assisted coaxial burner nozzles – An empirical model; *Applications in energy and combustion science*, 2021, doi:10.1016/j.jaecs.2020.100019

2020

Wachter, S.; Jakobs, T.; Kolb, T.; Effect of Solid Particles on Droplet Size Applying the Time-Shift Method for Spray Investigation, Applied Sciences, 2020, doi:10.3390/app10217615

Zhang, F.; Zirwes, T.; Müller, T.; **Wachter, S.;** Jakobs, T.; Habisreuther, P.; Zarzalis, N.; Trimis, D.; Kolb, T.; Effect of elevated pressure on air-assisted primary atomization of coaxial liquid jets : Basic research for entrained flow gasification, Renewable & sustainable energy reviews, 2020, doi:10.1016/j.rser.2020.110411

Chaussonnet, G.; Joshi, S.; **Wachter, S.;** Koch, R.; Jakobs, T.; Kolb, T.; Bauer, H.-J.; Air-Assisted Atomization at Constant Mass and Momentum Flow Rate: Investigation into the Ambient Pressure Influence With the Smoothed Particle Hydrodynamics Method, Journal of engineering for gas turbines and power, 2020, doi:10.1115/1.4044968

Wachter, S.; Jakobs, T.; Kolb, T.; Experimental investigation on the influence of system pressure on resulting spray quality and jet breakup applying pressure adapted twin-fluid nozzles, International journal of multiphase flow, 2020, doi:10.1016/j.ijmultiphaseflow.2019.103189

Gaedtke, M.; **Wachter, S.;** Kunkel, S.; Sonnicks, S.; Rädle, M.; Nirschl, H.; Krause, M. J.; Numerical study on the application of vacuum insulation panels and a latent heat storage for refrigerated vehicles with a large Eddy lattice Boltzmann method, Heat and mass transfer, 2020, doi:10.1007/s00231-019-02753-4

2019

Zhang, F.; Zirwes, T.; **Wachter, S.;** Jakobs, T.; Habisreuther, P.; Zarzalis, N.; Dimosthenis, T.; Kolb, T.; Numerical and Experimental Investigations of Primary Breakup of High-Viscous Fluid at Elevated Pressure, 2019, ILASS Paris, Presentation & Proceeding

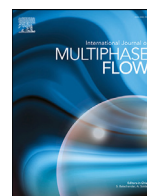
Wachter, S.; Jakobs, T.; Kolb, T.; Comparison of spray quality for two different flow configurations: Central liquid jet versus annular liquid sheet, 2019, ILASS Paris, Presentation & Proceeding

Wachter, S.; Jakobs, T.; Kolb, T.; Untersuchung von Brennerdüsen bei erhöhtem Systemdruck, 2019, Jahrestreffen ProcessNET „Hochtemperaturtechnik“, Karlsruhe, Poster

Zhang, F.; Müller, T.; Zirwes, T.; **Wachter, S.;** Jakobs, T.; Habisreuther, P.; Zarzalis, N.; Trimis, D.; Kolb, T.; Effect of elevated pressure on primary jet-breakup: Basic research for entrained flow gasification, 2019, 29. Deutscher Flammentag, Presentation & Proceeding

2018

Gaedtke, M.; **Wachter, S.**; Rädle, M.; Nirschl, H.; Krause, M. J.; Application of a lattice Boltzmann method combined with a Smagorinsky turbulence model to spatially resolved heat flux inside a refrigerated vehicle, Computers and mathematics with applications, 2018, doi:10.1016/j.camwa.2018.08.018



Experimental investigation on the influence of system pressure on resulting spray quality and jet breakup applying pressure adapted twin-fluid nozzles

Simon Wachter^{a,*}, Tobias Jakobs^a, Thomas Kolb^{a,b}

^a Institute of Technical Chemistry, Gasification Technology, Karlsruhe Institute of Technology, Eggenstein-Leopoldshafen, BW 76344, Germany

^b Engler-Bunte-Institute, Fuel Technology, Karlsruhe Institute of Technology, Karlsruhe, BW 76131, Germany

ARTICLE INFO

Article history:

Received 16 October 2019

Revised 19 November 2019

Accepted 15 December 2019

Available online 10 January 2020

Keywords:

Twin-fluid atomization

Viscosity

System pressure

Nozzle scaling

ABSTRACT

The present work aims for the isolated investigation of the influence of system pressure on spray quality of twin-fluid atomizers. An approach of pressure adapted nozzles was applied, allowing for constant mass flows, gas-to-liquid ratio as well as fluid velocities at the nozzle orifice independent of system pressure. Two Newtonian liquids featuring viscosities of 1 and 100 mPa · s were used, varying the system pressure from 1 to 16 bar for gas velocities of 60, 80 and 100 m · s⁻¹. A phase doppler analyzer was applied for measurement of resulting drop size and velocity. Primary breakup morphology was detected by a high-speed camera. Two regions with different dependencies of spray quality on system pressure were identified. Applying pressure adapted nozzles while increasing system pressure, first results in a decrease of droplet size followed by an increase. A maximum of the dynamic pressure of the gas phase was determined at minimum droplet size, which is explained based on the theory of a free jet. The observations are underlined by images of the high-speed camera. Here, a change in breakup morphology from fiber type to a mixture of fiber type and non-axisymmetric Rayleigh type breakup at high system pressure was observed.

© 2020 Elsevier Ltd. All rights reserved.

1. Introduction

Although spraying processes are often used in industrial applications, the influence of process conditions and liquid properties is not yet fully understood. Especially knowledge of the twin-fluid atomization process at high system pressure relevant for energy conversion systems is scarce. Investigations on the liquid disintegration process in gas turbines (Lefebvre, 1998) and rocket propulsion (Haidn and Habiballah, 2003) at high system pressure were carried out, with varying nozzle geometries and under different process conditions. Mostly, low viscosity liquids ($\eta_{liq} < 50$ mPa · s) were used, without consideration of high viscosity fuels. Typically, high viscosity liquids or suspension fuels featuring viscosities up to 1000 mPa · s and complex rheological behaviour (e.g., non-Newtonian flow, viscoelasticity) are applied in entrained flow gasification systems (EFG), which are operated at elevated system pressure (absolute pressure up to 80 bar) (Fleck et al., 2018). Oxygen is used as gasification agent and at the same time serves as atomization agent, i.e. stoichiometry and gas-to-liquid mass flow ratio

(GLR) are directly coupled. Based on the required low stoichiometry of the gasification reaction, the spray nozzle has to be operated at $GLR \leq 1$. For optimization of the atomization process at conditions relevant for an EFG or for design and scale-up of burner nozzles applied in an EFG, it is an essential research objective to gain fundamental knowledge concerning the atomization behaviour of high viscosity liquids at high process pressure (Jakobs et al., 2012).

Theoretical and experimental investigations regarding the atomization of low viscosity liquids using twin-fluid atomizers at atmospheric system pressure are common (Marmottant and Villermaux, 2004). An overview comparing different twin-fluid nozzle concepts is given by Hede et al. (2008). Chigier and Faragó (1992) used a high-speed camera to investigate the primary breakup of a water jet applying twin-fluid nozzles. A regime classification for liquid breakup morphology was proposed for different nozzle geometries, using Re_{liq} and We_{aero} , according to Eqs. (1) and (2) to describe process conditions:

$$Re_{liq} = \frac{D_{liq} \cdot v_{liq} \cdot \rho_{liq}}{\eta_{liq}} \quad (1)$$

$$We_{aero} = \frac{(v_{gas} - v_{liq})^2 \cdot \rho_{gas} \cdot D_{liq}}{\sigma} \quad (2)$$

* Corresponding author.

E-mail address: simon.wachter@kit.edu (S. Wachter).

Table 1

Summary of investigations applying external mixing twin-fluid nozzles with $\eta_{liq} > 50 \text{ mPa} \cdot \text{s}$ at $p_{sys} = 1 \text{ bar}$.

Author (year)	Measurement	GLR	η_{liq} in $\text{mPa} \cdot \text{s}$	$(I)D_{32} \sim \eta_{liq}^x$
Lorenzetto and Lefebvre (1977)	LDS	2–3.67	1.3–76	$(I)D_{32} \sim \eta_{liq}^1$
Jasuja (1982)	LDS	2–12	1.3–74.9	$(I)D_{32} \sim \eta_{liq}^{0.8}$
Walzel (1990)	LDS	N/A	1–100	$(I)D_{32} \sim \eta_{liq}^1$
Aliseda et al. (2008)	PDA, HSC	7.69	1–77.6	$(I)D_{32} \sim \eta_{liq}^{0.67}$
Li et al. (2009)	SZ, HSC	1–2.5	1–805	N/A
Sanger (2018)	PDA, HSC	0.4–13.8	100–400	M: $(I)D_{32} \sim \eta_{liq}^{0.47}$ F: $(I)D_{32} \sim \eta_{liq}^{0.15}$

with liquid jet diameter (D_{liq}), velocity (v), density (ρ), dynamic viscosity (η_{liq}), and surface tension (σ) as relevant process parameters. The subscripts gas and liq denote gas and liquid phase, respectively. For low We_{aero} , the primary atomization is characterized by the so-called Rayleigh type regime, where the liquid jet disintegrates into large droplets on the centerline of the spray. With increasing We_{aero} , the membrane type breakup is reached, where gas-filled membranes near the nozzle orifice can be detected. These membranes break into tiny droplets at the thinnest position, whereas the accumulated rim disintegrates according to Rayleigh-Plateau-instabilities. At high We_{aero} , the fiber type regime leads to a complete disintegration of the liquid jet into fibers near the nozzle orifice. These ligaments typically disintegrate into small droplets according to the Rayleigh-Plateau-instability. The fiber type regime is divided into the submodes pulsating and superpulsating; the latter is characterized by a fluctuation of droplet number density in the spray. Lasheras and Hopfinger (2000) included the effect of dynamic pressure ratio of gas and liquid phase for the characterization of the fiber type breakup.

The effect of liquid viscosity on primary jet breakup of suspensions applying twin-fluid nozzles was investigated by Zhao et al. (2012). The authors used the Ohnesorge number, see Eq. (3), to expand the previous regime classification towards viscosity-effects of liquid jets. As a comparison of their work with coal-water slurries, the liquid breakup morphology was described by Oh and We_{aero} , classifying the regimes into Rayleigh type, fiber type, and atomization.

$$Oh = \frac{\eta_{liq}}{\sqrt{\rho_{liq} \cdot \sigma \cdot D_{liq}}} \quad (3)$$

There is a large number of publications that focus on the drop size distribution, whereby most investigations were conducted for low viscosity liquids ($\eta_{liq} < 50 \text{ mPa} \cdot \text{s}$) and at atmospheric system pressure. Commonly scarce are investigations on the influence of liquid viscosity and system pressure on the atomization. A summary of investigations performed with external mixing twin-fluid nozzles applying high viscosity liquids ($\eta_{liq} > 50 \text{ mPa} \cdot \text{s}$) at atmospheric system pressure is given in Table 1.

Lorenzetto and Lefebvre (1977) and Jasuja (1982) investigated the atomization of heavy crude oil with viscosities up to $\eta_{liq} = 76 \text{ mPa} \cdot \text{s}$ for gas turbines and combustors. With decreasing gas velocity as well as increasing dynamic viscosity, an increasing drop size was detected with a laser diffraction system (LDS). First investigations on model fuels like mixtures of glycerol/water with $1 < \eta_{liq} < 100 \text{ mPa} \cdot \text{s}$ were carried out by Walzel (1990), deducing a correlation for drop size estimation based on an energy balance, which shows a linear dependency of the integral Sauter mean diameter on dynamic viscosity. This was in good agreement with the work of Lorenzetto and Lefebvre (1977) and Jasuja (1982). GLR was not given by Walzel. Aliseda et al. (2008) first used a high-speed camera (HSC) visualizing the jet breakup and a phase doppler analyzer (PDA) system for measurements of drop size and velocity applying viscous liquids with up to $\eta_{liq} = 78 \text{ mPa} \cdot \text{s}$. The comparison

of liquids with different viscosities showed damping effects on the formation of liquid jet instabilities with increased viscosity, resulting in larger droplet sizes. Further investigations applying high viscosity liquids were performed by Li et al. (2009). The authors used liquids with a dynamic viscosity up to $\eta_{liq} = 805 \text{ mPa} \cdot \text{s}$ applying a shadowsizer (SZ) for local droplet size measurement and a HSC for visualization of the primary breakup. A negligible effect of dynamic viscosity between $\eta_{liq} = 147 \text{ mPa} \cdot \text{s}$ on droplet size was detected, whereas for a liquid viscosity of $\eta_{liq} = 805 \text{ mPa} \cdot \text{s}$ no jet disintegration occurred anymore. Sanger (2018) applied different liquids with viscosities up to $\eta_{liq} = 400 \text{ mPa} \cdot \text{s}$. A dependency of droplet size on primary breakup morphologies, like membrane type (M) and fiber type (F) was reported. Summing up, the previous investigations showed that increasing dynamic viscosity dampens the instabilities relevant for jet breakup, resulting in increased primary jet length and droplet size. Detailed experiments on the external twin-fluid atomization of high viscosity liquids ($\eta_{liq} > 50 \text{ mPa} \cdot \text{s}$) at pressures above ambient are even more scarce. An overview is given in Table 2.

One of the first studies on the atomization of low viscosity liquids applying a twin-fluid nozzle was carried out by Rizkalla and Lefebvre (1975), applying a prefilming atomizer. A laser diffraction system was used for measurement of drop sizes, varying the system pressure between $p_{sys} = 1 - 8.5 \text{ bar}$. System pressure p_{sys} stands in the following for the ambient pressure in the atomization chamber. A pressurized pipe with an internal nozzle enabling constant liquid mass flow and constant gas velocity v_{gas} defined at the nozzle orifice was used. A decrease of drop size with increasing pressure was detected. The atomization of viscous liquids ($\eta_{liq} < 75 \text{ mPa} \cdot \text{s}$) at pressure conditions up to $p_{sys} = 14.2 \text{ bar}$, using external mixing twin-fluid nozzles with a swirling gas flow, was performed by Jasuja (1982). For different system pressures, the GLR and gas velocity at the nozzle orifice were set to be constant, while the liquid mass flow was adapted. The authors report that increasing system pressure leads to smaller Sauter mean diameters (D_{32}). With increasing liquid viscosity, this effect decreases. Elkotb et al. (1982) used a coated glass plate (CGP) and optical measurement techniques for detection of droplet sizes from the atomization of low viscosity liquids at elevated pressures $p_{sys} = 18 \text{ bar}$. Due to simultaneous changes in system pressure and gas velocity, specific influences on atomization cannot be separated. Investigations on the influence of liquid physical properties and varying system pressure were carried out by Rizk and Lefebvre (1984). GLR and relative exit velocities at the nozzle orifice were kept constant by variation of the gas and liquid mass flows. No information concerning the distance between measuring plane and nozzle orifice was given by the authors. With increasing system pressure from $p_{sys} = 1.3 - 18.3 \text{ bar}$, a decreasing Sauter mean diameter was detected, using two external mixing twin-fluid nozzles with different liquid orifice diameters. Risberg and Marklund (2009) conducted experiments using external mixing twin-fluid nozzles to atomize high viscosity liquids ($\eta_{liq} = 1 - 500 \text{ mPa} \cdot \text{s}$). A HSC was used for qualitative investigation of large droplets and velocity.

Table 2
Summary of investigations applying external mixing twin-fluid nozzles with $\eta_{liq} > 1 \text{ mPa} \cdot \text{s}$ at $p_{sys} > 1 \text{ bar}$.

Author (year)	Measurement	η_{liq} in mPa · s	p_{sys} in bar	$(I)D_{32} \sim p_{sys}^x$
Rizkalla and Lefebvre (1975)	LDS	1–44	1–8.5	$(I)D_{32} \sim p_{sys}^{-1}$
Jasuja (1982)	LDS	1.3–43.5	1–14.2	$(I)D_{32} \sim p_{sys}^{-0.45}$
Elkotb et al. (1982)	CGP	33.5	1–8	$(I)D_{32} \sim p_{sys}^{-0.29}$
Rizk and Lefebvre (1984)	LDS	1.3–18.3	1–7.7	$(I)D_{32} \sim p_{sys}^{-0.4}$
Risberg and Marklund (2009)	HSC	1–500	1–10	N/A
Gullberg and Marklund (2012)	HSC	25	1–5	N/A
Sänger (2018)	PDA, HSC	100–400	1–21	M: $(I)D_{32} \sim p_{sys}^{-0.88}$ F: $(I)D_{32} \sim p_{sys}^{-0.47}$

The variation of system pressure was carried out at constant GLR . A dependency of system pressure on droplet size was not found. Continuing experiments were conducted by Gullberg and Marklund (2012), applying pyrolysis oil as low viscosity fuel. The liquid supply was realized via an annular gap of the external twin-fluid nozzle. For increasing system pressure, gas velocities at the nozzle orifice and GLR were kept constant. To achieve these constant conditions while varying the system pressure, liquid and gas mass flow were adapted. An increase in primary jet length, fractions of larger droplets and droplet number density were detected with increasing system pressure by high-speed camera images. Further investigations on the atomization of high viscosity liquids at elevated system pressure $p_{sys} = 21 \text{ bar}$ were performed by Sänger (2018). With increasing system pressure and constant gas velocity, a decreasing Sauter mean diameter was found. In order to achieve these constant conditions, GLR was increased from 0.4 at $p_{sys} = 1 \text{ bar}$ up to 13.8 at $p_{sys} = 21 \text{ bar}$. Furthermore, it was reported that increasing the dynamic pressure of the gas phase $\rho_{gas} \cdot v_{gas}^2$ by either variation of gas density or gas velocity shows different results on droplet size.

Summing up the literature review, it must be stated that previous investigations cannot provide a comprehensive picture on local data for sprays under high system pressure conditions using high viscosity liquids. On the one hand, some studies mentioned show inconsistent results. On the other hand, the investigated parameters influencing the spray quality cannot be separated completely. Additional, previous investigation applying elevated system pressure were typically performed with one single nozzle, which results for high system pressures and constant gas velocity in high GLR values. As an example for water measurements at increased system pressure, Mayer (1994) gives a good overview. These conditions are not relevant for an application like gasification, where low GLR is required (Fleck et al., 2018).

To get a better insight in the disintegration process of liquid jets applying twin-fluid nozzles and the initiating instabilities under high pressure conditions, more detailed data such as qualitative measurements of primary jet breakup and local high-resolution measurements of drop size and velocity distributions are required. Due to this deficit of knowledge, the present study focuses on external mixing twin-fluid atomization of high viscosity liquids at elevated system pressure. As previous investigations of Jakobs (2015) and Sänger (2018) show, liquid velocity, gas velocity, and GLR are important parameters influencing the droplet size distribution of the spray. In order to investigate only the influence of system pressure on the atomization, these parameters were kept constant. To maintain constant boundary conditions, pressure adapted nozzles are used in the present study, i.e. nozzles with reduced cross section of the gas outlet are applied for every system pressure increment (see Table 3). With this approach, increasing system pressure results in constant GLR , momentum flow ratio, Re_{liq} , as well as gas velocity, while We_{aero} and Re_{gas} increase with system pressure. Applying this set of nozzles is the first investigation of geometrical scaling to higher system pressure.

Table 3
Nozzle data (Nozzle 1 - 5) for each system pressure step.

	p_{sys} in bar	D_{liq} in mm	D_{gas} in mm	A_{gas} in mm ²
Nozzle 1	1	2.00	7.96	45.94
Nozzle 2	2	2.00	5.84	22.97
Nozzle 3	6	2.00	3.82	7.66
Nozzle 4	11	2.00	3.19	4.18
Nozzle 5	16	2.00	2.91	2.87

2. Experimental setup

As described by Sänger et al. (2015), the experimental setup consists of the pressurized atomization test rig (PAT), a PDA, a shadow sizing measurement system, and a high-speed camera. For the experiments, 5 pressure adapted external mixing twin-fluid atomizers with similar geometry were used for the atomization of water and a glycerol/water - mixture. A scheme of the spray test rig PAT with exhaust air system and a horizontal cross-sectional view (A-A) is given in Fig. 1. The pressure chamber has an internal diameter of 300 mm and a total height of 3000 mm. It is designed for operation at system pressures up to $p_{sys} = 21 \text{ bar}$. The external mixing twin-fluid atomizer is mounted on the axially (z-direction) movable twin-fluid lance, which is fed by one of the two eccentric screw pumps with liquids featuring viscosities up to $\eta_{liq} = 1000 \text{ mPa} \cdot \text{s}$. Liquid mass flow can be controlled in the range of P1: $\dot{M}_{liq} = 10 - 60 \text{ kg} \cdot \text{h}^{-1}$ / P2: $\dot{M}_{liq} = 60 - 200 \text{ kg} \cdot \text{h}^{-1}$ using different screw pumps. Liquid mass flow and density are measured by a Coriolis flow meter with an uncertainty of $< 0.5\%$ and controlled by FIRC (flow indication recording control) systems. The compressed air volume flow \dot{V}_{gas} is detected by a turbine meter measuring in a range of $\dot{V}_{gas} = 0.85 - 25 \text{ m}^3 \cdot \text{h}^{-1}$ with an uncertainty of $< 0.5\%$ and controlled by an FIRC system. A recalculation of volume to mass flow is done using the local measured gas temperature and pressure at the measurement turbine. System pressure control in the pressure chamber was made by a PIRC (pressure indication recording control) system and three corresponding valves after the gas/liquid separator. The liquid height in the separator tank was controlled by a LCA (level control alarm) system. To ensure well-defined nozzle inlet conditions, the liquid can be stirred and tempered in a range of $T = 10 \text{ }^\circ\text{C} - 50 \text{ }^\circ\text{C}$. The test rig is equipped with three glass windows (no inclusions or cords) that allow for optical access to the spray chamber and avoid any disturbances of the laser beam. Two optical ports are located at $\Phi_R = 0^\circ$ and 70° to enable Phase Doppler measurements in scattering mode with preferably highest intensity (first-order refraction) (Albrecht, 2003). The third optical port is positioned at $\Phi_R = 180^\circ$ to allow for spray investigations in backlight mode with optical measurement systems. To ensure the protection from window deposits at the $\Phi_R = 70^\circ$ window location, a wiper was used between the measurements, using compressed air for movement. A flow straightener (honeycomb structure) is located below the

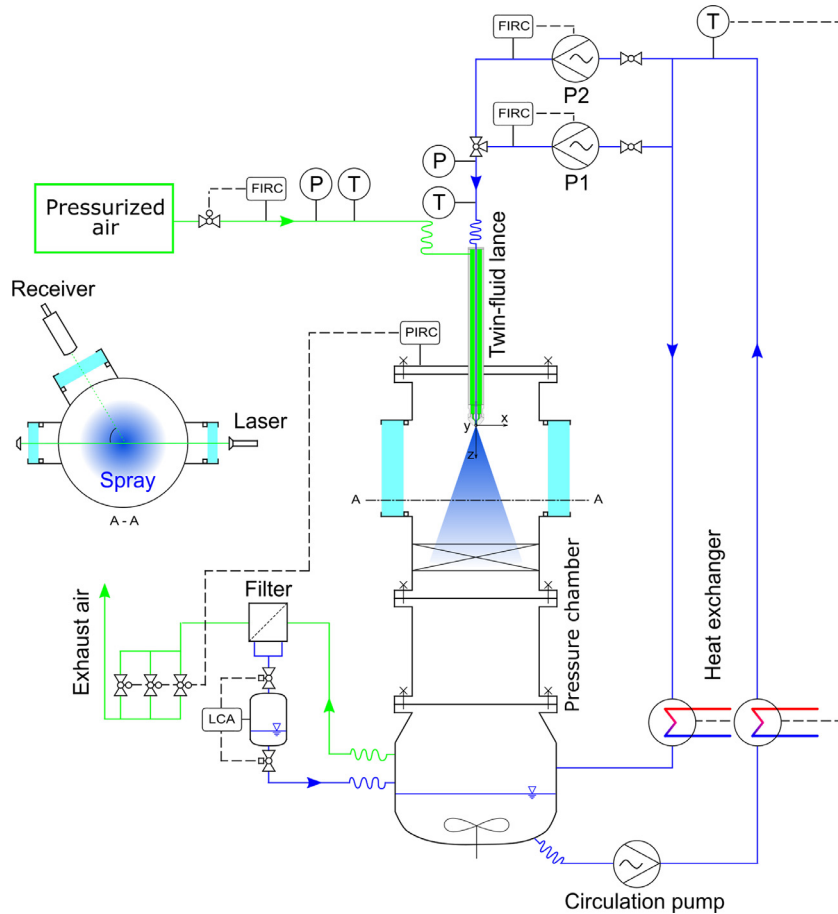


Fig. 1. Scheme of the experimental setup - Pressurized Atomization Test Rig (PAT).

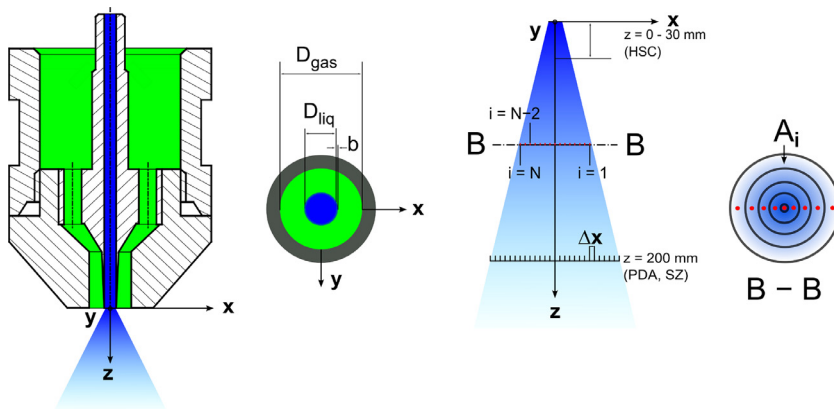


Fig. 2. Scheme of the external mixing twin-fluid nozzle.

measuring plane to avoid influences on the measurement due to recirculation of droplets into the region of interest.

All investigations were conducted with 5 pressure adapted external mixing twin-fluid nozzles as shown in Fig. 2. The liquid (blue) is supplied through a circular central tube ($D_{liq} = 2$ mm) at the nozzle axis. The liquid jet is surrounded by a coaxial gas stream (green). The nozzle has parallel flow channels to avoid disturbance of the liquid jet due to gas flow angle. In addition, the influence of the tube separating gas and liquid at the nozzle orifice was minimized by reduction of the wall thickness b to 0.1 mm. This configuration results in an undisturbed gas flow at the exit of the nozzle. For every system pressure, the related area of the annular gas orifice was adapted in order to achieve a constant gas

velocity, GLR and mass flows, resulting in 5 different nozzles 1 - 5, geometries given in Table 3. Those special nozzle configurations allow for solely varying the system pressure while keeping all other operating conditions (v_{gas} , GLR , M_{liq}) constant. Exemplary follows for a system pressure of $p_{sys} = 16$ bar, a nozzle area ratio between nozzle 1 and nozzle 5 of $A_{gas,1}/A_{gas,5} = 16$.

To investigate the influence of dynamic viscosity on the atomization process, water ($\eta_{liq} = 1$ mPa · s) and a glycerol/water - mixture ($\eta_{liq} = 100$ mPa · s) were used. The physical properties of these Newtonian fluids were measured at $T = 20$ °C and $p = 1$ bar, see Table 4. Dynamic viscosity was measured using a Searle-type (GFG, 1912) rheometer. Surface tension was determined using the du Noüy ring method (du Noüy, 1925) with a tensiometer, and

Table 4
Physical properties of the investigated fluids at $T = 20$ °C and $p = 1$ bar.

	η_{liq} in mPa · s	σ in N · m ⁻¹	ρ_{liq} in kg · m ⁻³	Oh
water	1	0.0719	998	0.0026
glycerol/water (84.3 wt. %)	100	0.0649	1220	0.2513

liquid density by the weighing method. The influence of system pressure on both, dynamic viscosity (Mezger, 2006) and surface tension (Massoudi and King, 1974) is negligible for the investigated liquids.

A high-speed camera for qualitative investigation of the primary breakup process was applied in the nozzle nearfield. The camera features a frame rate of 3.6 kHz operation at 1024×1024 pixel resolution and frame rates up to 500 kHz at reduced resolution. A lens with focal length of $f_{HG} = 105$ mm was used to capture primary breakup morphologies. In this case, images have dimensions of 40.0×30.0 mm² or 40.0×48.0 mm² with a spatial resolution of $62.5 \mu\text{m} \cdot \text{pix}^{-1}$. The frame rate was set to 12 kHz or 7.5 kHz, respectively. The images were captured by backlight illumination of the region of interest with a special lighting setup. An array of 9 high-power light-emitting diodes (LED) with total luminous flux of 9×4500 lm was used. The position of each single LED within the LED array was optimized for best light spread. Due to the high intensity and the homogeneous distribution of the light, very short exposure times ($t_{Exp} \sim 7 \mu\text{s}$) could be applied. This light setup allowed for a sharp representation of the droplets even in case of fast flow conditions. To guarantee for representative data of the liquid disintegration process, a set of 4000 high-speed images was recorded at every operating condition as well as a background reference image without liquid flow.

For observation of single droplets within the spray, a shadow-sizer was employed and used (i) to optimize the PDA hardware settings (receiver mask), (ii) to determine the measuring plane where reliable measurements with the PDA system can be conducted (spherical droplets), (iii) to qualitatively confirm the tendencies measured by the PDA, and (iv) as a validation tool for the PDA system to remove deviations arising from the Gaussian beam effect (Araneo et al., 2002). The shadow sizing system consists of a CCD camera operating in backlight mode with a high efficiency diffuser that is powered by an Nd:YAG laser for illumination. The far-field microscope mounted on the camera allows for very small measuring volume of $2.8 \times 2.8 \times 0.8$ mm³. The measuring volume, in combination with the camera resolution of 4 megapixels, results in a spatial resolution of $\sim 1.4 \mu\text{m}/\text{pixel}$ and allows for the detection of all relevant droplet sizes. The accuracy of the shadow sizing system was checked using a calibration target with points of known size (10 μm). The biggest measurement error was $< 10 \mu\text{m}$. Due to the fact that the shadow sizing system was used for qualitative investigations of large droplets only, the accuracy was considered as adequate. In order to obtain a reliable amount of droplets, a set of 1000 shadow images at an axial distance of $z = 200$ mm from the nozzle orifice was recorded and analyzed. Droplets without detectable contour were rejected.

Droplet size and velocity were measured with high spatial and temporal resolution within the spray cone by a fiber PDA system by Dantec Dynamics. For data collection, the PDA was operated in forward scattering arrangement and refraction mode (1st order). The receiver was set to an off-axis angle of $\Phi_R = 70$ °. In order to (i) get a well-defined detection volume dimension, (ii) to ensure for high data rates at dense spray conditions and (iii) to enable flux calculation, a slit with a physical length of $l_S = 200 \mu\text{m}$ was used, to reduce the length of the measurement volume. To guarantee for the detection of large droplets as expected by the atomization of high viscosity liquids and avoid sizing errors due to the Gaussian beam effect, lenses with a focal length of 1000 mm were used for

Table 5
Settings of the fiber PDA evaluated by the sensitivity analysis.

Parameters	Values	Unit
Transmitter focal length f_T	1000	mm
Receiver focal length f_R	1000	mm
Beam expander ratio E	1	–
Receiver slit width (physical) l_S	200	μm
Laser wavelength λ_L	514.5	nm
Laser power (transmitter exit)	25	mW
Off-axis angle Φ_R	70	°
Frequency shift	40	MHz

both, transmitter f_T and receiver f_R (Araneo et al., 2002). In addition, the asymmetric Mask B was mounted in the receiver to eliminate possible measurement errors due to the Gaussian beam effect (trajectory effect). With this optical configuration, the PDA system allowed for detection of droplets with minimum size of 1 μm and maximum size of 1307 μm for water and 1330 μm for the glycerol/water - mixture, depending on the refractive index of the liquid (Albrecht, 2003). To improve the PDA instrument settings towards small droplets (e.g. data rate and validation rate), the optimum PDA user settings were evaluated in advance by a sensitivity study (Kapulla and Najera, 2006). The PDA settings are given in Table 5.

To enable drop size measurements at different positions within the spray cone, receiver and transmitter were mounted on a 3D traverse system, which guarantees for spatially operation with a reproducibility < 0.1 mm. Data were obtained by moving the detection volume relatively to the nozzle position. The measurements were taken at several radial (traverse along x -axis) positions with a radial increment of $\Delta x = 2$ mm. According to the orientation of the coordinate system as indicated in Fig. 2 and the alignment of the fringes of the laser beam couple ($\lambda_L = 514.5$ nm - green), the axial droplet velocity component v_z could be measured. To ensure a reliable database for every radial position during PDA measurements, the sample size was set to 50,000 droplets. Only for the outermost radial measuring position, the sample size of 50,000 droplets was not reached for all operating conditions. Nevertheless, at least 4000 droplets were detected at the boundary of the spray cone. The raw data from the manufacturer software were used to compute arithmetic means, statistical data, as well as additional information (i.e. mass flux and $ID_{32,m}$, etc.) using the toolbox SprayCAT (Sänger, 2018). For global characterization of the spray, the computation of a global characteristic diameter, i.e. mass-weighted integral Sauter mean diameter $ID_{32,m}$, was carried out by a weighted average, including all measurement positions of a radial profile at a fixed axial position z . The integral Sauter mean diameter $ID_{32,m}$ is calculated according to Eq. (4), based on the local volume mean diameter $D_{30,i}$ and local surface mean diameter $D_{20,i}$. These diameters are weighted by local mass flux \dot{m}_i and the annulus area A_i (see Fig. 2), corresponding to the measurement position i along the radial axis $x_{i-1} \leq x_i \leq x_N$ with N measurement positions. The outermost point x_N for each operating condition is defined by a minimum of the ratio of data rate f_i divided by maximum data rate f_{\max} along the radial profile, which was set to 0.1.

$$ID_{32,m} = \frac{\sum_{i=1}^N D_{30,i}^3 \dot{m}_i A_i}{\sum_{i=1}^N D_{20,i}^2 \dot{m}_i A_i} \quad (4)$$

Table 6
Operating conditions of the experiments.

p_{sys} in bar	\dot{M}_{gas} in $\text{kg} \cdot \text{h}^{-1}$	v_{gas} in $\text{m} \cdot \text{s}^{-1}$	GLR
1 / 2 / 6 / 11 / 16	12 / 16 / 20	60 / 80 / 100	0.6 / 0.8 / 1.0

Further information concerning computation of global size distribution and drop size moments can be obtained from DIN SPEC 91325 as well as from Albrecht (2003). The mass flux \dot{m}_i was calculated from PDA data according to Albrecht (2003) using the toolbox SprayCAT. All PDA measurements were conducted at an axial distance of $z = 200$ mm from the nozzle orifice and repeated at least 3 times. For each operating condition and nozzle, rotational symmetry of the spray cone was proven, taking a full radial profile in a first set of experiments. After rotational symmetry was proven, the following repetition measurements were performed taking half profiles from the spray edge to the center at $x = 0$ mm. The results of those sets of experiments were afterwards mirrored to get full profiles. Therefore, all radial Sauter mean diameter distributions are shown as mirrored profiles at $x = 0$ mm and the plotted and mirrored data points are shown as open symbols.

3. Results and discussion

In order to investigate the influence of (i) gas velocity v_{gas} , (ii) system pressure p_{sys} and (iii) dynamic viscosity η_{liq} on resulting droplet size and primary breakup at constant liquid mass flow of $\dot{M}_{\text{liq}} = 20 \text{ kg} \cdot \text{h}^{-1}$, pressure adapted nozzles were applied as a scaling approach. This results for every system pressure step in constant operating conditions, named \dot{M}_{gas} , \dot{M}_{liq} , GLR, v_{gas} . Additional, to examine the effect of gas velocity, three different gas mass flow rates \dot{M}_{gas} were chosen for the five system pressure settings p_{sys} . The operating conditions for all measurements are presented in Table 6. The atomization agent in all experiments was pressurized air at $T = 20$ °C. The supplied liquids were also tempered at $T = 20$ °C.

3.1. Influence of gas velocity, system pressure and dynamic viscosity on droplet velocity

In the following section the investigation on the influence of gas velocity on local axial droplet velocity are discussed for dif-

ferent system pressure and dynamic viscosity of the liquid. The measurements were performed at an axial distance of $z = 200$ mm downstream the nozzle exit, applying a PDA system. Exemplarily results for glycerol/water - mixture ($\eta_{\text{liq}} = 100 \text{ mPa} \cdot \text{s}$) at $v_{\text{gas}} = 60 \text{ m} \cdot \text{s}^{-1}$ (Fig. 3a) and a comparison of water ($\eta_{\text{liq}} = 1 \text{ mPa} \cdot \text{s}$) and glycerol/water - mixture ($\eta_{\text{liq}} = 100 \text{ mPa} \cdot \text{s}$) for $v_{\text{gas}} = 100 \text{ m} \cdot \text{s}^{-1}$ (Fig. 3b) are shown.

Fig. 3 shows the number-averaged axial droplet velocity $v_{\text{dr},z,\text{mean}}$ for gas velocities of $v_{\text{gas}} = 60 \text{ m} \cdot \text{s}^{-1}$ (Fig. 3a) and $v_{\text{gas}} = 100 \text{ m} \cdot \text{s}^{-1}$ (Fig. 3b) for system pressure of $p_{\text{sys}} = 1 - 16$ bar, $z = 200$ mm downstream the nozzle orifice. Additionally, Fig. 3b shows the influence of liquid viscosity on $v_{\text{dr},z,\text{mean}}$ ($\eta_{\text{liq}} = 1 \text{ mPa} \cdot \text{s}$ / left and $\eta_{\text{liq}} = 100 \text{ mPa} \cdot \text{s}$ / right). The typical Gaussian shaped radial profile of external mixing twin-fluid atomizers was detected. All velocity profiles show rotational symmetry with deviations smaller than $\Delta v_{\text{dr},z} = 1 \text{ m} \cdot \text{s}^{-1}$ between left and corresponding right side of the centerline. In addition, the error bars plotted in Fig. 3 indicate the repeatability of the experiments. It was detected that droplets of a size range between $1 - 5 \mu\text{m}$ at $z = 200$ mm show velocity deviations smaller than $\Delta v_{\text{dr},z} = 0.8 \text{ m} \cdot \text{s}^{-1}$ towards the number-averaged droplet velocity of all droplets shown in Fig. 3, i.e. slip between droplet and gas phase can be neglected, secondary breakup of droplets is finished, thus $z = 200$ mm is a reasonable measuring position to characterize droplet size of the spray.

For increasing gas velocity at the nozzle orifice, higher axial droplet velocities are detected, see Fig. 3a at $v_{\text{gas}} = 60 \text{ m} \cdot \text{s}^{-1}$ compared to Fig. 3b at $v_{\text{gas}} = 100 \text{ m} \cdot \text{s}^{-1}$. Applying pressure adapted nozzles at increasing system pressure, the axial droplet velocity over the whole spray width decreases for all gas velocities and liquid viscosities. This can be explained by the free jet theory and Eq. (5) for calculation of the gas free jet, which is based on the assuming of conservation of momentum (Schlichting et al., 2006).

$$\frac{v(z)}{v_{\text{gas}}} = 6.37 \cdot \frac{d_{\text{eq}}}{z} \cdot \sqrt{\frac{\rho_0}{\rho}} \quad (5)$$

Here, v_{gas} is the gas velocity at the nozzle orifice, $v(z)$ is the gas velocity at distance z on the spray axis, ρ_0 is the gas density at the nozzle orifice, ρ is the density of the ambient gas phase and d_{eq} is the equivalent diameter of the gas exit of the nozzle. With increasing system pressure the gas outlet area A_{gas} of the nozzle is reduced due to the pressure adapted scaling approach (see Table 3).

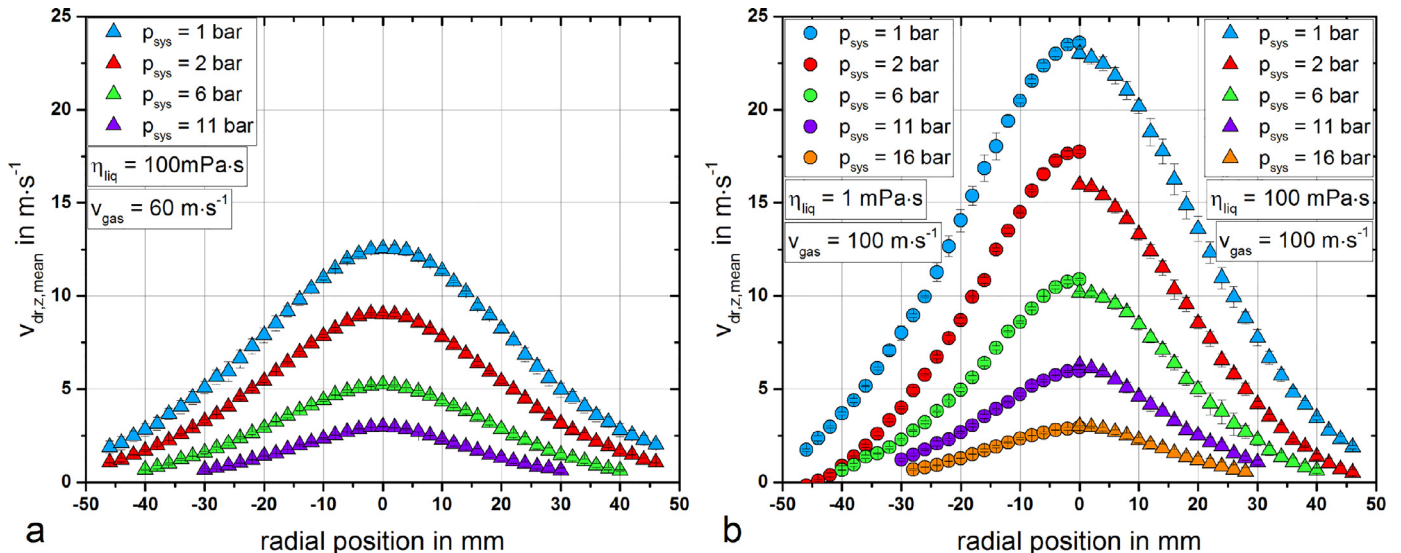


Fig. 3. Radial measurements of the number-averaged axial droplet velocity distributions as a function of system pressure a) for glycerol/water - mixture ($\eta_{\text{liq}} = 100 \text{ mPa} \cdot \text{s}$) at $v_{\text{gas}} = 60 \text{ m} \cdot \text{s}^{-1}$ and b) a comparison of water ($\eta_{\text{liq}} = 1 \text{ mPa} \cdot \text{s}$) and glycerol/water - mixture ($\eta_{\text{liq}} = 100 \text{ mPa} \cdot \text{s}$) at $v_{\text{gas}} = 100 \text{ m} \cdot \text{s}^{-1}$.

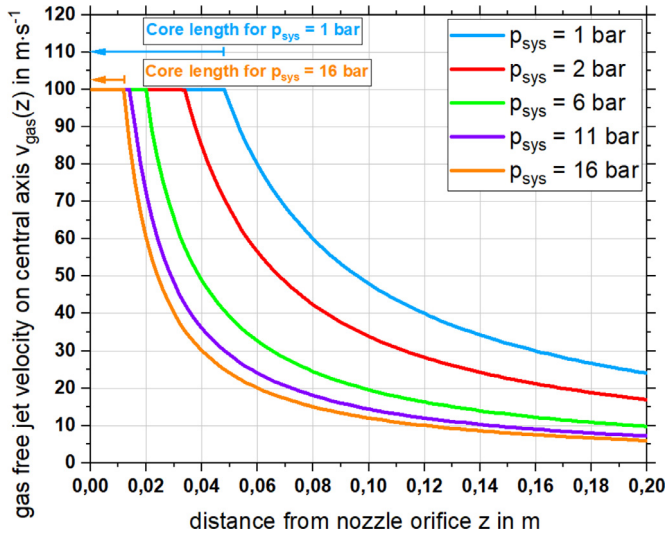


Fig. 4. Calculation of the gas free jet velocity on central axis for $v_{gas} = 100 \text{ m} \cdot \text{s}^{-1}$ applying pressure adapted nozzles at $p_{sys} = 1 - 16 \text{ bar}$. The core length of constant gas velocity is marked as arrows for $p_{sys} = 1 \text{ bar}$ and $p_{sys} = 16 \text{ bar}$.

A decrease in the gas orifice area leads to smaller equivalent diameter of the gas exit d_{eq} . The ratio ρ_0 over ρ does not depend on system pressure, due to the small and therefore negligible difference between ambient gas and atomizing air density. Smaller d_{eq} values lead, according to Eq. (5), towards lower values of the gas velocity $v(z)$ at same distance z , while the exiting gas velocity at the nozzle orifice remains constant. Physically, this deceleration of gas velocity downstream the nozzle can be explained by the entrainment of ambient gas into the atomization gas jet emerging from the nozzle. As system pressure is increased and pressure adapted nozzles are applied, the entrainment increases, due to the decreasing equivalent diameter d_{eq} . This change in nozzle geometry affects the gas jet core length, which is characterized by constant gas velocity, as shown exemplarily for $v_{gas} = 100 \text{ m} \cdot \text{s}^{-1}$ in Fig. 4 (Schlichting et al., 2006).

For increasing system pressure while applying the pressure adapted scaling approach, a decrease in the gas velocity $v(z)$ for

every distance z is calculated. This results in a shorter core length, where the slow liquid phase is exposed to the fast atomization gas jet. As a consequence, this decreased core length leads to a decrease in gas-liquid-interaction and therefore to droplets with lower velocities.

3.2. Influence of gas velocity, system pressure and dynamic viscosity on Sauter mean diameter

For quantitative investigation, the influence of gas velocity, system pressure, and dynamic viscosity on spray quality was detected by a PDA system using D_{32} as a characterization criterion. Sauter mean diameter profiles across the whole spray cone at an axial distance of $z = 200 \text{ mm}$ downstream the nozzle orifice for water ($\eta_{liq} = 1 \text{ mPa} \cdot \text{s}$) and glycerol/water - mixture ($\eta_{liq} = 100 \text{ mPa} \cdot \text{s}$) were performed. The results for the high viscosity liquid ($\eta_{liq} = 100 \text{ mPa} \cdot \text{s}$) are presented in Fig. 5 as radial profiles.

3.2.1. Influence of gas velocity on Sauter mean diameter

Fig. 5 shows exemplarily the radial distribution of D_{32} for system pressure of $p_{sys} = 1 - 16 \text{ bar}$ at $v_{gas} = 60 \text{ m} \cdot \text{s}^{-1}$ (Fig. 5a) and $v_{gas} = 100 \text{ m} \cdot \text{s}^{-1}$ (Fig. 5b) for the glycerol/water mixture with viscosity of $\eta_{liq} = 100 \text{ mPa} \cdot \text{s}$. An increase of gas velocity leads to a decrease of Sauter mean diameter for each system pressure. The influence of gas velocity on the resulting D_{32} is more pronounced for system pressures $p_{sys} > 6 \text{ bar}$. The various shapes of the D_{32} profiles are discussed in detail in the following sections.

3.2.2. Influence of system pressure on Sauter mean diameter

For $v_{gas} = 60 \text{ m} \cdot \text{s}^{-1}$ increasing system pressure up to $p_{sys} = 6 \text{ bar}$ results in a slight reduction of the Sauter mean diameter, a further increase of the system pressure $p_{sys} > 6 \text{ bar}$ shows larger droplet sizes, especially near the spray axis. Similar dependencies were found for $v_{gas} = 100 \text{ m} \cdot \text{s}^{-1}$, where the influence of system pressure for $p_{sys} < 6 \text{ bar}$ is less pronounced compared to $v_{gas} = 60 \text{ m} \cdot \text{s}^{-1}$.

3.2.3. Shape of the Sauter mean diameter profiles

Fig. 5 clearly shows a change in shape of the Sauter mean diameter profiles with increasing system pressure and gas velocity. For $v_{gas} = 60 \text{ m} \cdot \text{s}^{-1}$ the flat D_{32} profiles for $p_{sys} < 6 \text{ bar}$ turn into a profile with a pronounced peak at the spray axis for

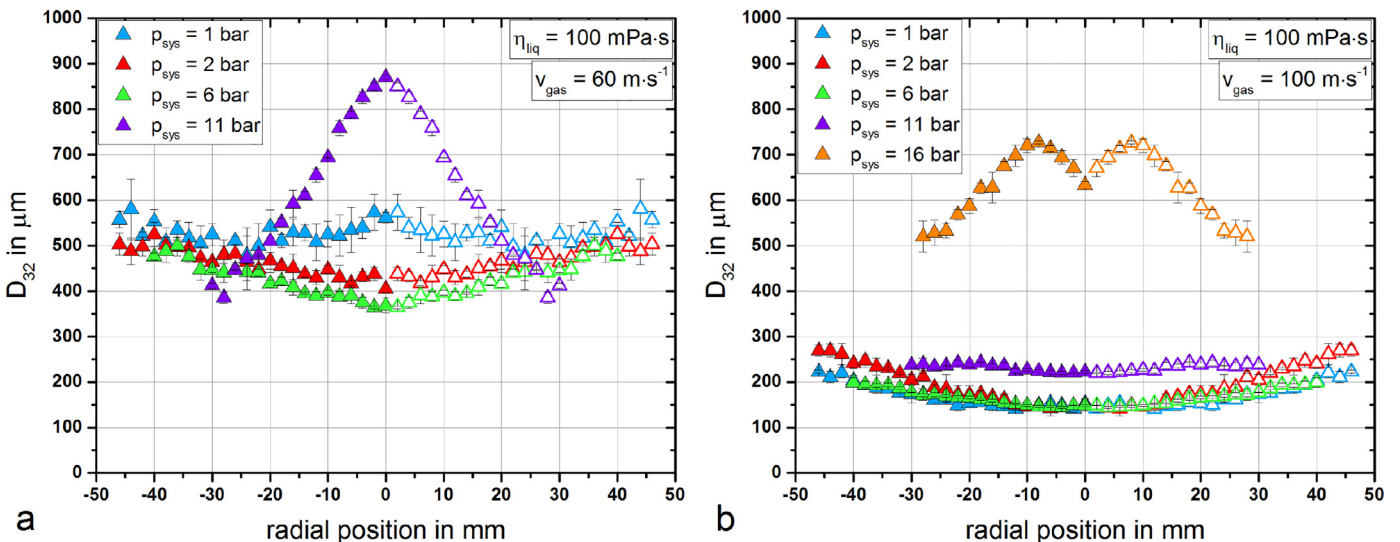


Fig. 5. Radial distribution of Sauter mean diameter at $z = 200 \text{ mm}$ below the nozzle orifice as a function of system pressure for glycerol/water - mixture ($\eta_{liq} = 100 \text{ mPa} \cdot \text{s}$) at a) $v_{gas} = 60 \text{ m} \cdot \text{s}^{-1}$ and b) $v_{gas} = 100 \text{ m} \cdot \text{s}^{-1}$ (open symbols denote mirrored positions).

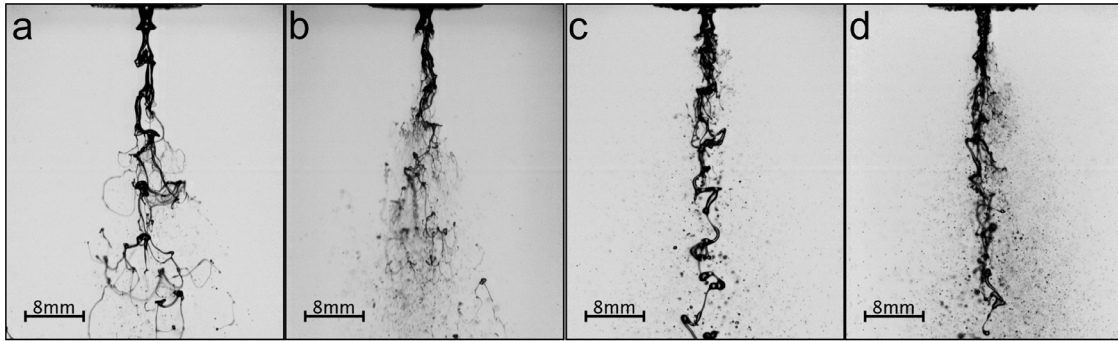


Fig. 6. High-speed camera images of primary jet breakup for glycerol/water - mixture ($\eta_{liq} = 100 \text{ mPa} \cdot \text{s}$) at a) $p_{sys} = 1 \text{ bar}$, $v_{gas} = 60 \text{ m} \cdot \text{s}^{-1}$, b) $p_{sys} = 1 \text{ bar}$, $v_{gas} = 100 \text{ m} \cdot \text{s}^{-1}$, c) $p_{sys} = 11 \text{ bar}$, $v_{gas} = 60 \text{ m} \cdot \text{s}^{-1}$ and d) $p_{sys} = 16 \text{ bar}$, $v_{gas} = 100 \text{ m} \cdot \text{s}^{-1}$.

$p_{sys} = 11 \text{ bar}$. For $v_{gas} = 100 \text{ m} \cdot \text{s}^{-1}$ the uniform profile is maintained up to $p_{sys} = 11 \text{ bar}$, but a further system pressure increase to $p_{sys} = 16 \text{ bar}$ leads to a significant increase in drop size with a pronounced M-shape radial profile. However, a M-shaped profile is observed by the measurement, due to the PDA measurement limit mentioned in the description above, see also Albrecht (2003). Without this measurement limit, the radial profile would also be inverse V-shaped. In order to understand the physical effects responsible for these findings, additional high-speed camera images were taken. Fig. 6 shows primary jet break-up for different process conditions, indicating that the shape of the profiles results from different breakup morphologies of the primary jet. In Fig. 6 only the glycerol/water - mixture with $\eta_{liq} = 100 \text{ mPa} \cdot \text{s}$ is shown in sense of simplicity, referring to $Re_{liq} = 35$ and $Oh = 0.2513$. Furthermore, breakup morphologies are classified and compared towards the findings of Lasheras and Hopfinger (2000), noting that the nozzle geometry was similar, but with different dimensions and liquid properties.

Fig. 6a ($p_{sys} = 1 \text{ bar}$, $v_{gas} = 60 \text{ m} \cdot \text{s}^{-1}$, $We_{aero} = 128$) shows a membrane type breakup; small droplets are formed by the disintegration of membranes and are partly accelerated in radial direction away from the spray axis, while larger droplets, originated from membrane rims, stay in the center of the spray. This results in the W-shaped radial distribution of D_{32} as shown in Fig. (5)a. For this atomization conditions (We_{aero} , Oh) the membrane type breakup was also proposed by Lasheras and Hopfinger (2000) and Zhao et al. (2012).

Fig. 6b ($p_{sys} = 1 \text{ bar}$, $v_{gas} = 100 \text{ m} \cdot \text{s}^{-1}$, $We_{aero} = 361$) shows a fiber type breakup situation. As a consequence of the higher relative velocity in the spray center compared to the boundary of the spray, liquid fragments in the center are disintegrated into smaller droplets. Liquid fragments at the spray boundary form droplets without further disintegration due to the low shear rate, leading to a U-shape distribution according to Fig. 5b. For this operating conditions Zhao et al. (2012) still estimate a membrane type breakup, whereas Lasheras and Hopfinger (2000) predict a transition region between membrane and fiber breakup, which is in good accordance to the prevailing breakup.

In Fig. 6c ($p_{sys} = 11 \text{ bar}$, $v_{gas} = 60 \text{ m} \cdot \text{s}^{-1}$, $We_{aero} = 1395$) the aerodynamic force of the gas jet is not sufficient to disintegrate the whole liquid jet. This leads to the peel off of some fibers from the primary jet close to the nozzle orifice, whereas the center of the jet is not affected. Finally, the liquid core breaks up into large droplets by Kelvin-Helmholtz and Rayleigh-Plateau instabilities. This explains the inverse V-shape of the radial D_{32} profile with maximum on the spray axis shown in Fig. 5a. For this operating conditions, Zhao et al. (2012) as well as Lasheras and Hopfinger (2000) predict a fiber type breakup, due to the high aerody-

amic We number calculated with values at the nozzle orifice. Due to the increased deceleration of the gas velocity with increased system pressure and the applied pressure scaling of the nozzles, near the nozzle orifice a fiber type breakup can be detected, while the liquid core remains constant and disintegrates according to the non-axisymmetric Rayleigh type breakup. This effect stays for system pressures $p_{sys} > 6 \text{ bar}$ in contrast to previous regime classifications.

The spray shown in Fig. 6d ($p_{sys} = 16 \text{ bar}$, $v_{gas} = 100 \text{ m} \cdot \text{s}^{-1}$, $We_{aero} = 5882$) corresponds to the M-shaped D_{32} -profile in Fig. 5b. Due to the partly prevailing non-axisymmetric Rayleigh-type breakup of the primary jet, droplet diameters $d > D_{liq}$ are found near the spray center shown in Fig. 6d. From shadowsize images the maximum detected droplet diameter on the centerline of the spray was $d_{max} = 3072 \mu\text{m}$. This leads to the conclusion that the local Sauter mean diameter would actually even be higher than predicted by the PDA measurements and form a Gaussian shaped profile. The minimum of Sauter mean diameter in the spray center is only detected, due to some smaller detectable droplets formed near the nozzle orifice and the exceeding droplet size over the measurement limit of the PDA system. Regarding regime classification the prediction of breakup morphology from both authors Lasheras and Hopfinger (2000) and Zhao et al. (2012) show same deviations as for Fig. 6c, due to the incomplete breakup detected at even higher aerodynamic We number.

Concluding the regime classification, for increase of v_{gas} , results were in good accordance to the literature. Applying the pressure adapted nozzles at increased system pressure, results at $p_{sys} > 6 \text{ bar}$ were not comparable with both authors Lasheras and Hopfinger (2000) and Zhao et al. (2012). One possible reason could be the fact that commonly used dimensionless numbers (We , Oh) do not include all relevant nozzle geometry parameters.

3.2.4. Influence of dynamic viscosity on sauter mean diameter

The influence of dynamic viscosity is discussed in detail on mass-weighted integral Sauter mean diameter, see in section below. Experimental data on Sauter mean diameter profiles, not given in this paper, show that increase in dynamic viscosity leads to the formation of membranes and ligaments due to the damping effect, as described by Zhao et al. (2012). Those ligaments disintegrate into large droplets which result in an increase of droplet size for all operating conditions. This effect is also shown by HSC images as shown in Fig. 11.

3.3. Influence of gas velocity, system pressure and dynamic viscosity on mass-weighted integral sauter mean diameter

In order to compare the spray quality at different operating conditions for both viscosities, local drop sizes measured at

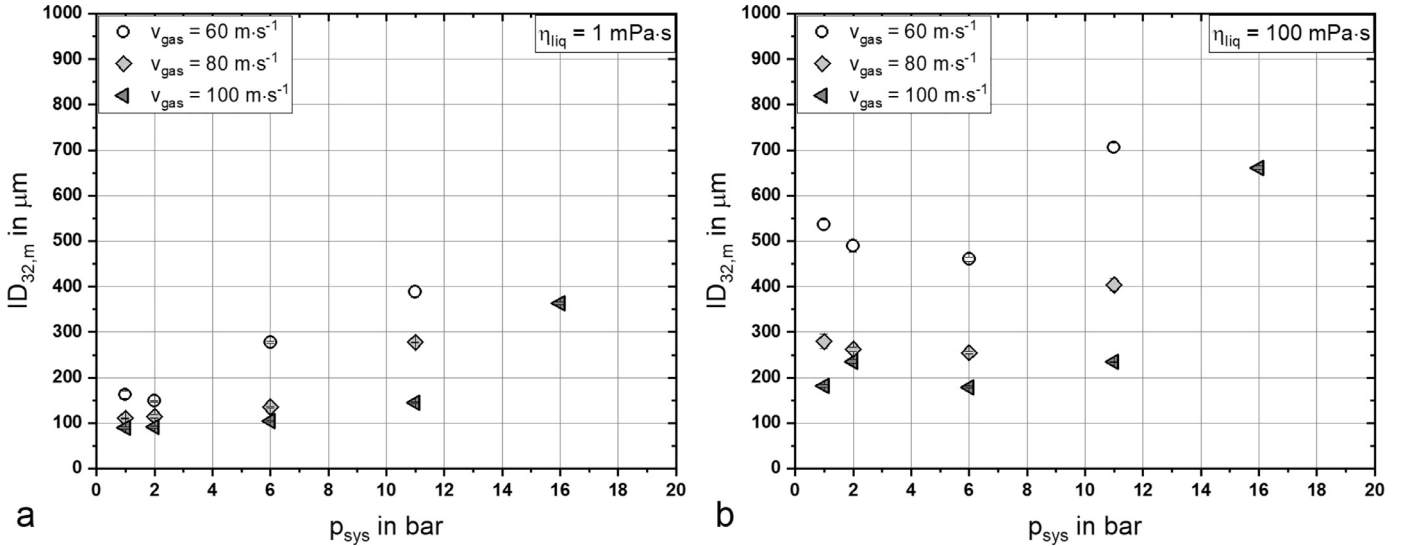


Fig. 7. Mass-weighted integral Sauter mean diameter as a function of system pressure p_{sys} and gas velocity v_{gas} for a) water ($\eta_{\text{liq}} = 1 \text{ mPa}\cdot\text{s}$) and b) glycerol/water - mixture ($\eta_{\text{liq}} = 100 \text{ mPa}\cdot\text{s}$).

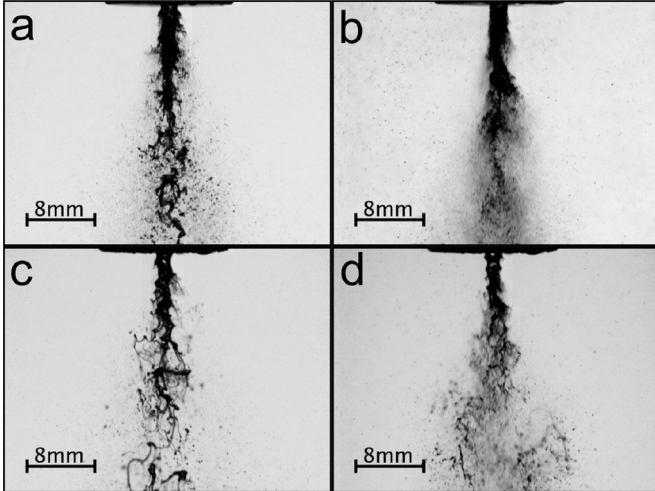


Fig. 8. High-speed camera images of primary jet breakup for water ($\eta_{\text{liq}} = 1 \text{ mPa}\cdot\text{s}$) at a) $p_{\text{sys}} = 6 \text{ bar}$, $v_{\text{gas}} = 60 \text{ m}\cdot\text{s}^{-1}$ and b) $p_{\text{sys}} = 6 \text{ bar}$, $v_{\text{gas}} = 100 \text{ m}\cdot\text{s}^{-1}$ and glycerol/water - mixture ($\eta_{\text{liq}} = 100 \text{ mPa}\cdot\text{s}$) at c) $p_{\text{sys}} = 6 \text{ bar}$, $v_{\text{gas}} = 60 \text{ m}\cdot\text{s}^{-1}$ and d) $p_{\text{sys}} = 6 \text{ bar}$, $v_{\text{gas}} = 100 \text{ m}\cdot\text{s}^{-1}$.

$z = 200 \text{ mm}$ were used to calculate the $ID_{32,m}$ according to Eq. (4). For different gas velocities and system pressures, the values of $ID_{32,m}$ are plotted as function of system pressure in Fig. 7. Fig. 7a shows the $ID_{32,m}$ for water with $\eta_{\text{liq}} = 1 \text{ mPa}\cdot\text{s}$ and Fig. 7b for glycerol/water - mixture with $\eta_{\text{liq}} = 100 \text{ mPa}\cdot\text{s}$, respectively.

3.3.1. Influence of gas velocity on mass-weighted integral Sauter mean diameter

A decrease of $ID_{32,m}$ with increasing gas velocity can be detected for all system pressures and liquid viscosities, see Fig. 7. For higher system pressure $p_{\text{sys}} \geq 6 \text{ bar}$ and higher liquid viscosity, the influence of gas velocity is even more pronounced. This effect is confirmed by the high-speed camera images of primary jet breakup shown in Fig. 8. Large ligaments are found in the nozzle nearfield for $v_{\text{gas}} = 60 \text{ m}\cdot\text{s}^{-1}$, see Fig. 8a and Fig. 8c, whereas only few small liquid fragments are detected for $v_{\text{gas}} = 100 \text{ m}\cdot\text{s}^{-1}$ in Fig. 8b and Fig. 8d. In addition, a reduction of the primary ligament length can be seen with increased gas velocity.

3.3.2. Influence of system pressure on mass-weighted integral Sauter mean diameter

With increasing system pressure, a minimum in the $ID_{32,m}$ can be detected for the glycerol/water - mixture at $p_{\text{sys}} = 6 \text{ bar}$ for all gas velocities, for water this effect is less pronounced at $p_{\text{sys}} = 2 \text{ bar}$ (see Fig. 7). The high-speed camera images in Fig. 9, where primary jet breakup is shown at $v_{\text{gas}} = 100 \text{ m}\cdot\text{s}^{-1}$ for water at system pressure of $p_{\text{sys}} = 1 \text{ bar}$ (Fig. 9a), 6 bar (Fig. 9b) and 16 bar (Fig. 9c) and for glycerol/water at system pressure of $p_{\text{sys}} = 1 \text{ bar}$ (Fig. 9d), 6 bar (Fig. 9e) and 16 bar (Fig. 9f) confirm these findings.

One possible explanation of this effect is the difference in the dynamic pressure of the gas jet $\rho_{\text{gas}} \cdot v_{\text{gas}}^2$, which describes the aerodynamic force on the liquid jet according to We_{gas} (Lasheras and Hopfinger, 2000; Sanger, 2018; Kumar and Sahu, 2018; Xiao et al., 2014). The gas velocity in the jet is reduced due to the entrainment of ambient gas (free jet behaviour, see Eq. (5)). This entrainment shows a higher effect on the deceleration of the gas phase, when increasing system pressure and applying pressure adapted nozzles, see Fig. 4. In order to quantify this assumption, the measured velocity of droplets in the size range from 1 - 5 μm was used to describe the local v_{gas} at $z = 200 \text{ mm}$ (Tropea et al., 2007). The derived radial distribution of the dynamic pressure of the gas jet is shown in Fig. 10 for glycerol/water - mixture at $p_{\text{sys}} = 1, 6 \text{ and } 16 \text{ bar}$ and $v_{\text{gas}} = 100 \text{ m}\cdot\text{s}^{-1}$. For constant gas velocity at the nozzle exit, a maximum of the dynamic pressure of the gas phase can be detected for $p_{\text{sys}} = 6 \text{ bar}$ on the spray axis. This maximum could lead to the formation of smaller droplets. For significantly increasing system pressure at $p_{\text{sys}} > 6 \text{ bar}$, the dynamic pressure of the gas phase is decreasing, see Fig. 10. The maximum of the dynamic pressure of the gas phase can be explained by opposite effects:

- With increasing system pressure, the density of the gas phase increases. This leads to increased aerodynamic forces between liquid and gas phase as well as higher dynamic pressure of the gas jet resulting in smaller droplets. According to this, the correlations listed in Table 2 show a decrease of droplet size with increasing system pressure.
- Applying the pressure adapted nozzle design at elevated system pressure an increased deceleration of the atomization jet velocity is detected which is described by Eq. (5). As described previously, the increased deceleration of the gas phase is caused by the reduction of A_{gas} (d_{eq}). As the reduction of the gas phase

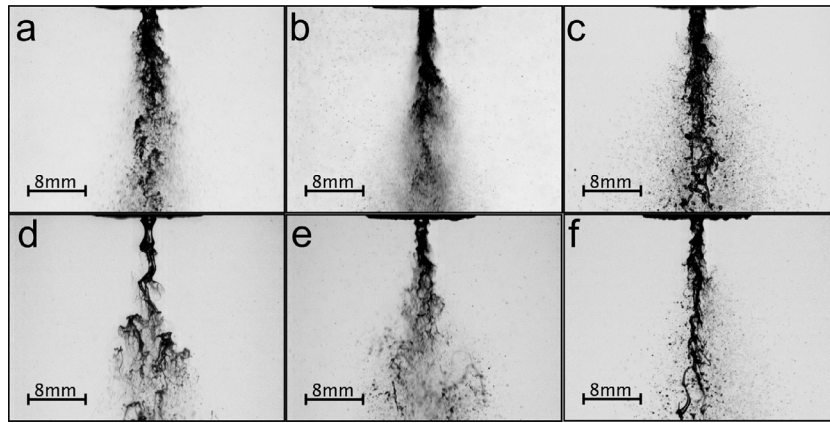


Fig. 9. High-speed camera images of primary jet breakup at $v_{gas} = 100 \text{ m} \cdot \text{s}^{-1}$ for water ($\eta_{liq} = 1 \text{ mPa} \cdot \text{s}$) at a) $p_{sys} = 1 \text{ bar}$, b) $p_{sys} = 6 \text{ bar}$ and c) $p_{sys} = 16 \text{ bar}$ and for the glycerol/water - mixture ($\eta_{liq} = 100 \text{ mPa} \cdot \text{s}$) at d) $p_{sys} = 1 \text{ bar}$, e) $p_{sys} = 6 \text{ bar}$ and f) $p_{sys} = 16 \text{ bar}$.

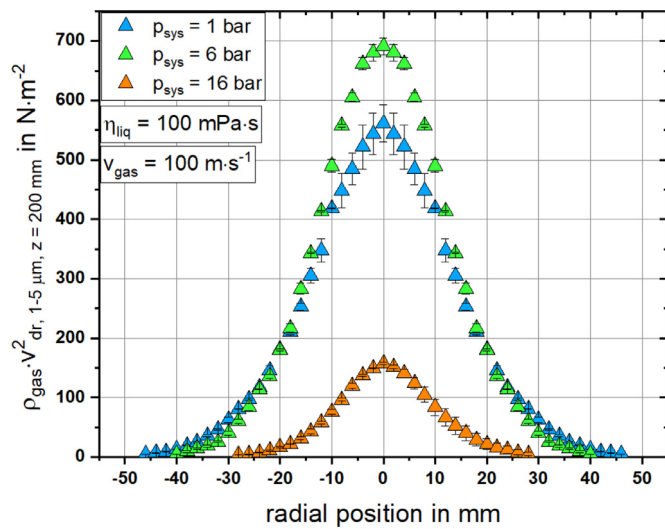


Fig. 10. Influence of system pressure p_{sys} on the radial distribution of dynamic pressure of the gas jet (calculated out of the velocity of droplets with a size of $1 - 5 \mu\text{m}$ at $z = 200 \text{ mm}$) for glycerol/water - mixture ($\eta_{liq} = 100 \text{ mPa} \cdot \text{s}$) and $v_{gas} = 100 \text{ m} \cdot \text{s}^{-1}$.

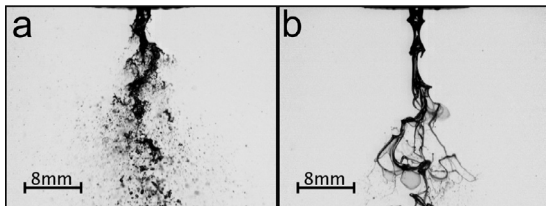


Fig. 11. High-speed camera images of primary jet breakup at $p_{sys} = 1 \text{ bar}$ and $v_{gas} = 60 \text{ m} \cdot \text{s}^{-1}$ for a) water ($\eta_{liq} = 1 \text{ mPa} \cdot \text{s}$) and b) glycerol/water - mixture ($\eta_{liq} = 100 \text{ mPa} \cdot \text{s}$).

velocity along the spray axis (see Fig. 4) shows little effect at $p_{sys} < 6 \text{ bar}$, for $p_{sys} > 6 \text{ bar}$ the reduction of gas phase velocity outside the nozzle affects the dynamic pressure of the gas jet and therefore the primary breakup, leading to a significant increase of droplet size.

Due to the fact, that for the calculation of the dynamic pressure of the gas jet the gas velocity is weighted by the power of 2, whereas gas density is weighted by the power of 1, for the given operating conditions in Fig. 10 the maximum is found at $p_{sys} = 6 \text{ bar}$.

3.3.3. Influence of dynamic viscosity on mass-weighted integral Sauter mean diameter

For increasing dynamic viscosity, bigger droplets were detected independent of system pressure and gas velocity, see Fig. 7. This is also confirmed by high-speed camera images of the primary jet breakup as exemplarily shown for $p_{sys} = 1 \text{ bar}$ and $v_{gas} = 60 \text{ m} \cdot \text{s}^{-1}$ in Fig. 11. For higher system pressure $p_{sys} > 6 \text{ bar}$ and $v_{gas} = 100 \text{ m} \cdot \text{s}^{-1}$, the droplet size increases with a steeper gradient at higher dynamic viscosity, see Fig. 7a and Fig. 7b. This can be explained by enhancing effects of the damping liquid and the low dynamic pressure of the gas jet and is in good accordance to the correlations shown in Table 1.

4. Conclusion

In the present study, the influence of system pressure and liquid viscosity on jet breakup and spray quality (D_{32} , $ID_{32,m}$) for two Newtonian liquids (1 and 100 mPa · s) was investigated. Nozzle geometry was adapted to the system pressure in order to keep all other operating conditions (v_{gas} , GLR , \dot{M}_{gas}) constant, independent of system pressure. Liquid mass flow was kept constant at $20 \text{ kg} \cdot \text{h}^{-1}$ while the gas velocity was varied between 60 and $100 \text{ m} \cdot \text{s}^{-1}$, which resulted in a variation of GLR from 0.6 to 1.0. High-speed camera images were classified according to the breakup regimes defined by Chigier and Faragó (1992) and discussed with regard to local measurements of droplet size. The following conclusions can be drawn:

1. Increasing the gas velocity always led to a decrease in droplet size independent of system pressure and liquid viscosity.
2. Increasing the liquid viscosity always led to an increase in droplet size independent of system pressure and gas velocity.
3. Increasing the system pressure while applying pressure adapted for constant gas velocity leads to a minimum in droplet size:
 - (a) For the given nozzle geometry and operating conditions, the droplet size minimum is detected at 6 bar for $100 \text{ mPa} \cdot \text{s}$, $60 - 100 \text{ m} \cdot \text{s}^{-1}$ and 2 bar for $1 \text{ mPa} \cdot \text{s}$, $60 \text{ m} \cdot \text{s}^{-1}$. A further increase of the system pressure above 6 bar led to an exponential increase of droplet size.
 - (b) High-speed camera images revealed a change in primary jet breakup morphology from fiber type towards a mixture of fiber type and non-axisymmetric Rayleigh type breakup at high system pressures. This effect was observed for both liquid viscosities (1 and $100 \text{ mPa} \cdot \text{s}$) and seems responsible for the trend observed.

- (c) One possible explanation for this effect is the maximum of the dynamic pressure of the gas jet. With higher system pressure, gas density increases, while the smaller gas orifice area due to the pressure adapted nozzles approach indicates an increased deceleration of the gas phase according to the free jet theory. Overlapping of both effects results in an increase of dynamic pressure of the gas phase for low system pressure towards a maximum, followed by a decrease for high system pressure.

Declaration of Competing Interest

The authors declare that they have no known competing financial interests or personal relationships that could have appeared to influence the work reported in this paper.

CRediT authorship contribution statement

Simon Wachter: Conceptualization, Validation, Formal analysis, Investigation, Visualization, Writing - original draft. **Tobias Jakobs:** Conceptualization, Supervision, Writing - review & editing. **Thomas Kolb:** Conceptualization, Supervision, Writing - review & editing.

Acknowledgements

The authors gratefully acknowledge the financial support by the Helmholtz Association of German Research Centers (HGF), within the research program Energy Efficiency, Materials and Resources (EMR). The present work contributes to the Helmholtz Virtual Institute for Gasification Technology - HVIGasTech (VH-VI-429). <http://www.hvigastech.org/>.

Supplementary materials

Supplementary material associated with this article can be found, in the online version, at doi:10.1016/j.ijmultiphaseflow.2019.103189.

References

- Albrecht, H.-E., 2003. *Laser Doppler and Phase Doppler Measurement Techniques*. Springer, Berlin and, New York.
- Aliseda, A., Hopfinger, E.J., Lasheras, J.C., Kremer, D.M., Berchielli, A., Connolly, E.K., 2008. Atomization of viscous and non-Newtonian liquids by a coaxial, high-speed gas jet. Experiments and droplet size modeling. *Int. J. Multiphase Flow* 34 (2), 161–175. doi:10.1016/j.ijmultiphaseflow.2007.09.003.
- Araneo, L., Damaschke, N., Tropea, C., 2002. Measurement and Prediction of the Gaussian Beam Effect in the PDA. Springer 189–208.
- Chigier, N., Faragó, Z., 1992. Morphological classification of disintegration of round liquid jets in a coaxial air stream. *Atom. Sprays* 2 (2), 137–153.
- du Nouÿ, P.L., 1925. An interfacial tensiometer for universal use. *J. Gen. Physiol.* 7 (5), 625.
- Elkott, M., El-Sayed Mahdy, M., Montaser, M., 1982. Investigation of External Mixing Air Blast Atomizers.
- Fleck, S., Santo, U., Hotz, C., Jakobs, T., Eckel, G., Mancini, M., Weber, R., Kolb, T., 2018. Entrained flow gasification part 1: gasification of glycol in an atmospheric-pressure experimental rig. *Fuel* 217, 306–319.
- GFG, S., 1912. Simple viscometer for very viscous liquids. In: *Proceedings of the Cambridge Philosophical Society, Mathematical and Physical Sciences*.
- Gullberg, M., Marklund, M., 2012. Spray characterization of twin fluid external mixing atomization of pyrolysis oil. *Atom. Sprays* 22 (11), 897–919. doi:10.1615/AtomizSpr.2013006240.
- Haidn, O.J., Habiballah, M., 2003. Research on high pressure cryogenic combustion. *Aerosp. Sci. Technol.* 7 (6), 473–491. doi:10.1016/S1270-9638(03)00052-X.
- Hede, P.D., Bach, P., Jensen, A.D., 2008. Two-fluid spray atomisation and pneumatic nozzles for fluid bed coating/agglomeration purposes: a review. *Chem. Eng. Sci.* 63 (14), 3821–3842. doi:10.1016/j.ces.2008.04.014.
- Jakobs, T., 2015. Einfluss des Reaktordrucks auf die Spraygüte Außenmischer Zweistoffdüsen. KIT, Karlsruhe Dissertation.
- Jakobs, T., Djordjevic, N., Fleck, S., Zazalis, N., Kolb, T., 2012. Influence of Ambient Pressure on Twin Fluid Atomization R&D Work for High Pressure Entrained Flow Gasification.
- Jasuja, A.K., 1982. Plain-jet airblast atomization of alternative liquid petroleum fuels under high ambient air pressure conditions. *Am. Soc. Mech. Eng.* (3).
- Kapulla, R., Najera, S.B., 2006. Operation conditions of a phase doppler anemometer: droplet size measurements with laser beam power, photomultiplier voltage, signal gain and signal-to-noise ratio as parameters. *Meas. Sci. Technol.* 17 (1), 221–227. doi:10.1088/0957-0233/17/1/034.
- Kumar, A., Sahu, S., 2018. Liquid jet breakup unsteadiness in a coaxial air-blast atomizer. *International Journal of Spray and Combustion Dynamics* 10 (3), 211–230. doi:10.1177/1756827718760905. 1756827718760905
- Lefebvre, A.H., 1998. *Gas Turbine Combustion*. CRC Press.
- Li, L.K.B., Dressler, D.M., Green, S.I., Davy, M.H., 2009. Experiments on air-blast atomization of viscoelastic liquids, part 1: quiescent conditions. *Atom. Sprays* 19 (2), 157–190.
- Lasheras, J.C., Hopfinger, E.J., 2000. Liquid jet instability and atomization in a coaxial gas stream. *Annu. Rev. Fluid Mech.* 32 (1), 275–308.
- Lorenzetto, G.E., Lefebvre, A.H., 1977. Measurements of drop size on a plain-jet airblast atomizer. *AIAA J.* 15 (7), 1006–1010.
- Marmottant, P., Villermaux, E., 2004. On spray formation. *J. Fluid Mech.* (498) 73–111.
- Massoudi, R., King, A.D., 1974. Effect of pressure on the surface tension of water. adsorption of low molecular weight gases on water at 25.deg. *J. Phys. Chem.* 78 (22), 2262–2266. doi:10.1021/j100615a017.
- Mayer, W., 1994. Coaxial atomization of a round liquid jet in a high speed gas stream: a phenomenological study. *Exp Fluids* 16 (6), 401–410.
- Mezger, T.G., 2006. *The Rheology Handbook: For Users of Rotational and Oscillatory Rheometers*. Vincentz Network GmbH & Co KG.
- Risberg, M., Marklund, M., 2009. Visualization of gas assisted atomization of black liquor and syrup water mixtures at elevated ambient pressures. *Atom. Sprays* 19 (10), 957–967.
- Rizk, N., Lefebvre, A., 1984. Spray characteristics of plain-jet airblast atomizers. *ASME* 634 (106).
- Rizkalla, A., Lefebvre, A.H., 1975. The influence of air and liquid properties on airblast atomization. *J. Fluids Eng.* 97 (3), 316–320.
- Sänger, 2018. *Zerstäubung Hochviskoser Fluide bei Variierendem Systemdruck - Grundlagenforschung zur Hochdruck-Flugstromvergasung*. Karlsruher Institut für Technologie (KIT), Karlsruhe Dissertation.
- Sänger, A., Jakobs, T., Djordjevic, N., Kolb, T., 2015. Experimental investigation on the influence of ambient pressure on twin-fluid atomization of liquids with various viscosities. In: *International Conference for Liquid Atomization and Spray System (ICLASS)*, Tainan, Taiwan, Aug, pp. 23–27.
- Schlichting, H., Gersten, K., Krause, E., 2006. *Grenzschicht-Theorie: Mit 22 Tabellen*, 10., überarbeitete auflage Springer-Verlag, Berlin, Heidelberg doi:10.1007/3-540-32985-4.
- Tropea, C., Yarin, A.L., Foss, J.F., 2007. *Handbook of Experimental Fluid Mechanics*, first ed Springer Berlin Heidelberg.
- Walzel, P., 1990. Zerstäuben von Flüssigkeiten. *Chem. Ing. Tech.* 62 (12), 983–994. doi:10.1002/cite.330621203.
- Xiao, F., Dianat, M., McQuirk, J.J., 2014. Les of turbulent liquid jet primary breakup in turbulent coaxial air flow. *Int. J. Multiphase Flow* 60, 103–118. doi:10.1016/j.ijmultiphaseflow.2013.11.013.
- Zhao, H., Liu, H.-F., Xu, J.-L., Li, W.-F., Cheng, W., 2012. Breakup and atomization of a round coal water slurry jet by an annular air jet. *Chem. Eng. Sci.* 78, 63–74. doi:10.1016/j.ces.2012.05.007.



Towards system pressure scaling of gas assisted coaxial burner nozzles – An empirical model



Simon Wachter^{a,*}, Tobias Jakobs^a, Thomas Kolb^{a,b}

^a Institute for Technical Chemistry, Karlsruhe Institute of Technology, 76344 Eggenstein-Leopoldshafen, Germany

^b Engler-Bunte-Institute, Karlsruhe Institute of Technology, 76131 Karlsruhe, Germany

ARTICLE INFO

Keywords:

Scaling
Nozzle
Pressure
Empirical model
Atomization

ABSTRACT

The present study investigates the influence of system pressure, gas velocity, and annular gas gap width on the resulting droplet size. Three external-mixing twin-fluid atomizers are operated at a constant liquid mass flow. The nozzle geometry is kept similar, except that the annular gas gap width is changed. At every system pressure level (1 – 21 bar), three different gas velocities were investigated by changing the gas mass flow. High-speed camera images are used for observation of primary breakup and discussed with regard to local measurements of droplet size performed by a phase Doppler anemometer. The gas momentum flux as well as the gas momentum flow were applied to describe the atomization process under varying operating conditions. Finally, an empirical model is derived, enabling the system pressure scaling of external-mixing twin-fluid atomizers for the range of gas momentum flow under investigation.

1. Introduction

Spray processes are often utilized in industrial production; however, the influence of process conditions on atomization is not yet fully understood. In particular, limited literature is available on twin-fluid atomization at increased system pressure that is commonly applied in high-pressure entrained flow gasifiers (EFGs). These large-scale energy conversion systems can play a key role in future resource and energy supply. In EFGs, highly viscous liquid or suspension fuels with complex flow behavior (e.g., non-Newtonian) are typically atomized at elevated system pressures (in the range of 40–80 bar) [1]. Oxygen and steam serve as atomization media to guarantee high-quality syngas. Using oxygen as a gasification agent and at the same time as atomization agent, leads to a coupling of process stoichiometry and nozzle operating conditions with respect to the gas-to-liquid mass flow ratio (GLR). Based on the low stoichiometry required for the gasification reaction, the burner nozzle must be operated at $GLR \leq 1$ [2,3]. For the optimization of the atomization process under relevant conditions for EFG and scale-up of burner nozzles, it is essential to gain fundamental knowledge concerning atomization behavior at high system pressures [4].

In this study, the influence of gas velocity, system pressure, and nozzle geometry on spray formation is investigated for varying GLRs, concerning droplet size and jet breakup. The study aims to develop a system pressure scaling approach for external-mixing, twin-fluid atomizers based on gas momentum flow.

Many investigations concerning primary breakup and resulting spray quality in terms of Sauter mean diameter at atmospheric system pressure are reported in the literature by Marmottant and Villermaux [5], Hede et al. [6] and Faragò and Chigier [7] applying coaxial gas-assisted atomizers. A morphological study on primary jet breakup was performed by Faragò and Chigier [7] for water applying different nozzle geometries. As a result, the different breakup regimes were classified with regard to Re_{liq} and We_{aero} , as per Eqs. (1) and (2):

$$Re_{liq} = \frac{D_{liq} \cdot v_{liq} \cdot \rho_{liq}}{\eta_{liq}} \quad (1)$$

$$We_{aero} = \frac{(v_{gas} - v_{liq})^2 \cdot \rho_{gas} \cdot D_{liq}}{\sigma} \quad (2)$$

with liquid jet diameter (D_{liq}), velocity (v), density (ρ), dynamic viscosity (η), and surface tension (σ) as relevant process parameters. The subscripts *gas* and *liq* denote the gas and liquid phases, respectively. For increasing We_{aero} , the primary breakup regimes of a liquid jet change from Rayleigh-type breakup to membrane-type breakup and finally fiber-type breakup. The latter can be divided into the submodes pulsating and superpulsating as described in detail by Faragò and Chigier [7]. The effect of dynamic pressure ratio (in the following called momentum flux ratio) of the gas and liquid phase, according to Eq. (3), was added in a later

* Corresponding author at: Hermann-von-Helmholtz Platz 1, 76344 Eggenstein-Leopoldshafen, Germany.

E-mail address: simon.wachter@kit.edu (S. Wachter).

investigation by Lasheras and Hopfinger [8].

$$j = \frac{j_{\text{gas}}}{j_{\text{liq}}} = \frac{v_{\text{gas}}^2 \cdot \rho_{\text{gas}}}{v_{\text{liq}}^2 \cdot \rho_{\text{liq}}} \quad (3)$$

As the nozzle geometry and gas density were kept constant in the investigations by Lasheras and Hopfinger [8], the results on the primary breakup length and spray angle were assigned only on the basis of the momentum flux ratio, which is therefore only a function of the gas phase velocity. Moreover, the momentum flow ratio as outlined in Eq. (4), is often used for spray characterization [9–12].

$$J = \frac{J_{\text{gas}}}{J_{\text{liq}}} = \frac{v_{\text{gas}}^2 \cdot \rho_{\text{gas}} \cdot A_{\text{gas}}}{v_{\text{liq}}^2 \cdot \rho_{\text{liq}} \cdot A_{\text{liq}}} \quad (4)$$

Typically, investigations of twin-fluid atomization explain the influence of gas velocity on the primary breakup and droplet size distribution by changing the gas mass flow and thereby, the GLR. The increase in gas velocity generally leads to a decrease in droplet size across the entire spray cone [13,14] due to an increase in the aerodynamic forces. The influence of the gas velocity and GLR on the droplet size decreases at $\text{GLR} \gg 1$, as reported by many researchers [15–17].

Several authors have studied the influence of system pressure on the resulting spray with respect to droplet size [18–23]. Reducing the literature overview on publications, which aim for the scaling of twin-fluid atomizers yields the following. Jakobs et al. [24] investigated the influence of the absolute system pressure on the resulting droplet size of a water spray between a $p_{\text{sys}} = 1 - 21$ bar for one nozzle at constant We_{aero} . To achieve a constant aerodynamic Weber number with increasing system pressure (i.e., ρ_{gas}), the gas velocity at the nozzle orifice was reduced. This led to an increase in the droplet size at higher system pressures and constant We_{aero} , and thus to the conclusion that the gas velocity is an essential parameter in the scaling of twin-fluid atomizers. Continuing these experiments, Sanger et al. [25] investigated the influence of system pressures between $p_{\text{sys}} = 1-21$ bar at constant gas velocity and different liquid viscosities ($\eta_{\text{liq}} = 1-400$ mPa·s) by applying one nozzle. Here, with increasing system pressure, the gas mass flow (i.e., GLR) was increased to keep the gas velocity constant. This approach led to a finer spray i.e., decreased droplet size with increase in the system pressure, owing to the increase in the aerodynamic forces. Additionally, for increasing j_{gas} , different dependencies of the resulting droplet size on system pressure and gas velocity were detected at $\eta_{\text{liq}} = 100$ mPa·s. Sanger [26] explained this by the influence of different induced liquid instabilities on the corresponding primary breakup morphology. To investigate the influence of system pressure at constant GLR, gas mass flow, and gas velocity, Wachter et al. [27] performed experiments at $p_{\text{sys}} = 1-16$ bar using pressure adapted twin-fluid atomizers. To increase the system pressure, the annular gap width ($s_{\text{gas}} = 0.35-2.88$ mm) was reduced to achieve constant operating conditions with respect to gas and liquid velocities and mass flows at the nozzle orifice, independent of the system pressure. As a result, for low system pressures ($p_{\text{sys}} < 6$ bar), a slight decrease in droplet size was detected owing to the higher aerodynamic forces. For higher system pressures, a sharp increase in the resulting droplet size was detected. The small gas gap width resulted in a fast deceleration of the gas phase, even close to the nozzle orifice, due to the entrainment of the gas phase. This investigation revealed the significant influence of the gas gap width on the resulting droplet size.

Further qualitative investigations of changes in the gas gap width s_{gas} were performed by Zhao et al. [28] at atmospheric system pressure in the range of $s_{\text{gas}} = 1.9-10$ mm and $j = 0.01-620$ using a high-speed camera. As a result, the authors represented a breakup regime classification depending on a modified momentum flux ratio j_m and aerodynamic Weber number We_m , as shown in Eqs. (5) and (6), below.

$$j_m = \frac{j}{1 + 50 \cdot \frac{A_{\text{liq}}}{A_{\text{gas}}}} \quad (5)$$

$$We_m = \frac{We}{1 + 1.4 \cdot \frac{A_{\text{liq}}}{A_{\text{gas}}}} \quad (6)$$

Leroux et al. [29,30] published research on the scaling of twin-fluid atomizers at atmospheric system pressure. These investigations were categorized into the nozzle nearfield (dense core zone) [29] and nozzle farfield (diluted zone) [30]. Applying several twin-fluid atomizers, the liquid jet diameter was varied between $D_{\text{liq}} = 0.4-2$ mm and the gas gap width between $s_{\text{gas}} = 0.25-3.5$ mm. Investigations of the dense core zone of the liquid jet were performed with a shadowgraph system to determine the breakup regimes as per Lasheras et al. [8] and correlations for the liquid core length and spray angle were derived depending on the momentum flux ratio j . The measurements led to the conclusion that the liquid core length is not a function of the spray regime and decreases with increasing momentum flux ratio. In contrast, the spray angle depends on the spray regime. The angle first increases within the fiber-type pulsating submode, whereas a further increase in j leads to a decrease within the superpulsation submode [29]. Measurements of droplet size distributions in the diluted spray zone were performed with a Phase Doppler Analyzer (PDA) at different axial positions ($z = 14, 42$, and 140 mm) and radially from -20 mm $< x < 20$ mm. As a result, two correlations for the pulsating and superpulsating submodes are presented, leading to the conclusion that the droplet size increases as D_{liq} increases and decreases with higher v_{gas} [30]. An approach considering increased mass flows, for twin-fluid atomizer scaling was not outlined.

As the literature review shows, no scaling approach considering increased system pressure for twin-fluid nozzles has been reported by previous investigations. Furthermore, empirical correlations for the calculation of the resulting droplet size at increased system pressure for variations in the parameters forming J_{gas} have not been derived. In summary as per past research, the gas velocity at the nozzle orifice and the gas orifice area (i.e., the gas gap width) have a distinct influence on the resulting droplet size of twin-fluid atomizers.

Therefore, this work investigates the influence of gas velocity, system pressure, and gas gap width on spray formation. A high-speed camera was used to detect the primary breakup and PDA for measuring the local droplet velocity and size. Three different nozzles with a constant liquid jet diameter but varying gas gap widths were operated at increased system pressure and constant gas velocity. To achieve a constant gas velocity with increasing system pressure, the gas mass flow was increased. Experiments were performed with three different gas velocities at each system pressure level. An empirical model for the calculation of the resulting droplet size at varying system pressure, depending on fitting parameters and gas momentum flow J_{gas} was developed based on the experimental results. This model allows for the system pressure scaling of twin-fluid atomizers in the investigated range of J_{gas} .

2. Experimental setup

As described by Wachter et al. [27], the experimental setup consists of the pressurized atomization test rig (PAT), a PDA and a high-speed camera. Three external-mixing twin-fluid atomizers having identical liquid orifice area, but different gas orifice area (varying gas gap width) were used to atomize water with pressurized air.

A schematic and a horizontal cross-sectional view (A-A) of the PAT spray test rig with an exhaust air system is shown in Fig. 1. The pressure chamber has an internal diameter of 300 mm and a total height of 3000 mm. It is designed for operation at system pressures up to $p_{\text{sys}} = 21$ bar. The external-mixing twin-fluid atomizer is mounted on the axially (z -direction) movable twin-fluid lance, which is fed by one of the two eccentric screw pumps with liquids featuring viscosities up to $\eta_{\text{liq}} = 1000$ mPa·s. The liquid mass flow can be controlled in the range of P1: $\dot{M}_{\text{liq}} = 10-60$ kg·h⁻¹ / P2: $\dot{M}_{\text{liq}} = 60-200$ kg·h⁻¹ using different screw pumps. The liquid mass flow and density were measured using a Coriolis flow meter with an uncertainty of $< 0.5\%$. The com-

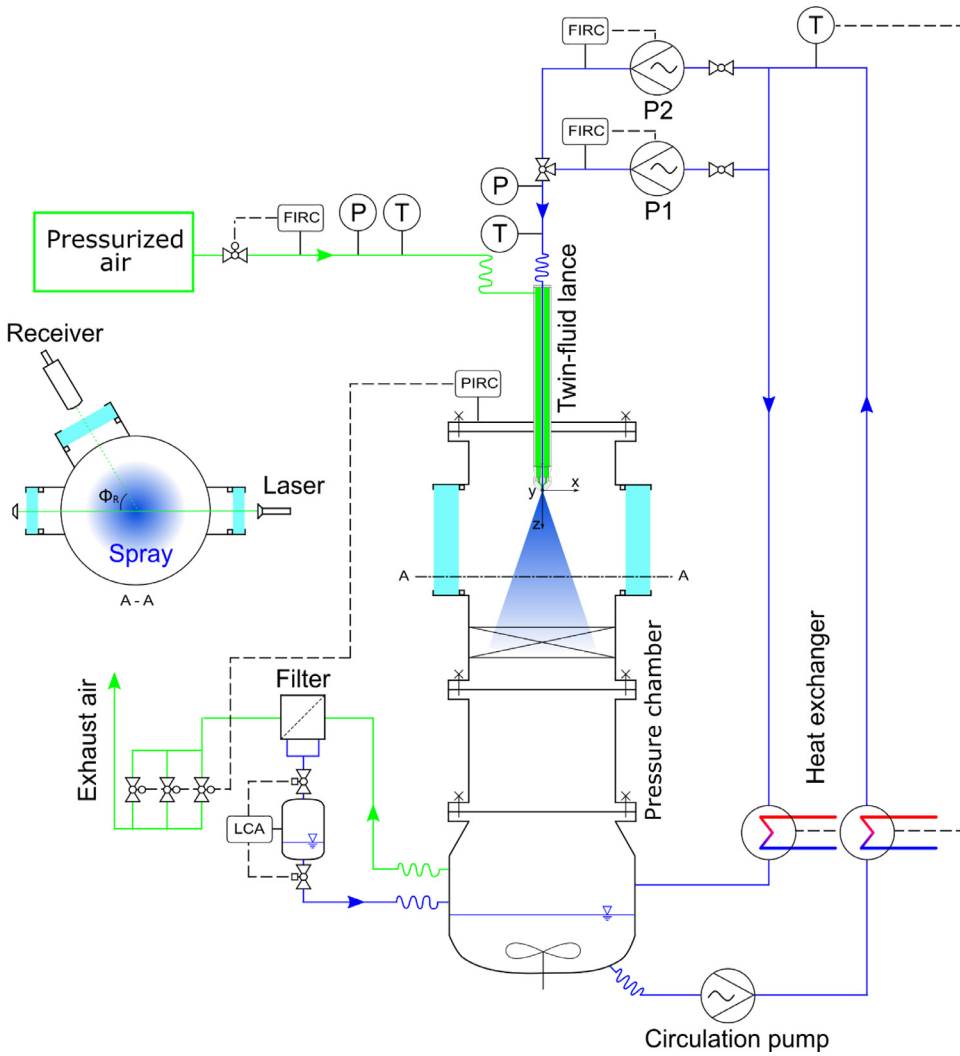


Fig. 1. Schematic of the experimental setup – Pressurized Atomization Test Rig (PAT).

pressed air volume flow V_{gas} was measured by a turbine meter with a measuring range of $V_{\text{gas}} = 0.85\text{--}25 \text{ m}^3\cdot\text{h}^{-1}$ and uncertainty of $< 0.5\%$. A recalculation of the volume to the mass flow was performed using the measured local gas temperature and pressure at the turbine. To ensure well-defined nozzle inlet conditions, the liquid temperature can be adjusted in the range of $T = 10\text{--}50 \text{ }^\circ\text{C}$. The test rig is equipped with three high-quality glass windows that allow for optical access to the spray chamber. Two optical ports are located at $\Phi_R = 0^\circ$ and 70° to enable Phase Doppler measurements in scattering mode with the highest intensity (first-order refraction) [31]. The third optical port is positioned at $\Phi_R = 180^\circ$ to allow for spray investigations in backlight mode with optical measurement system. A flow straightener (honeycomb structure) is located below the measuring plane to avoid influences on the measurement owing to the recirculation of droplets into the region of interest.

All investigations were conducted with 3 external-mixing twin-fluid nozzles, as shown in Fig. 2. The liquid (blue) was supplied through a circular central tube ($D_{\text{liq}} = 2 \text{ mm}$) at the nozzle axis. D_{liq} was kept constant for all nozzles. The liquid jet was surrounded by a coaxial gas stream (green), the width of the gas gap was adjusted between $s_{\text{gas}} = 0.6\text{--}2.0 \text{ mm}$, as listed in Table 1. The nozzle has parallel flow channels in order to avoid disturbance of the liquid jet owing to the gas flow angle and turbulence effects. In addition, the influence of the tube separating the gas and liquid at the nozzle orifice was minimized by reducing the wall thickness b to 0.1 mm . This configuration results in an undisturbed gas flow at the exit of the nozzle [32].

Table 1

Nozzle data (Nozzle 1–3) with similar geometry and varying gas gap widths s_{gas} .

	D_{liq} in mm	s_{gas} in mm	D_{gas} in mm	A_{gas} in mm^2
Nozzle 1	2.00	2.00	6.20	26.42
Nozzle 2	2.00	1.20	4.60	13.02
Nozzle 3	2.00	0.60	3.40	5.25

A high-speed camera for the qualitative observation of the primary breakup of the liquid jet was utilized in the nozzle nearfield. The camera features a frame rate of 3.6 kHz operation at 1024×1024 -pixel resolution and frame rates of up to 500 kHz at reduced resolution. A lens with a focal length of $f_{\text{HG}} = 105 \text{ mm}$ was used to capture primary breakup morphologies. In this study, the frame rate was set to 7.5 kHz at a reduced resolution of 768×640 pixel. Thus, the images have dimensions of $41.4 \times 34.4 \text{ mm}^2$ with a spatial resolution of $54 \text{ } \mu\text{m}\cdot\text{pix}^{-1}$. The images were captured through backlight illumination of the region of interest with a special lighting setup. An array of 9 high-power light-emitting diodes (LEDs) with a total luminous flux of $9 \times 4500 \text{ lm}$ was used. The position of each single LED within the LED array was optimized to achieve the best possible light distribution. Owing to the high intensity and homogeneous distribution of the light, very short exposure times ($t_{\text{Exp}} \sim 7 \text{ } \mu\text{s}$) were employed. This light setup allowed for a sharp representation of droplets even at fast flow conditions. To ensure

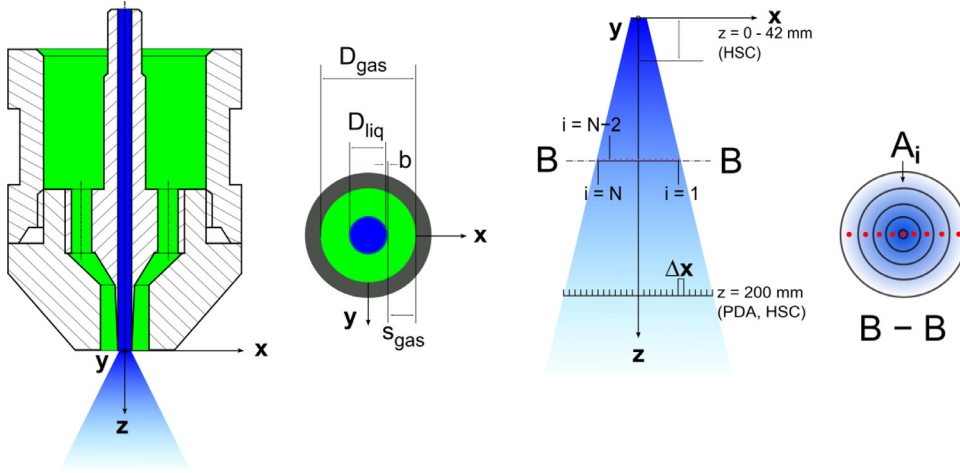


Fig. 2. Scheme of the external-mixing twin-fluid nozzle.

Table 2
Settings of the fiber PDA evaluated by the sensitivity analysis.

Parameters	Values	Unit	Parameters	Values	Unit
Transmitter focal length f_T	1000	mm	Laser wavelength λ_L	561	nm
Receiver focal length f_R	1000	mm	Laser power (transmitter exit)	40	mW
Beam expander ratio E	1	–	Off-axis angle Φ_R	70	°
Receiver slit width (physical) l_S	200	μm	Frequency shift f_Δ	80	MHz

appropriate recording of representative data of the liquid disintegration process, a set of at least 2000 high-speed images was recorded at every operating condition along with a background reference image without liquid flow.

For the observation of single droplets within the spray at $z = 200$ mm from the nozzle orifice, also the high-speed camera was applied. In addition, the same camera was used: (i) to optimize the PDA hardware settings (receiver mask); (ii) for sphericity check of the droplets in the measuring plane to ensure reliable PDA data; (iii) to qualitatively confirm the tendencies measured by the PDA; and (iv) as a validation tool for the PDA data in order to eliminate deviations arising out of the Gaussian beam effect [33]. For the detection of droplets across the entire spray cone, 10 000 images were recorded over the radial measurement area $x = \pm 44$ mm at $z = 200$ mm downstream of the nozzle orifice in the measuring plane. The largest measurement error concerning droplet size was $\Delta d_p < 30$ μm . Because the droplet measurement with the high-speed camera setup was only used for qualitative investigations of large droplets, the accuracy was considered to be adequate. Droplets without detectable contours were rejected from recording.

The droplet size and velocity were measured at a high spatial and temporal resolution within the spray cone using a fiber PDA and SprayExplorer system by Dantec Dynamics. For data collection, the PDA was operated in a forward scattering arrangement and refraction mode (1st order). The receiver was set to off-axis angle of $\Phi_R = 70^\circ$. A slit with a length of $l_S = 200$ μm was used in order to (i) obtain a well-defined detection volume dimension; (ii) ensure high data rates under dense spray conditions; and (iii) to enable flux calculation. To guarantee the detection of large droplets and minimize sizing errors due to the Gaussian beam effect, lenses with a focal length of 1000 mm were used for both transmitter f_T and receiver f_R [33]. In addition, the asymmetric Mask B was chosen for the receiver to eliminate possible measurement errors due to the Gaussian beam effect (trajectory effect). With this optical configuration, the PDA system allows for the detection of water droplets with a minimum size of 1 μm and maximum size of 1357 μm [31]. To improve the PDA instrument settings with respect to small droplets (e.g., data rate and validation rate), the optimum PDA user settings were evaluated in advance by a sensitivity study [34]. The final PDA settings are displayed in Table 2.

To enable drop size measurements at different positions within the spray cone, a receiver and transmitter were mounted on a 3D traverse system, which guarantees spatial reproducibility of < 0.1 mm. Data were obtained by moving the detection volume relative to the nozzle position. The measurements were taken at several radial (traverse along the x-axis) positions with a radial increment of $\Delta x = 2\text{--}4$ mm, depending on the position in the spray. The axial droplet velocity component v_z was measured using the orientation of the coordinate system, as indicated in Fig. 2, and the alignment of the fringes of the laser beam couple ($\lambda_L = 561$ nm – yellow). To ensure a reliable database for every radial position during the PDA measurements, the sample size was set to 50 000 droplets. For the outermost radial measuring position, a sample size of 50 000 droplets was not reached under all operating conditions. Nevertheless, at least 5000 droplets were detected at the boundary of the spray cone, which is still a statistically reliable number [26]. The raw data from the manufacturer software were used to compute the arithmetic mean, statistical data, and additional information (i.e., mass flux and $ID_{32,m}$) using the toolbox *SprayCAT* [26]. For the global characterization of the spray, a global characteristic diameter was computed i.e., a mass-weighted integral Sauter mean diameter ($ID_{32,m}$) including all measurement positions of a radial profile, at a fixed axial position z . The integral Sauter mean diameter $ID_{32,m}$ was calculated according to Eq. (7) and based on the local volume mean diameter $D_{30,i}$ and local surface mean diameter $D_{20,i}$. These diameters were weighted by the local mass flux \dot{m}_i and the annulus area A_i (see Fig. 2), corresponding to the measurement position i along the radial axis $x_1 \leq x_i \leq x_N$ with N measurement positions. The outermost point x_N for each operating condition was set to $x = \pm 44$ mm.

$$ID_{32,m} = \frac{\sum_{i=1}^N D_{30,i}^3 \dot{m}_i A_i}{\sum_{i=1}^N D_{20,i}^2 \dot{m}_i A_i} \quad (7)$$

Further information regarding the computation of the global size distribution and drop size moments can be obtained from DIN SPEC 91,325 [35], and Albrecht [31]. The mass flux \dot{m}_i was calculated from the PDA data according to Albrecht [31], using the *SprayCAT* toolbox. All PDA measurements were conducted at an axial distance of $z = 200$ mm from the nozzle orifice and repeated at least 3 times. For each operating condi-

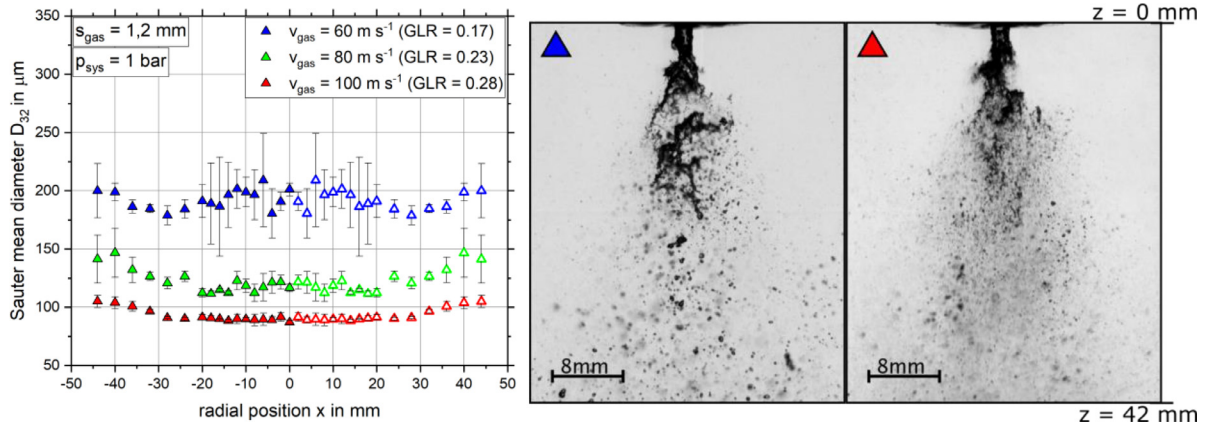


Fig. 3. Radial distribution of the Sauter mean diameter at $z = 200$ mm with $s_{\text{gas}} = 1.2$ mm as a function of the gas velocity at $p_{\text{sys}} = 1$ bar (open symbols denote mirrored positions); High-speed camera images of primary jet breakup at $p_{\text{sys}} = 1$ bar and $v_{\text{gas}} = 60$ m s⁻¹ (left) / $v_{\text{gas}} = 100$ m s⁻¹ (right).

Table 3

Operating conditions of the experiments.

	s_{gas} in mm	s_{gas} in mm	s_{gas} in mm
	2.0	1.2	0.6
	v_{gas} in m s ⁻¹	v_{gas} in m s ⁻¹	v_{gas} in m s ⁻¹
	60 / 80 / 100	60 / 80 / 100	60 / 80 / 100
p_{sys} in bar	\dot{M}_{gas} in kg h ⁻¹	\dot{M}_{gas} in kg h ⁻¹	\dot{M}_{gas} in kg h ⁻¹
1	6.9 / 9.2 / 11.5	3.4 / 4.5 / 5.6	- / - / -
3	20.7 / 27.6 / 34.5	10.2 / 13.5 / 16.8	4.1 / 5.6 / 6.9
6	41.4 / 55.2 / 69.0	20.4 / 27.0 / 33.6	8.2 / 11.1 / 13.8
11	75.9 / 101.2 / -	37.4 / 49.5 / 61.6	15.1 / 20.4 / 25.3
16	- / - / -	54.4 / 72.0 / 89.6	21.9 / 29.6 / 36.8
21	- / - / -	71.4 / 94.5 / -	28.8 / 38.9 / 48.3

tion and nozzle, the rotational symmetry of the spray cone was checked, taking a full radial profile in the first set of experiments. After the rotational symmetry was proven, the following repetition measurements were performed taking half-profiles from the spray edge to the center at $x = 0$ mm. The results of these sets of experiments were then mirrored to obtain full profiles. Therefore, the following figures show all radial Sauter mean diameter distributions as mirrored profiles at $x = 0$ mm, while the plotted and mirrored data points are shown as open symbols.

3. Results and discussion

In order to investigate the influence of (i) gas velocity v_{gas} , (ii) system pressure p_{sys} and (iii) gas gap width s_{gas} on primary breakup and resulting droplet size at a constant liquid mass flow of $\dot{M}_{\text{liq}} = 20$ kg h⁻¹, the three nozzles described in Table 1 were subjected to three different gas velocities and six different system pressures. The operating conditions for all the measurements are presented in Table 3. In all experiments, pressurized air at $T = 20$ °C was used as atomization agent. The supplied water was maintained at $T = 20$ °C. All PDA measurements were performed at an axial distance of $z = 200$ mm downstream of the nozzle exit. The dashed operation points in Table 3 indicate a spray beyond the scope of the PDA measuring system because of the detectable droplet size being out of range and shading effects.

(i) Influence of gas velocity on Sauter mean diameter at constant system pressure and gas gap width

In this section, the results regarding the influence of the gas velocity on the local Sauter mean diameter profiles at constant system pressure and gas gap width are discussed. The gas velocity was changed by varying the gas mass flow (i.e., GLR). The results for the nozzle with a slit

width of $s_{\text{gas}} = 1.2$ mm at a $p_{\text{sys}} = 1$ bar are shown in Fig. 3 (left). Furthermore, high-speed camera images of primary jet breakup under these operating conditions are presented in Fig. 3 (right) for $v_{\text{gas}} = 60$ m s⁻¹ and $v_{\text{gas}} = 100$ m s⁻¹.

The PDA data in Fig. 3 show that an increase in the gas velocity (i.e., GLR) leads to a decrease in the Sauter mean diameter. This is in accordance with the findings reported in the literature [15,36]. This tendency is identified for each system pressure and all the nozzles under investigation. This can be explained by an increase in the aerodynamic force of the gas phase (with increasing gas velocity, i.e., GLR), leading to improved disintegration of the liquid jet and liquid fragments. For the maximum gas velocity of $v_{\text{gas}} = 100$ m s⁻¹, the produced spray is homogeneous (see high-speed camera image in Fig. 3 (right)), which corresponds to the measured radial profile with small standard deviations. Larger Sauter mean diameters were detected at the spray boundary due to smaller aerodynamic forces in this area. For a low gas velocity ($v_{\text{gas}} = 60$ m s⁻¹), larger fragments even farther downstream from the nozzle orifice were detected. This results in a radial D_{32} -profile with a higher standard deviation (see Fig. 3 (left)). The effect of gas velocity on the Sauter mean diameter decreases with increasing system pressure, owing to the already significantly high aerodynamic forces at increased system pressure, as discussed in the following section.

(ii) Influence of system pressure on Sauter mean diameter at constant gas velocity and gas gap width

This section focuses on the influence of system pressure (i.e., gas density) on the local Sauter mean diameter profiles at constant gas velocity and gas gap width. The change in system pressure at constant gas velocity for constant nozzle geometry leads to an increase in the gas mass flow (i.e., GLR) owing to the higher gas density. The results of the nozzle with a slit width of $s_{\text{gas}} = 1.2$ mm at $v_{\text{gas}} = 60$ m s⁻¹ are shown in Fig. 4 (left). In addition, high-speed camera images of primary jet breakup under these operating conditions are presented in Fig. 4 (right) for $p_{\text{sys}} = 1$ bar and $p_{\text{sys}} = 21$ bar.

An increase in the system pressure at constant gas velocity results in an increase in the GLR. For $s_{\text{gas}} \geq 1.2$ mm and $v_{\text{gas}} = 60$ – 100 m s⁻¹, the increase in the system pressure results in smaller Sauter mean diameters for all radial positions and a more homogeneous spray without larger droplet size deviations. The system pressure dependency of the Sauter mean diameter decreases with increasing system pressure until $p_{\text{sys}} = 11$ bar ($s_{\text{gas}} = 1.2$ mm), which can be seen in Fig. 4 and is consistent with findings reported in the literature [9,18,26]. This dependency can also be determined for $s_{\text{gas}} = 0.6$ mm at $v_{\text{gas}} = 80$ – 100 m s⁻¹ and $s_{\text{gas}} = 2$ mm at $v_{\text{gas}} = 60$ – 100 m s⁻¹.

High-speed camera images confirm these measurements, as shown in Fig. 4. Both operating conditions are in the fiber-type breakup mode,

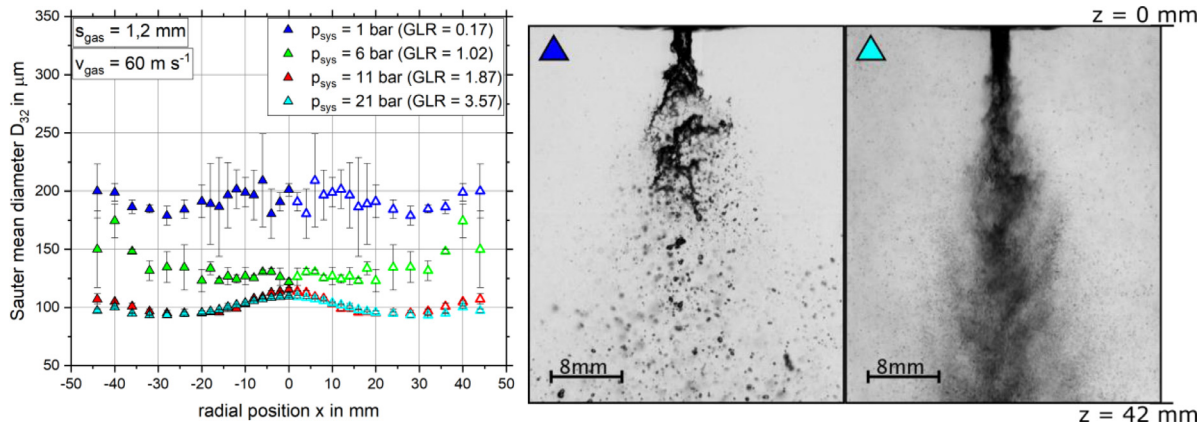


Fig. 4. Radial distribution of the Sauter mean diameter at $z = 200 \text{ mm}$ with $s_{\text{gas}} = 1.2 \text{ mm}$ as a function of the system pressure at $v_{\text{gas}} = 60 \text{ m s}^{-1}$ (the open symbols denote the mirrored positions); High-speed camera images of the primary jet breakup at $v_{\text{gas}} = 60 \text{ m s}^{-1}$ and $p_{\text{sys}} = 1 \text{ bar}$ (left) / $p_{\text{sys}} = 21 \text{ bar}$ (right).

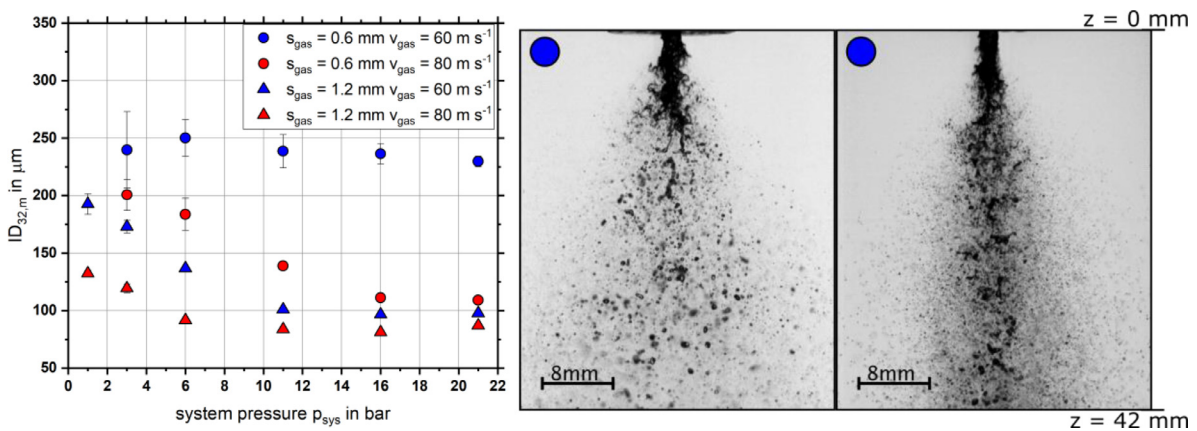


Fig. 5. Mass-weighted integral Sauter mean diameter at $z = 200 \text{ mm}$ with $s_{\text{gas}} = 1.2 \text{ mm}$ and $s_{\text{gas}} = 0.6 \text{ mm}$ as a function of the system pressure for $v_{\text{gas}} = 60 \text{ m s}^{-1}$ and $v_{\text{gas}} = 80 \text{ m s}^{-1}$; High-speed camera images of the primary jet breakup applying $s_{\text{gas}} = 0.6 \text{ mm}$ and $v_{\text{gas}} = 60 \text{ m s}^{-1}$ at $p_{\text{sys}} = 3 \text{ bar}$ (left) and $p_{\text{sys}} = 21 \text{ bar}$ (right).

according to [7]. Here, the disintegration at increased system pressure leads to the formation of a homogeneous spray with an increased droplet number density. This is caused, due to the higher aerodynamic forces and increased gas mass flow (i.e., GLR).

For $s_{\text{gas}} = 0.6 \text{ mm}$ and $v_{\text{gas}} = 60 \text{ m s}^{-1}$, only a negligible influence of the system pressure on the resulting Sauter mean diameter was observed between the $p_{\text{sys}} = 3\text{--}21 \text{ bar}$ (Fig. 5 (left)). To gain a deeper insight, Fig. 5 (right) shows the corresponding high-speed camera images at $p_{\text{sys}} = 3 \text{ bar}$ and $p_{\text{sys}} = 21 \text{ bar}$, which both reveal a fiber-type breakup. As illustrated, at increased system pressure the formation of tiny droplets, at the boundary of the spray cone, out of the fibers improves. After the primary breakup, the gas velocity is decelerated owing to the entrainment of the surrounding gas phase, inhibiting further breakup via secondary atomization. Therefore, large droplets are detected by the PDA, leading to an almost constant Sauter mean diameter and only a slight reduction with increasing system pressure for the nozzle with $s_{\text{gas}} = 0.6 \text{ mm}$ and $v_{\text{gas}} = 60 \text{ m s}^{-1}$.

The influence of system pressure on the droplet size for different gas gap widths shows that with increasing s_{gas} , the plateau of the Sauter mean diameters is reached at lower system pressures.

One explanation of this finding can be given by the theory of a gas-free jet. A free jet can be described as a shear flow into free space, where the gas jet is in contact with quiescent air. Owing to the velocity gradient, surrounding gas entrains the emerging jet, whereby the moving mass increases in conjunction with a decrease in velocity, while the overall momentum is conserved [37].

Here, a decrease in the gas orifice area (i.e., s_{gas}) leads to lower values of the gas velocity at the same distance to the nozzle orifice. This deceleration in the gas velocity can be explained by the entrainment of ambient gas into the atomization gas jet emerging from the nozzle, according to the free jet theory. This effect was studied in detail for similar atomizers at various s_{gas} values by Wachter et al. [27]. Additionally, the gas mass flow (i.e., GLR) is increased for wider gas gaps to keep the gas velocity constant, enhancing the previously discussed effect.

(iii) Influence of gas gap width on Sauter mean diameter at constant gas velocity and system pressure

In this section, the influence of the gas gap width on the local Sauter mean diameter profiles at constant gas velocity and system pressure is discussed. Increasing the gas gap width at constant gas velocity results in an increase in the gas mass flow (i.e., GLR) owing to the larger gas orifice area. The results of all three nozzles ($s_{\text{gas}} = 0.6 / 1.2 / 2.0 \text{ mm}$) for $v_{\text{gas}} = 80 \text{ m s}^{-1}$ and $p_{\text{sys}} = 3 \text{ bar}$ are shown in Fig. 6. In addition, high-speed camera images are also presented in Fig. 6 for $s_{\text{gas}} = 0.6 \text{ mm}$ (left) and $s_{\text{gas}} = 2.0 \text{ mm}$ (right).

As illustrated in Fig. 6 for $p_{\text{sys}} = 3 \text{ bar}$ and $v_{\text{gas}} = 80 \text{ m s}^{-1}$, an increase in the gas gap width (i.e., GLR) at a constant gas velocity and system pressure leads to a decrease in the Sauter mean diameter. A similar dependency was detected under all operating conditions investigated in this study. This can be explained by two effects: (i) for wider gas gaps, the gas phase emerging from the nozzle remains at a higher velocity over a longer distance from the nozzle orifice in accordance with the

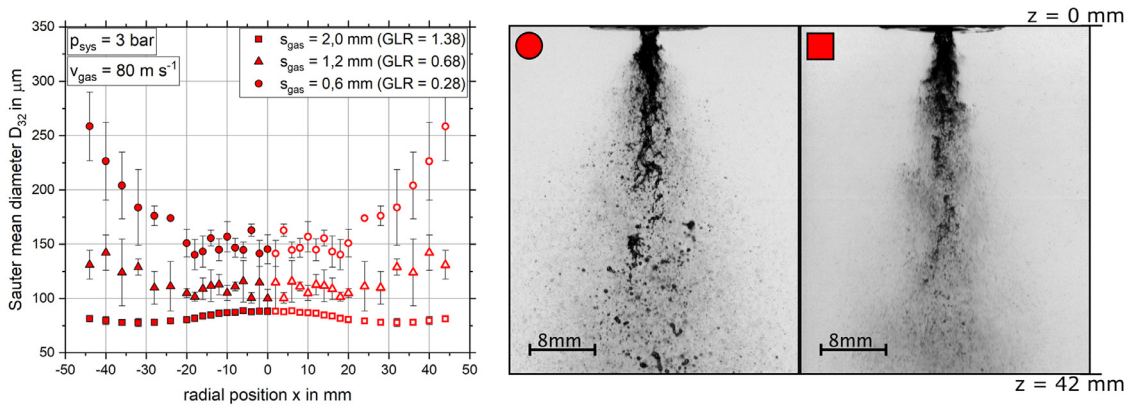


Fig. 6. Radial distribution of the Sauter mean diameter at $z = 200 \text{ mm}$ as a function of the gas gap width at $p_{\text{sys}} = 3 \text{ bar}$ and $v_{\text{gas}} = 80 \text{ m s}^{-1}$ (open symbols denote mirrored positions); High-speed camera images of the primary jet breakup at $p_{\text{sys}} = 3 \text{ bar}$ and $v_{\text{gas}} = 80 \text{ m s}^{-1}$ applying $s_{\text{gas}} = 0.6 \text{ mm}$ (left) and $s_{\text{gas}} = 2.0 \text{ mm}$ (right).

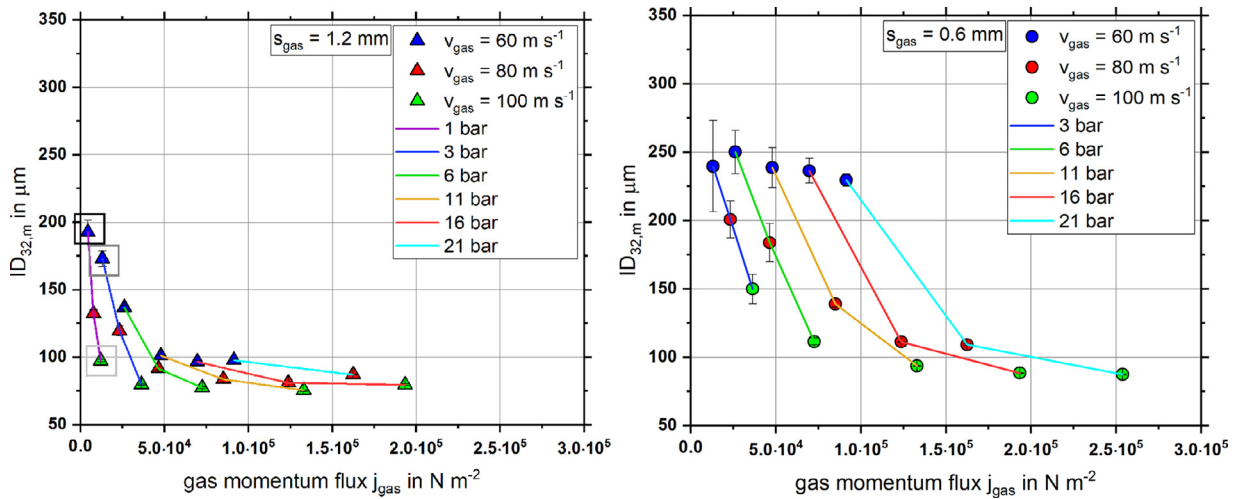


Fig. 7. Mass-weighted integral Sauter mean diameter at $z = 200 \text{ mm}$ as a function of gas momentum flux j_{gas} for different gas velocities and system pressures, applying $s_{\text{gas}} = 1.2 \text{ mm}$ (left) and $s_{\text{gas}} = 0.6 \text{ mm}$ (right).

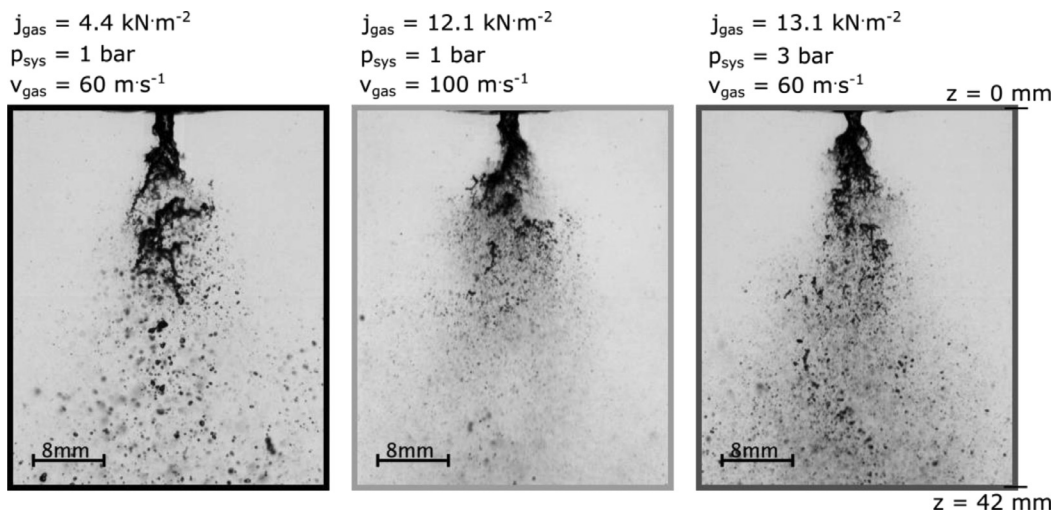


Fig. 8. High-speed camera images of the primary jet breakup applying $s_{\text{gas}} = 1.2 \text{ mm}$ at $p_{\text{sys}} = 1 \text{ bar}$ and $v_{\text{gas}} = 60 \text{ m s}^{-1}$ (left), $p_{\text{sys}} = 1 \text{ bar}$ and $v_{\text{gas}} = 100 \text{ m s}^{-1}$ (middle) and $p_{\text{sys}} = 3 \text{ bar}$ and $v_{\text{gas}} = 60 \text{ m s}^{-1}$ (right).

free-jet theory; (ii) a higher gas mass flow leads to a higher aerodynamic force being available for the disintegration of the liquid jet. The discussed dependency is qualitatively proven by the high-speed camera images presented in Fig. 6 (right). The high deviations in the local Sauter mean diameter at $s_{\text{gas}} = 0.6$ mm can be explained by comparably large droplets across the entire spray cone. In contrast, the small deviations in the local Sauter mean diameter for $s_{\text{gas}} = 2.0$ mm can be explained by the homogeneity of the spray. As seen in the high-speed camera image for $s_{\text{gas}} = 2.0$ mm, no large liquid fragments remain in the spray, leaving the detection area at $z = 42$ mm. This is consistent with the results of Zhao et al. [28], where a morphological study of the primary breakup was presented, showing that an increase in the gas orifice area A_{gas} leads to a fiber-type breakup with small droplets and a more homogeneous spray.

In the literature, the momentum flux ratio j or the corresponding aerodynamic Weber number We_{aero} were used: (i) to scale nozzles within the investigated limits [29]; (ii) to describe the spray morphology [38]; or (iii) to explain the Sauter mean diameter dependencies [39]. The effect of the gas momentum flux on resulting $ID_{32,m}$ is discussed in the next section.

(iv) Dependence of integral Sauter mean diameter on the gas momentum flux j_{gas}

In order to compare the influence of gas velocity and system pressure on the integral, mass-weighted Sauter mean diameter for a distinct gas gap width, the gas momentum flux (i.e., We_{aero}) was used. The results of two different gas gap widths ($s_{\text{gas}} = 1.2$ mm, left and $s_{\text{gas}} = 0.6$ mm, right) at $v_{\text{gas}} = 60\text{--}100$ m·s⁻¹ and $p_{\text{sys}} = 1\text{--}21$ bar are shown in Fig. 7. Here, each system pressure is represented by a specific colored line, whereas the same colored symbols represent a specific gas velocity.

With increasing gas momentum flux j_{gas} , the droplet size decreases for both the constant system pressure and constant gas velocity. This effect was observed for all gas gap widths, except for $s_{\text{gas}} = 0.6$ mm at $v_{\text{gas}} = 60$ m·s⁻¹. For a gas gap width of $s_{\text{gas}} = 1.2$ mm in Fig. 7 (left), the gas velocity at the nozzle orifice exhibits a greater influence on the droplet size compared to the system pressure. With increasing system pressure, the dependency of gas velocity decreases significantly, leading to a plateau in the droplet size for $j_{\text{gas}} > 5 \times 10^4$ N·m⁻². In contrast, for lower gas gap widths ($s_{\text{gas}} = 0.6$ mm), the influence of gas velocity on droplet size is even higher at increased system pressure and gas momentum flux.

Additionally, the influence of the gas velocity or system pressure on the droplet size can be discussed when changing the gas momentum flux by a fixed value [26]. As an example, Fig. 8 (left) shows the high-speed camera images of primary breakup with the gas momentum flux $j_{\text{gas}} = 4.3$ kN·m⁻² under the conditions, $s_{\text{gas}} = 1.2$ mm, $p_{\text{sys}} = 1$ bar, and $v_{\text{gas}} = 60$ m·s⁻¹. When the gas momentum flux is increased by $\Delta j_{\text{gas}} \approx 8$ kN·m⁻², different results are detected, using the system pressure or gas velocity for the increment of j_{gas} . The primary breakup of Fig. 8 (middle) results from changing the momentum flux by a variation in the gas velocity from $v_{\text{gas}} = 60$ m·s⁻¹ to $v_{\text{gas}} = 100$ m·s⁻¹. In contrast, Fig. 8 (right) shows the primary breakup for the same gas momentum flux difference applied by a variation in system pressure from $p_{\text{sys}} = 1$ bar to $p_{\text{sys}} = 3$ bar. Comparing the results owing to variation in the gas velocity, and variation in system pressure, a difference in the spray characteristics can be seen from the high-speed camera images and is confirmed by the data plotted in Fig. 7 (left) (see gray colored frames in the diagram and corresponding high-speed camera images). The spray, resulting from the variation of j_{gas} through changes in gas velocity, is more homogeneous and results in smaller droplets. In contrast, the variation through changes in system pressure led to a slight reduction in droplet size, and several larger droplets remaining after completion of the primary atomization process.

(v) Dependence of integral Sauter mean diameter on the gas momentum flow J_{gas} and scaling approach

Table 4

Resulting parameters A, B and C as a function of the system pressure for $p_{\text{sys}} = 3, 11$ and 21 bar.

p_{sys} in bar	A(p_{sys}) in μm	B in N	C(p_{sys}) in μm
3	250	0.19	70
11	600	0.19	80
21	1500	0.19	90

Finally, the gas momentum flow J_{gas} is applied to interpret the experimental results as this variable includes all the investigated parameters (A_{gas} , v_{gas} , and ρ_{gas}). Fig. 9 (left) shows the results of $ID_{32,m}$ at different system pressures, $p_{\text{sys}} = 3, 11,$ and 21 bar, considering all gas gap widths under investigation $s_{\text{gas}} = 0.6$ mm ● / 1.2 mm ▲ / 2.0 mm ■ and gas velocities at the nozzle orifice $v_{\text{gas}} = 60 / 80 / 100$ m·s⁻¹.

With increasing gas momentum flow J_{gas} at a constant system pressure, a decrease in the droplet size was observed owing to increase in the gas velocity and/or an increase in the gas gap width. Increments in system pressure at a constant gas momentum flow lead to an increase in droplet size because of a shift in either the gas gap width or gas velocity towards smaller values. For large gas momentum flows, the $ID_{32,m}$ FIT-curves exhibit a plateau at all system pressures, indicating that a further increase in the gas momentum flow causes only minor changes in the droplet size. At high GLR values (GLR $\gg 1$), the same effect was observed by several authors at atmospheric system pressure [15–17].

With the objective of pressure scaling for external-mixing twin-fluid atomizers and considering the importance of the influence of gas momentum flow on Sauter mean diameter, an empirical model was derived to explain the droplet size behavior. The potential fit was chosen considering the shape of the plot of Sauter mean diameter results plotted as a function of the gas momentum flow (see Fig. 9 (left)). Eq. (8) shows the empirical model, which describes $ID_{32,m}$ as a function of system pressure and gas momentum flow.

$$ID_{32,m} = A(p_{\text{sys}}) \cdot e^{-\frac{J_{\text{gas}}}{B}} + C(p_{\text{sys}}) \quad (8)$$

For different system pressures, a constant variable B and two pressure-dependent parameters A and C were applied and correlated using a least-square method. The parameters for the pressure steps (as shown in Fig. 9) are listed in Table 4.

Based on the fact, that the parameters A and C are dependent on system pressure, Eqs. (9) and (10) are obtained.

$$A(p_{\text{sys}}) = 3.0 \cdot p_{\text{sys}}^2 + 220 \quad (9)$$

$$C(p_{\text{sys}}) = 1.1 \cdot p_{\text{sys}} + 67 \quad (10)$$

In order to demonstrate the accuracy of the model, a parity plot showing the measured versus calculated $ID_{32,m}$ values is shown in Fig. 9 (right). Across all measurement conditions, the parity plot shows good agreement between the calculated $ID_{32,m}$ and the measured values. The maximum deviation of 12.7% was observed for $p_{\text{sys}} = 3$ bar, $v_{\text{gas}} = 100$ m·s⁻¹ and $s_{\text{gas}} = 1.2$ mm, leading to a difference of $\Delta ID_{32,m} = 11$ μm .

To evaluate this model with respect to the calculated integral Sauter mean diameters against different system pressures, the measurements of droplet size at $p_{\text{sys}} = 6$ and 16 bar (as shown in Fig. 10 as a function of the gas momentum flow and plotted as dots) were used as assessment criteria. The curves representing the model approach (see Eqs. (8), (9), and (10)) for the respective system pressures are plotted as lines. For all of the assessment criteria, the deviation is below 12% except for the point at $p_{\text{sys}} = 6$ bar and $J_{\text{gas}} = 0.69$ N, where the deviation is $\Delta ID_{32,m} = 18$ μm , which equals 22%.

The evaluation of the model for $p_{\text{sys}} = 6$ and 16 bar showed that the deviation between the calculated and measured $ID_{32,m}$ values is small and generally within the accuracy at low J_{gas} . As a result, the applica-

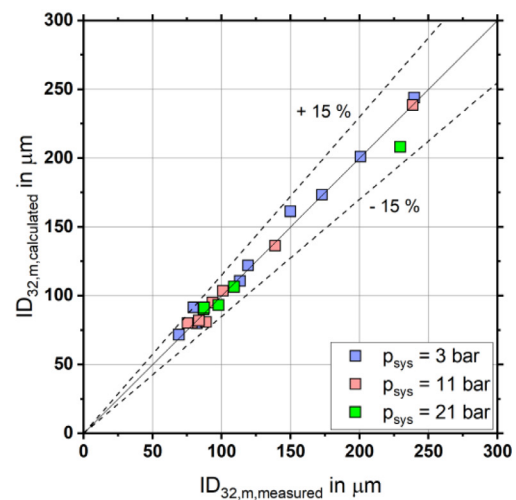
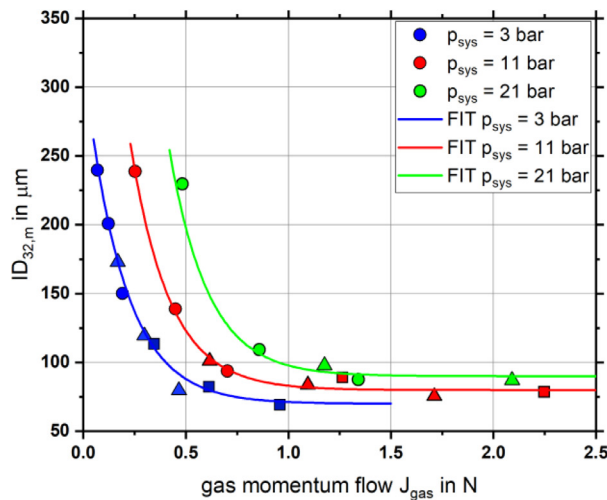


Fig. 9. Mass-weighted integral Sauter mean diameter at $z = 200$ mm as a function of gas momentum flow J_{gas} for different system pressures, applying different gas gap widths ($s_{\text{gas}} = 0.6\text{--}2.0$ mm) and gas velocities ($v_{\text{gas}} = 60\text{--}100$ m s $^{-1}$). As lines, an empirical model is presented for different system pressures (left). Parity plot comparing the calculated $ID_{32,m}$ via an empirical model with the measured $ID_{32,m}$ (right).

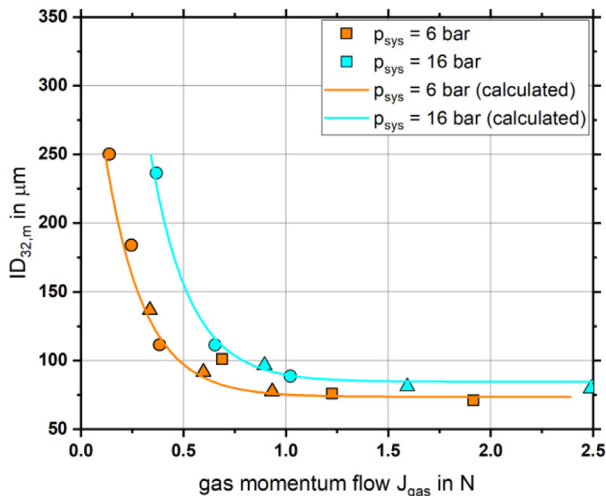


Fig. 10. Mass-weighted integral Sauter mean diameter at $z = 200$ mm as a function of the gas momentum flow J_{gas} for different system pressures, applying different gas gap widths ($s_{\text{gas}} = 0.6\text{--}2.0$ mm) and gas velocities ($v_{\text{gas}} = 60\text{--}100$ m s $^{-1}$). The lines indicate the results of the empirical model for system pressures $p_{\text{sys}} = 6$ bar and 16 bar.

bility of the model for system pressures between $p_{\text{sys}} = 1\text{--}21$ bar and $J_{\text{gas}} = 0.07\text{--}2.5$ N is proven for $\dot{M}_{\text{liq}} = 20$ kg h $^{-1}$.

Extrapolations of the model approach towards higher system pressures, as commonly applied in EFG (i.e., $p_{\text{sys}} = 40$ or 80 bar), allow for an estimation of the expected droplet size.

Conversely, to achieve a specific droplet size, the nozzle gas orifice area and the required operating conditions can be calculated as follows: (i) for a requested $ID_{32,m}$ value and a given system pressure, the necessary gas momentum flow is calculated by means of the empirical correlation (see Eq. (8)); (ii) with a required GLR for the demanded process conditions, the related gas velocity, and thereby, the gas gap width for the twin-fluid atomizer is obtained.

4. Conclusion

This study investigated the influence of system pressure, gas velocity, and gas gap width on spray quality (D_{32} , $ID_{32,m}$) for twin-fluid atomizers operated at liquid mass flow of $\dot{M}_{\text{liq}} = 20$ kg h $^{-1}$. The nozzle geometry

was kept similar, except that the gas gap width was changed. At every system pressure level between $p_{\text{sys}} = 1\text{--}21$ bar, three different gas velocities ($v_{\text{gas}} = 60 / 80 / 100$ m s $^{-1}$) were investigated by changing the gas mass flow (i.e., GLR). High-speed camera images were used to observe the primary breakup, and to explain local measurements of droplet size performed by a phase Doppler anemometer. Thereafter, the gas momentum flux as well as the gas momentum flow were applied to describe the atomization process. Finally, an empirical model was derived, enabling the system pressure scaling of twin-fluid atomizers for the range of gas momentum flow under investigation. The results of the experiments can be summarized as follows:

- Increasing the gas velocity leads to a decrease in the droplet size at a constant system pressure and gas gap width.
- Increasing the system pressure leads to a decrease in the droplet size at constant gas velocity and gas gap width. This effect was observed under all operating conditions except for the smallest gas gap width and low gas velocity. The droplet size was nearly constant with increase in the system pressure at smallest gas gap width and low gas velocity.
- Increasing the gas gap width leads to a decrease in the droplet size at constant gas velocity and system pressure.
- A distinct change in the gas momentum flux via either changes in the gas velocity or system pressure leads to different results in spray quality ($ID_{32,m}$). This indicates that the gas momentum flux alone is not sufficient for describing the spray quality at varying system pressures.
- By using the gas momentum flow for the characterization of atomization behavior, an empirical model was derived, which enables system pressure scaling across the investigated range of the gas momentum flow.

Declaration of Competing Interests

The authors declare that they have no known competing financial interests or personal relationships that could have appeared to influence the work reported in this paper.

Acknowledgments

The authors gratefully acknowledge the financial support of the Helmholtz Association of German Research Centers (HGF) in the context of the research program, Energy Efficiency, Materials and Re-

sources (EMR). The present work contributes to the Helmholtz Virtual Institute for Gasification Technology (VH-VI-429). <http://www.hvigestech.org/>.

References

- [1] Higman C, van der Burgt M. Gasification. Amsterdam, Boston: Gulf Professional Pub/Elsevier Science; 2008.
- [2] Giuffrida A, Romano MC, Lozza G. Thermodynamic analysis of air-blown gasification for IGCC applications. *Appl Energy* 2011;88(11):3949–58.
- [3] Fleck S, Santo U, Hotz C, et al. Entrained flow gasification Part 1: gasification of glycol in an atmospheric-pressure experimental rig. *Fuel* 2018;217:306–19.
- [4] Carisson P, Gebart R, Grönberg C, et al. Spatially resolved measurements of gas composition in a pressurised black liquor gasifier. *Environ Prog Sustain Energy* 2009;28(3):316–23.
- [5] Marmottant P, Villermaux E. On spray formation. *J. Fluid Mech.* 2004;498:73–111.
- [6] Hede PD, Bach P, Jensen AD. Two-fluid spray atomization and pneumatic nozzles for fluid bed coating/agglomeration purposes: a review. *Chem Eng Sci* 2008;63:3821–42.
- [7] Chigier N, Faragó Z. Morphological classification of disintegration of round liquid jets in a coaxial air stream. *Atomization Sprays* 1992;2(2):137–53.
- [8] Lasheras JC, Hopfinger EJ. Liquid jet instability and atomization in a coaxial gas stream. *Annu Rev Fluid Mech* 2000;32(1):275–308.
- [9] Rizk NK, Lefebvre AH. Spray characteristics of plain-jet airblast atomizers. *ASME* 1984;634(106).
- [10] Xiao F, Dianat M, McQuirk JJ. LES of turbulent liquid jet primary breakup in turbulent coaxial air flow. *Int J Multiphase Flow* 2014;60:103–18.
- [11] Engelbert C, Hardalupas Y, Whitelaw JH. Breakup phenomena in coaxial airblast atomizers. *Proc R Soc Lond Series A: Math Phys Sci* 1997;451(1941):189–229.
- [12] Xia Y, Alshehhi M, Hardalupas Y, et al. Spray characteristics of free air-on-water impinging jets. *Int J Multiphase Flow* 2018;100:86–103.
- [13] Hardalupas Y, Whitelaw JH. Characteristics of sprays produced by coaxial airblast atomizers. *J Propulsion Power* 1994;10(4):453–60.
- [14] H. Lohner, C. Czisch, and U. Fritsching, “Impact of the gas nozzle arrangement on the flow field of a twin fluid atomizer with external mixing,”
- [15] Lefebvre AH. Twin-Fluid atomization Factors influencing mean drop size. *Atomization Sprays* 1992;2:101–19.
- [16] Liu H-F, Li W-F, Gong X, et al. Effect of liquid jet diameter on performance of coaxial two-fluid airblast atomizers. *Chem Eng Process* 2006;45:240–5.
- [17] Kim KY, Marshall WR Jr. Drop-Size Distributions from pneumatic atomizers. *AIChE J* 1971;17(3).
- [18] T.U. Yu and J.M. Beér, “Secondary Atomization of coal-water fuel at elevated pressure, 1988”.
- [19] Jasuja AK. Plain-jet airblast atomization of alternative liquid petroleum fuels under high ambient air pressure conditions. *Am Soc Mech Eng* 1982(3).
- [20] Smith CF, Sojka PE, Lefebvre AH. Plain-Jet airblast atomization of coal-water slurry fuels. Warrendale, PA: SAE International; 1985.
- [21] Mayer WOH. Coaxial atomization of a round liquid jet in a high speed gas stream: a phenomenological study. *Exp Fluids* 1994;16(6):401–10.
- [22] Gullberg M, Marklund M. Spray characterization of twin fluid external mixing atomization of pyrolysis oil. *Atomization Sprays* 2012;22(11):897–919.
- [23] Risberg M, Marklund M. Visualizations of gas-assisted atomization of black liquor and syrup/water mixtures at elevated ambient pressures. *Atomization Sprays* 2009:957–67.
- [24] Jakobs T, Djordjevic N, Sängler A, et al. Influence of reactor pressure on twin-fluid atomization: basic investigations on burner design for high-pressure entrained flow gasifier. *Atomization Sprays* 2015;25(12):1081–105.
- [25] Sängler A, Jakobs T, Djordjevic N, et al. Experimental investigation on the influence of ambient pressure on twin-fluid atomization of liquids with various viscosities. In: *Proceedings of the 13th triennial international conference on liquid atomization and spray systems*, Tainan, Taiwan, August 23-27, 2015 (ICLASS); 2015.
- [26] A. Sängler, *Zerstäubung hochviskoser fluide bei variierendem systemdruck - Grundlagenforschung zur hochdruck-flugstromvergasung*, Dissertation, Karlsruher Institut für Technologie (KIT).
- [27] Wachter S, Jakobs T, Kolb T. Experimental investigation on the influence of system pressure on resulting spray quality and jet breakup applying pressure adapted twin-fluid nozzles. *Int J Multiphase Flow* 2020;125.
- [28] Zhao H, Liu H-F, Tian X-S, et al. Influence of atomizer exit area ratio on the breakup morphology of coaxial air and round water jets. *AIChE J* 2014;60(6):2335–45.
- [29] Leroux B, Delabroy O, Lacas F. Experimental study of coaxial atomizers scaling. Part 1: dense core zone. *Atomization Sprays* 2007;17:381–407.
- [30] Leroux B, Delabroy O, Lacas F. Experimental study of coaxial atomizers scaling. Part 2: diluted zone. *Atomization Sprays* 2007;17:409–30.
- [31] Albrecht H-E. Laser doppler and phase doppler measurement techniques. Berlin, New York: Springer; 2003.
- [32] Tian X-S, Zhao H, Liu H-F, et al. Effect of central tube thickness on wave frequency of coaxial liquid jet. *Fuel Process Technol* 2014;119:190–7.
- [33] Araneo L, Damaschke N, Tropea C. Measurement and prediction of the Gaussian beam effect in the PDA. Springer; 2002. p. 189–208.
- [34] Kapulla R, Najera SB. Operation conditions of a phase Doppler anemometer: droplet size measurements with laser beam power, photomultiplier voltage, signal gain and signal-to-noise ratio as parameters. *Measur Sci Technol* 2006;17(1):221–7.
- [35] “DIN SPEC 91325:2015-06, Charakterisierung von Sprays und Sprühprozessen durch die Messung der Größe und der Geschwindigkeit nicht-transparenter Tropfen” 2015.
- [36] Mulhem B, Schulte G, Fritsching U. Solid-liquid separation in suspension atomization. *Chem Eng Sci* 2006;61(8):2582–9.
- [37] Hussein HJ, Capp SP, George WK. Velocity measurements in a high-Reynolds-number, momentum-conserving, axisymmetric, turbulent jet. *J Fluid Mech* 1994;258(-1):31.
- [38] Lasheras JC, Villermaux E, Hopfinger EJ. Break-up and atomization of a round water jet by high-speed annular air jet. *J. Fluid Mech.* 1998;357:351–79.
- [39] Varga CM, Lasheras JC, Hopfinger EJ. Initial breakup of a small-diameter liquid jet by a high-speed gas stream. *J. Fluid Mech.* 2003;497:405–34.

Comparison of Central Jet and Annular Sheet Atomizers at Identical Gas Momentum Flows

Simon Wachter,* Tobias Jakobs, and Thomas Kolb

Cite This: *Ind. Eng. Chem. Res.* 2021, 60, 11502–11512

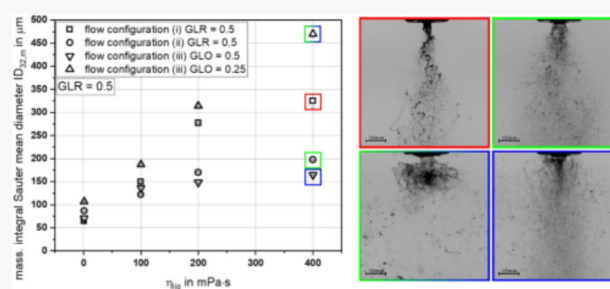
Read Online

ACCESS |

Metrics & More

Article Recommendations

ABSTRACT: This study compares three different nozzle flow configurations—central liquid jet with surrounding gas phase, liquid sheet with central gas phase, and liquid sheet with inner and outer gas phases. To guarantee constant velocities, as well as momentum flows at the nozzle orifice, a nozzle with identical orifice areas (a central tube with inner and outer slits) was utilized in the experiments. The influence of gas velocity (GLR), dynamic viscosity of the liquid, and nozzle configuration on the resulting droplet sizes (D_{32} , $ID_{32,m}$) and primary breakup was investigated at constant liquid mass flow. A high-speed camera (HSC) was used for the detection of primary breakup, whereas droplet size measurements were performed with a phase Doppler anemometer. The variation of nozzle configuration exhibited distinct influence on the resulting breakup morphology and droplet size. Especially, for atomizing high-viscosity liquids, application of sheet configurations led to smaller droplet sizes compared to liquid jet configuration.



1. INTRODUCTION

Gas-assisted nozzles are applied to a wide field of applications in industrial processes. Beneath utilization in spray drying and gas cleaning, there are also applications in combustion and synthesis processes. This type of atomizer is available in several flow configurations: (i) central liquid jet and coaxial annular gas stream, (ii) annular liquid sheet with central gas jet, and (iii) annular liquid sheet with inner and outer gas stream. Each configuration can be utilized in energy-conversion systems, such as entrained flow gasifiers (EFGs). Here, biomass or waste-based feedstock are typically applied and feature high viscosities of up to 1000 mPa·s, as well as a complex rheological behavior. The feedstock are converted into syngas ($\text{CO} + \text{H}_2$), whereas oxygen serves as the gasification and atomization agent. As a result of the low stoichiometry required for the gasification reaction ($\lambda < 1$), the burner nozzle is typically operated at gas-to-liquid mass flow ratios of $\text{GLR} < 1$. Despite the large field of applications and the comparably simple atomizer geometry, there is still no fundamental understanding of the prevailing phenomena and physics.

For the optimization of the atomization process at conditions relevant to EFG, it is an essential research objective to gain deeper insights into the atomization process by applying various nozzle configurations and liquid properties. In particular, because of the fact that nozzles featuring central liquid jets reveal a limitation in disintegrating large liquid jet diameters, at increased liquid mass flow and low liquid velocity, the present work aims at investigating and comparing potentially scalable annular liquid sheet nozzles.

2. THEORETICAL BACKGROUND

The three different nozzle flow configurations under investigation are shown in Figure 1 as configurations (i–iii). Configuration (i) represents the central liquid jet configuration with an annular coaxial gas jet; (ii) illustrates an annular liquid sheet atomizer with a central gas jet; and (iii) is an annular

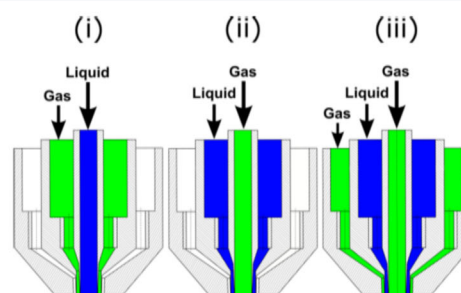


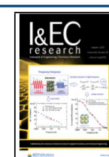
Figure 1. Schemes of the investigated nozzle flow configurations (i–iii).

Received: April 23, 2021

Revised: June 23, 2021

Accepted: June 25, 2021

Published: July 14, 2021



liquid sheet atomizer with central and coaxial surrounding gas jet.

Faragò and Chigier performed detailed investigations of liquid jet breakup morphology, utilizing configuration (i) for air/water.¹ A classification for primary breakup was suggested for different atomizer geometries in terms of the jet diameter and gas orifice area by applying the liquid Reynolds number Re_{liq} and aerodynamic Weber number We_{aero} , according to eqs 1 and 2, to describe the jet breakup:

$$Re_{liq} = \frac{D_{liq} \times v_{liq} \times \rho_{liq}}{\eta_{liq}} \quad (1)$$

$$We_{aero} = \frac{D_{liq} \times (v_{gas} - v_{liq})^2 \times \rho_{gas}}{\sigma} \quad (2)$$

with liquid jet diameter D_{liq} , velocity v , density ρ , dynamic viscosity η , and surface tension σ . The subscripts *gas* and *liq* denote the gas and liquid phases, respectively. For constant Re_{liq} , the following representative spray conditions can be identified: the Rayleigh-type breakup (small We_{aero}), in which the liquid jet is fragmented into large droplets close to the spray center. With increasing We_{aero} , the membrane-type breakup is detected, with membranes near the nozzle orifice being generated and broken into small droplets. The accumulated rim of the membranes disintegrates into larger droplets, according to Rayleigh–Plateau instabilities. At high We_{aero} , the fiber-type regime is reached, which leads to a complete disintegration of the liquid jet into fibers near the nozzle orifice. The produced fibers disintegrate into small droplets according to the Rayleigh–Plateau instability. The fiber-type regime is divided into the submodes pulsating and superpulsating. Lasheras and Hopfinger² used the momentum flux ratio of gas and liquid phases j , according to eq 3, for characterizing the fiber-type breakup:

$$j = \frac{j_{gas}}{j_{liq}} = \frac{v_{gas}^2 \times \rho_{gas}}{v_{liq}^2 \times \rho_{liq}} \quad (3)$$

Zhao et al.³ investigated the impact of dynamic viscosity on the primary breakup by applying suspensions in twin-fluid atomizers with a central liquid jet. In order to expand the regime classification concerning viscosity effects, the Ohnesorge number, which is in accordance with eq 4, was used. The breakup morphology was described by We_{aero} and Oh and was also classified into Rayleigh-type, fiber-type, and atomization.

$$Oh = \frac{\eta_{liq}}{\sqrt{D_{liq} \times \sigma \times \rho_{liq}}} \quad (4)$$

For the liquid-jet annular gas stream configuration, a large number of studies on the atomization of low-viscosity liquids ($\eta_{liq} < 50$ mPa·s) can be found in the literature.^{4–8} A summary of the publications featuring $\eta_{liq} > 50$ mPa·s was presented by Wachter et al.⁹ The dynamic viscosity was varied in the range of $\eta_{liq} = 1–805$ mPa·s. In general, an increase in the droplet diameter with increasing viscosity was reported.^{8,10–13} This effect was explained by the damping effects of the liquid on the formation of instabilities. Furthermore, the dependency of the resulting droplet size on the spray morphology was demonstrated by Sanger,¹⁴ who subdivided the proposed droplet size correlation into membrane-type and fiber-type regimes.

The second flow configuration (ii) provides the liquid as the annular sheet, whereas the gas stream emerges from the central tube. Investigations of the atomization of water with this nozzle configuration were performed by Leboucher et al.¹⁵ and Zhao et al.,¹⁶ who presented different diagrams for morphological classification. Both authors detected the bubble and Christmas-tree breakup regime. As the bubble regime occurs for low gas velocities and leads to gas-filled bubbles with liquid impingement,¹⁷ the Christmas-tree breakup at an increased gas velocity creates a pulsating sheet that breaks into droplets. This breakup regime was further divided by Choi et al.¹⁸ into the aerodynamic force-dominant and hydrodynamic force-dominant modes. Leboucher et al.¹⁵ classified the regimes with gas and liquid momentum flow J_{gas} and J_{liq} whereas Zhao et al.¹⁶ used $We_{aero,sheet}$ see eq 5, and a dimensionless geometry ratio of sheet thickness-to-diameter of the entire liquid orifice.

$$We_{aero,sheet} = \frac{s_{liq} \times (v_{gas} - v_{liq})^2 \times \rho_{gas}}{\sigma} \quad (5)$$

Here, s_{liq} represents the liquid sheet thickness. For increased liquid sheet thickness, a fiber-type regime was detected, leading to a sheet disintegration with small fibers in the perpendicular direction to the sheet. Li et al. performed droplet size measurements, applying this nozzle configuration at $v_{gas} > 180$ m·s⁻¹.¹⁹ As a result, a V-shaped radial Sauter mean diameter D_{32} profile was detected with a phase Doppler anemometer (PDA). For a significant increase in gas velocity, only a small decrease in the droplet size across the entire spray cone was detected. Leboucher et al.¹⁵ presented results for different system pressures and gas swirl configurations. Radial profiles of the droplet diameter are only shown for the swirl variation, exhibiting a nearly constant droplet size for a wide range of swirl ratios.

Flow configuration (iii) has a liquid annular sheet, with two gas streams emerging, one from the central tube and one from the coaxial outer annular gap around the liquid sheet. Carvalho et al.²⁰ employed a high-speed camera (HSC) to investigate nozzles with this flow configuration with angled outer gas atomizing water. In the experiments v_{liq} , $v_{gas,i}$, $v_{gas,o}$, the liquid sheet thickness as well as the gas swirl ratio were varied, whereas the index *i* and *o* represent the inner and outer gas orifices, respectively. The inner gas stream velocity was varied up to $v_{gas,i} = 200$ m·s⁻¹ and was identified as being more relevant for the breakup of the liquid sheet. In contrast, the outer gas stream only led to a slight decrease in the primary breakup length. Nevertheless, the outer gas velocity was only increased up to $v_{gas,o} = 40$ m·s⁻¹. The primary breakup length was also decreased when the swirl was added to the outer gas stream. For increasing the liquid sheet thickness, an increase in the primary breakup length was detected. Wahono et al.²¹ also used a HSC to investigate the primary breakup of an atomizer with flow configuration (iii) that featured parallel exiting channels. The authors observed an amplified Kelvin–Helmholtz surface wave on the liquid sheet during primary breakup, which caused the rupture of the sheet into ligaments. The breakup was mainly dependent on the momentum flow ratios J_i and J_o for the respective gas flow (eqs 6 and 7), as well as the entire gas momentum flow (eq 8). Only for J_o , a dependency on the breakup frequency of the liquid sheet was discovered.

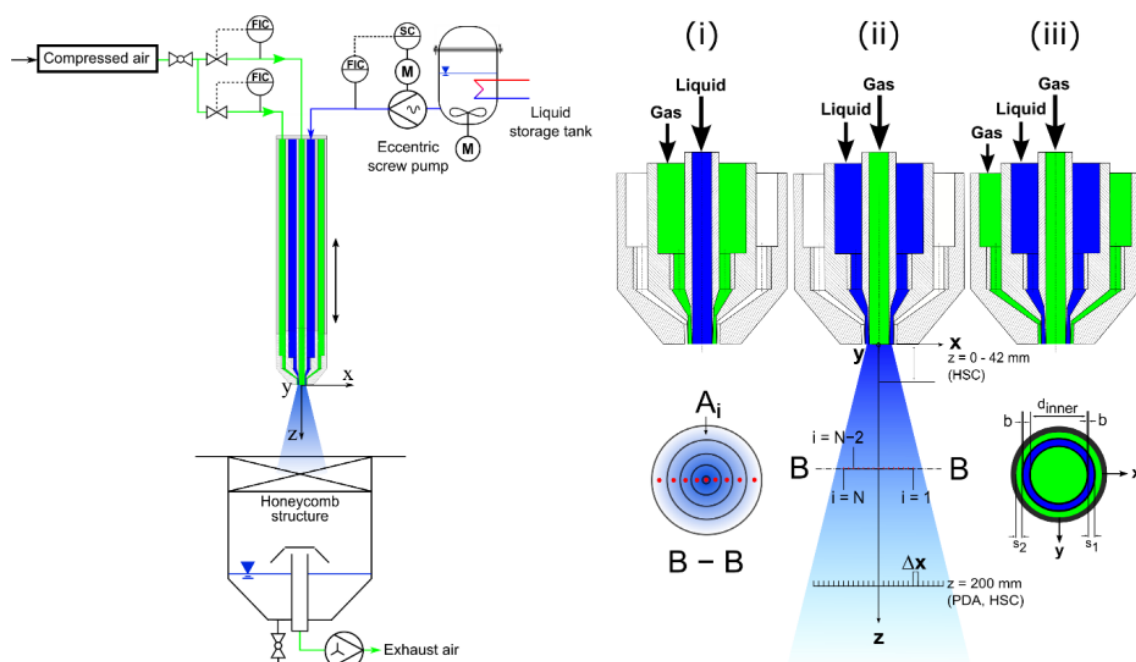


Figure 2. Schematic of the experimental setup applying nozzle configuration (iii), atmospheric spray test rig (ATMO) (left); schematic of the nozzle geometry applying the three investigated configurations (right).

$$J_i = \frac{J_{\text{gas},i}}{J_{\text{liq}}} = \frac{v_{\text{gas},i}^2 \times \rho_{\text{gas}} \times A_{\text{gas},i}}{v_{\text{liq}}^2 \times \rho_{\text{liq}} \times A_{\text{liq}}} \quad (6)$$

$$J_o = \frac{J_{\text{gas},o}}{J_{\text{liq}}} = \frac{v_{\text{gas},o}^2 \times \rho_{\text{gas}} \times A_{\text{gas},o}}{v_{\text{liq}}^2 \times \rho_{\text{liq}} \times A_{\text{liq}}} \quad (7)$$

$$J_{\text{gas}} = J_{\text{gas},i} + J_{\text{gas},o} \quad (8)$$

Duke et al.^{22,23} performed an instability analysis for a nozzle with flow configuration (iii) and noted two physical instabilities: the Kelvin–Helmholtz instability (shear layer) and a nonlinear rupturing instability. As observed by Duke et al.,²² the primary Kelvin–Helmholtz instability is only formed in the presence of a sufficiently high relative velocity of the outer gas stream $v_{\text{gas},o}$ and liquid sheet v_{liq} . The required relative velocity was $\Delta v = 30 \text{ m}\cdot\text{s}^{-1}$. Further theoretical investigations of the liquid sheet breakup were performed by Cao et al.,²⁴ Ibrahim et al.,²⁵ and Lee et al.²⁶ In these studies, linear instability analyses were performed, with the researchers coming to the conclusion that the inner gas jet exhibits higher efficiency in terms of atomization compared to the outer gas stream. In addition to the investigation of instabilities, a scaling analysis was performed. As a result, the liquid sheet thickness showed a dominant effect on the resulting spray characteristics, as reported by Duke et al.²⁷

The first PDA measurements of nozzles with flow configuration (iii) were performed by Leboucher et al.,²⁸ who applied water/air with different swirl configurations. This investigation demonstrated that the inner gas jet is more effective than the outer gas stream in terms of reducing droplet size. It should be noted that in this investigation, the maximum velocity of the outer gas stream was $v_{\text{gas},o} = 90 \text{ m}\cdot\text{s}^{-1}$, whereas the inner gas stream velocity was increased up to $v_{\text{gas},i} = 180 \text{ m}\cdot\text{s}^{-1}$, which could be a reason for the dominating effect of the

inner gas stream compared to the outer one. Zhao et al.²⁹ used this flow configuration to perform laser diffraction measurements with water/air. Varying the exiting gas velocities, a maximum droplet diameter was detected when the outer gas jet was around $v_{\text{gas},o} = 30\text{--}40 \text{ m}\cdot\text{s}^{-1}$, which is independent of the inner gas velocities. Zhao et al.²⁹ assumed that the outer gas jet increases the velocity of the liquid phase, without disintegrating the liquid sheet, leading to a lower relative velocity between the liquid phase and the central gas stream, which dominated the atomization.

To summarize the literature overview, especially for atomizers in configuration (iii), the influence of the inner versus outer gas jet velocities or momentum flow ratios was not finally clarified. Nevertheless, the gas orifice area was not kept constant in previous experiments, leading to different dependencies of gas velocity on GLR, which results in varying gas momentum flows.

In order to overcome this effect, in the experiments described in this study, a nozzle with identical orifice areas (central tube/inner slit/outer slit) was used. The atomizer was operated in the previously outlined configurations (i), (ii), and (iii), which allows for their comparison at constant momentum flow ratios. Water and three different liquids with increasing viscosities were atomized at varying gas momentum flows. The resulting droplet size measurements and primary jet/sheet breakup detection were performed by means of a PDA and a HSC.

3. EXPERIMENTAL SETUP

The experiments were performed at the ATMOSpheric spray test rig (ATMO), which is described by Wachter et al.³⁰ and depicted in Figure 2. A PDA system and a HSC were applied for spray investigations. The three-fluid lance was supplied with liquid using a pump and controlled via a Coriolis mass flow and density meter. A stirred and tempered liquid tank was

applied in order to avoid temperature deviations. Two hot wire anemometers with valves were used to control the atomizing air mass flow. To avoid recirculation of small droplets, a high-power suction system was applied to the exhaust air; additionally, a honeycomb structure was placed at the inlet of the collection tank in order to serve as a flow straightener. The fittings at the top of the three-fluid lance were constructed in an identical manner to enable changes in the gas and liquid flow configurations between each channel of the lance and the nozzle-exiting position, respectively. The atomizer has a central tube with $d_{\text{inner}} = 5.4$ mm and two surrounding slits of $s_1 = 1.09$ mm and $s_2 = 0.83$ mm. In order to guarantee for constant velocities at the nozzle orifice, independent of the chosen flow configuration, all orifice areas were manufactured equal in size. The thicknesses of the tubes separating the flow at the nozzle orifice are reduced to $b = 0.1$ mm, which results in an undisturbed gas flow according to Tian et al.³¹ The nozzle features parallel flow channels to enable the experimental results to be compared with other investigation results, such as those of Faragò and Chigier,¹ Zhao et al.,¹⁶ and Wahono et al.²¹

For the variation of dynamic viscosity, water and three different glycerol/water mixtures were used. Surface tension and density of the four liquids applied were almost constant (see Table 1). The dynamic viscosity of the liquid phase was

Table 1. Physical Properties of All Applied Liquids at 20 °C and 1 atm

	η_{liq} in mPa·s	σ in N·m ⁻¹	ρ_{liq} in kg·m ⁻³	Oh
water	1	0.0719	998	0.0026
glycerol/water (84.3 wt %)	100	0.0649	1220	0.2513
glycerol/water (89.5 wt %)	200	0.0642	1233	0.5027
glycerol/water (93.8 wt %)	400	0.0636	1244	1.0056

measured using a Physica MCR 101 rheometer from Anton Paar in Searle-type configuration.³² Surface tension and density were determined using an EasyDyne tensiometer from Krüss, via the Du Noüy ring³³ and weighing methods. Relevant values of all liquids are presented in Table 1 for 20 °C and 1 atm.

In the following paragraphs, only a short overview of the applied measurement systems is given. A detailed description is available in previous studies.^{30,34,35}

A HSC (Photron SA4) was used for the detection of primary breakup. The setup was operated in backlight illumination with a 9×4500 lm high power light-emitting diode array. Sets of 2000 images were recorded for each operating point to ensure for a reliable data base.

At a distance of $z = 200$ mm, 10,000 images were taken, in order to (i) guarantee for optimal PDA settings; (ii) sphericity check the droplets in the measuring plane; (iii) qualitatively confirm tendencies measured by the PDA; and (iv) validation

of PDA data in order to remove deviations according to the Gaussian beam effect.³⁶

A fiber PDA with Spray Explorer by Dantec Dynamics was applied for the local investigation of droplet diameter and velocity. The system was operated in forward scattering arrangement (first-order refraction). Details of the settings are presented in Table 2. The settings of the system were optimized according to previous studies.^{36,37} In this configuration, the maximum detectable droplet diameter is 1357 μm , as explained in a previous study.³⁸

To guarantee for a high-quality data, a set of 50,000 droplets was taken at each measuring point. For some of the outermost measuring points, the sample size was not reached. However, minimum 10,000 droplets were measured at the spray boundary ($x = \pm 44$ mm), ensuring statistical reliability, as reported in a previous study.³⁹ The toolbox *SprayCAT*³⁵ was used to compute arithmetic means as the mass-weighted integral Sauter mean diameter $ID_{32,m}$, according to eq 9.

$$ID_{32,m} = \frac{\sum_{i=1}^N D_{30,i}^3 \dot{m}_i A_i}{\sum_{i=1}^N D_{20,i}^2 \dot{m}_i A_i} \quad (9)$$

Detailed information concerning the calculation of the global size distribution and size moments is given by DIN SPEC 91325⁴⁰ and Albrecht.³⁸ The mass flux \dot{m}_i was calculated from PDA data according to Albrecht.³⁸ All PDA measurements were performed at $z = 200$ mm distance from the nozzle orifice and repeated 3 times. For each operating point, the rotational symmetry of the measured profiles was checked, taking a full radial profile. Afterward, the repetition measurements were performed, taking half-profiles from the spray boundary to the center.

4. RESULTS AND DISCUSSION

In order to investigate the effect of the nozzle configuration on the resulting droplet size and primary breakup, nozzle configurations (i) and (ii) were compared at varying GLR (i.e., gas velocity v_{gas}) and dynamic viscosity η_{liq} at constant liquid mass flow of $\dot{M}_{\text{liq}} = 30$ kg·h⁻¹. The atomization agent in all experiments was pressurized air at $T = 20$ °C. The supplied liquids were also tempered at $T = 20$ °C.

4.1. Comparison of Nozzle Configurations (i) and (ii) on the Droplet Size and Primary Breakup. For a comparison of nozzle configurations (i) and (ii), the operating conditions for both investigated parameters GLR and dynamic viscosity η_{liq} are presented in Table 3.

4.1.1. Influence of Nozzle Configurations (i) and (ii) on the Droplet Size and Primary Breakup at Varying GLR (i.e., v_{gas}) and Constant $\eta_{\text{liq}} = 1$ mPa·s. For a quantitative comparison of the two nozzle configurations, as well as for the description of the influence of GLR (v_{gas}) on the Sauter mean diameter, radial measurements were performed, as shown in Figure 3 (right).

Table 2. Settings of the PDA Evaluated by the Sensitivity Analysis

parameters	values	unit	parameters	values	unit
transmitter focal length f_T	1000	mm	laser wavelength λ_L	561	nm
receiver focal length f_R	1000	mm	laser power (transmitter exit)	40	mW
beam expander ratio E	1		off-axis angle Φ_R	70	°
receiver slit width (physical) l_s	200	μm	frequency shift f_Λ	80	MHz

Table 3. Operating Conditions of the Experiments for the Comparison of Nozzle Configurations (i) and (ii) at a Constant Liquid Mass Flow of $\dot{M}_{\text{liq}} = 30 \text{ kg h}^{-1}$

nozzle configuration	GLR in -	v_{gas} in $\text{m}\cdot\text{s}^{-1}$	η_{liq} in $\text{mPa}\cdot\text{s}$
(i)/(ii)	0.2	60	1
(i)/(ii)	0.3	90	1
(i)/(ii)	0.4	120	1
(i)/(ii)	0.5	150	1/100/200/400

The dependency of the Sauter mean diameter on GLR, for all measurements of (i) and (ii), the mass-weighted integral Sauter mean diameter $ID_{32,m}$ is shown in Figure 3 (left). As expected, with increasing GLR, for both nozzle configurations (i) and (ii), a decreasing Sauter mean diameter was measured. This effect results from an increase in the gas velocity ($v_{\text{gas}} = 60 - 150 \text{ m}\cdot\text{s}^{-1}$), which leads to higher aerodynamic forces that disintegrate the liquid jet or sheet. With increasing GLR, the influence on the resulting droplet size levels off. The influence of GLR on the resulting Sauter mean diameter, applying nozzle configuration (ii) at $\text{GLR} > 0.4$ ($v_{\text{gas}} > 120 \text{ m}\cdot\text{s}^{-1}$), is smaller compared to that using nozzle configuration (i).

In order to explain this effect, the radial Sauter mean diameter, for all measurements of (i) and (ii) is shown in Figure 3 (right). For $\text{GLR} \leq 0.3$, the $ID_{32,m}$ is significantly lower for nozzle configuration (ii). In contrast to this, an increase above $\text{GLR} > 0.4$ leads to lower $ID_{32,m}$ values for configuration (i) (see Figure 3 (left)). For nozzle configuration (i), a W-shaped radial profile was detected, whereas configuration (ii) led to a V-shaped radial distribution, which is in accordance with the results of Li et al.¹⁹ Typically, the flat W-shaped profile is achieved when the liquid jet is disintegrated by the high-velocity gas phase in the fiber-type breakup mode. As shown in Figure 4b), this mode leads to a slight increase in the droplet size at the spray center and a decrease at the spray boundary because of small, disintegrated fibers, leading to fine droplets following the gas phase. In this configuration, the liquid jet is fully disintegrated by the surrounding gas jet at high gas velocity. In contrast, the liquid sheet is already disintegrated into droplets for low gas velocities (see Figure 4c)), as against the liquid jet at the same gas velocity (see Figure 4a)). Applying configuration (ii)

for increased gas velocity (see Figure 4d)), tiny droplets could be detected in the center of the spray, comparable to configuration (i), but larger droplets remained at the spray boundary without any further disintegration because of the lack of aerodynamic forces. As this breakup mode did not change with further increase in gas velocity and the droplet size at the spray boundary did not decrease, $ID_{32,m}$ exhibits only low sensitivity to GLR above $\text{GLR} \geq 0.4$.

As can be seen in the HSC images, the spray angle differed significantly between nozzle configurations (i) and (ii). For configuration (i), the resulting jet fragments and droplets were accelerated in the axial direction, resulting in narrow spray angles. In contrast, the disintegration of the liquid sheet by the central gas stream at configuration (ii) led to a significant increase in the spray angle.

4.1.2. Influence of Nozzle Configurations (i) and (ii) on the Droplet Size and Primary Breakup at Varying Liquid Viscosities and Constant $\text{GLR} = 0.5$. To conduct a quantitative comparison of the two nozzle configurations (i) and (ii), as well as for the description of the influence of η_{liq} on the Sauter mean diameter, additional droplet size measurements were performed at an increased liquid viscosity of up to 400 mPa·s. The results are shown as $ID_{32,m}$ values in Figure 5.

As the measurements indicate, an increase in the droplet size could be detected for both nozzle configurations with increasing dynamic viscosity. This result had already been observed by many researchers, who typically applied flow configuration (i).^{8,10–13} As damping effects of the liquid phase cause this effect, the same influence for increasing the liquid viscosity was expected for flow configuration (ii). However, configuration (ii) shows a minor influence of viscosity on the droplet size. As the application of configuration (i) led to a smaller droplet size of low-viscosity liquids ($\eta_{\text{liq}} = 1 \text{ mPa}\cdot\text{s}$), the droplet size results were already turned over for $\eta_{\text{liq}} = 100 \text{ mPa}\cdot\text{s}$. The same influence of viscosity and nozzle configuration was also apparent in the HSC images of the primary breakup, which are displayed in Figure 6.

Upon increasing the dynamic viscosity from $\eta_{\text{liq}} = 1 \text{ mPa}\cdot\text{s}$ to $\eta_{\text{liq}} = 400 \text{ mPa}\cdot\text{s}$ while applying nozzle configuration (i), the primary breakup significantly changed from the superpululating fiber type, which resulted in a homogeneous spray with mostly

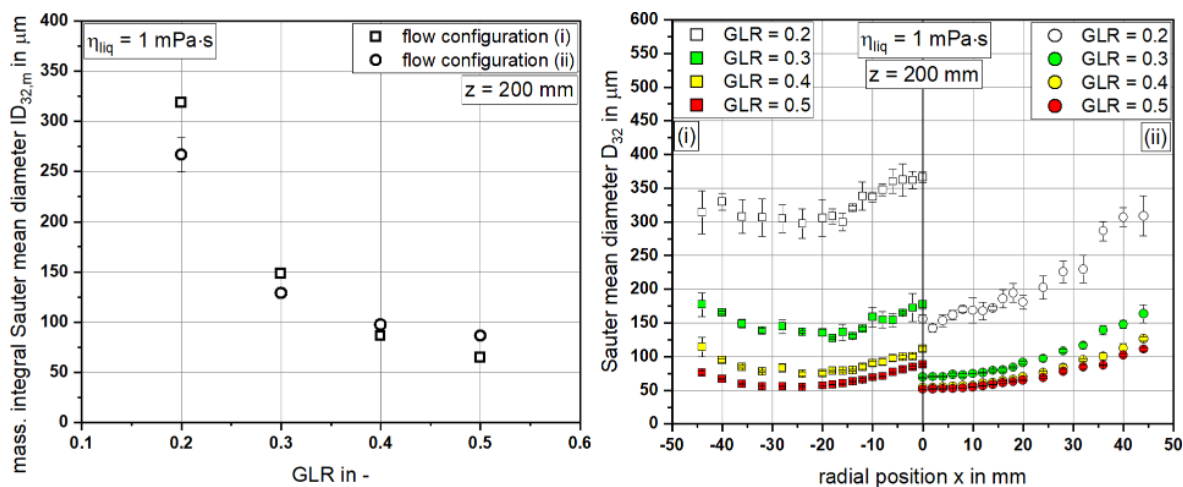


Figure 3. Resulting mass-weighted integral Sauter mean diameters (left) and radial measurements of the local Sauter mean diameter (right) using nozzle configurations (i) and (ii) at varying GLRs (i.e., v_{gas}) and constant dynamic viscosity $\eta_{\text{liq}} = 1 \text{ mPa}\cdot\text{s}$ at $z = 200 \text{ mm}$.

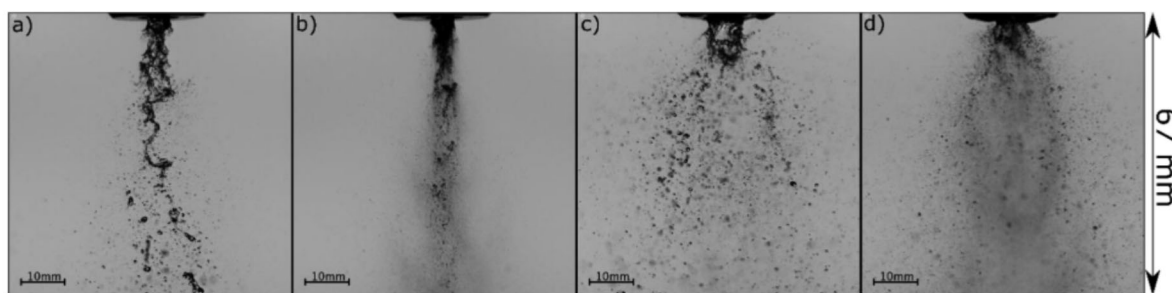


Figure 4. HSC images of the primary breakup of water ($\eta_{\text{liq}} = 1 \text{ mPa}\cdot\text{s}$) applying: (a) nozzle configuration (i) at $\text{GLR} = 0.2$ ($v_{\text{gas}} = 60 \text{ m}\cdot\text{s}^{-1}$); (b) nozzle configuration (i) at $\text{GLR} = 0.5$ ($v_{\text{gas}} = 150 \text{ m}\cdot\text{s}^{-1}$); (c) nozzle configuration (ii) at $\text{GLR} = 0.2$ ($v_{\text{gas}} = 60 \text{ m}\cdot\text{s}^{-1}$); and (d) nozzle configuration (ii) at $\text{GLR} = 0.5$ ($v_{\text{gas}} = 150 \text{ m}\cdot\text{s}^{-1}$).

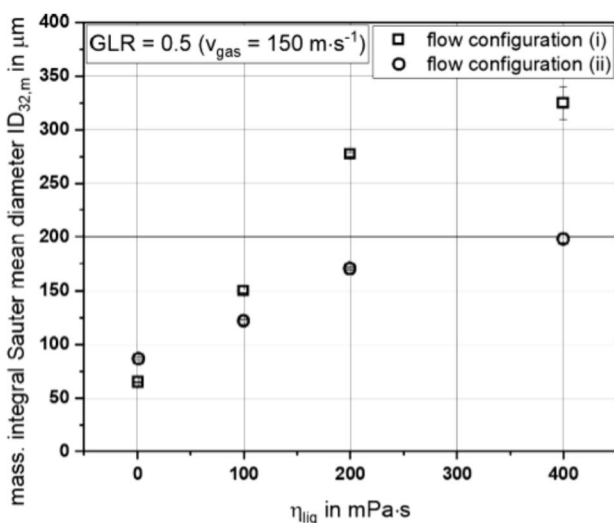


Figure 5. $ID_{32,m}$ measurements at constant $\text{GLR} = 0.5$ ($v_{\text{gas}} = 150 \text{ m}\cdot\text{s}^{-1}$) for nozzle configurations (i) and (ii) at varying dynamic viscosities.

very small droplets to the membrane-type breakup that revealed long ligaments and liquid fragments, along with an increased droplet size. In contrast, for nozzle configuration (ii), the breakup morphology did not significantly change with an increased liquid viscosity. Because of the fact that the emerging fuel sheet for configuration (ii) was thinner in size compared to the jet of configuration (i), almost no ligaments resulted from the primary breakup [even for the highest viscosity liquids ($\eta_{\text{liq}} = 400 \text{ mPa}\cdot\text{s}$) under investigation], leading to a smaller droplet size throughout the entire spray cone.

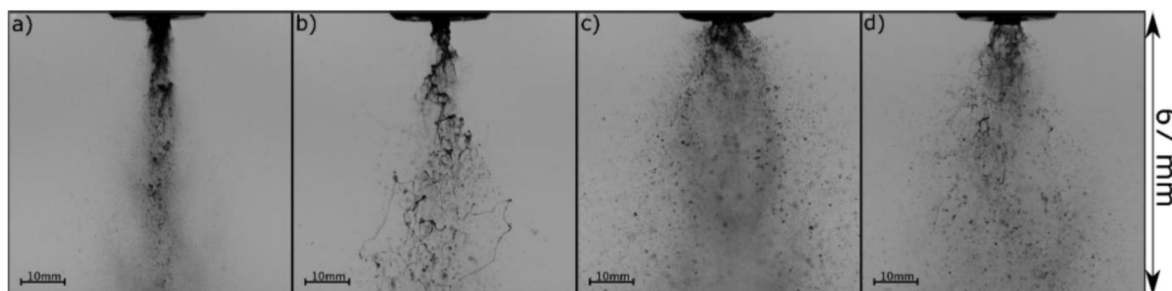


Figure 6. HSC images of the primary breakup at $\text{GLR} = 0.5$ ($v_{\text{gas}} = 150 \text{ m}\cdot\text{s}^{-1}$) applying (a) nozzle configuration (i) with $\eta_{\text{liq}} = 1 \text{ mPa}\cdot\text{s}$; (b) nozzle configuration (i) with $\eta_{\text{liq}} = 400 \text{ mPa}\cdot\text{s}$; (c) nozzle configuration (ii) with $\eta_{\text{liq}} = 1 \text{ mPa}\cdot\text{s}$; and (d) nozzle configuration (ii) with $\eta_{\text{liq}} = 400 \text{ mPa}\cdot\text{s}$.

4.2. Extension of the Nozzle Geometry with the Outer Gas Gap to Configuration (iii). Being aware of the influence of the fast-flowing gas phase on the primary breakup and the resulting droplet size in terms of twin-fluid nozzles, an additional outer gas gap was employed in the liquid sheet configuration to reduce the increasing droplet size at the spray boundary shown in Figure 3. As fast gas phase emerges via two orifices, two mass flow ratios GLO and GLI were defined. GLO represents the mass flow ratio between the outer gas flow through the gas slit and liquid sheet, whereas GLI stands for the mass flow ratio between the inner gas flow through the central tube and liquid sheet. This definition yields the following equations:

$$\text{GLR} = \text{GLO} + \text{GLI} \quad \text{GLO} = \frac{\dot{M}_{\text{gas,o}}}{\dot{M}_{\text{liq}}} \quad \text{GLI} = \frac{\dot{M}_{\text{gas,i}}}{\dot{M}_{\text{liq}}} \quad (10)$$

In an initial set of measurements, GLO (i.e., $v_{\text{gas,o}}$) and GLI (i.e., $v_{\text{gas,i}}$) were varied for constant GLR values at $\eta_{\text{liq}} = 1 \text{ mPa}\cdot\text{s}$. In addition, dynamic viscosity was investigated at $\text{GLR} = 0.5$ for $\text{GLO} = 0, 0.25, \text{ and } 0.5$, resulting in $v_{\text{gas,o}} = 0, 75, \text{ and } 150 \text{ m}\cdot\text{s}^{-1}$. Thereafter, a comparison between nozzle configurations (i–iii) was performed for $\text{GLR} = 0.5$.

4.2.1. Influence of GLO/GLI on the Droplet Size and Primary Breakup Applying Nozzle Configuration (iii) at Constant Liquid Viscosity and Constant $\text{GLR} = 0.3, 0.5, \text{ and } 0.7$. In order to compare the primary breakup and droplet size, nozzle configuration (iii) was applied at constant liquid viscosity $\eta_{\text{liq}} = 1 \text{ mPa}\cdot\text{s}$ and $\text{GLR} = 0.3, 0.5, \text{ and } 0.7$, but varying GLO and GLI. The measurements listed in Table 4 were performed. For a quantitative comparison of the resulting droplet sizes, the values for the $ID_{32,m}$ were used.

Table 4. Operating Conditions of the Experiments for Nozzle Configuration (iii) at a Constant Liquid Mass Flow of $\dot{M}_{\text{liq}} = 30 \text{ kg h}^{-1}$, Liquid Viscosity of $\eta_{\text{liq}} = 1 \text{ mPa}\cdot\text{s}$, and GLR = 0.3, 0.5, and 0.7, but Varying GLI/GLO

GLR in -	GLO in -	GLI in -	$v_{\text{gas},o}$ in m s^{-1}	$v_{\text{gas},i}$ in m s^{-1}
0.3/0.5	0/0	0.3/0.5	0/0	90/150
0.3/0.5/0.7	0.06/0.1/0.14	0.24/0.4/0.56	18/30/42	72/120/168
0.3/0.5/0.7	0.12/0.2/0.28	0.18/0.3/0.42	36/60/84	54/90/126
0.3/0.5/0.7	0.15/0.25/0.35	0.15/0.25/0.35	45/75/105	45/75/105
0.3/0.5/0.7	0.18/0.3/0.42	0.12/0.2/0.28	54/90/126	36/60/84
0.3/0.5/0.7	0.24/0.4/0.56	0.06/0.1/0.14	72/120/168	18/30/42
0.3/0.5	0.3/0.5	0/0	90/150	0/0

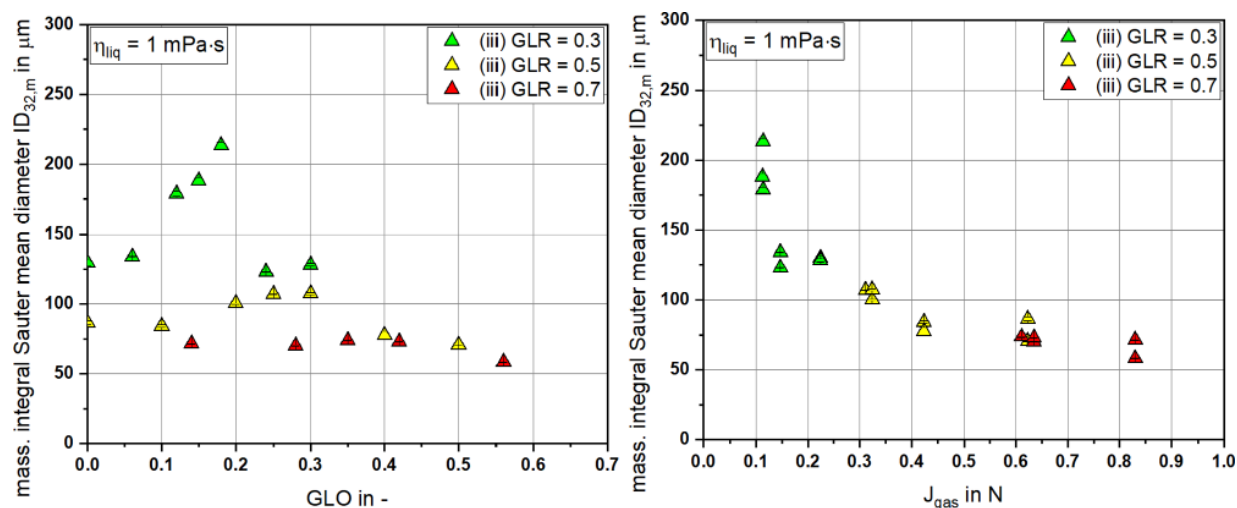


Figure 7. $ID_{32,m}$ measurements applying nozzle configuration (iii) at constant $\eta_{\text{liq}} = 1 \text{ mPa}\cdot\text{s}$ and GLR = 0.3, 0.5, and 0.7, with varying GLO (left); the same measurements plotted over the entire gas momentum flow J_{gas} (see eq 8) (right).

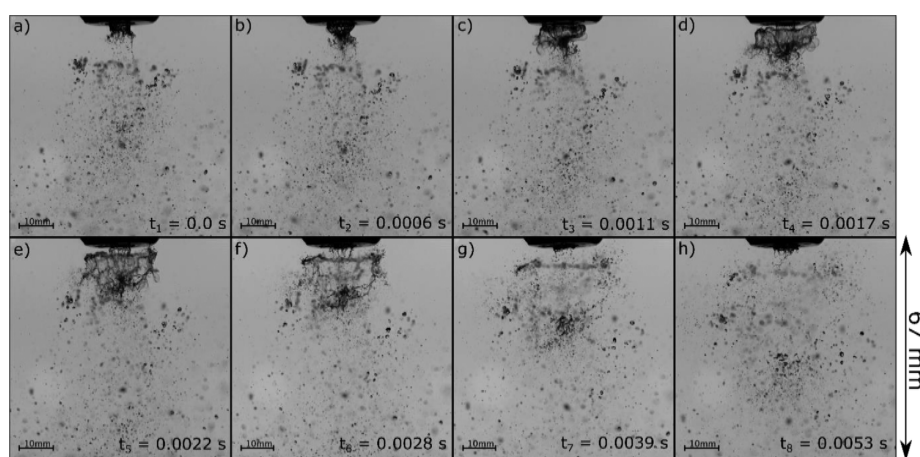


Figure 8. Primary breakup of the liquid sheet while pulsating at GLO = GLI applying nozzle configuration (iii), GLR = 0.3, and constant $\eta_{\text{liq}} = 1 \text{ mPa}\cdot\text{s}$. The time difference shown is respective to t_1 .

Starting with a constant GLR = 0.3 shown in Figure 7 (left), for an increase in GLO (i.e., $v_{\text{gas},o}$), which also leads to a decrease in GLI (i.e., $v_{\text{gas},i}$), first between GLO = 0–0.06, the $ID_{32,m}$ remains near $130 \mu\text{m}$. For further increase in GLO = 0.12–0.18, a steep increase in the $ID_{32,m}$ values can be noted, resulting in a maximum for GLO = 0.18. A further increase in GLO, up to GLO = 0.3, leads to a decrease in $ID_{32,m}$, even below the size at GLI = 0.3. These results are in accordance with those of Zhao et al.,²⁹ namely, the resulting droplet size primarily depends on the gas flow featuring higher velocity

applying configuration (iii). For GLR = 0.5, the values for $ID_{32,m}$ remain lower compared to those for GLR = 0.3 through all the investigated GLOs. Increasing GLR from 0.5 to 0.7 only leads to a slight decrease in the droplet size. When GLR is increased from 0.5 to 0.7, the maximum in $ID_{32,m}$ around GLO \approx GLI no longer exists. Both the mentioned effects can be explained by the aerodynamic force of the gas phase. The decreasing influence of GLR on the droplet size for increasing GLR was already shown and explained in Figure 3 (right). In order to understand the development of a maximum in the

resulting droplet size, Figure 7 (right) presents the $ID_{32,m}$ values plotted as a function of the total emerging gas momentum flow. Here, a significant decrease in the latter was identified around the operating conditions of $GLO \approx GLI$, which was caused by the comparably low velocity of both the emerging gas streams.

In addition, the HSC images taken at $GLO \approx GLI$ show a pulsation of the liquid sheet for all the investigated GLR values. As the frequency of the pulsation increases with increasing GLR, a time lapse of the pulsation with the HSC images could be detected best at $GLR = 0.3$, as shown in Figure 8. In Figure 8a, the liquid sheet was formed, as typical for nozzles in configurations (ii) or (iii). After $\Delta t = 0.0011$ s, the liquid sheet swelled, as shown in Figure 8c. At $t_5 = 0.0022$ s, the interaction of the swelled sheet with the high-velocity outer gas flow resulted in a detachment from the nozzle. As the swelled sheet was moved in the axial direction, large membranes were formed with a thick horizontal rim. After the rupture of the sheet at $t_8 = 0.0053$ s, the pulsation process began again with a new liquid sheet formed at the nozzle orifice. Because of the fact that the membrane rim falls apart into large droplets at low gas momentum flow, the droplet size at $GLO \approx GLI$ was increased for $GLR < 0.7$ compared to the operational conditions where $GLO \neq GLI$.

The description of the disintegration process of the liquid sheet at $GLO \approx GLI$ for nozzle configuration (iii) can be given in accordance with the study by Zhao et al.²⁹ Here, it was assumed that the liquid sheet was disintegrated by Kelvin–Helmholtz instabilities, which formed a horizontal wave on the outer and inner sides of the sheet. This instability is caused by changes in the local static pressure, which is induced by differences in gas- and liquid-phase velocities.^{41,42} The frequency f_{KH} and velocity u_c of these instabilities were defined by Villermaux et al.⁴³ and Dimotakis et al.,⁴⁴ according to eqs 11 and 12:

$$f_{KH} \sim \frac{u_c}{\delta_{gas}} \times \left(\frac{\rho_{gas}}{\rho_{liq}} \right)^{0.5} \quad (11)$$

$$u_c = \frac{\sqrt{\rho_{liq}} \times v_{liq}}{\sqrt{\rho_{liq}} + \sqrt{\rho_{gas}}} + \frac{\sqrt{\rho_{gas}} \times v_{gas}}{\sqrt{\rho_{liq}} + \sqrt{\rho_{gas}}} \quad (12)$$

Here, δ_{gas} stands for the gas boundary layer thickness. As the frequency, the gas boundary layer thickness, and the velocity of the instability were mainly the functions of gas velocity, these values were nearly equal for $GLO \approx GLI$ ($v_{gas,o} \approx v_{gas,i}$). In the event that the Kelvin–Helmholtz waves from both shear layers (inside and outside) emerged at the same time, the pulsation of the primary breakup was achieved and remains stable because of the comparable wave frequency and velocity. Furthermore, the increase in the instability frequency for increasing GLR values also corresponds to eq 12.

4.2.2. Influence of GLO/GLI on the Droplet Size and Primary Breakup Applying Nozzle Configuration (iii) at Varying Liquid Viscosities and Constant $GLR = 0.5$. In order to compare the primary breakup and droplet size applying nozzle configuration (iii) at constant $GLR = 0.5$, but varying GLO and GLI, as well as dynamic viscosity, the measurements specified in Table 4 were also performed for $\eta_{liq} = 100$ mPa·s. For $\eta_{liq} = 200$ and 400 mPa·s, a reduced measurement matrix at $GLR = 0.5$ with $GLO = 0, 0.25$, and 0.5 was conducted, the results of which are shown in Figure 9.

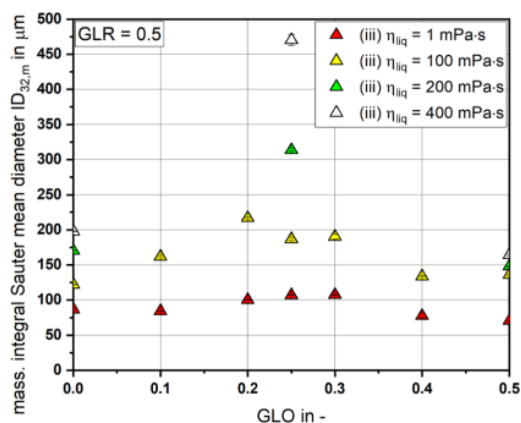


Figure 9. $ID_{32,m}$ measurements applying nozzle configuration (iii) at constant $GLR = 0.5$ with varying GLO and varying $\eta_{liq} = 1 - 400$ mPa·s.

As the dynamic viscosity of the liquid was increased from $\eta_{liq} = 1$ to 100 mPa·s, an increase in the droplet size was detected over the entire range of GLO. At $GLO = 0$, an increment in dynamic viscosity was observed, with $\Delta ID_{32,m} = 36$ μm and the smallest effect on the $ID_{32,m}$ value. An even more pronounced maximum in the $ID_{32,m}$ value was also found at an increased viscosity, again in the region of $GLO \approx GLI$ ($v_{gas,o} \approx v_{gas,i}$). A further increase in dynamic viscosity to $\eta_{liq} = 200$ –400 mPa·s led to higher $ID_{32,m}$ values for all GLO values. The smallest gradient in the droplet size for a further increase in viscosity was found at $GLO = 0.5$. The maximum of $ID_{32,m}$ at $GLO \approx GLI$ ($v_{gas,o} \approx v_{gas,i}$) showed a significant enlargement at viscosities of $\eta_{liq} = 200$ –400 mPa·s. In order to explain these results, HSC images from the primary sheet breakup at $GLO = 0, 0.25$, and 0.5 are shown for $\eta_{liq} = 400$ mPa·s in Figure 10.

As already noted in the description of Figure 6d, upon applying configuration (ii) at $GLR = 0.5$ and $\eta_{liq} = 400$ mPa·s, almost no ligaments occur after the primary breakup because of the direct disintegration of the liquid sheet into droplets. When GLO is changed from $GLO = 0$ to $GLO = 0.25$, the pulsation described in Figure 8 can be detected, and it is even more pronounced for increased viscosity (see Figure 10b). Based on the significant damping effects of the liquid at $\eta_{liq} = 400$ mPa·s compared to $\eta_{liq} = 1$ mPa·s, the pulsation frequency of the liquid sheet is reduced with increased viscosity. The detachment of the liquid sheet, also shown in Figure 8c for $\eta_{liq} = 1$ mPa·s, at higher viscosity, results in a large quantity of blown-up membranes. After the pulsation process with the membrane disintegration, large parts of the membrane rim slowly move in the axial direction. As the number density of the droplets at $GLO \approx GLI$ ($v_{gas,o} \approx v_{gas,i}$) is low and contains large liquid rim fragments because of the lower aerodynamic forces of the gas jets, the $ID_{32,m}$ values shown in Figure 9 are significantly increased. A further increase to $GLO = 0.5$ results in a maximum of the spray angle, as depicted in Figure 10c. This increased spray angle can be seen for all viscosities ≥ 100 mPa·s at $GLO = 0.5$. The increment in the spray angle can be explained by Kelvin–Helmholtz instabilities, which develop on the liquid sheet as a result of shear forces between the fast gas and slower liquid stream. As the liquid accumulation disintegrates, the local pressure difference generates a radial velocity compound and results in this spray angle. The trend, that for $GLO = 0.5$ the smallest $ID_{32,m}$ value at $\eta_{liq} = 400$ mPa·s

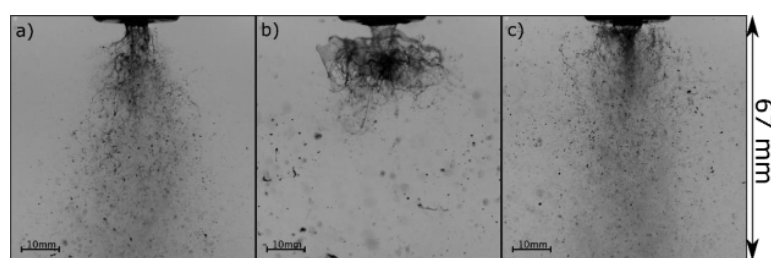


Figure 10. Primary breakup of the liquid sheet applying nozzle configuration (iii), GLR = 0.5, and constant $\eta_{\text{liq}} = 400$ mPa·s at (a) GLO = 0; (b) GLO = 0.25; and (c) GLO = 0.5.

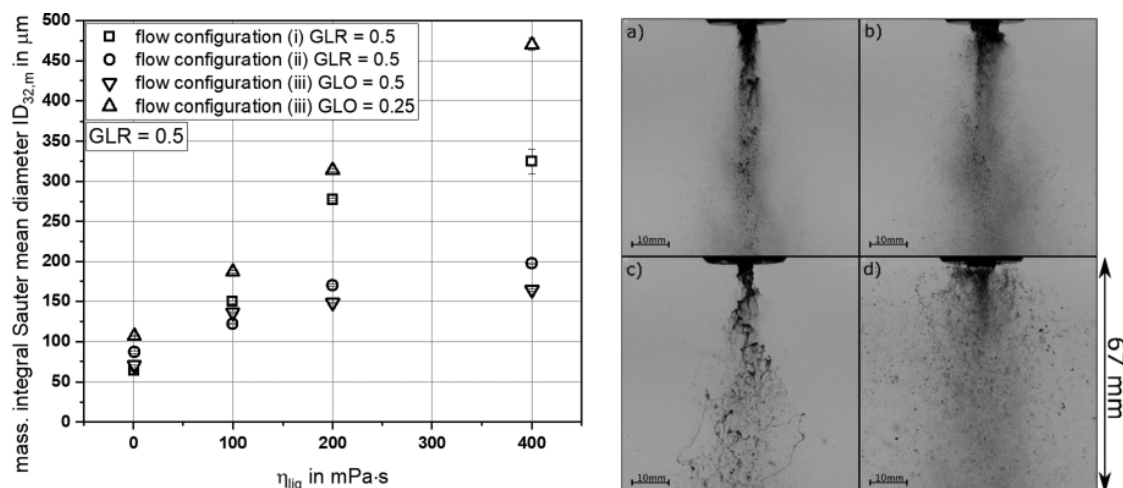


Figure 11. $ID_{32,m}$ measurements at constant GLR = 0.5 and varying $\eta_{\text{liq}} = 1$ –400 mPa·s for nozzle configurations (i), (ii), and (iii) at GLO = 0.25 and (iii) GLO = 0.5 (left); primary breakup applying GLR = 0.5 for (a) configuration (i) and $\eta_{\text{liq}} = 1$ mPa·s; (b) configuration (iii) at GLO = 0.5 and $\eta_{\text{liq}} = 1$ mPa·s; (c) configuration (i) and $\eta_{\text{liq}} = 400$ mPa·s; and (d) configuration (iii) at GLO = 0.5 and $\eta_{\text{liq}} = 400$ mPa·s (right).

was detected compared to GLO = 0 and 0.25, is also apparent in the high-speed images.

4.3. Comparison of Nozzle Configurations (i), (ii), and (iii) at Constant GLR = 0.5. For the comparison of the applied nozzle configurations at constant GLR = 0.5 and varying liquid viscosity, four different setups were chosen: central liquid jet configuration (i), central gas jet configuration (ii) (the same as configuration (iii) at GLO = 0), nozzle configuration (iii) at GLO = 0.25, and configuration (iii) at GLO = 0.5. The resulting $ID_{32,m}$ values of the measurements are shown in Figure 11 (left). Figure 11 (right) presents the primary breakup at GLR = 0.5, applying two nozzle configurations (i) and (iii) at GLO = 0.5 with two viscosities $\eta_{\text{liq}} = 1$ and 400 mPa·s.

As already discussed in the previous section, for all of the nozzle configurations with increasing liquid viscosity, an increase in the droplet size was detected. The resulting droplet size exhibits a distinct dependence on the nozzle configuration used. As the variation in the resulting droplet size is $\Delta ID_{32,m} = 45$ μm at $\eta_{\text{liq}} = 1$ mPa·s, the difference at $\eta_{\text{liq}} = 400$ mPa·s is calculated as $\Delta ID_{32,m} = 315$ μm . For nozzle configuration (iii) at GLO = 0.25, the highest droplet size was detected at each applied dynamic viscosity. This was in accordance with the comparably low gas momentum flow and the trend toward the pulsation of the liquid sheet, as discussed in the previous chapters. Although the central liquid jet configuration (i) showed the smallest values in $ID_{32,m}$ at $\eta_{\text{liq}} = 1$ mPa·s, a significant increase in the droplet size was detected at higher

viscosities. The increment in the droplet size at high viscosities results from the relation between the thickness of the primary ligament ($d_{\text{inner}} = 5.4$ mm) and the damping effects of the viscosity. Following primary atomization, ligaments and fragments are formed out of the jet, which leads to large droplets. Nozzle configurations (ii) at GLR = 0.5 and (iii) at GLO = 0.5 indicated the smallest gradient in the droplet size for increasing the dynamic viscosity, which could be explained by the high gas momentum flow in conjunction with the disintegration of a thin liquid sheet of $s_1 = 1.09$ mm. The lowest $ID_{32,m}$ value at increased viscosity was achieved by configuration (iii) at GLO = 0.5.

As configuration (iii) at GLO = 0.5 and configuration (i) at GLR = 0.5 are both designs with inner liquid discharge and a fast surrounding gas jet [(i) is the central liquid jet with the surrounding gas jet and (iii) at GLO = 0.5 is a liquid sheet with the surrounding gas jet], the difference in the resulting droplet size was also related to the difference in the liquid jet/sheet thickness. This significant difference is also shown in Figure 11 (right). The comparison of the flow configurations (i)–(iii) revealed, especially for increased liquid viscosities ($\eta_{\text{liq}} \geq 100$ mPa·s), a more efficient atomization for the sheet configurations (ii) and (iii) in relation to the jet configuration (i).

With reference to the literature review and the predominating gas stream applying configuration (iii), previous studies showed, depending on atomization conditions, that either the inner or the outer gas stream can be more relevant for

atomization and sheet disintegration. In the present case of constant momentum flow ratios at $GLO = 0.5$ ($GLI = 0$) compared to $GLI = 0.5$ ($GLO = 0$), the outer high-velocity gas stream led to smaller droplets and thus was more relevant for atomization.

5. CONCLUSIONS

This study compares three different nozzle flow configurations: a central liquid jet with the surrounding gas phase, a liquid sheet with the central gas phase, and a liquid sheet with inner and outer gas phases. To guarantee constant velocities, as well as momentum flows at the nozzle orifice, one nozzle with identical orifice areas (a central tube with inner and outer slits) was utilized in the experiments. The influence of gas velocity (GLR), dynamic viscosity of the liquid, and nozzle configuration on the resulting droplet sizes (D_{32} , $ID_{32,m}$) and primary breakup was investigated at a constant liquid mass flow of $\dot{M}_{liq} = 30 \text{ kg h}^{-1}$. On the basis of these findings, the following conclusions can be drawn:

- An increase in the gas momentum flow always resulted in a decrease in the droplet size for all flow configurations.
- An increase in dynamic viscosity always led to an increase in the resulting droplet size for all flow configurations and gas momentum flows.
- Comparing the flow configurations, the liquid sheet (ii and iii) revealed smaller droplet sizes against the liquid jet configuration (i).
- Operating the sheet nozzle in configuration (iii) with identical gas velocity for the inner and outer gas streams, pulsation of the liquid sheet was detected. Increasing the gas velocity (inner and outer) resulted in an increase in the pulsation frequency, leading to a reduced number of ligaments. Higher liquid viscosity resulted in the formation of large ligaments.
- In contrast to the literature, no dominant effect of the central gas jet compared to the outer gas stream was identified. Instead, the outer gas momentum flow seems to be more effective in terms of droplet size, especially when atomizing high-viscosity liquids.

AUTHOR INFORMATION

Corresponding Author

Simon Wachter – Institute for Technical Chemistry, Karlsruhe Institute of Technology, 76344 Eggenstein-Leopoldshafen, Germany; orcid.org/0000-0001-8264-8246;
Email: simon.wachter@kit.edu

Authors

Tobias Jakobs – Institute for Technical Chemistry, Karlsruhe Institute of Technology, 76344 Eggenstein-Leopoldshafen, Germany

Thomas Kolb – Institute for Technical Chemistry, Karlsruhe Institute of Technology, 76344 Eggenstein-Leopoldshafen, Germany; Engler-Bunte Institute, Karlsruhe Institute of Technology, 76131 Karlsruhe, Germany

Complete contact information is available at:
<https://pubs.acs.org/10.1021/acs.iecr.1c01526>

Notes

The authors declare no competing financial interest.

ACKNOWLEDGMENTS

The authors gratefully acknowledge the financial support of the Helmholtz Association of German Research Centers (HGF) in the context of the research program as well as Materials and Technologies for the Energy Transition (MTET). The present work contributes to the Helmholtz Virtual Institute for Gasification Technology – HVIGasTech (VH-VI-429) (<http://www.hvigastech.org/>).

REFERENCES

- (1) Chigier, N.; Faragó, Z. Morphological Classification of Disintegration of Round Liquid Jets in a Coaxial Air Stream. *Atomiz. Spr.* **1992**, *2*, 137–153.
- (2) Lasheras, J. C.; Hopfinger, E. J. Liquid jet instability and atomization in a coaxial gas stream. *Annu. Rev. Fluid Mech.* **2000**, *32*, 275–308.
- (3) Zhao, H.; Hou, Y.-B.; Liu, H.-F.; Tian, X.-S.; Xu, J.-L.; Li, W.-F.; Liu, Y.; Wu, F.-Y.; Zhang, J.; Lin, K.-F. Influence of rheological properties on air-blast atomization of coal water slurry. *J. Non-Newton. Fluid Mech.* **2014**, *211*, 1–15.
- (4) Rizk, N. K.; Lefebvre, A. H. Spray characteristics of plain-jet airblast atomizers. *Amer. Soc. Mech. Engineer.* **1984**, *106*, 634–638.
- (5) Jakobs, T.; Djordjevic, N.; Sanger, A.; Zazalis, N.; Kolb, T. Influence of reactor pressure on twin-fluid atomization: Basic investigations on burner design for high-pressure entrained flow gasifier. *Atomiz. Spr.* **2015**, *25*, 1081–1105.
- (6) Wittig, S.; Aigner, M.; Sakbani, K.; Sattelmayer, T. *Optical Measurements of Droplet Size Distributions: Special Considerations in the Parameter Definition for Fuel Atomizers*; In AGARD Combust. Probl. in Turbine Eng., 1984.
- (7) Elkotb, M.M.; El-Sayed Mahdy, M.A.; Montaser, M.E. *Investigation of external mixing air blast atomizers*; International Conference on Liquid Atomization and Spray Systems (ICLASS), 1982.
- (8) Jasuja, A. K. Plain-Jet Airblast Atomization of Alternative Liquid Petroleum Fuels Under High Ambient Air Pressure Conditions. *Amer. Soc. Mech. Engineer.* **1982**, *7*.
- (9) Wachter, S.; Jakobs, T.; Kolb, T. Experimental investigation on the influence of system pressure on resulting spray quality and jet breakup applying pressure adapted twin-fluid nozzles. *Int. J. Multiphase Flow* **2020**, *125*, 103189.
- (10) Lorenzetto, G. E.; Lefebvre, A. H. Measurements of drop size on a plain-jet airblast atomizer. *AIAA Journal* **1977**, *15*, 1006–1010.
- (11) Schmidt, P.; Walzel, P. Zerstauben von Flussigkeiten. *Chem. Ing. Tech.* **1980**, *52*, 304–311.
- (12) Aliseda, A.; Hopfinger, E. J.; Lasheras, J. C.; Kremer, D. M.; Berchielli, A.; Connolly, E. K. Atomization of viscous and non-Newtonian liquids by a coaxial, high-speed gas jet. Experiments and droplet size modeling. *Int. J. Multiphase Flow* **2008**, *34*, 161–175.
- (13) Li, L. K. B.; Dressler, D. M.; Green, S. I.; Davy, M. H. Experiments on air-blast atomization of viscoelastic liquids, Part 1: quiescent conditions. *Atomiz. Spr.* **2009**, *19*, 157–190.
- (14) Sanger, A.; Jakobs, T.; Kolb, T. *Using Primary Instability Analysis for Determination of Apparent Liquid Viscosity at Jet Breakup Atomizing Non-Newtonian Fluids*. 27th Annual Conference on Liquid Atomization and Spray Systems, 2016.
- (15) Leboucher, N.; Roger, F.; Carreau, J.-L. Characteristics of the spray produced by the atomization of an annular liquid sheet assisted by an inner gas jet. *Atomiz. Spr.* **2012**, *22*, 515–542.
- (16) Zhao, H.; Xu, J.-L.; Wu, J.-H.; Li, W.-F.; Liu, H.-F. Breakup morphology of annular liquid sheet with an inner round air stream. *Chem. Eng. Sci.* **2015**, *137*, 412–422.
- (17) Kendall, J. M. Experiments on annular liquid jet instability and on the formation of liquid shells. *Phys. Fluids* **1986**, *29*, 2086.
- (18) Choi, C. J.; Lee, S. Y. Droplet formation from a thin hollow liquid jet with a core air flow. *Atomiz. Spr.* **2005**, *15*, 469–488.
- (19) Li, X.; Shen, J. Experimental Study of Sprays from Annular Liquid Jet Breakup. *J. Propul. Power* **1999**, *15*, 103–110.

- (20) Carvalho, I. S.; Heitor, M. V. Liquid film break-up in a model of a prefilming airblast nozzle. *Exp. Fluids* **1998**, *24*, 408–415.
- (21) Wahono, S.; Honnery, D.; Soria, J.; Ghajel, J. High-speed visualisation of primary break-up of an annular liquid sheet. *Exp. Fluids* **2008**, *44*, 451–459.
- (22) Duke, D.; Honnery, D.; Soria, J. Experimental investigation of nonlinear instabilities in annular liquid sheets. *J. Fluid Mech.* **2012**, *691*, 594–604.
- (23) Duke, D.; Honnery, D.; Soria, J. The growth of instabilities in annular liquid sheets. *Exp. Therm. Fluid Sci.* **2015**, *68*, 89–99.
- (24) Cao, J. Theoretical and experimental study of atomization from an annular liquid sheet. *Proc. Instit. Mech. Eng., Part D: J. Automob. Engineer.* **2005**, *217*, 735–743.
- (25) Ibrahim, A. A.; Jog, M. A. Nonlinear instability of an annular liquid sheet exposed to gas flow. *Int. J. Multiphase Flow* **2008**, *34*, 647–664.
- (26) LEE, J.-G.; CHEN, L.-D. Linear stability analysis of gas-liquid interface. *AIAA Journal* **1991**, *29*, 1589–1595.
- (27) Duke, D.; Honnery, D.; Soria, J. *Empirical Scaling Analysis of Atomising Annular Liquid Sheets*; International Conference of Liquid Atomization and Spray Systems (ICLASS), 2012.
- (28) Leboucher, N.; Roger, F.; Carreau, J. L. Atomization characteristics of an annular liquid sheet with inner and outer gas flows. *Atomiz. Spr.* **2014**, *24*, 1065–1088.
- (29) Zhao, H.; Wu, Z.-W.; Li, W.-F.; Xu, J.-L.; Liu, H.-F. Nonmonotonic Effects of Aerodynamic Force on Droplet Size of Prefilming Air-Blast Atomization. *Ind. Eng. Chem. Res.* **2018**, *57*, 1726–1732.
- (30) Wachter, S.; Jakobs, T.; Kolb, T. Effect of Solid Particles on Droplet Size Applying the Time-Shift Method for Spray Investigation. *Appl. Sci.* **2020**, *10*, 7615.
- (31) Tian, X.-S.; Zhao, H.; Liu, H.-F.; Li, W.-F.; Xu, J.-L. Effect of central tube thickness on wave frequency of coaxial liquid jet. *Fuel Process. Technol.* **2014**, *119*, 190–197.
- (32) Searle, G.F.C. *A simple viscometer for very viscous liquids*; Proc. Cambridge Philos. Soc., 1912.
- (33) Du Noüy, P. L. An Interfacial Tensiometer For Universal Use. *J. Gen. Physiol.* **1925**, *7*, 625–631.
- (34) Wachter, S.; Jakobs, T.; Kolb, T. *Comparison of spray quality for two different flow configurations: Central liquid jet versus annular liquid sheet*; 29th European Conference on Liquid Atomization and Spray Systems (ILASS) 2019.
- (35) Wachter, S.; Jakobs, T.; Kolb, T. Towards system pressure scaling of gas assisted coaxial burner nozzles – An empirical model. *Appl. Energ. Comb. Sci.* **2021**, *5*, 100019.
- (36) Araneo, L.; Damaschke, N.; Tropea, C. Measurement and Prediction of the Gaussian Beam Effect in the PDA. *Laser Techniq. Fluid Mech.* **2002**, 189–207.
- (37) Kapulla, R.; Najera, S. B. Operation conditions of a phase Doppler anemometer: droplet size measurements with laser beam power, photomultiplier voltage, signal gain and signal-to-noise ratio as parameters. *Meas. Sci. Technol.* **2006**, *17*, 221–227.
- (38) Albrecht, H.-E. *Laser doppler and phase doppler measurement techniques*; Springer: Berlin, New York, 2003.
- (39) Schäfer, W.; Rosenkranz, S.; Brinckmann, F.; Tropea, C. Analysis of pneumatic atomizer spray profiles. *Particuology* **2016**, *29*, 80–85.
- (40) DIN SPEC 91325:2015–06. *Charakterisierung von Sprays und Sprühprozessen durch die Messung der Größe und der Geschwindigkeit nicht-transparenter Tropfen; Text Deutsch und Englisch*; Beuth Verlag GmbH: Berlin, 2015.
- (41) Helmholtz. XLIII. On discontinuous movements of fluids. *London, Edinburgh Dublin Philos. Mag. J. Sci.* **1868**, *36*, 337–346.
- (42) Thomson, W. XLVI. Hydrokinetic solutions and observations. *London, Edinburgh Dublin Philos. Mag. J. Sci.* **1871**, *42*, 362–377.
- (43) Marmottant, P.; Villermaux, E. On spray formation. *J. Fluid Mech.* **2004**, 73–111.
- (44) Dimotakis, P. E. Two-dimensional shear-layer entrainment. *AIAA Journal* **1986**, *24*, 1791–1796.

Mass Flow Scaling of Gas-Assisted Coaxial Atomizers

Simon Wachter ^{1,*} , Tobias Jakobs ¹  and Thomas Kolb ^{1,2} 

¹ Institute for Technical Chemistry, Karlsruhe Institute of Technology, 76344 Eggenstein-Leopoldshafen, Germany; tobias.jakobs@kit.edu (T.J.); thomas.kolb@kit.edu (T.K.)
² Engler-Bunte-Institute, Karlsruhe Institute of Technology, 76131 Karlsruhe, Germany
* Correspondence: simon.wachter@kit.edu

Abstract: This study aims to derive basic principles for liquid mass flow scaling of gas-assisted coaxial nozzles. Four liquid mass flow steps were investigated in the range of $\dot{M}_{liq} = 20\text{--}500 \text{ kg} \cdot \text{h}^{-1}$, applying four atomizers with similar geometry designed at $We_{aero} = \text{const}$. High-speed camera and phase Doppler anemometer were utilized to detect the local droplet size distribution. To estimate a reliable measurement plane, a detection method and determination according to the free jet theory was used. The resulting droplet size was analyzed, applying the aerodynamic Weber number, as well as the gas momentum flow. An empirical model was derived out of the measured data, which allows for liquid mass flow scaling when process parameters such as GLR , liquid mass flow, and required Sauter mean diameter are specified. The model was developed as a first step towards liquid mass flow scaling of gas-assisted coaxial atomizers within the investigated range of operating conditions.

Keywords: mass flow scaling; gas-assisted nozzles; Weber number; empirical model



Citation: Wachter, S.; Jakobs, T.; Kolb, T. Mass Flow Scaling of Gas-Assisted Coaxial Atomizers.

Appl. Sci. **2022**, *12*, 2123.

<https://doi.org/10.3390/app12042123>

app12042123

Academic Editor: Manuel Armada

Received: 1 February 2022

Accepted: 14 February 2022

Published: 17 February 2022

Publisher's Note: MDPI stays neutral with regard to jurisdictional claims in published maps and institutional affiliations.



Copyright: © 2022 by the authors. Licensee MDPI, Basel, Switzerland. This article is an open access article distributed under the terms and conditions of the Creative Commons Attribution (CC BY) license (<https://creativecommons.org/licenses/by/4.0/>).

1. Introduction

Gas-assisted coaxial atomizers with central liquid jets are commonly utilized in industrial applications such as spray drying and coating [1], food-processing [2], combustion [3], and gasification processes [4]. Despite the noted variety of possible applications, physical as well as atomization phenomena forming a droplet collective from a liquid jet through a high-velocity gas stream are not yet fully understood. As this topic is of fundamental interest in the field of two-phase flows, extensive research was already performed on the morphological classification of liquid jet breakup [5], the secondary breakup of liquid fragments [6,7], or spray characterization [8,9]. Research in the field of gas-assisted atomization was mostly performed at the laboratory scale. Here, the utilized atomizers were mainly operated at low liquid and gas mass flows to identify subsequent effects more clearly [10,11]. After adjustment of the lab-scale atomizer to produce an adequate spray for the later process, the upscaling step of mass flows toward industrial conditions was performed empirically in most cases, as discussions on scaling rules in literature are scarce.

Against this background, the present work aims to derive key principles of scaling regulations from experimental data. The experimental work is focused on the scale-up of the liquid mass flow of coaxial gas-assisted atomizers with central liquid jets without changes in droplet size. Typically, dimensionless numbers are used for scale-up [12]. In atomization literature, several dimensionless numbers, such as gas-to-liquid ratio, momentum flow and flux ratio, aerodynamic Weber number, Reynolds numbers for gas and liquid phase, Ohnesorge number as well as nozzle dimension ratios, are used for description of spray processes. As the increase in liquid mass flow affects dimensionless numbers to a different extent, an approach that keeps the most common dimensionless numbers constant (We_{aero} , GLR) while increasing liquid mass flow and adapting nozzle geometry (d_{liq} , s_{gas}) was selected for this study.

2. Theoretical Background

As previously noted, various studies investigated the effects of liquid properties, nozzle geometries, and operating conditions on the primary jet breakup of coaxial gas-assisted atomizers (see Figure 1) at lab-scale. In the following, several relevant studies addressing the atomization of liquid jets with high-velocity gas streams, which describe jet breakup and parameters influencing spray characteristics, are summarized. A classification of different primary breakup regimes was performed by Faragò and Chigier for different nozzle geometries at $d_{liq} = 1\text{--}1.5\text{ mm}$ [13].

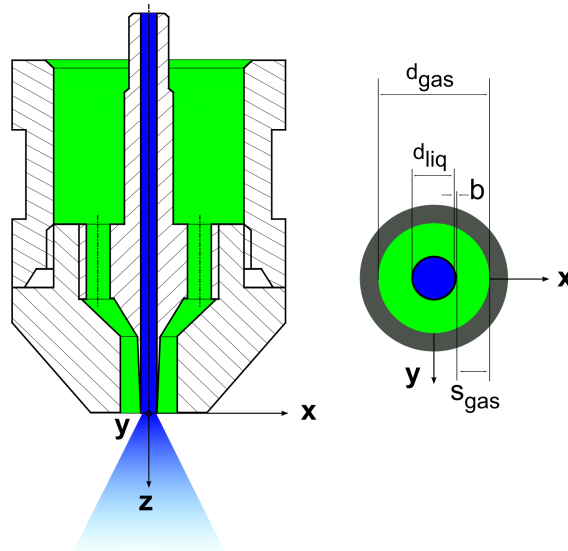


Figure 1. Schematic of a gas-assisted coaxial atomizer with central liquid jet (blue) and annular gas stream (green).

The jet breakup morphologies were classified using the dimensionless numbers Re_{liq} and We_{aero} , in accordance with Equations (1) and (2), in which the liquid jet diameter d_{liq} , velocity v , density ρ , dynamic viscosity η , and surface tension σ were used for the calculations. The subscripts *gas* and *liq* represent the gas and liquid phase, respectively:

$$Re_{liq} = \frac{d_{liq} \cdot v_{liq} \cdot \rho_{liq}}{\eta_{liq}} \tag{1}$$

$$We_{aero} = \frac{(v_{gas} - v_{liq})^2 \cdot \rho_{gas} \cdot d_{liq}}{\sigma} \tag{2}$$

The Rayleigh-type breakup leads to the disintegration of a liquid jet into large droplets close to the center line of the spray, and it occurs at $We_{aero} < 25$. For $25 < We_{aero} < 70$, the membrane-type breakup is detected. In this regime, gas-filled membranes near the nozzle orifice are formed, which disintegrate into small droplets and an accumulated liquid rim. For $We_{aero} > 100$, the fiber-type breakup is divided into two submodes; namely, pulsating and superpulsating. In the pulsating submode, small fibers are peeled off the liquid jet near the nozzle orifice, and the liquid jet is atomized into small liquid fragments. Superpulsating results in droplet number density fluctuations in the resulting spray, while the liquid jet is atomized immediately after the nozzle discharge [13]. In subsequent investigations, Lasheras and Hopfinger [14] used the momentum flux ratio j , presented in Equation (3), to distinguish between the fiber-type breakup submodes:

$$j = \frac{j_{gas}}{j_{liq}} = \frac{v_{gas}^2 \cdot \rho_{gas}}{v_{liq}^2 \cdot \rho_{liq}} \tag{3}$$

As the dynamic viscosity η_{liq} significantly affects the primary jet breakup, due to the damping effects of the liquid, investigations on primary jet breakup of high-viscosity liquids were performed inter alia by Zhao et al. [15] and Sanger et al. [16].

The resulting spray after the primary and secondary breakup is characterized in the literature concerning influencing parameters such as liquid properties, nozzle geometry, and operating conditions. Most investigations of liquid properties regarding spray formation have focused on changes in liquid viscosity by either the application of Newtonian liquids [17] or shear-thinning fuels [18–21] at increased viscosities. A common result when utilizing high-viscosity liquids is an increased droplet size, primary ligament length, and spray angle. Wachter et al. [22] performed investigations intended to specify the influence of particles on the resulting droplet size by comparing pure liquids and suspensions at constant viscosity. An increase in droplet size was reported in the presence of particles, which could be explained by the tensile strength approach reported by Mulhem et al. and Capes [23,24].

The effect of nozzle geometry on the resulting droplet size can be structured in studies of liquid jet diameter, gas gap width, gas/liquid wall thickness, and gas channel angle. Liquid jet diameter between $d_{liq} = 2\text{--}17$ mm at $A_{gas} = 248$ mm² was investigated by Liu et al. [25], which revealed a nonmonotonic trend on the resulting droplet size with a minimum that moves for small $GLR \approx 0.27$, from $d_{liq} = 2$ mm to $d_{liq} = 10$ mm at $GLR = 5.48$. Kumar et al. [26] performed atomization experiments with $d_{liq} = 4/6/8$ mm and constant $d_{gas} = 15$ mm. The investigations focused on the instability frequencies, primary breakup morphology, and ligament length. By comparing the results at constant $j = 2.8$ and decreasing J (see Equation (4)), a significant increase in the primary breakup length was identified [26]:

$$J = \frac{J_{gas}}{J_{liq}} = \frac{v_{gas}^2 \cdot \rho_{gas} \cdot A_{gas}}{v_{liq}^2 \cdot \rho_{liq} \cdot A_{liq}} \quad (4)$$

The effect of an increase in the gas gap width from $s_{gas} = 0.6\text{--}2$ mm was investigated by Wachter et al. [27], which led to a decrease in the droplet size, and was explained by the free jet theory and Equation (5), with equivalent diameters of the gas orifice d_{eq} and axial distance z [28]:

$$\frac{v(z)}{v_{gas}} = 6.37 \cdot \frac{d_{eq}}{z} \cdot \sqrt{\frac{\rho_0}{\rho}} \quad (5)$$

According to this theory, for increased gas gap width, the velocity of the gas phase exiting the nozzle orifice remains high over a longer distance, due to the decreased gas mass flow entrainment of the surrounding gas phase [28]. This effect results in a longer and more intense interaction between gas and liquid phase, which results in smaller droplet size. Tian et al. [29] conducted investigations concerning the gas/liquid wall thickness. For increasing wall thickness, the interaction point between the emerging phases was shifted to a higher distance from the nozzle orifice, which results in a recirculation zone [29] and enhances the formation of flapping instabilities [30]. The effect of an increase in the gas channel angle was analyzed by several authors, leading to the conclusion that aerodynamic forces are enhanced and droplet size is reduced for low gas velocities [31–33].

Variations in operating conditions and exiting velocities (mostly \dot{M}_{gas} and corresponding v_{gas}) were extensively addressed in the literature by GLR variations (see (6)):

$$GLR = \frac{\dot{M}_{gas}}{\dot{M}_{liq}} \quad (6)$$

For increasing gas velocity or gas mass flow, a decrease in the resulting droplet size was detected by many authors for a variety of different liquid properties and nozzle geometries [34–37]. At high gas velocities, the effect of further gas velocity increments on droplet size decreases. According to Lefebvre [8], an increase in the liquid jet velocity or

liquid mass flow-applying one nozzle-leads to an increase in the resulting droplet size, mostly due to a decrease in the relative velocity between the two emerging phases.

Even though there are many studies that deal with the effects of single parameters on the atomization process and spray characteristics, literature focusing on nozzle scaling is scarce. Leroux et al. [10] considered the effects of nozzle scaling for three primary jet thicknesses $d_{liq} = 0.4/1/2$ mm and gas gap widths $d_{gas} = 3.5/6/8$ mm. The authors choose the approach of comparing nozzles of different primary jet thickness with a constant Re_{liq} and momentum flow ratio J (see Equation (4)) with respect to the primary breakup morphology. For constant dimensionless parameters, different breakup morphology was detected, as the application of a small d_{liq} led to prompt atomization, whereas a large d_{liq} resulted in long primary ligaments and large droplets [10]. In a second study, Leroux et al. [11] performed droplet size measurements, and concluded, that droplet size is most affected by the primary breakup morphology. A scaling rule, concerning nozzle geometry or process parameters, for increased liquid mass flows, leading to constant droplet sizes for variable liquid mass flows, was not specified.

The literature review reveals that many investigations were performed at lab-scale, concerning the influence of specific parameters as liquid properties, nozzle geometry, and operating conditions on primary jet breakup or resulting droplet size. In contrast, for nozzle scaling towards increased liquid mass flows, only a few studies were published, but no scaling rules were established. To reduce this knowledge gap in the domain of nozzle scaling, the present study focuses on liquid mass flow scaling. The first set of experiments was performed with one nozzle that was applied at high gas velocity while increasing the liquid mass flow. Thereafter, experiments keeping We_{aero} constant were conducted, as this dimensionless number is most relevant in the field of atomization and was also used for morphology characterization [13]. Therefore, the following three steps were applied:

- The liquid velocity v_{liq} was kept constant for increasing \dot{M}_{liq} , which requires an increase in d_{liq} ;
- GLR was kept constant, which requires an increase in \dot{M}_{gas} for increasing \dot{M}_{liq} ;
- We_{aero} was kept constant, which requires a decrease in v_{gas} for increasing d_{liq}

The experiments were conducted at $\dot{M}_{liq} = 20/50/100/500$ kg \cdot h⁻¹ and $We_{aero} = 250/500/750/1000$.

3. Experimental Setup

As the experiments were carried out over a wide range of liquid mass flows ($\dot{M}_{liq} = 20$ – 500 kg \cdot h⁻¹), two different spray test rigs were employed. The ATMOSpheric spray test rig (ATMO), which is described in detail in Wachter et al. [38], was utilized for liquid mass flows at the lab-scale between $\dot{M}_{liq} = 20$ – 100 kg \cdot h⁻¹.

The burner test rig (BTR), which is shown in Figure 2, was applied for the investigation of the nozzles featuring liquid mass flows on the industrial scale of $\dot{M}_{liq} = 500$ kg \cdot h⁻¹.

The nozzle was mounted on a twin-fluid lance, that was supplied with liquids from a storage tank. The liquid mass flow was adjusted by a Coriolis mass flow and density meter and pumped through an eccentric screw pump with a mass flow range of $\dot{M}_{liq} = 400$ – 1300 kg \cdot h⁻¹. Pressurized gas was provided by a screw compressor with a 5 m³ pressure vessel at $p_{sys} = 11$ bar. The measurement and regulation of the gas mass flow ($\dot{M}_{gas} = 50$ – 400 kg \cdot h⁻¹) was performed by a hot wire anemometer with a coupled valve.

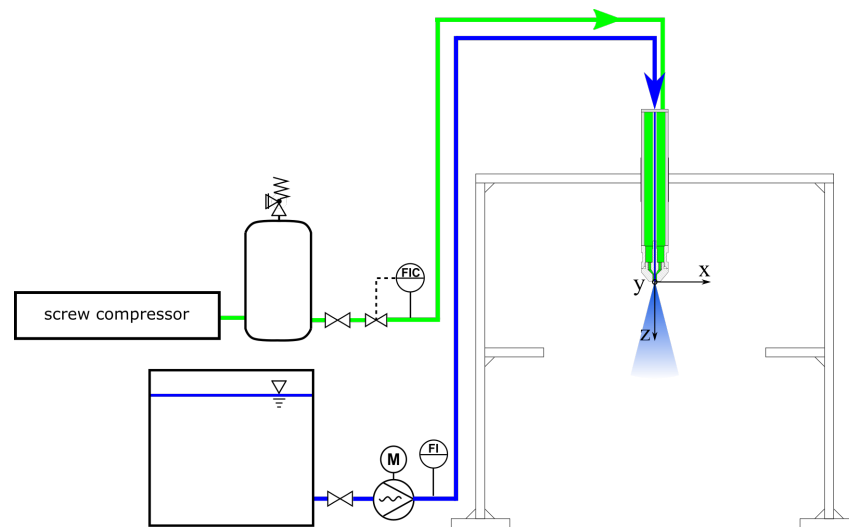


Figure 2. Schematic of experimental setup—Burner Test Rig (BTR).

The nozzle dimensions are given in Table 1. As the central tube thickness between liquid and gas phase b has a significant influence on the resulting spray [26], b was reduced to a minimum size of $b = 0.1$ mm. According to Tian et al. [29], b has to be minimized to avoid disturbances at the exit of the nozzle. To enable a comparison with earlier studies, all applied nozzles feature parallel flow channels of the gas and liquid phase.

Table 1. Dimensions of applied atomizers at nozzle orifice for $v_{liq} = 1.7$ m · s^{−1}.

Nozzle Number	\dot{M}_{liq} in kg · h ^{−1}	d_{liq} in mm	b in mm	d_{gas} in mm
N1	20	2.0	0.1	5.3
N2	50	3.2	0.1	9.2
N3	100	4.5	0.1	14.1
N4	500	10.0	0.1	37.3

Water was used at $T = 20$ °C and $p_{sys} = 1$ bar, with $\eta_{liq} = 1$ mPa · s, $\sigma = 0.0719$ N · m^{−1} and $\rho_{liq} = 998$ kg · m^{−3}.

For the detection of primary jet breakup and for validation of the droplet size results, a high-speed camera was used in all experiments. An appropriate illumination of the images was achieved by a 9×4500 lm light-emitting diodes (LED) array in a backlight configuration. For every operating condition, a set of 2000 images was recorded near the nozzle orifice, as well as in the measuring plane of the phase Doppler anemometer to guarantee a high-quality data base. The camera enabled images with 1 megapixel at a 3600 Hz frame rate. A more detailed description of the setup is given in [22].

At the industrial scale, the high-speed camera was also used to investigate the droplet size distribution. For each operating condition, 2000 images in the measurement plane were recorded, whereas every 20th image was applied for the droplet size calculation to avoid the double determination of droplets. The calculation was performed by means of an algorithm with a global threshold method by Otsu [39]. Out of 100 images, at least 29,000 droplets were analyzed per operating condition, achieving a reliable data base [40]. The lowest detectable droplet size was $d_{drop} = 225$ μm, which equaled three pixels in the high-speed camera sensor. As the droplet size at the industrial scale was expected to be significantly above the measurement limitation, the resolution was considered to be sufficient.

For spray characterization at the lab-scale, a fiber phase Doppler anemometer (PDA) with a SprayExplorer was utilized in a forward scattering arrangement (first-order refraction) to investigate the droplet diameter locally. The settings of the setup were optimized in accordance with [41], which led to a measuring range of droplet diameter from 2–1357 μm

for water, respectively [42]. The settings, evaluated by means of a sensitivity analysis adapted from Kapulla et al. [43], are presented in Table 2.

Table 2. Evaluated settings of fiber PDA for application in labscale experiments.

Parameters	Values	Unit
Transmitter focal length f_T	1000	mm
Receiver focal length f_R	1000	mm
Beam expander ratio E	1	-
Receiver slit width (physical) l_S	200	μm
Laser wavelength λ_L	561	nm
Laser power (transmitter exit)	40	mW
Off-axis angle Φ_R	70	°
Frequency shift	80	MHz

For each operating condition, radial measurements of droplet size and velocity were performed between $-30 \text{ mm} \leq x \leq 30 \text{ mm}$ with $\Delta x = 2\text{--}4 \text{ mm}$. To ensure high-quality data sets, radial measurements were conducted three times (with one full profile for a symmetry check and two mirrored profiles from the spray boundary to the spray center after symmetry was proved). At each radial position, a measurement of 50,000 droplets or for the duration of 60 seconds was applied. The toolbox *SprayCAT* utilized the calculation of arithmetic means as the mass-weighted integral Sauter mean diameter $ID_{32,m}$ in Equation (7):

$$ID_{32,m} = \frac{\sum_{i=1}^N D_{30,i}^3 \cdot \dot{m}_i \cdot A_i}{\sum_{i=1}^N D_{20,i}^2 \cdot \dot{m}_i \cdot A_i} \quad (7)$$

Further information on the computation of the mass flux \dot{m}_i , global size distribution, and size moments are summarized in DIN SPEC 91325 [44] and in Albrecht [42].

4. Results and Discussion

For an illustration of the necessity of liquid mass flow scaling rules, in an initial set of experiments, nozzle N1 (see Table 1) was operated at varying liquid mass flows of $\dot{M}_{liq} = 20/35/50 \text{ kg} \cdot \text{h}^{-1}$ (i.e., $v_{liq} = 1.7/3.1/4.4 \text{ m} \cdot \text{s}^{-1}$). The gas mass flow was kept constant at $\dot{M}_{gas} = 14 \text{ kg} \cdot \text{h}^{-1}$ (i.e., $We_{aero} = 1000$ and gas velocity $v_{gas} \approx 178 \text{ m} \cdot \text{s}^{-1}$).

In a second set of experiments, the four mass flow steps at four different We_{aero} values were investigated. The operating conditions and relevant calculated dimensionless numbers for the respective nozzle are listed in Table 3.

Table 3. Operating conditions and calculated dimensionless numbers.

Nozzle Number	\dot{M}_{liq} in $\text{kg} \cdot \text{h}^{-1}$	GLR	We_{aero}	v_{gas} in $\text{m} \cdot \text{s}^{-1}$	j	J
N1	20	0.36	250	88	2.99	29.80
N2	50	0.36	250	70	1.98	24.27
N3	100	0.36	250	59	1.38	20.23
N4	500	0.36	250	40	0.62	13.54
N1	20	0.50	500	124	5.93	41.99
N2	50	0.50	500	98	3.89	33.98
N3	100	0.50	500	83	2.73	28.46
N4	500	0.50	500	56	1.21	18.96
N1	20	0.61	750	151	8.80	51.13
N2	50	0.61	750	120	5.83	41.61
N3	100	0.61	750	101	4.04	34.63
N4	500	0.61	750	68	1.78	23.03
N1	20	0.70	1000	174	11.68	58.92
N2	50	0.70	1000	138	7.71	47.85
N3	100	0.70	1000	117	5.42	40.11
N4	500	0.70	1000	79	2.41	26.75

4.1. Significance of Liquid Mass Flow Scaling Rules

Figure 3 depicts the effect of an increase in the liquid mass flow on the resulting droplet size as a radial distribution (left) and high-speed camera images (right) while operating nozzle N1.

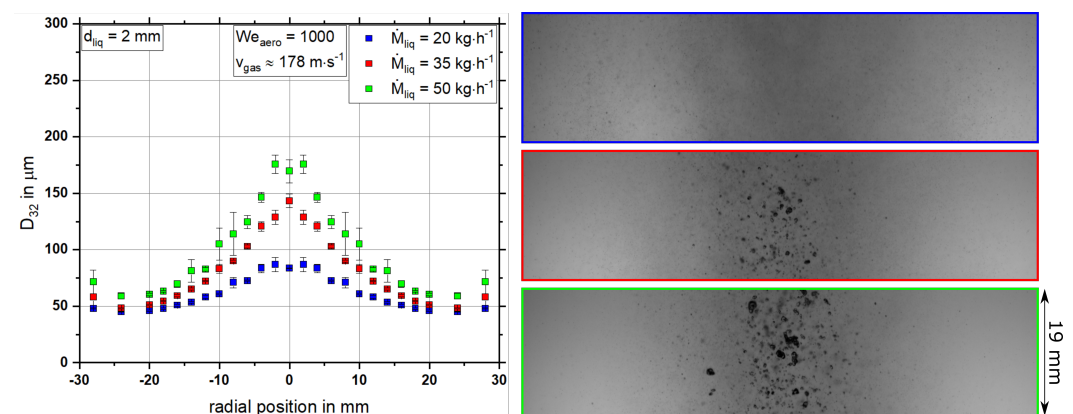


Figure 3. Radial distribution of Sauter mean diameter (left) and high-speed camera images at $z = 130$ mm (right) utilizing nozzle N1 at $\dot{M}_{gas} = 14 \text{ kg} \cdot \text{h}^{-1}$, $We_{aero} = 1000$ applying $\dot{M}_{liq} = 20/35/50 \text{ kg} \cdot \text{h}^{-1}$.

As expected, for an increment in the liquid mass flow \dot{M}_{liq} , the Sauter mean diameter is increased significantly over the entire measured radial distribution. In particular, an increasing droplet size was detected near the centerline of the spray. The high-speed camera images shown in Figure 3 (right) underpin the results of the quantitative measurement technique, as the centerline of the spray reveals a huge quantity of large droplets at high liquid mass flows, even though a high gas velocity of $v_{gas} \approx 178 \text{ m} \cdot \text{s}^{-1}$ is applied. The remaining large liquid droplets originate from the incomplete primary breakup of the liquid jet near the nozzle orifice, due to the insufficiently high aerodynamic forces of the gas phase [17]. To reduce the droplet size for high liquid mass flow, two different approaches can be selected: (i) increasing the gas velocity up to sonic speed for a constant nozzle geometry; or (ii) adaptation of the nozzle geometry without significant further increase in gas velocity. The first approach is limited by sonic speed. Additionally, relevant process conditions, e.g., reaction zone position, residence time, and flow field should not be affected by nozzle scaling to guarantee reliable process operation. Beyond that, the effect of gas velocity on resulting droplet size levels off with increasing gas velocity [9,45].

Those drawbacks can be avoided over a large range of liquid mass flow rates by adapting the nozzle geometry, as described in Section 2.

4.2. Evaluation of the Relevant Measurement Position for Coaxial Nozzles

To estimate the ideal measurement position for droplet size detection, primary breakup was investigated using high-speed camera images. When performing droplet size measurements, the measurement plane must fulfill various criteria: (i) the secondary breakup of liquid droplets and fragments must be completed; (ii) droplets must be spherical, which enables the application of quantitative measurement techniques such as PDA; and (iii) droplet number density must be adequate to minimize measurement errors via shading and the Gaussian beam effect from consideration [42]. As shown in Figure 4, these criteria were fulfilled for $\dot{M}_{liq} = 20 \text{ kg} \cdot \text{h}^{-1}$ and also for the lowest investigated We_{aero} at $z = 130 \text{ mm}$. For increasing We_{aero} the atomization process was even finished at lower z values. In contrast to this, the primary breakup of the nozzle N4 at $\dot{M}_{liq} = 500 \text{ kg} \cdot \text{h}^{-1}$ and $We_{aero} = 250$ reveals that at $z = 130 \text{ mm}$, none of the mentioned criteria is achieved, as the primary breakup length in particular significantly increases with increasing liquid mass flow. To guarantee the best possible comparability of the data, the measurement plane was chosen based on the theory of similarity at constant dimensionless ratio z/d_{eq} based on the equivalent diameter d_{eq} of free jet theory [46]. This method is commonly applied for gas flame length calculation and is based on momentum conservation, as described in further detail in Hotz et al. [47]. Here, this concept was utilized for two phase free jets emerging from coaxial atomizers, where the equivalent diameter d_{eq} was calculated using Equation (8) for each nozzle:

$$d_{eq} = \sqrt{\frac{4 \cdot A_{gas}}{\pi}} \tag{8}$$

For nozzle N1 operated at $\dot{M}_{liq} = 20 \text{ kg} \cdot \text{h}^{-1}$, the measurement plane was set to $z = 130 \text{ mm}$, which represents $z/d_{eq} = 26$. The application of nozzles N2–N4, which have higher d_{eq} values, leads to a constant $z/d_{eq} = 26$ in measurement positions of $z = 220/340/930 \text{ mm}$. The verification of this concept was performed with high-speed camera images, which revealed that all of the mentioned criteria for measurement positions were fulfilled for the respective measurement plane. As an example, the measurement plane of nozzle N4 is shown in Figure 4, when applying $\dot{M}_{liq} = 500 \text{ kg} \cdot \text{h}^{-1}$ at $We_{aero} = 250$.

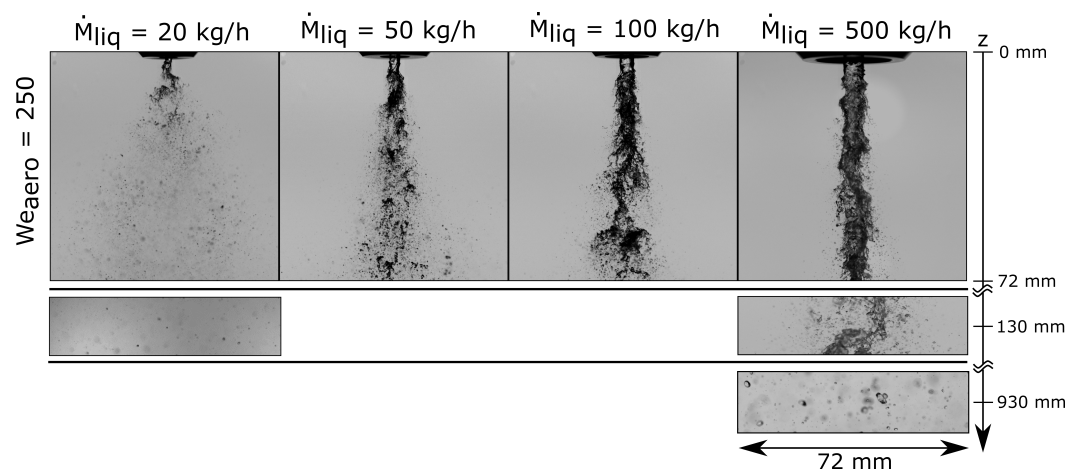


Figure 4. High-speed camera images of primary breakup at $We_{aero} = 250$ at varying liquid mass flows and different axial positions $z = 0, 130, 930 \text{ mm}$.

Following the evaluation of the concrete measurement positions for each nozzle, measurement techniques were applied to detect the resulting droplet sizes as described in Section 4.3.

Finally, for all liquid mass flows $\dot{M}_{liq} = 20\text{--}500 \text{ kg} \cdot \text{h}^{-1}$ and $We_{aero} = 250$ primary breakup is always in fiber type mode (see Figure 4), which is characterized by small liquid fibers that are peeled off the liquid jet, according to [13]. As for further experimental investigation, We_{aero} was further increased up to 1000, and primary breakup was in fiber type for the whole set of experiments.

4.3. Mass Flow Scaling

In the following, all integral results of the experiments listed in Table 3 are presented in Figure 5 as a function of the liquid mass flow (left) and We_{aero} (right). The quadratic symbols represent calculations of the integral mass-weighted Sauter mean diameter according to Equation (7) derived from radial measurements with PDA. The triangular symbols represent droplet size based on measurements from high-speed camera analyzed with the detection routine for droplets described in Section 3.

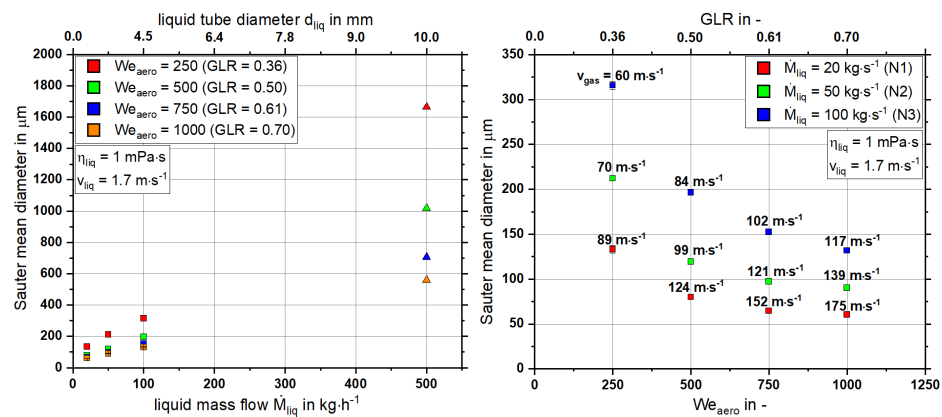


Figure 5. Integral Sauter mean diameter for varying liquid mass flow (or liquid tube diameter) (left) and aerodynamic Weber number (or GLR) (right); symbols: \square stands for data from PDA, \triangle represents data from high-speed camera.

For an increase in liquid mass flow and constant GLR , an increase in the resulting droplet size can be detected. This effect can be explained by a decrease in gas velocity, which leads to lower aerodynamic forces for the atomization of higher liquid mass flows. In contrast to this, an increase in the We_{aero} led to a decrease in the droplet size due to the higher aerodynamic forces available for atomization and increased GLR . As presented in Figure 5 (right), with increasing We_{aero} , the effect of We_{aero} on droplet size is significantly decreased. Solely keeping We_{aero} and GLR constant for liquid mass flow scaling is not sufficient to achieve a constant resulting droplet size. However, to obtain constant droplet size of $ID_{32,m} = 140 \mu\text{m}$, such as between $\dot{M}_{liq} = 20 \text{ kg} \cdot \text{h}^{-1}$ and $\dot{M}_{liq} = 100 \text{ kg} \cdot \text{h}^{-1}$, We_{aero} must be increased by a factor of four, whereas gas velocity needs an increase of about 30%. As previous studies of the authors focused on the gas momentum flow to achieve a scaling principle for system pressure [27], in the following section, the measurements are plotted over this parameter.

4.4. Empirical Model for Liquid Mass Flow Scaling

To derive a liquid mass flow scaling principle for gas-assisted coaxial nozzles, the droplet size results were plotted over the gas momentum flow J_{gas} as presented in Figure 6 (left).

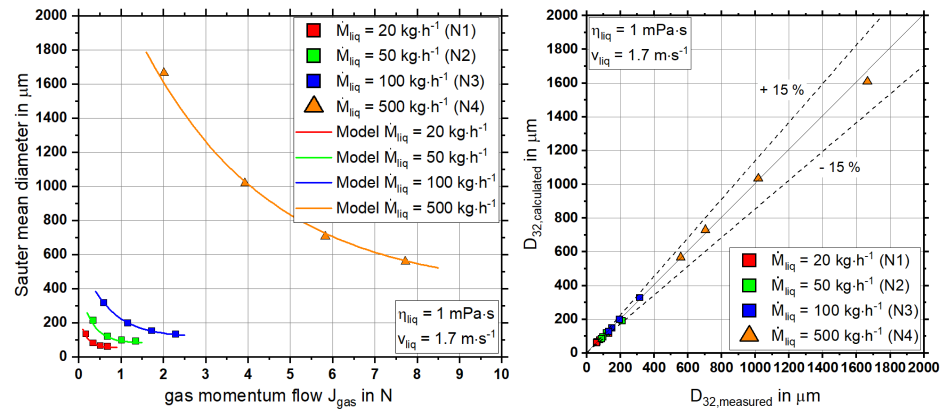


Figure 6. Integral Sauter mean diameter for varying gas momentum flow as symbols for measurements and lines as calculation of proposed scaling model (left); parity plot for deviation observation between measured and calculated droplet sizes via proposed model (right). Symbols: □ stands for data from PDA; △ represents data from high-speed camera.

The diagram shows that for an increase in the liquid mass flow, an offset in droplet size to higher values occurs. This implies that achieving a constant droplet size with an increased liquid mass flow requires increased gas momentum flows. The gas momentum flow is defined by the factors of gas velocity, gas density, and the gas orifice area of the nozzle. As gas density is a typical process condition, a potential nozzle scaling approach must enable the calculation of the gas velocity and gas orifice area. With this objective for a liquid mass flow scaling approach, a potential fit with the dependence of \dot{M}_{liq} and J_{gas} was selected, according to Equation (9), due to the shape of the Sauter mean diameter plots.

$$ID_{32,m} = A(\dot{M}_{liq}) \cdot e^{-\frac{J_{gas}}{B(\dot{M}_{liq})}} + C(\dot{M}_{liq}) \quad (9)$$

For varying liquid mass flows \dot{M}_{liq} , three mass flow dependent parameters A, B, and C were applied and correlated via the least-square method. The dependence on liquid mass flows was kept linear to maintain the model’s simplicity, as is reflected in Equations (10)–(12):

$$A(\dot{M}_{liq}) = 4.6 \cdot \dot{M}_{liq} + 91 \quad (10)$$

$$B(\dot{M}_{liq}) = 0.006 \cdot \dot{M}_{liq} + 0.03 \quad (11)$$

$$C(\dot{M}_{liq}) = 0.67 \cdot \dot{M}_{liq} + 45 \quad (12)$$

The parity plot in Figure 6 (right) depicts the accuracy of the model, as the measured and calculated droplet sizes are compared. For all measurement conditions, good agreement between the measured and calculated values was achieved. The maximum percentage deviation with 13.2 % ($\Delta D_{32} = 17.6 \mu\text{m}$) was observed at $\dot{M}_{liq} = 100 \text{ kg} \cdot \text{h}^{-1}$ and $We_{aero} = 250$. In contrast, the maximum deviation in absolute droplet size was $\Delta D_{32} = 55.5 \mu\text{m}$ (3.3 %) at $\dot{M}_{liq} = 500 \text{ kg} \cdot \text{h}^{-1}$ and $We_{aero} = 250$.

Thus, the model approach presented in Equation (9) is considered adequate for the mass flow scaling of gas-assisted nozzles with central liquid jets in the range of $\dot{M}_{liq} = 20\text{--}500 \text{ kg} \cdot \text{h}^{-1}$ for $v_{liq} = 1.7 \text{ m} \cdot \text{s}^{-1}$.

The principle must be applied as follows: (i) using Equation (9), the applied liquid mass flow, requested droplet size, and necessary gas momentum flow can all be calculated; (ii) GLR must be specified as process condition and gas mass flow calculation; (iii) as the liquid velocity remained constant in the investigation, the liquid tube diameter can be determined; and (iv) with the definition of the gas mass and momentum flows, the gas velocity and gas gap width are provided.

5. Conclusions

This study aims to lay the groundwork for liquid mass flow scaling of gas-assisted coaxial atomizers. An approach that keeps the most relevant dimensionless parameters constant (We_{aero} , GLR) was chosen. Four liquid mass flow steps (20/50/100/500 kg · h⁻¹), each operated at $We_{aero} = 250/500/750/1000$, were investigated in terms of spray quality (D_{32} , $ID_{32,m}$) and primary breakup. For each liquid mass flow, a specific nozzle was designed. A high-speed camera as well as a phase Doppler anemometer were utilized for spray investigation. The following conclusions can be drawn:

1. Comparable measurement planes for varying liquid mass flows based on the free jet theory were determined;
2. An increase in liquid mass flow led to an increase in droplet size while keeping We_{aero} and GLR constant;
3. An increase in We_{aero} led to a reduction in droplet size at constant liquid mass flow;
4. An empirical model for liquid mass flow scale-up of gas-assisted coaxial nozzles was derived, based on gas momentum flow J_{gas} .

Author Contributions: Conceptualization, S.W. and T.J.; investigation, S.W.; data curation, S.W.; writing—original draft preparation, S.W.; writing—review and editing, T.J. and T.K.; visualization, S.W.; supervision, T.K. All authors have read and agreed to the published version of the manuscript.

Funding: The authors gratefully acknowledge the financial support of the Helmholtz Association of German Research Centers (HGF) in the context of the research program Materials and Technologies for the Energy Transition (MTET). We acknowledge support by the KIT-Publication Fund of the Karlsruhe Institute of Technology.

Conflicts of Interest: The authors declare no conflict of interest.

References

1. Ronsse, F.; Duangkhamchan, W.; Dewettinck, K.; Pieters, J. Computational Fluid Dynamics (CFD) modelling of the fluidised bed coating process. In *7th International conference on Simulation and Modeling in the Food and Bio-Industry (Foodsim)*; Eurosis-ETI: Ostend, Belgium, 2012.
2. Mlkvik, M.; Stähle, P.; Schuchmann, H.P.; Gaukel, V.; Jedelsky, J.; Jicha, M. Twin-fluid atomization of viscous liquids: The effect of atomizer construction on breakup process, spray stability and droplet size. *Int. J. Multiph. Flow* **2015**, *77*, 19–31, doi:10.1016/j.ijmultiphaseflow.2015.06.010.
3. Haidn, O.J.; Habiballah, M. Research on high pressure cryogenic combustion. *Aerosp. Sci. Technol.* **2003**, *7*, 473–491, doi:10.1016/S1270-9638(03)00052-X.
4. Carisson, P.; Gebart, R.; Grönberg, C.; Marklund, M.; Risberg, M.; Wiinikka, H.; Öhrman, O. Spatially resolved measurements of gas composition in a pressurised black liquor gasifier. *Environ. Prog. Sustain. Energy* **2009**, *28*, 316–323, doi:10.1002/ep.10380.
5. Zhao, H.; Liu, H.F.; Tian, X.S.; Xu, J.L.; Li, W.F.; Lin, K.F. Influence of atomizer exit area ratio on the breakup morphology of coaxial air and round water jets. *AIChE J.* **2014**, *60*, 2335–2345, doi:10.1002/aic.14414.
6. Pilch, M.; Erdman, C.A. Use of breakup time data and velocity history data to predict the maximum size of stable fragments for acceleration-induced breakup of a liquid drop. *Int. J. Multiph. Flow* **1987**, *13*, 741–757, doi:10.1016/0301-9322(87)90063-2.
7. Khare, P.; Ma, D.; Chen, X.; Yang, V. Phenomenology of Secondary Breakup of Newtonian Liquid Droplets. In *50th AIAA Aerospace Sciences Meeting including the New Horizons Forum and Aerospace Exposition*; American Institute of Aeronautics and Astronautics: Reston, VA, USA, 2013; doi:10.2514/6.2012-171.
8. Lefebvre, A. Twin-Fluid atomization: Factors influencing mean drop size. *At. Sprays* **1992**, *2*, 101–119, doi:10.1615/AtomizSpr.v2.i2.30.
9. Hede, P.D.; Bach, P.; Jensen, A.D. Two-fluid spray atomization and pneumatic nozzles for fluid bed coating/agglomeration purposes: A review. *Chem. Eng. Sci.* **2008**, *63*, 3821–3842, doi:10.1016/j.ces.2008.04.014.
10. Leroux, B.; Delabroy, O.; Lacas, F. Experimental study of coaxial atomizers scaling. Part 1: Dense core zone. *At. Sprays* **2007**, *17*, 381–407, doi:10.1615/AtomizSpr.v17.i5.10.
11. Leroux, B.; Delabroy, O.; Lacas, F. Experimental study of coaxial atomizers scaling. Part 2: Diluted zone. *At. Sprays* **2007**, *17*, 409–430, doi:10.1615/AtomizSpr.v17.i5.20.
12. Zlokarnik, M.. Dimensional Analysis and Scale-Up in Theory and Industrial Application. In *Pharmaceutical Process Scale-Up*; CRC Press: Boca Raton, FL, USA, 2005; pp. 35–90, doi:10.1201/9781420026658-5.
13. Chigier, N.; Faragó, Z. Morphological Classification of Disintegration of Round Liquid Jets in a Coaxial Air Stream. *At. Sprays* **1992**, *2*, 137–153, doi:10.1615/AtomizSpr.v2.i2.50.

14. Lasheras, J.C.; Hopfinger, E.J. Liquid Jet Instability and Atomization in a Coaxial Gas Stream. *Annu. Rev. Fluid Mech.* **2000**, *32*, 275–308, doi:10.1146/annurev.fluid.32.1.275.
15. Zhao, H.; Liu, H.F.; Xu, J.L.; Li, W.F.; Cheng, W. Breakup and atomization of a round coal water slurry jet by an annular air jet. *Chem. Eng. Sci.* **2012**, *78*, 63–74, doi:10.1016/j.ces.2012.05.007.
16. Sanger, A.; Jakobs, T.; Djordjevic, N.; Kolb, T. Experimental investigation on the influence of ambient pressure on twin-fluid atomization of liquids with various viscosities. In Proceedings of the 13th International Conference on Liquid Atomization and Spray Systems (ICLASS), Tainan, Taiwan, 23–27 August 2015.
17. Wachter, S.; Jakobs, T.; Kolb, T. Experimental investigation on the influence of system pressure on resulting spray quality and jet breakup applying pressure adapted twin-fluid nozzles. *Int. J. Multiph. Flow* **2020**, *125*, 103189, doi:10.1016/j.ijmultiphaseflow.2019.103189.
18. Aliseda, A.; Hopfinger, E.J.; Lasheras, J.C.; Kremer, D.M.; Berchielli, A.; Connolly, E.K. Atomization of viscous and non-newtonian liquids by a coaxial, high-speed gas jet. Experiments and droplet size modeling. *Int. J. Multiph. Flow* **2008**, *34*, 161–175, doi:10.1016/j.ijmultiphaseflow.2007.09.003.
19. Jasuja, A.K. *Plain-Jet Airblast Atomization of Alternative Liquid Petroleum Fuels under High Ambient Air Pressure Conditions*; The American Society of Mechanical Engineers: New York, NY, USA, 1982; doi:10.1115/82-GT-32.
20. Li, L.K.B.; Dressler, D.M.; Green, S.I.; Davy, M.H. Experiments on air-blast atomization of viscoelastic liquids, Part 1: quiescent conditions. *At. Sprays* **2009**, *19*, 157–190, doi:10.1615/AtomizSpr.v19.i2.30.
21. Sanger, A.; Jakobs, T.; Kolb, T. Using Primary Instability Analysis for Determination of Apparent Liquid Viscosity at Jet Breakup Atomizing Non-Newtonian Fluids. In Proceedings of the 27th Annual Conference on Liquid Atomization and Spray Systems (ILASS), Brighton, UK, 4–7 September 2016.
22. Wachter, S.; Jakobs, T.; Kolb, T. Effect of Solid Particles on Droplet Size Applying the Time-Shift Method for Spray Investigation. *Appl. Sci.* **2020**, *10*, 7615, doi:10.3390/app10217615.
23. Mulhem, B.; Schulte, G.; Fritsching, U. Solid–liquid separation in suspension atomization. *Chem. Eng. Sci.* **2006**, *61*, 2582–2589, doi:10.1016/j.ces.2005.11.035.
24. Capes, C.E. *Particle Size Enlargement*; Elsevier: Amsterdam, The Netherlands, 2013.
25. Liu, H.F.; Li, W.F.; Gong, X.; Cao, X.K.; Xu, J.L.; Chen, X.L. Effect of liquid jet diameter on performance of coaxial two-fluid airblast atomizers. *Chem. Eng. Process. Process Intensif.* **2006**, *45*, 240–245, doi:10.1016/j.cep.2005.08.003.
26. Kumar, A.; Sahu, S. Influence of nozzle geometry on primary and large-scale instabilities in coaxial injectors. *Chem. Eng. Sci.* **2020**, *221*, 115694, doi:10.1016/j.ces.2020.115694.
27. Wachter, S.; Jakobs, T.; Kolb, T. Towards system pressure scaling of gas assisted coaxial burner nozzles—An empirical model. *Appl. Energy Combust. Sci.* **2021**, *5*, 100019, doi:10.1016/j.jaecs.2020.100019.
28. Schlichting, H.; Gersten, K.; Krause, E. *Grenzschicht-Theorie: Mit 22 Tabellen*, 10 uberarbeitete auflage ed.; Springer: Berlin/Heidelberg, Germany, 2006; doi:10.1007/3-540-32985-4.
29. Tian, X.S.; Zhao, H.; Liu, H.F.; Li, W.F.; Xu, J.L. Effect of central tube thickness on wave frequency of coaxial liquid jet. *Fuel Process. Technol.* **2014**, *119*, 190–197, doi:10.1016/j.fuproc.2013.11.011.
30. Sanger, A.; Jakobs, T.; Djordjevic, N.; Kolb, T. Effect of primary instability of a high viscous liquid jet on the spray quality generated by a twin-fluid atomizer. In Proceedings of the 26th Annual Conference on Liquid Atomization and Spray Systems (ILASS), Bremen, Germany, 8–10 September 2014.
31. Varga, C.M.; Lasheras, J.C.; Hopfinger, E.J. Initial breakup of a small-diameter liquid jet by a high-speed gas stream. *J. Fluid Mech.* **2003**, *497*, 405–434, doi:10.1017/S0022112003006724.
32. Hardalupas, Y.; Whitelaw, J.H. Characteristics of sprays produced by coaxial airblast atomizers. *J. Propuls. Power* **1994**, *10*, 453–460, doi:10.2514/3.23795.
33. Wachter, S.; Jakobs, T.; Kolb, T. Effect of gas jet angle on primary breakup and droplet size applying coaxial gas-assisted atomizers. *ICLASS Int. Conf. Liq. At. Spray Syst.* **2021**, *1*, doi:10.2218/iclass.2021.5808.
34. Lorenzetto, G.E.; Lefebvre, A.H. Measurements of drop size on a plain-jet airblast atomizer. *AIAA J.* **1977**, *15*, 1006–1010, doi:10.2514/3.60742.
35. Yuan, K.; Chen, L.; Wu, C. Study on characteristics of different types of nozzles for coal-water slurry atomization. *J. Therm. Sci.* **2001**, *10*, 331–335, doi:10.1007/s11630-001-0040-7.
36. Doohar, J.P. Fundamental Considerations for Coal Slurry Atomization. *At. Sprays* **2005**, *15*, 585–602, doi:10.1615/AtomizSpr.v15.i5.60.
37. Mulhem, B.; Fritsching, U.; Schulte, G.; Bauckhage, K. Effect of solid particle characteristics on suspension atomization. *At. Sprays* **2003**, *13*, 321–343, doi:10.1615/AtomizSpr.v13.i23.100.
38. Wachter, S.; Jakobs, T.; Kolb, T. Comparison of Central Jet and Annular Sheet Atomizers at Identical Gas Momentum Flows. *Ind. Eng. Chem. Res.* **2021**, *60*, 11502–11512, doi:10.1021/acs.iecr.1c01526.
39. Otsu, N. A Threshold Selection Method from Gray-Level Histograms. *IEEE Trans. Syst. Man, Cybern.* **1979**, *9*, 62–66, doi:10.1109/TSMC.1979.4310076.
40. Schafer, W.; Rosenkranz, S.; Brinckmann, F.; Tropea, C. Analysis of pneumatic atomizer spray profiles. *Particuology* **2016**, *29*, 80–85, doi:10.1016/j.partic.2015.12.002.
41. Araneo, L.; Damaschke, N.; Tropea, C. *Measurement and Prediction of the Gaussian Beam Effect in the PDA*; Springer: Berlin/Heidelberg, Germany, 2002; pp. 189–208, doi:10.1007/978-3-662-08263-8_12.

42. Albrecht, H.E. *Laser Doppler and Phase Doppler Measurement Techniques*; Springer: Berlin, Germany; New York, NY, USA, 2003.
43. Kapulla, R.; Najera, S.B. Operation conditions of a phase Doppler anemometer: Droplet size measurements with laser beam power, photomultiplier voltage, signal gain and signal-to-noise ratio as parameters. *Meas. Sci. Technol.* **2006**, *17*, 221–227, doi:10.1088/0957-0233/17/1/034.
44. *DIN SPEC 91325:2015-06*. Charakterisierung von Sprays und Sprühprozessen durch die Messung der Größe und der Geschwindigkeit nicht-transparenter Tropfen. 2015.
45. Lefebvre, A.H. Properties of sprays. *Part. Part. Syst. Charact.* **1989**, *6*, 176–186, doi:10.1002/ppsc.19890060129.
46. Pantouflas, E. *Untersuchung des Strahlzerfalls von Flüssigkeiten und Suspensionen bei hohen Luftgeschwindigkeiten Innerhalb einer Innenmischenden Zweistoffdüse*, 1 ed.; docupoint: Magdeburg, Germany, 2009.
47. Hotz, C.; Haas, M.; Wachter, S.; Fleck, S.; Kolb, T. Two-phase free jet model of an atmospheric entrained flow gasifier. *Fuel* **2021**, *304*, 121392, doi:10.1016/j.fuel.2021.121392.

Comparison of spray quality for two different flow configurations: Central liquid jet versus annular liquid sheet

Simon Wachter*¹, Tobias Jakobs¹, Thomas Kolb^{1,2}

¹Karlsruhe Institute of Technology, Institute for Technical Chemistry, 76344 Eggenstein-Leopoldshafen, Germany

²Karlsruhe Institute of Technology, Engler-Bunte-Institute, 76131 Karlsruhe, Germany

*Corresponding author: simon.wachter@kit.edu

Abstract

The research work of the present study is focused on the detailed comparison of two external mixing twin fluid nozzle concepts: (i) a central liquid jet with annular gas stream, (ii) an annular liquid sheet with central gas jet. Both nozzle types are applied in high pressure entrained flow gasifiers (EFG), where atomization is characterized by low Gas-to-liquid ratio (GLR) and high fuel viscosity. In order to compare spray formation as well as atomization efficiency in terms of Sauter mean diameter, a nozzle with equal orifice area of the gas and liquid exit is investigated. The nozzle enables equal atomization conditions concerning GLR, liquid mass flow, velocity of liquid and gas, as well as momentum flow ratio for both nozzle configurations. 4 Newtonian liquids: water and three glycerol/water mixtures with viscosity of 1mPas, 50mPas, 100mPas and 200mPas are used for the experiments in both nozzle configurations at various GLR. For spray analysis, a high speed camera, a shadowgraphy system as well as a phase-doppler analyzer are applied. The use of three different measuring techniques allows for characterization of primary breakup as well as local drop size distribution. With the high speed camera the breakup regime morphology is detected and classified for both operating configurations. Radial measurements of the local Sauter mean diameter are conducted with the phase-doppler analyzer. Furthermore, the spray angle is detected and the integral Sauter mean diameters for all operating conditions is compared for both nozzle configurations to evaluate atomization efficiency.

Keywords

External mixing twin-fluid atomization; comparison jet vs sheet nozzle; breakup morphology; drop size distribution

Introduction

High pressure entrained flow gasification (EFG) is a key technology to enable a future carbon neutral circular economy, by closing the carbon cycle through conversion of biomass and waste based feedstocks to syngas (CO + H₂). EFG typically uses oxygen as gasification agent, which also serves as atomization agent, in consequence Gas-to-Liquid ratios (GLR) < 1 are applied [1]. Commonly external mixing twin-fluid atomizers are used, due to their advantages concerning abrasion and clogging. Experimental and theoretical investigations regarding external mixing twin-fluid atomization, can be divided into two different configurations. The first configuration provides the liquid via a central tube surrounded by a concentric high-velocity annular gas sheet. Detailed investigations on liquid jet breakup morphology of this configuration using water were performed by Faragò, Chigier [2] and expanded by Lasheras and Hopfinger [3]. The breakup was classified into spray regimes showing with increasing Weber number at constant liquid Reynolds number a transition from the Rayleigh type to Membrane and fiber type breakup with the submodes pulsating and superpulsating. Studies on drop size resulting from this configuration applying Newtonian viscous liquids in a viscosity range of $\eta_{liq} = 1 - 100\text{mPas}$ and $\text{GLR} = 1 - 12$ were conducted by Lorenzetto [4], Jasuja [5], Rizk [6] and Walzel [7]. For $\text{GLR} < 1$ and various liquid viscosities, Sängler [8] reported integral drop sizes and detected moreover two different new primary instability modes influencing the resulting drop size. The second nozzle configuration provides the liquid through an annular gap forming a liquid sheet with a high-speed gas jet emerging from a central tube. Applying this configuration, Leboucher et al. [9] and Zhao et al. [10] reported morphological studies on liquid sheet disintegration for water, using different diagrams for interpretation of their results. The authors classified the breakup regimes bubble type, Christmas tree and fibre-type breakup with increasing Weber number depending additionally on the geometry of the nozzle orifice. Experimental work including drop size measurements of water were conducted by Li et al. [11], applying gas velocities $v_{gas} > 180\text{ms}^{-1}$ and Leboucher et al. [9], using different system pressures and swirl configurations.

Summing up, for atomization using external mixing twin-fluid atomizers with liquid supplied through an annular gap most experimental investigations were performed using low viscous liquids and $\text{GLR} > 1$, which is not relevant for EFG operation. Additionally, previous studies do not allow for a comparison of primary breakup and drop size between the two nozzle configurations, due to different measurement and operating conditions or nozzle designs. In this context, the present research applies both nozzle configurations, with equal orifice areas leading to constant

operating conditions in terms of GLR, \dot{m}_{liq} , v_{gas} and momentum flux ratio in both operating modes. Measurements were conducted for liquids with different dynamic viscosities and GLRs relevant for EFG, using a high-speed camera for visualization of primary jet breakup, a shadow sizer for validation purpose and a phase doppler analyzer for local drop size measurements with high radial resolution.

Experimental setup

The experimental setup used in the present work consists of an atmospheric spray test rig (ATMO), a phase doppler analyzer (PDA), a shadowgraphy system and a high-speed camera. For spray generation an external mixing twin-fluid atomizer was applied for atomization of water and several glycerol/water-mixtures.

The spray test rig ATMO is schematically shown in Figure 1. The atomizer is mounted on the twin-fluid lance with liquid supply from a tempered tank. The liquid is delivered by an eccentric screw pump (mass flow range $5 - 40\text{kg h}^{-1}$) and controlled by a Coriolis mass flow meter. Liquid viscosity η_{liq} can be applied in a range of 1 to 1000mPas. Compressed air in the range of $1-20\text{kg h}^{-1}$ is fed to the top of the lance, the air mass flow \dot{m}_{gas} is controlled by a mass flow controller. A honeycomb structure at the inlet of the collection tank serves as flow conditioner, a suction of exhaust air prevents recirculation of small droplets. Fully optical access to the spray enables the use of different laser based measurement systems as well as a high-speed camera.

Experiments were carried out using the external mixing twin-fluid atomizer shown in Figure 1, which can be operated in both configurations discussed above, due to the equal area of the inner and outer orifice, the wall thickness b was set to 0.1mm. In addition, to reduce the influence of flow induced disturbances, as well as to enable comparability towards experimental results of Faragò, Chigier [12] and Zhao et al [10], the nozzle has parallel flow channels.

- (i): Liquid in central tube, gas flow through concentric annular gap.
- (ii): Gas in central tube, liquid flow through concentric annular gap.

The central tube has a diameter of $D_{inner} = 5.4\text{mm}$ and is surrounded by an annular gap with a width of 1.09mm, which leads to identical orifice areas. For minimization of the area between inner and outer orifice, the wall thickness b was set to 0.1mm. In addition, to reduce the influence of flow induced disturbances, as well as to enable comparability towards experimental results of Faragò, Chigier [12] and Zhao et al [10], the nozzle has parallel flow channels.

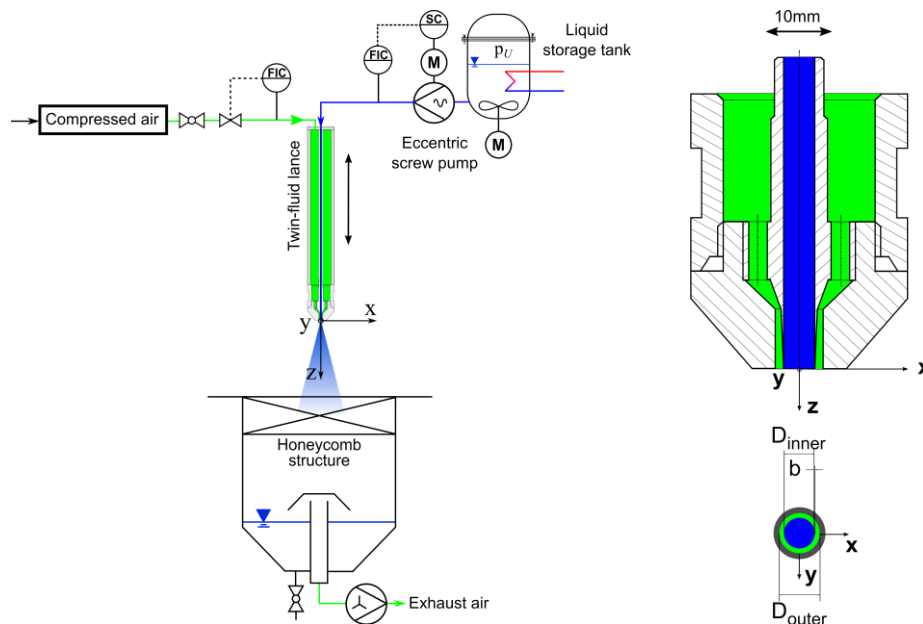


Figure 1. Schematic of the experimental setup applying nozzle configuration (i) – atmospheric spray test rig (ATMO) (left); Schematic of the nozzle geometry and orifice view applying nozzle configuration (i) (right)

Table 1. Physical properties of all used liquids at 20°C and 1atm

	η_{liq} [mPas]	σ [kgs ⁻²]	ρ_{liq} [kgm ⁻³]
water	1	0.0728	998
glycerol/water (78.5 wt.%)	50	0.0656	1204
glycerol/water (84.5 wt.%)	100	0.0649	1220
glycerol/water (89.5 wt.%)	200	0.0642	1233

For the investigation of liquid viscosity η_{liq} on the primary spray breakup and drop size, water and three different glycerol/water – mixtures were used. Surface tension and density of the four liquids applied are almost constant (see Table 1). Liquid viscosity was quantified applying a Physica MCR 101 rheometer from Anton Paar with Searle

type measuring system [13]. Surface tension and density were measured with an EasyDyne tensiometer from Krüss using the Du Noüy ring method [14] and the weighing method, respectively. Mass ratio, viscosity, surface tension and density for all liquids are shown for 20°C and 1atm in Table 1.

A Photron SA4 high speed camera for qualitative investigation of the primary breakup process was employed close to the nozzle orifice. The camera features a frame rate of 3.6kHz at a resolution of 1024 x 1024 pixel and frame rates up to 500kHz at reduced resolution. The images were captured by backlight illumination with a special lighting setup, including an array of 9 high-power light-emitting diodes (LED) with total luminous flux of 9 x 4500lm. To guarantee for a qualitative investigation of the liquid disintegration process a set of 1000 high-speed images was recorded at every operating condition as well as a background reference image without liquid flow. To measure droplet size with high spatial and temporal resolution within the spray cone a Fiber PDA by Dantec Dynamics was used. For data collection the PDA was operated in forward scattering arrangement, refraction mode (1st – order) using the asymmetric Mask B. To guarantee for the detection of large droplets as expected by the atomization of high viscous liquids and avoid sizing errors due to the Gaussian beam effect according to Araneo [15] the PDA was set as shown in Table 2. With this optical configuration, the PDA system allows for detection of droplets with minimum size of 1µm and maximum size of 1307µm in case of water and 1330µm in case of the glycerol/water mixtures, related to the refractive index of the liquid [16]. To improve the PDA settings a sensitivity study as described in [17] was performed. For validation purpose towards sphericity of the droplets a shadowsizer was employed, recording 1000 images for each operational condition.

Table 2. Settings of the Fiber PDA evaluated by the sensitivity analysis

Parameters	Values	Unit	Parameters	Values	Unit
Transmitter focal length	1000	mm	Laser wavelength	514.5	nm
Receiver focal length	1000	mm	Laser power (Transmitter exit)	25	mW
Beam expander ratio	1	-	Off-axis angle	70	°
Receiver slit width (physical)	200	µm	Frequency shift	40	MHz

To enable drop size measurements at several horizontal positions within the spray cone, receiver and transmitter were mounted on a traverse, which guarantees for spatially reproducible operation < 0.1mm. Data were obtained by moving the detection volume relatively to the nozzle position. The measurements were taken at several radial (traverse along x – axis) positions with a radial increment of $\Delta x = 2 - 4$ mm depending on the operating conditions. According to the orientation of the coordinate system as indicated in Figure 1 and the alignment of the fringes of the laser beam couple ($\lambda_L = 514.5$ nm - green), axial- v_z droplet velocity component could be measured. To ensure a reliable database for every radial position during PDA measurements as termination criterion sample size and measurement time were set to 50000 droplets or 60 seconds, respectively. For every radial position, at least 15000 droplets were detected. The raw data from the manufacturer software were used to compute arithmetic means, statistical data as well as additional information using the toolbox *SprayCAT*, according to Sängler [8]. Further Information concerning computation of global size distribution and drop size moments can be obtained from DIN SPEC 91325 as well as from Albrecht [16]. All PDA measurements were conducted at an axial distance of $z = 200$ mm from the nozzle orifice and repeated at least 3 times. For each operating condition and nozzle configuration, rotational symmetry of the spray cone was proven, taking a full radial profile in a first set of experiments. After rotational symmetry was proven, the following repetition measurements were performed taking half profiles from the spray edge to the centre at $x = 0$ mm. The results of those set of experiments were afterwards mirrored to get full profiles. Therefore all radial Sauter diameter distributions are shown as mirrored profiles at $x = 0$ mm.

Results and discussion

In order to investigate the influence of the nozzle configuration on spray quality for the external mixing twin-fluid atomizer described above, experiments were conducted at operating conditions presented in Table 3. For all experiments, pressurized air at 20°C was used as atomization agent.

Table 3. Operating conditions of the experiments for both nozzle configurations

η_{liq} [mPas]	\dot{m}_{gas} [kgh ⁻¹]	\dot{m}_{liq} [kgh ⁻¹]	v_{gas} [ms ⁻¹]	GLR [-]
1/50/100/200	3/6/9/12/15	30	30/60/90/120/150	0.1/0.2/0.3/0.4/0.5

Influence of the nozzle configuration on spray quality

For quantitative comparison of the two nozzle configurations as well as for the description of the influence of liquid viscosity and GLR on Sauter mean diameter, radial measurements were performed (see Figure 2). For reasons of improved clarity, only data for GLR = 0.3 and 0.5 are shown as radial profiles. It has to be mentioned, that Figure 2 shows local values for $\eta_{liq} = 1\text{mPas}$ ($x \leq 0\text{mm}$) and $\eta_{liq} = 50\text{mPas}$ ($x \geq 0\text{mm}$).

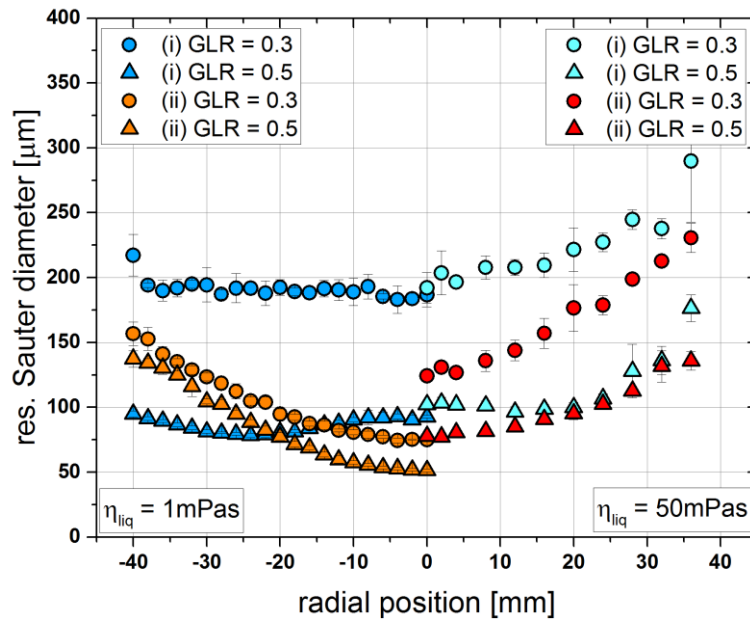


Figure 2. Radial measurements ($z = 200\text{mm}$) of resulting Sauter Diameter using both nozzle configurations (i) at GLR = 0.3 and 0.5 – liquid viscosity $\eta_{liq} = 1\text{mPas}$ (left), liquid viscosity $\eta_{liq} = 50\text{mPas}$ (right)

Comparing the radial shape of droplet size distributions, nozzle configuration (i) shows an almost constant Sauter mean diameter over the radial profile for low liquid viscosity, whereas at higher liquid viscosity a v-shaped profile is detected, with higher droplet size at the outer boundary. For nozzle configuration (ii) a v-shaped profile was detected for both viscosities and GLR with a minimum Sauter mean diameter on the spray axis.

As expected, with increasing GLR, for both nozzle configurations and both viscosities, a decreasing Sauter mean diameter was measured. With increasing liquid viscosity, Sauter mean diameters for all operating conditions are increased. For low liquid viscosity applying nozzle configuration (i) the decrease of droplet size is significantly higher, compared to nozzle configuration (ii), i.e. nozzle configuration (ii) is less sensitive to GLR. Comparing the nozzle configurations applying higher liquid viscosity, an increasing GLR leads to significant lower Sauter mean diameters for both nozzle configurations.

In order to compare all experiments with the two different nozzle configurations (i) and (ii) regarding spray quality, the mass weighted integral Sauter diameter (ID_{32}) was calculated as proposed by Sanger [8]; data are plotted in Figure 3. For all experiments a decrease in ID_{32} with increasing GLR is observed. With increasing liquid viscosity, the ID_{32} value increases significantly for both nozzle configurations for $GLR < 0.4$. For $GLR \geq 0.4$ and different viscosities the deviation in the ID_{32} value is marginal. Comparing both nozzle configurations, the ID_{32} value is decreasing with a larger gradient using nozzle configuration (i). In contrast to this, the ID_{32} value for nozzle configuration (ii) is remarkably lower at $GLR < 0.4$ compared to configuration (i). At $GLR = 0.5$, it is worth mentioning, that nozzle configuration (i) has already a lower ID_{32} than configuration (ii). This is caused by slow droplets at the edge of the spray cone, resulting from the disintegrated sheet of nozzle configuration (ii), moving in a region with small aerodynamic forces.

For additional comparison, spray angle was estimated based on 1000 high speed camera images at each operating condition was done, applying the method for spray angle determination according to Sanger [8]. Exemplarily and for improved clarity only two viscosities at different GLR are shown in Figure 4.

Applying low viscosity for nozzle configuration (i) a strictly monotonic decrease of spray angle with increasing GLR is observed, whereas configuration (ii) shows nearly constant spray angle values for all GLR. With increased viscosity applying nozzle configuration (i), same dependence on GLR is detected for larger spray angles. For nozzle

configuration (ii) and increased viscosity, lower spray angle values are detected, showing also constant values for GLR variation, except for GLR = 0.5.

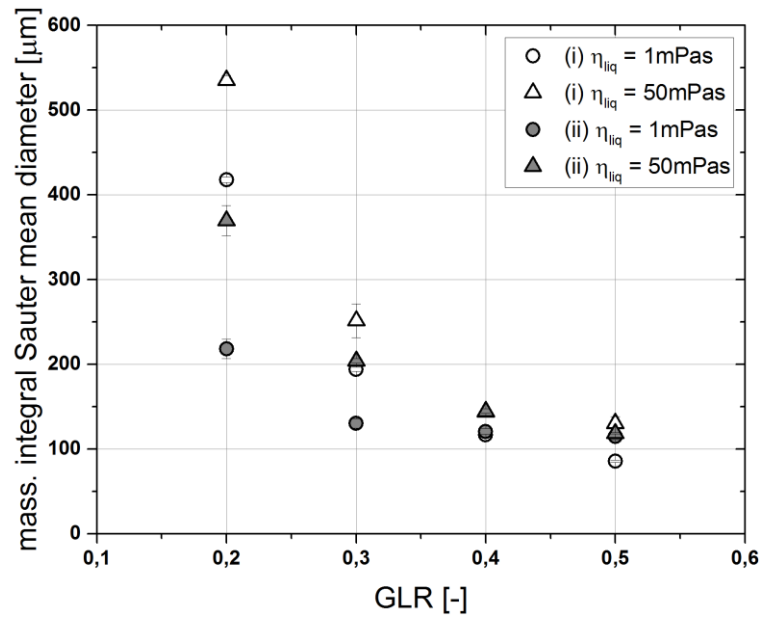


Figure 3. Influence of liquid viscosity and GLR on mass weighted integral Sauter diameter comparing nozzle configurations at $z = 200\text{mm}$

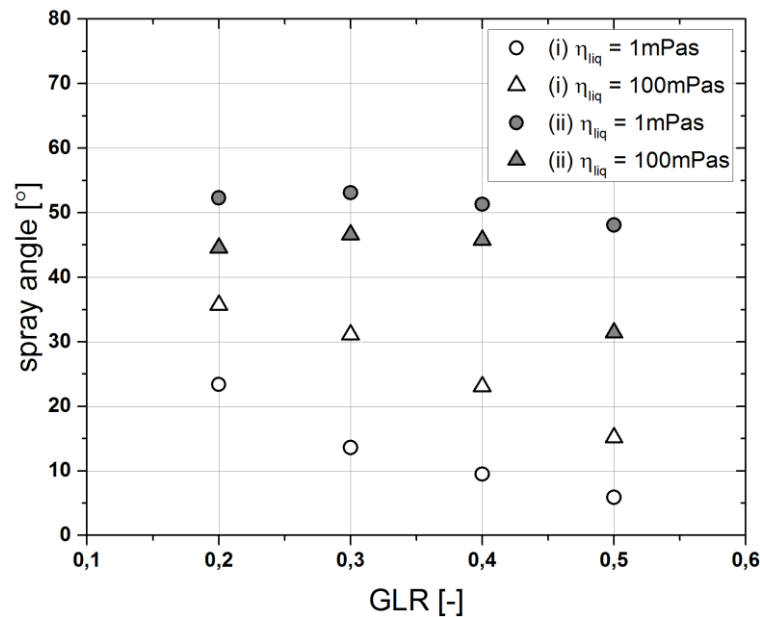


Figure 4. Influence of liquid viscosity and GLR on spray angle, measured by high speed camera images, comparing nozzle configurations

Observed primary breakup for different nozzle configurations, liquid viscosity and GLR

For visualization of the spray, high speed camera images of primary jet breakup applying nozzle configuration (i) at different GLR and liquid viscosity are shown in Figure 5. The images are framed in different colours indicating various spray quality.

Increasing viscosity at low GLR (blue) leads to the formation of membranes at the spray centre, which result in large elongated ligaments after disintegration of the membrane; this is caused by the damping effects of increased liquid viscosity. For viscosities up to 100mPas and increasing $\text{GLR} \geq 0.3$ (green) the jet disintegration occurs close to the nozzle orifice due to the fast surrounding gas flow, producing a homogeneous spray according to Figure 2(left) with a decreasing spray angle as shown in Figure 4. Applying liquid viscosities up to 200mPas and $\text{GLR} \geq 0.3$ (red) the

primary jet is disintegrated into partly radial elongated ligaments, which move out of the spray centre, leading to larger droplets at the spray outer boundary and an increased spray angle as also shown in Figure 4.

According to the regime classification of Lasheras et al. [3] and Zhao et al. [10], for low gas velocities at the nozzle orifice ($GLR = 0.1$), the liquid jet is slightly elongated and reduced in diameter due to aerodynamic forces, which leads to Rayleigh type breakup. For increasing gas velocity ($GLR = 0.2$), and with increasing liquid viscosity even more visible, the membrane type breakup disintegrates the liquid jet, producing long ligaments and large membranes. Between $GLR = 0.3$ and $GLR = 0.4$ the fiber type pulsating mode occurs, which atomizes the liquid jet directly at the nozzle orifice into small fibres and droplets. Changes in local droplet density mark the transition region between the submodes pulsating and superpulsating at higher gas velocities ($GLR = 0.5$).

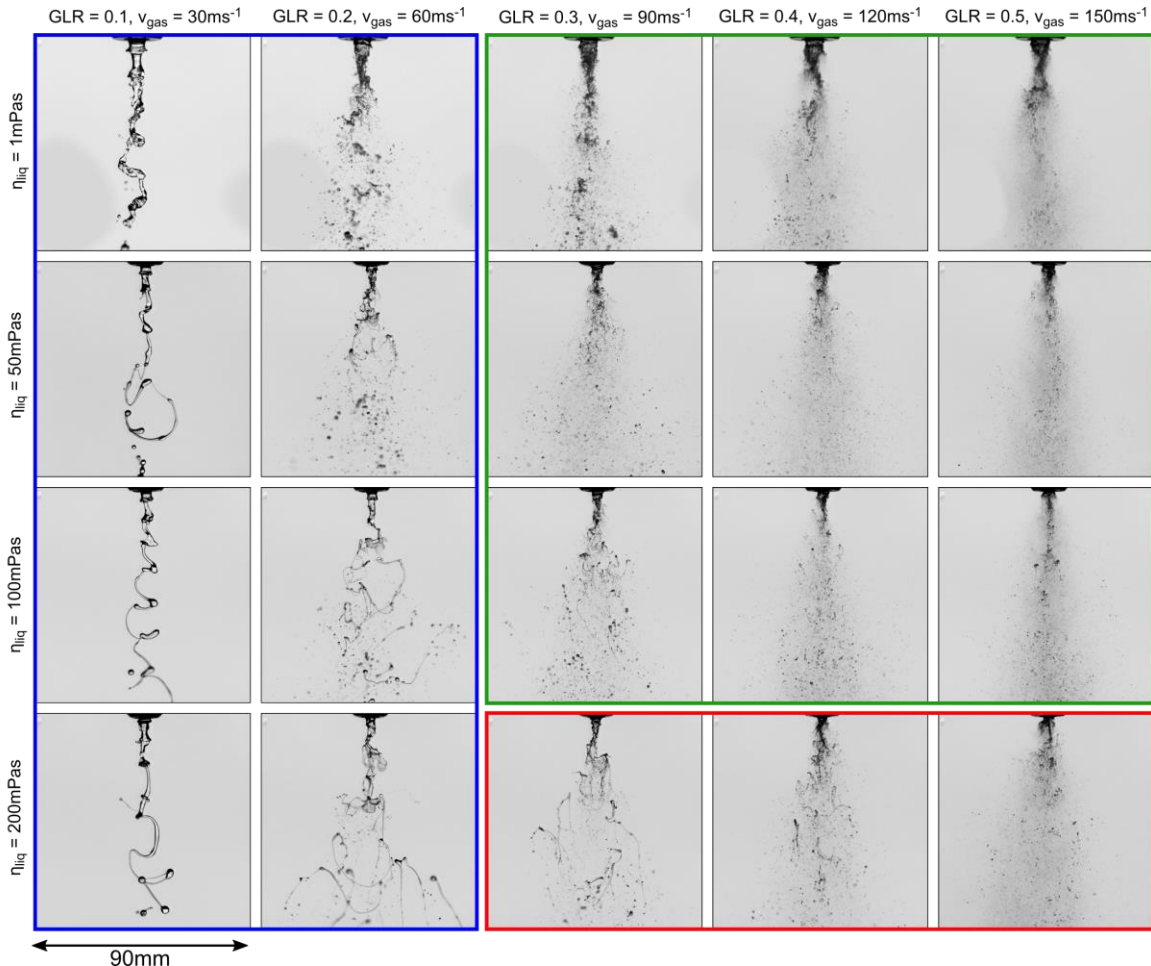


Figure 5. High-speed camera images of the primary liquid disintegration process using nozzle configuration (i), different liquid viscosities and GLR (i.e. v_{gas})

The corresponding high-speed camera images for nozzle configuration (ii) are shown in Figure 6. For increasing viscosity and low GLR (blue), a compact sheet exits the nozzle orifice and is disintegrated into large droplets or ligaments, due to the low gas velocity. With increasing GLR and for all viscosities (red), the liquid sheet disintegrates closer to the nozzle orifice into droplets. Due to the faster gas jet in the spray centre, the resulting droplets are smaller, whereas ligaments moving out of the spray centre are not further disintegrated, due to the slow gas flow in this region. For further increasing GLR and all viscosities (green), the drop size in the spray centre is decreasing, which leads to regions with varying droplet number density. The further decrease in drop size at the edge of the spray cone is marginal, due to the low gas velocity in this area. A nearly constant spray angle is detected, which is independent of gas velocity, due to the steady disintegration of the liquid sheet at the nozzle orifice (see Figure 4).

For $GLR > 0.2$, the classification diagram of Zhao et al. [10] predicts the Christmas tree breakup with characteristic horizontal compact liquid fragments for nozzle configuration (ii); this effect cannot be seen in the high speed images of Figure 6. However changes of the morphology of jet disintegration for higher gas velocities ($GLR \geq 0.3$), like small fibres near the nozzle orifice and droplet density variations in the spray centre similar to a fibre type breakup in pulsating or superpulsating submode according to Lasheras et al. [2,3] can be observed.

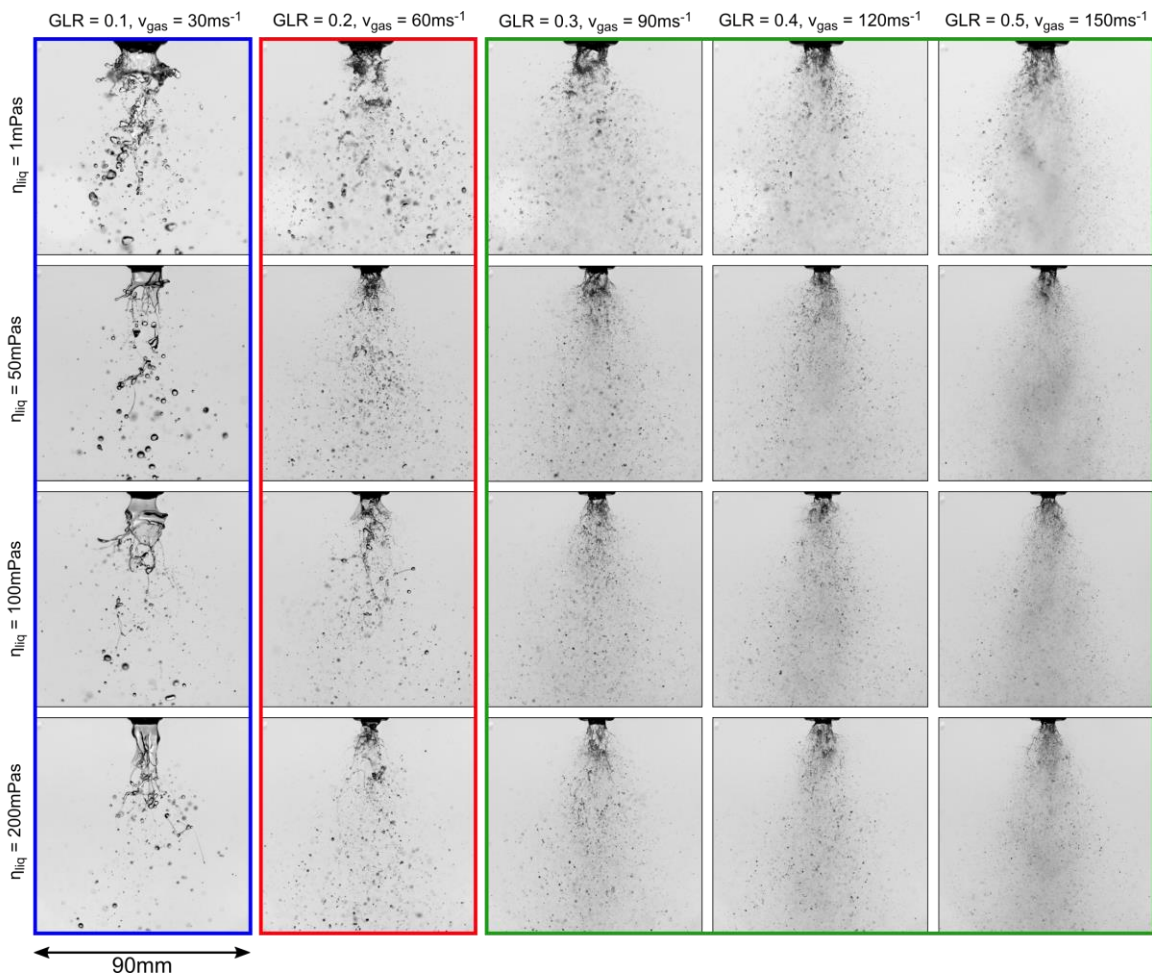


Figure 6. High-speed camera images of the primary liquid disintegration process using nozzle configuration (ii), different liquid viscosities and GLR (i.e. v_{gas})

Conclusions

In the present study two different external mixing twin-fluid nozzle configurations (central liquid jet (i) and liquid sheet (ii)) with equal orifice areas for liquid and gas are compared. This nozzle geometry allows for constant operating conditions (GLR, \dot{m}_{liq} , v_{gas} and momentum flux ratio) for both configurations. Liquid viscosity and GLR (i.e. gas velocity) were varied and local Sauter mean diameter, mass weighted integral Sauter diameter, as well as spray angle and primary breakup morphology were detected.

In general, nozzle configuration (i) achieves better spray quality (i.e. lower integral Sauter mean diameter) for increased GLR and low liquid viscosity. Applying nozzle configuration (ii) improved spray quality for low GLR and higher liquid viscosities is observed. As a drawback larger droplets at the boundary of the spray occur. Furthermore nozzle configuration (ii) leads to increased and constant spray angles, compared to configuration (i). Comparing quantitative and qualitative findings, the following detailed conclusions can be drawn:

- (1) For nozzle configuration (i), a nearly constant radial Sauter mean diameter profile is observed for low liquid viscosity and both GLRs. For all operating conditions applying configuration (ii) larger droplets at the boundary of the spray cone are detected.
- (2) With higher liquid viscosity for both nozzle configurations, Sauter mean diameters are increased, caused by the damping effects of the liquid. The sensitivity of Sauter mean diameter on GLR is higher applying nozzle configuration (i) than for nozzle configuration (ii).
- (3) The measured spray angle stays nearly constant for nozzle configuration (ii) over the range of investigated GLR. With increasing liquid viscosity, the spray angle is slightly decreased. Applying configuration (i), the spray angle decreases with increasing GLR for both viscosities. With higher liquid viscosity, the spray angle is increased, due to the radially elongated ligaments produced.

Acknowledgements

The authors gratefully acknowledge the financial support by the Helmholtz Association of German Research Centers (HGF), within the research field Energy, Material and Resources, Topic 4 Gasification (34.14.02). The present work contributes to the Helmholtz Virtual Institute for Gasification Technology–HVI GasTech (VH-VI-429).

Nomenclature

b	wall thickness [mm]	GLR	Gas-to-liquid ratio [-]	v_{gas}	orifice gas velocity [ms^{-1}]
D_{inner}	inner diameter [mm]	ID_{32}	integral Sauter diam. [μm]	x, y, z	coordinate axis [mm]
D_{outer}	outer diameter [mm]	\dot{m}_{gas}	gas mass flow [kg h^{-1}]	η_{liq}	dy. liquid viscosity [mPas]
D_{32}	Sauter diameter [μm]	\dot{m}_{liq}	liquid mass flow [kg h^{-1}]	ρ_{liq}	liquid density [kg m^{-3}]
f	data rate [s^{-1}]	r	length [mm]	σ	surface tension [Nm^{-1}]

References

- [1] Jakobs T., Djordjevic N., Fleck S., Mancini M., Weber R., and Kolb T., 2012, "Gasification of high viscous slurry R&D on atomization and numerical simulation," *Applied Energy*, **93**, pp. 449–456.
- [2] Chigier N., and Faragó Z., 1992, "Morphological Classification of Disintegration of Round Liquid Jets in a Coaxial Air Stream," *Atomization and Sprays*, **2**(2), pp. 137–153.
- [3] Lasheras J. C., Villermaux E., and Hopfinger E. J., 1998, "Break-up and atomization of a round water jet by high-speed annular air jet," *J. Fluid Mech.*, **357**, 351–379.
- [4] Lorenzetto G. E., and Lefebvre A. H., "Measurements of Drop Size on a Plain-Jet Airblast Atomizer," *AIAA Journal*, **15**(7), pp. 1006–1010.
- [5] Jasuja A. K., 1982, "Plain-Jet Airblast Atomization of Alternative Liquid Petroleum Fuels Under High Ambient Air Pressure Conditions," *The American Society of Mechanical Engineers*(3).
- [6] Rizk N.K., and Lefebvre A.H., 1984, "Spray characteristics of plain-jet airblast atomizers," *ASME*, **634**(106).
- [7] Schmidt P., and Walzel P., 1980, "Zerstäuben von Flüssigkeiten," *Chemie Ingenieur Technik*, **52**(4), pp. 304–311.
- [8] Alexander Daniel Sängler, 2018. *Zerstäubung hochviskoser Fluide bei variierendem Systemdruck - Grundlagenforschung zur Hochdruck-Flugstromvergasung*.
- [9] Leboucher N., Roger F., and Carreau J.-L., 2012, "Characteristics of the spray produced by the atomization of an annular liquid sheet assisted by an inner gas jet," *Atomization and Spray*, **22**(6), pp. 515–542.
- [10] Zhao H., Xu J.-L., Wu J.-H., Li W.-F., and Liu H.-F., 2015, "Breakup morphology of annular liquid sheet with an inner round air stream," *Chemical Engineering Science*, **137**, pp. 412–422.
- [11] Li X., and Shen J., 1999, "Experimental Study of Sprays from Annular Liquid Jet Breakup," *Journal of Propulsion and Power*, **15**(1), pp. 103–110.
- [12] Chigier N. A., and Farago Z., 1992, "Morphological classification of disintegration of round liquid jets in a coaxial air stream," *Atomization and Sprays*, pp. 137–153.
- [13] Searle G.F.C., "Simple Viscometer for Very Viscous Liquids," *Proceedings of the Cambridge Philosophical Society, Mathematical and physical sciences*, **1912**.
- [14] du Nouy, P. L., 1925, "An Interfacial Tensiometer for Universal use," *The Journal of General Physiology*, **7**(5), pp. 625–631.
- [15] Araneo L., Damaschke N., and Tropea C., 2002, "Measurement and Prediction of the Gaussian Beam Effect in the PDA," *Springer*, pp. 189–208.
- [16] Albrecht H.-E., 2003. *Laser doppler and phase doppler measurement techniques*, Springer, Berlin, New York.
- [17] Kapulla R., and Najera S. B., 2006, "Operation conditions of a phase Doppler anemometer: droplet size measurements with laser beam power, photomultiplier voltage, signal gain and signal-to-noise ratio as parameters," *Meas. Sci. Technol.*, **17**(1), pp. 221–227.
- [18] Hede P. D., Bach P., and Jensen A. D., 2008, "Two-fluid spray atomization and pneumatic nozzles for fluid bed coating / agglomeration purposes: a review," *Chemical Engineering Science*, **63**, pp. 3821–3842.

Effect of gas jet angle on primary breakup and droplet size applying coaxial gas-assisted atomizers

Simon Wachter,^{*1} Tobias Jakobs¹ and Thomas Kolb^{1,2}

¹Karlsruhe Institute of Technology, Institute for Technical Chemistry, 76344 Eggenstein-Leopoldshafen, Germany

²Karlsruhe Institute of Technology, Engler-Bunte-Institute, 76131 Karlsruhe, Germany

*Corresponding author email: simon.wachter@kit.edu

Abstract

This study investigates the influence of gas jet angle on primary jet breakup and the resulting droplet size distribution for coaxial gas-assisted atomizers. In industrial applications, the gas jet of these atomizers are typically angled towards the liquid jet, whereas in most spray investigations in literature, parallel flow configurations are used. To enable a detailed analysis of the influence of the gas jet angle, three atomizers with angles of 0°, 15° and 30° were examined. Other geometric parameters, such as liquid jet diameter, gas gap width and wall thickness were kept constant. For each atomizer, two gas velocities at constant liquid mass flow were investigated i.e., two gas-to-liquid ratios (GLRs). An additional set of experiments was performed at increased system pressure using three atomizers with identical gas jet angles, but with an adapted gas orifice area in order to keep gas velocity, GLR and momentum flow ratio constant for all pressure levels. Water and a glycerol/water-mixture were applied in order to investigate the influence of liquid viscosity. The primary breakup process was monitored by a high-speed camera, whereas the resulting droplet size was detected using a phase-Doppler anemometer. For all system pressures and liquid viscosities under investigation, a distinct influence of gas jet angle on primary breakup as well as on resulting droplet size distribution was observed for low gas velocity.

Keywords

Gas-assisted atomizer, angled gas jet, atomizer geometry, viscosity, system pressure

Introduction

High-pressure entrained flow gasification (EFG) is a key technology in the realization of a future, carbon-neutral circular economy, as it is an enabling technology to close the carbon cycle through the conversion of biomass and waste-based feedstocks into syngas (CO + H₂). EFG typically uses oxygen as gasification agent, which also serves as atomization agent; as a result gas-to-liquid ratios (GLRs) < 1 are applied [1]. Coaxial gas-assisted atomizers are typically used, due to their advantages with respect to abrasion and clogging. Faragò and Chigier [2] performed detailed investigations concerning breakup morphology, where liquid was provided from a central tube with a concentric gas stream. The breakup of water was classified into spray regimes, showing a transition from the Rayleigh-type to the membrane and fiber type breakup with increasing Weber number at constant liquid Reynolds number. Lasheras and Hopfinger [3] expanded the regime classification for different momentum flux ratios. Studies on the droplet size that resulted from this configuration applied Newtonian viscous liquids in a viscosity range of $\eta_{liq} = 1 - 100$ mPa·s and $GLR = 1 - 12$, and were conducted by Lorenzetto [4], Jasuja [5], Rizk [6] and Walzel [7]. For $GLR < 1$ and 4 liquid viscosities, Sängler et al. [8] detected 2 different primary instability modes (flapping and pulsating) that influenced the resulting drop size.

In the aforementioned studies, high-velocity annular gas streams with a straight exit channel were typically utilized. Nonetheless, industrial applications typically use a converging exit (straight inner, angled outer wall) or an angled gas exit (inner and outer wall angled) [9–13].

The change from straight to converging gas-exiting channels and its effect on the resulting droplet size was first reported by Hardalupas et al. [14]. In their experiments, the straight exit was changed to a converging angle of $\alpha = 28^\circ$. As a result, a decrease in droplet size over the entire spray cone, depending on the gas-to-liquid velocity ratio $v_{\text{gas}}/v_{\text{liq}}$, was identified. An increase in the gas-to-liquid velocity ratio above 50 revealed no further changes in droplet size [14]. Additionally, Varga et al. [15] compared a nozzle with a straight gas channel with a converging gas channel for varying $v_{\text{gas}} = 50 - 165 \text{ m}\cdot\text{s}^{-1}$ and constant $v_{\text{liq}} = 1.7 \text{ m}\cdot\text{s}^{-1}$. In contrast to the previously-mentioned study, a constant reduction of droplet size of $\Delta d_{32} \approx 18 \mu\text{m}$ was detected (variance in droplet size of 19 – 33 %) for all operating conditions when changing from the straight nozzle exit to a converging exit channel. Varga et al. [15] denoted that the reduction in droplet size could be attributed to a reduction in the boundary layer thickness when utilizing the converging gas channel. In the studies mentioned, straight gas channels were compared to converging gas channels, which feature an inner straight wall and outer wall with a distinct angle. Investigations of angled gas channels (inner and outer walls), as well as a variation and comparison of the angle with a straight gas channel have not been reported yet.

In this context, this study is focused on the influence of the gas channel angle on resulting droplet size distribution and primary jet breakup at operating conditions relevant for EFG. A high-speed camera was used to detect the primary breakup and a phase Doppler analyzer (PDA) for measuring the local droplet velocity and size. 3 different gas channel angles were investigated at 2 gas velocities, 2 dynamic viscosities and 2 system pressure levels while applying pressure-adapted atomizers [16]. Additional measurements using particle image velocimetry were also performed in order to obtain a deeper insight into the gas flow field in the near-nozzle region.

Experimental setup

The experimental setup consists of the pressurized atomization test rig (PAT), a phase Doppler analyzer, a high-speed camera and 6 different atomizers. A schema of the PAT spray test rig with exhaust air system and a horizontal cross-sectional view (A-A) is presented in Wachter et al. [17].

The pressure chamber has an internal diameter of 300 mm and a total height of 3000 mm. It is designed for operation at system pressures of up to $p_{\text{sys}} = 21 \text{ bar}$. The external-mixing twin-fluid atomizer is mounted on the axially (z-direction) movable twin-fluid lance, which is fed by one of the two eccentric screw pumps with liquids that featured viscosities of up to $\eta_{\text{liq}} = 1000 \text{ mPa}\cdot\text{s}$. The liquid mass flow can be controlled in the range of P1: $\dot{M}_{\text{liq}} = 10 - 60 \text{ kg}\cdot\text{h}^{-1}$ / P2: $\dot{M}_{\text{liq}} = 60 - 200 \text{ kg}\cdot\text{h}^{-1}$ using different screw pumps. The liquid mass flow and density are measured using a Coriolis flow meter with an uncertainty of $< 0.5 \%$. The compressed air volume flow \dot{V}_{gas} is detected by a turbine meter with a measuring range of $\dot{V}_{\text{gas}} = 0.85 - 25 \text{ m}^3\cdot\text{h}^{-1}$ and an uncertainty of $< 0.5 \%$. A recalculation of volume to mass flow is done using the locally-measured gas temperature and pressure at the measurement turbine. To ensure well-defined nozzle inlet conditions, the liquid can be stirred and tempered in the range of $T = 10 \text{ }^\circ\text{C} - 50 \text{ }^\circ\text{C}$. The test rig is equipped with three glass windows (no inclusions or cords) that allow for optical access to the spray chamber and avoid any disturbances to the laser beam. Two optical ports are located at $\Phi_{\text{R}} = 0^\circ$ and 70° to enable Phase Doppler measurements in scattering mode with – preferably – the highest intensity (first-order refraction) [18]. The third optical port is positioned at $\Phi_{\text{R}} = 180^\circ$ to allow for spray investigations in backlight mode using optical measurement systems. In order to ensure protection from window deposits at the $\Phi_{\text{R}} = 70^\circ$ window location, a wiper is used between each measurement section, which employs compressed air for movement. A flow-straightener (honeycomb structure) is located below the

measuring plane to avoid recirculation of droplets. For all experiments, pressurized air at 20 °C was utilized as atomization agent.

The experiments were conducted with 3 coaxial gas-assisted atomizers – for each pressure range investigated, as shown in Figure 1, exemplarily, for $p_{\text{sys}} = 1$ bar. In all cases, the central tube had a diameter of $D_{\text{liq}} = 2.0$ mm. To minimize flow induced turbulence, the wall thickness b between the inner and outer orifice was set to $b = 0.1$ mm. The nozzles designed for $p_{\text{sys}} = 1$ bar had a gas orifice diameter of $D_{\text{gas}} = 7.96$ mm, whereas the diameter was reduced to $D_{\text{gas}} = 3.18$ mm for the nozzles designed for $p_{\text{sys}} = 11$ bar. This concept allows for solely varying the system pressure, keeping all other operating conditions constant (v_{liq} , v_{gas} , GLR, \dot{M}_{liq} , \dot{M}_{gas}), as according to Wachter et al. [16].

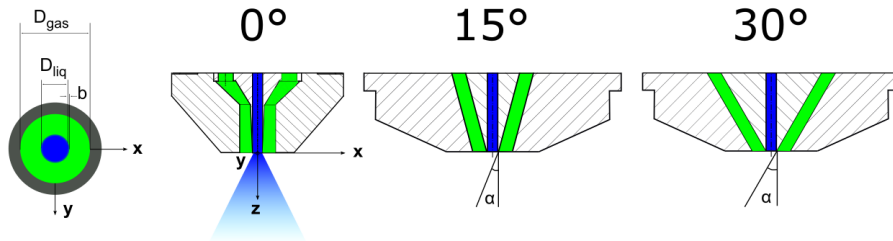


Figure 1. Scheme of the external-mixing atomizers for $p_{\text{sys}} = 1$ bar and 3 different gas channel angles $\alpha = 0, 15$ and 30° .

Table 1. Physical properties of applied liquids at 20 °C and atmospheric pressure.

	η_{liq} in mPa·s	σ in kg·s ⁻²	ρ_{liq} in kg·m ⁻³
Water	1	0.0728	998
Glycerol/water (89.5 wt.%)	200	0.0642	1233

For the investigation of liquid viscosity η_{liq} on the primary jet breakup and droplet size, water and a glycerol/water – mixture were used. The surface tension and density of the two liquids applied are almost constant (see Table 1). The liquid viscosity was quantified by applying a Physica MCR 101 rheometer from Anton Paar with a Searle-type measuring system [19]. The surface tension and density were measured by means of an EasyDyne tensiometer from Krüss that employed the Du Noüy ring [20] and weighing methods, respectively. Table 1 displays the mass ratio, viscosity, surface tension and density for both liquids at 20 °C and atmospheric pressure.

A high-speed camera was placed in the nozzle nearfield for the qualitative observation of the primary breakup of the liquid jet. The camera featured a frame rate of 3.6 kHz at a resolution of 1024 x 1024 pixel and frame rates of up to 500 kHz at reduced resolution. A lens with a focal length of $f_{\text{HG}} = 105$ mm was used to capture the primary breakup morphologies. In this study, the frame rate was set to at least 7.5 kHz with the respective resolutions given in the images. The images were captured via backlight illumination of the region of interest by means of a special lighting setup of 9 x 4500 lm. Owing to the high intensity and homogeneous distribution of the light, very short exposure times ($t_{\text{Exp}} \sim 7 \mu\text{s}$) were employed. A set of at least 2000 high-speed images was recorded at every operating condition, along with a background reference image without the liquid flow.

In addition, the same camera was used at $z = 200$ mm in order to: (i) optimize the PDA hardware settings (receiver mask); (ii) for the sphericity check of the droplets in the measuring plane to ensure the reliability of the PDA data; (iii) qualitatively confirm the tendencies measured by the PDA; and (iv) as a validation tool for the PDA data in order to eliminate the deviations arising from the Gaussian beam effect [21].

Table 2. Settings of the Fiber PDA evaluated by the sensitivity analysis.

Parameters	Values	Unit	Parameters	Values	Unit
Transmitter focal length	1000	mm	Laser wavelength	561	Nm
Receiver focal length	1000	mm	Laser power	40	mW
Beam expander ratio	1	-	Off-axis angle	70	°
Receiver slit width	200	µm	Frequency shift	80	MHz

The measurement of droplet size within the spray cone at a high spatial and temporal resolution was performed with a Fiber PDA by Dantec Dynamics at $z = 200$ mm. For data collection the PDA was operated in a forward scattering arrangement, with the refraction mode (1st – order) using the asymmetrical Mask B. To guarantee for the detection of large droplets, as expected by the atomization of highly viscous liquids and avoid sizing errors due to the Gaussian beam effect according to Araneo [21], the PDA was set as displayed in Table 2. With this optical configuration, the PDA system enabled the detection of droplets with a minimum size of $1 \mu\text{m}$ and maximum size of $1357 \mu\text{m}$ in the case of water, and $1380 \mu\text{m}$ in that of the glycerol/water mixtures, related to the refractive index of the liquid [18]. To improve the PDA settings, a sensitivity study, as described in [22], was performed.

The receiver and transmitter were mounted on a traverse, which guarantees for spatially-reproducible operation < 0.1 mm and enabled droplet size measurements at distinct positions within the spray cone. The measurements were recorded at several radial positions (traverse along the $x -$ axis) with a radial increment of $\Delta x = 2 - 4$ mm depending on the measurement position. In order to ensure a reliable database for every radial position during PDA measurements as a termination criterion, the sample size and measurement time were set to 50,000 droplets or 60 seconds, respectively. At least 5000 droplets were detected at every radial position. The raw data from the manufacturer software were used to compute arithmetic means and statistical data, as well as additional information using the toolbox *SprayCAT*; see Wachter [17]. For the global characterization of the spray, the computation of a global characteristic diameter, i.e., mass-weighted integral Sauter mean diameter $Id_{32,m}$, was carried out by means of a weighted average, including all measurement positions of a radial profile at a fixed axial position z . The integral Sauter mean diameter $Id_{32,m}$ was calculated according to Equation (1), below, based on the local volume mean diameter $D_{30,i}$ and local surface mean diameter $D_{20,i}$. These diameters were weighted by local mass flux \dot{m}_i and the annulus area A_i , corresponding to the measurement position i along the radial axis $x_1 \leq x_i \leq x_N$ with N measurement positions.

$$Id_{32,m} = \frac{\sum_{i=1}^N D_{30,i}^3 \dot{m}_i A_i}{\sum_{i=1}^N D_{20,i}^2 \dot{m}_i A_i} \quad (1)$$

Further information concerning the computation of global size distribution and droplet size moments can be obtained from DIN SPEC 91325, as well as from Albrecht [18]. Each measurement series was repeated at least 3 times. For each operating condition and nozzle configuration, the rotational symmetry of the spray cone was proven, taking a full radial profile in a first set of experiments. After the rotational symmetry was proven, the following repetition measurements were performed, taking half profiles from the spray edge to the centre at $x = 0$ mm.

Particle image velocimetry (PIV) measurements were performed with a PIV system from Dantec Dynamics that consisted of a CCD camera and a Nd:YAG double-pulse laser for

illumination. The camera was equipped with a $f = 105$ mm lens and spacer rings, resulting in a field of view of 28×28 mm² at a resolution of 4 megapixels. The gas phase was seeded with di-ethyl-hexyl-sebacat (DEHS) droplets in the size range of $d_{\text{DEHS}} = 1 - 5$ μm in order to follow the gas phase undisturbed [23], using a seeding generator from LaVision. As liquid flow, while PIV measurements, would lead to a strong reflection that overexposes the camera sensor; when hit by the laser sheet, a black-coloured pin with an identical diameter and 10 mm in length was used to replace the liquid jet for the measurements. Each resulting image was averaged out of 50 double images.

Results and Discussion

In order to investigate the influence of the gas channel angle on resulting droplet size and primary breakup for the coaxial gas-assisted atomizers described above, the experiments were conducted using the operating conditions presented in Table 3. As the liquid mass flow was set constant at $\dot{M}_{\text{liq}} = 20$ kg·h⁻¹. Liquid velocity changed from $v_{\text{liq}} = 1.77$ m·s⁻¹ for water to $v_{\text{liq}} = 1.45$ m·s⁻¹ for the glycerol/water mixture with $\eta_{\text{liq}} = 200$ mPa·s. The system pressure was varied between $p_{\text{sys}} = 1$ and 11 bar, applying pressure-adapted nozzles.

Table 3. Operating conditions of the experiments for all of the investigated gas channel angles.

\dot{M}_{liq} in kg·h ⁻¹	\dot{M}_{gas} in kg·h ⁻¹	v_{gas} in m·s ⁻¹	GLR
20	12 / 20	60 / 100	0.6 / 1.0

(i) Influence of the gas channel angle on the droplet size and primary breakup

For the quantitative comparison of the resulting droplet size while utilizing different gas channel angles, radial PDA measurements were first performed for the higher liquid viscosity $\eta_{\text{liq}} = 200$ mPa·s and angles $\alpha = 0 - 30^\circ$. Applying liquids with higher viscosity facilitates a better insight into the jet breakup phenomena, due to the damping effects of the viscosity. For the experiments in chapter (i), A_{gas} , p_{sys} and ρ_{gas} were not changed. The measured values for d_{32} at $v_{\text{gas}} = 60$ m·s⁻¹ and $p_{\text{sys}} = 1$ bar are shown in Figure 2 (left).

An increase in gas channel angle leads to a decrease in droplet size, especially at the spray center. This result corresponds to the results of Hardalupas et al. [14] for converging gas channels, as the gas velocity ratio was $v_{\text{gas}}/v_{\text{liq}} = 41.4 < 50$. Typically, a decrease in droplet size is attributed to an increase in the aerodynamic forces, mostly as described by the gas momentum flow ($J_{\text{gas}} = \rho_{\text{gas}} \cdot v_{\text{gas}}^2 \cdot A_{\text{gas}}$). In order to understand this effect, the radial mean velocity profiles of the droplets are also displayed in Figure 2. For an increasing gas channel angle from $\alpha = 0$ to 30° , a significant increase in the droplet mean velocity of $\Delta v_z = 3$ m·s⁻¹ could be detected at the spray center. As the gas velocity at the nozzle orifice remained constant at $v_{\text{gas}} = 60$ m·s⁻¹ for every gas channel angle, a double-pulse PIV was used to detect differences in the flow field of the exiting gas phase, which may be correlated to a change in the gas channel angle. In order to get a better impression of the flow field close to the nozzle orifice, in a first set of PIV measurements 50 double-pulse images for each operating condition were taken. Figure 2 (right) shows the resulting absolute gas phase velocity v_{abs} for the different gas channel angles at $v_{\text{gas}} = 60$ m·s⁻¹ and $p_{\text{sys}} = 1$ bar. As can be seen from the absolute gas phase velocities, the high-velocity gas phase that emerged from the nozzle with $v_{\text{gas}} = 60$ m·s⁻¹ was calculated. For $\alpha = 0^\circ$, the gas stream sheared the pin without a distinct impact and velocity slightly decreased with further distance from the nozzle orifice. In contrast to this, for $\alpha = 30^\circ$, the gas phase hits the pin, whereby the cross-sectional area of the gas flow was reduced, resulting in an increase in velocity in the range of $\Delta v_{\text{gas}} \approx 20$ m·s⁻¹. The decrease in the shear layer thickness corresponds to the findings of Varga et al. [15], who proposed this effect when utilizing converging nozzle geometries.

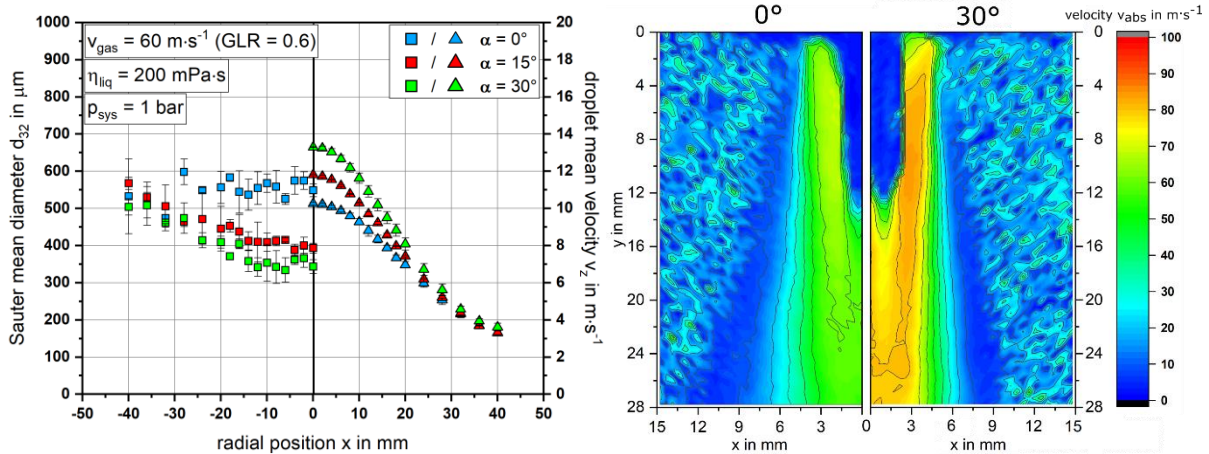


Figure 2. Radial measurement of d_{32} and v_z for $\alpha = 0, 15$ and 30° at $v_{\text{gas}} = 60 \text{ m}\cdot\text{s}^{-1}$ (GLR = 0.6), $\eta_{\text{liq}} = 200 \text{ mPa}\cdot\text{s}$ and $p_{\text{sys}} = 1 \text{ bar}$ (left); PIV measurements of the seeded gas phase at the nozzle orifice for different gas channel angles ($\alpha = 0, 30^\circ$) at $v_{\text{gas}} = 60 \text{ m}\cdot\text{s}^{-1}$ and $p_{\text{sys}} = 1 \text{ bar}$ (right).

The gas velocity remains high even after the impact and the alignment over the entire measurement length in z -direction. The noted impact on the liquid jet, as well as the reduced shear layer thickness, leads to an increase in the aerodynamic forces, which increases droplet velocities and decreases droplet size.

The effect of gas channel angle on primary breakup is depicted by high-speed camera images in Figure 3 (left) at the investigated $\alpha = 0 - 30^\circ$, $v_{\text{gas}} = 60 \text{ m}\cdot\text{s}^{-1}$, $\eta_{\text{liq}} = 200 \text{ mPa}\cdot\text{s}$ and $p_{\text{sys}} = 1 \text{ bar}$.

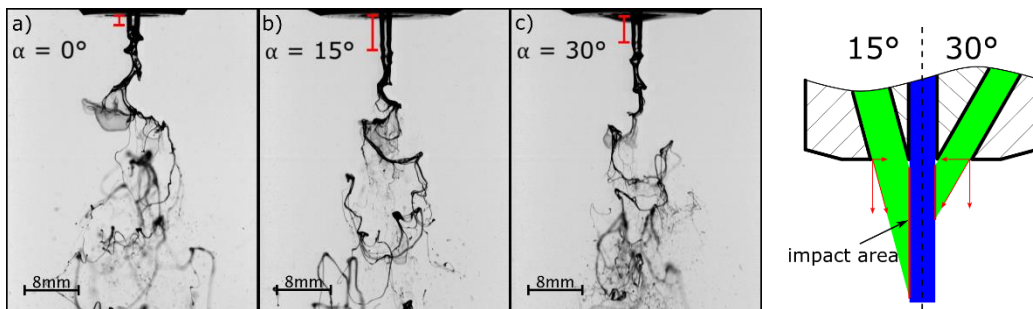


Figure 3. High-speed camera images of the primary breakup at varying gas channel angles $\alpha = 0, 15$ and 30° , with the atomizers applied at $v_{\text{gas}} = 60 \text{ m}\cdot\text{s}^{-1}$, $p_{\text{sys}} = 1 \text{ bar}$, with $\eta_{\text{liq}} = 200 \text{ mPa}\cdot\text{s}$ (left); scheme of the gas emerging from the nozzles with $\alpha = 15$ and 30° in the respective gas channel angle and with the respective impact region (right).

As shown in Figure 3 (left, a–c), there was no significant change in the primary breakup morphology of the liquid jet from $\alpha = 0^\circ$ to 30° . However, the only detectable difference can be seen on the liquid jet near the nozzle orifice. Comparing the high-speed camera images at this position from Figure 3 (a) to (b), a straight emerging jet without disturbances or formation of instabilities near the nozzle orifice is detectable (red mark). A further increase up to $\alpha = 30^\circ$, results in a shorter stable liquid jet (see Figure 3 (c)).

This effect may be explained by the gas channel angle, leading to a velocity component in radial direction and thus to radial forces stabilizing the jet. For $\alpha = 15^\circ$, the radial component is comparably low in value, but has a significant high impact area (see Figure 3 (right, 15°)). For increasing α to 30° , the radial force increases, but the stabilizing impact area is reduced, as presented in Figure 3 (right, 30°).

The stabilization inhibits the formation of the Kelvin-Helmholtz instabilities (KHIs) that normally develops near the nozzle orifice. In an additional set of experiments, the necessary gas mass flow to form a KHI within the region of the red mark was investigated.

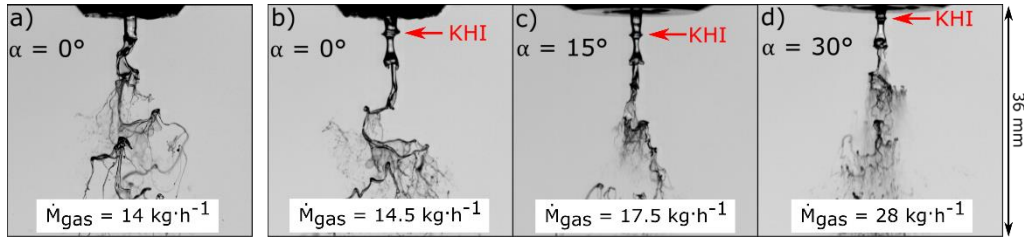


Figure 4. High-speed camera images of primary jet breakup at $p_{sys} = 1$ bar with $\eta_{liq} = 200$ mPa·s for: a) $\alpha = 0^\circ$ and $v_{gas,KHI} = 70$ m·s⁻¹; b) $\alpha = 0^\circ$ and $v_{gas,KHI} = 72.5$ m·s⁻¹; c) $\alpha = 15^\circ$ and $v_{gas,KHI} = 87.5$ m·s⁻¹; as well as d) $\alpha = 30^\circ$ and $v_{gas,KHI} = 140$ m·s⁻¹.

The data in Figure 4 show, that with increasing gas channel angle, a higher velocity component stabilizes the liquid jet. As a result, a higher gas mass flow is needed to form the KHI for increasing gas channel angle.

(ii) Influence of dynamic viscosity and system pressure on droplet size for different gas channel angles

For a quantitative comparison of the resulting integral Sauter mean diameter utilizing 3 different gas channel angles, radial PDA measurements were performed for varying dynamic viscosities, gas velocities and system pressures. In order to indicate the resulting influences more clearly, the calculated $Id_{32,m}$ values are displayed in Figure 5 (left).

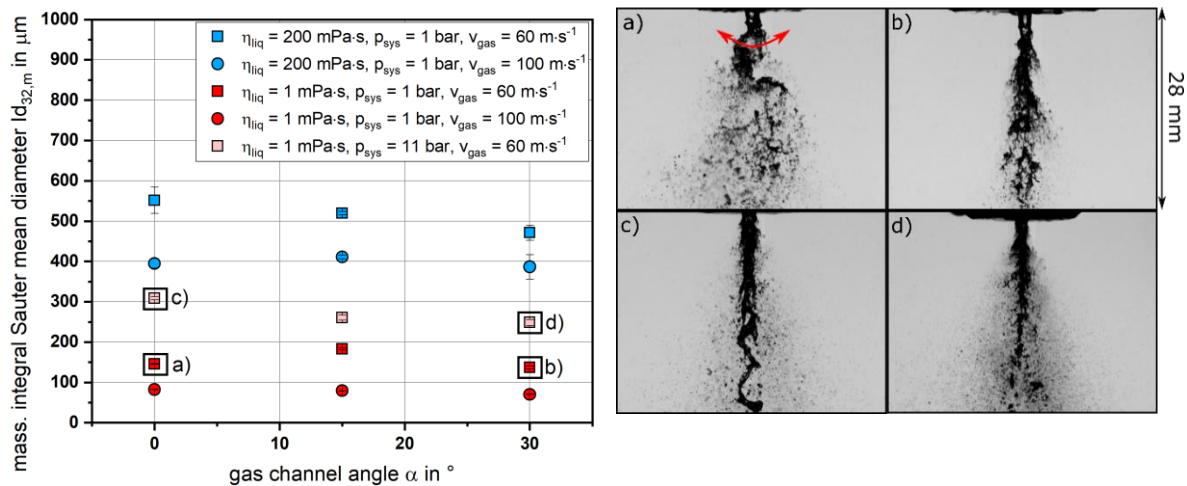


Figure 5. Calculated $Id_{32,m}$ values for varying gas channel angles $\alpha = 0, 15$ and 30° as a function of the dynamic viscosity, gas velocity and system pressure (left); high-speed camera images of the primary jet breakup for $\eta_{liq} = 1$ mPa·s, $v_{gas} = 60$ m·s⁻¹ at: a) $p_{sys} = 1$ bar, $\alpha = 0^\circ$ (flapping instability¹); b) $p_{sys} = 1$ bar, $\alpha = 30^\circ$; c) $p_{sys} = 11$ bar, $\alpha = 0^\circ$; and d) $p_{sys} = 11$ bar, $\alpha = 30^\circ$ (right).

As presented in Figure 5 (left), for all gas channel angles it can be stated: For increasing liquid viscosity, an increase in droplet size was detected for both gas velocities under investigation. The damping effects of the liquid at higher viscosity explain this effect.

An increase in gas velocity from $v_{gas} = 60$ to 100 m·s⁻¹ leads to a reduction in $Id_{32,m}$ for both viscosities. This effect can be explained by the higher aerodynamic forces, enhancing the jet breakup and droplet formation.

For increasing system pressure p_{sys} , when applying the pressure-adapted nozzles approach, an increase in the droplet size was detected (see Figure 5 (right, c)). This result corresponds

¹ As the results of $\eta_{liq} = 1$ mPa·s and $v_{gas} = 60$ m·s⁻¹ show lower values at $\alpha = 0^\circ$ compared to $\alpha = 15^\circ$, it has to be mentioned, that for $\alpha = 0^\circ$, a flapping primary instability was developed (see Figure 5 (right, a)), leading to a different breakup morphology and to smaller droplets as for $\alpha = 15^\circ$, which was in accordance with Sanger et al. [8].

to previous investigations concerning atomizers with straight gas channels [16]. The effect may be explained by the stronger deceleration of the gas phase by entrainment of surrounding gas with increased system pressure with the given nozzle configuration.

In general, an increase of gas channel angle shifts the $Id_{32,m}$ towards smaller values for low gas velocity $v_{gas} = 60 \text{ m}\cdot\text{s}^{-1}$. This effect was observed for all liquid viscosities and system pressures investigated. As the gas momentum flow J_{gas} was constant for all α , the decrease in the droplet size with increasing gas channel angle may also be explained by the increase in the local gas velocity near the liquid jet.

For gas velocity $v_{gas} = 100 \text{ m}\cdot\text{s}^{-1}$, the effect of the gas channel angle was found to be negligible for both dynamic viscosities investigated. As reported in literature, the effect of J_{gas} on the resulting droplet size weakens with increasing J_{gas} [24–26]. For high J_{gas} , the acceleration of axial velocity, due to an increase in gas channel angle, cannot induce a relevant effect on the liquid jet break up and resulting droplet size.

Conclusions

This study investigated the influence of the gas channel angle at different gas velocity (i.e. GLR), dynamic viscosity and system pressure (applying pressure-adapted nozzles) on the spray quality (d_{32} , $Id_{32,m}$) of coaxial gas-assisted atomizers operated at a liquid mass flow of $\dot{M}_{liq} = 20 \text{ kg}\cdot\text{h}^{-1}$. The atomizer geometry was kept similar, except that the gas channel angle was changed in steps of $\alpha = 0^\circ$, 15° and 30° . Two different gas velocities ($v_{gas} = 60 / 100 \text{ m}\cdot\text{s}^{-1}$) were investigated by changing the gas mass flow (i.e., GLR). The dynamic viscosity was varied by applying water and a glycerol/water mixture with $\eta_{liq} = 200 \text{ mPa}\cdot\text{s}$. The measurements were performed at two system pressure levels ($p_{sys} = 1 / 11 \text{ bar}$) utilizing pressure-adapted nozzles in order to keep v_{gas} , \dot{M}_{gas} and GLR constant. High-speed camera images were used to observe the primary breakup and to explain local measurements of droplet size performed by a phase Doppler anemometer. The results of the experiments can be summarized as follows:

- For all investigated gas channel angles, an increase in gas velocity, as well as a reduction of liquid viscosity resulted in smaller droplet size. The increase of system pressure, applying pressure adapted nozzles, led to larger droplets.
- For increasing the gas channel angle, a decrease in the droplet size was detected for a gas velocity of $v_{gas} = 60 \text{ m}\cdot\text{s}^{-1}$. This is caused by the gas jet impact on the liquid jet, leading to increased local gas velocities and thus aerodynamic forces.
- For all investigated gas channel angles, a stabilized region on the liquid jet near the nozzle orifice was detected, inhibiting the formation of Kelvin-Helmholtz instabilities. With increasing gas channel angle, the stabilized area decreased, but the necessary gas mass flow to form the KHI increased significantly due to an increase in the radial stabilizing forces.
- For increased gas velocity of $v_{gas} = 100 \text{ m}\cdot\text{s}^{-1}$, the influence of the gas channel angle was negligibly small and independent of the investigated viscosity.

Acknowledgments

The authors gratefully acknowledge the financial support by the Helmholtz Association of German Research Centers (HGF) in the context of the research program, Materials and Technologies for the Energy Transition (MTET). The present work contributes to the Helmholtz Virtual Institute for Gasification Technology–HViGasTech (VH-VI-429) (<http://www.hvigastech.org/>).

Nomenclature

A_{gas}	orifice area [mm ²]	A_i	area i [mm ²]	b	tube thickness [mm ²]
d_{DEHS}	diameter [μm]	D_{gas}	diameter [mm]	D_{liq}	diameter [mm]
GLR	Gas-to-Liquid ratio [-]	Id_{32}	diameter [μm]	$Id_{32,m}$	diameter [μm]
J_{gas}	momentum flow [N]	\dot{m}_i	mass flux [kg·s ⁻¹ ·m ⁻²]	\dot{M}_{gas}	mass flow [kg·s ⁻¹]
\dot{M}_{liq}	mass flow [kg·s ⁻¹]	p_{sys}	pressure [bar]	T	temperature [°C]
V_{abs}	velocity [m·s ⁻¹]	v_{gas}	velocity [m·s ⁻¹]	$v_{gas,KHI}$	velocity [m·s ⁻¹]
V_{liq}	velocity [m·s ⁻¹]	v_z	velocity [m·s ⁻¹]	V_{gas}	volume flow [m ³ ·h ⁻¹]
x,y,z	position [mm]	α	channel angle [°]	η_{liq}	viscosity [mPa·s]
ρ_{gas}	density [kg·m ⁻³]	ρ_{liq}	density [kg·m ⁻³]	σ	surface tension [kg·s ⁻²]

References

- [1] Jakobs, T., Djordjevic, N., Fleck, S., Mancini, M., Weber, R., and Kolb, T. "Gasification of high viscous slurry R&D on atomization and numerical simulation." *Applied Energy* Vol. 93 (2012): pp. 449–456. DOI 10.1016/j.apenergy.2011.12.026.
- [2] Chigier, N. and Faragó, Z. "Morphological Classification of Disintegration of Round Liquid Jets in a Coaxial Air Stream." *Atomization and Sprays* Vol. 2 No. 2 (1992): pp. 137–153.
- [3] Lasheras, J. C., Villermaux, E., and Hopfinger, E. J. "Break-up and atomization of a round water jet by high-speed annular air jet." *Journal of Fluid Mechanics* Vol. 357 (1998): 351–379. DOI 10.1017/S0022112097008070.
- [4] Lorenzetto, G. E. and Lefebvre, A. H. "Measurements of Drop Size on a Plain-Jet Airblast Atomizer." *AIAA Journal* Vol. 15 No. 7: pp. 1006–1010.
- [5] Jasuja, A. K. "Plain-Jet Airblast Atomization of Alternative Liquid Petroleum Fuels Under High Ambient Air Pressure Conditions." *The american society of mechanical engineers* No. 3 (1982).
- [6] Rizk, N.K and Lefebvre, A.H. "Spray characteristics of plain-jet airblast atomizers." *ASME* Vol. 634 No. 106 (1984).
- [7] Schmidt, P. and Walzel, P. "Zerstäuben von Flüssigkeiten." *Chemie Ingenieur Technik* Vol. 52 No. 4 (1980): pp. 304–311. DOI 10.1002/cite.330520405.
- [8] Sängler, A., Jakobs, T., Djordjevic, N., and Kolb, T. "Effect of primary instability of a high viscous liquid jet on the spray quality generated by a twin-fluid atomizer." *ILASS – Europe 2014 Bremen, 26th Annual Conference on Liquid Atomization and Spray Systems*. DOI 10.5445/IR/1000129940.
- [9] Nasr, G. G., Yule, Andrew J., and Bendig, L. *Industrial sprays and atomization: Design, analysis and applications*. Springer, London, New York (2002).
- [10] Fleck, S., Santo, U., Hotz, C., Jakobs, T., Eckel, G., Mancini, M., Weber, R., and Kolb, T. "Entrained flow gasification Part 1: Gasification of glycol in an atmospheric-pressure experimental rig." *Fuel* Vol. 217 (2018): pp. 306–319. DOI 10.1016/j.fuel.2017.12.077.
- [11] Kim, K. Y. and Marshall, W. R. "Drop-Size Distributions from Pneumatic Atomizers." *A. I. CH. E. Journal* Vol. 17 No. 3: pp. 575–584.
- [12] Yuan, K., Chen, L., and Wu, C. "Study on characteristics of different types of nozzles for coal-water slurry atomization." *Journal of Thermal Science* Vol. 10 No. 4 (2001).
- [13] Carisson, P., Gebart, R., Grönberg, C., Marklund, M., Risberg, M., Wiinikka, H., and Öhrman, O. "Spatially resolved measurements of gas composition in a pressurised black liquor gasifier." *Environmental Progress & Sustainable Energy* Vol. 28 No. 3 (2009): pp. 316–323.

- [14] Hardalupas, Y. and Whitelaw, J. H. "Characteristics of sprays produced by coaxial airblast atomizers." *Journal of Propulsion and Power* Vol. 10 No. 4 (1994): pp. 453–460. DOI 10.2514/3.23795.
- [15] Varga, C. M., Lasheras, J. C., and Hopfinger, E. J. "Atomization of a small-diameter liquid jet by a high-speed gas stream." *American Physical Society (ADS)* Vol. 54 (2001).
- [16] Wachter, S., Jakobs, T., and Kolb, T. "Experimental investigation on the influence of system pressure on resulting spray quality and jet breakup applying pressure adapted twin-fluid nozzles." *International Journal of Multiphase Flow* Vol. 125 (2020): p. 103189. DOI 10.1016/j.ijmultiphaseflow.2019.103189.
- [17] Wachter, S., Jakobs, T., and Kolb, T. "Towards system pressure scaling of gas assisted coaxial burner nozzles – An empirical model." *Applications in Energy and Combustion Science* Vol. 5 (2021): p. 100019. DOI 10.1016/j.jaecs.2020.100019.
- [18] Albrecht, H.-E. *Laser doppler and phase doppler measurement techniques*. Springer, Berlin, New York (2003).
- [19] Searle, G.F.C. "Simple Viscometer for Very Viscous Liquids." *Proceedings of the Cambridge Philosophical Society, Mathematical and physical sciences* Vol. 1912.
- [20] du Nouy, P. L. "An Interfacial Tensiometer for Universal use." *The Journal of General Physiology* Vol. 7 No. 5 (1925): pp. 625–631. DOI 10.1085/jgp.7.5.625.
- [21] Araneo, L., Damaschke, N., and Tropea, C. "Measurement and Prediction of the Gaussian Beam Effect in the PDA." *Springer* (2002): pp. 189–208.
- [22] Kapulla, R. and Najera, S. B. "Operation conditions of a phase Doppler anemometer: droplet size measurements with laser beam power, photomultiplier voltage, signal gain and signal-to-noise ratio as parameters." *Measurement Science and Technology* Vol. 17 No. 1 (2006): pp. 221–227. DOI 10.1088/0957-0233/17/1/034.
- [23] Tropea, C., Yarin, A. L., and Foss, J. F. *Handbook Of Experimental Fluid Mechanics*. Springer Berlin Heidelberg (2007).
- [24] Lefebvre, A.H. "Twin-Fluid atomization Factors influencing mean drop size." *Atomization and Sprays* Vol. 2 (1992): pp. 101–119.
- [25] Liu, H.-F., Li, W.-F., Gong, X., Cao, X.-K., Xu, J.-L., and Chen, X.-L. "Effect of liquid jet diameter on performance of coaxial two-fluid airblast atomizers." *Chemical Engineering and Processing: Process Intensification* No. 45 (2006): pp. 240–245. DOI 10.1016/j.cep.2005.08.003.
- [26] Kim, K. Y. and Marshall, Jr., W. R. "Drop-Size Distributions from pneumatic atomizers." *AIChE Journal* Vol. 17 No. 3 (1971).